Scaled Earthquake Resistant Structures

A thesis submitted to The University of Manchester for the degree of
Doctor of Philosophy
in the Faculty of Science and Engineering

2021

Muhammed Atar

Department of Mechanical, Aerospace and Civil Engineering
The University of Manchester

List of contents

List of figures

List of tables

Abstract

Scaled Earthquake Resistant Structures

Muhammed Atar, 2021

For the degree of PhD/Faculty of Science and Engineering

The University of Manchester

Because testing facilities are limited, and small-scale models are more economically viable, small-scale models are commonly employed to evaluate the seismic performance of buildings. Similarity laws are provided that are assumed to characterise the system of interest, and a smaller or bigger model is created from the related circumstances that will behave in a predictable manner if the scaling laws are accurate. Scaled experiments in earthquake-resistant structural testing have a fundamental problem. Unfortunately, dimensional analysis kind of similitude seldom applies to complicated systems, which is especially troublesome when scaling ratios are significant. The present study provides a novel method to reconstruct full-scale behaviour without the use of any additional techniques such as additional mass, makeshift scaling rules, and artificially high accelerations on experimental models, which are common in traditional scaling approaches. This study aims to present two different types of similitude as part of a new scaling theory called finite similitude for earthquake-resistant structures and structural dynamics. This method is not based on dimensionless forms but rather on the assumption that scaling may be seen as an imaginary process in which space is constricted or extended. The projection of the governing physics, defined on a scaled space, onto the original full-scale space lies at the heart of the new method. It is shown here how the notion may be utilised to build experiments, with numerical and analytical studies used to validate the single and two scaled experiments. This research shows how one and two scaled experimentations can be applied to classical linear and non-linear continuous and discrete structural systems, and practical structural dynamics case studies such as high-rise steel buildings equipped with nonlinear-fluid viscous dampers under earthquake loadings. Furthermore, it has been also shown that the presented scaling technique can more easily deal with the scaled experimentations when the geometrical similarity is broken.

Declaration

No portion of the work referred to in thesis has been submitted in support of an application for another degree or qualification of this or any other university or other institute of learning.

Copyright statement

I. The author of this thesis (including any appendices and /or schedules to this thesis) owns certain copyright or related rights in it (the “Copy-right”) and s/he has given The University of Manchester certain rights to use such Copyright, including for administrative purposes.

II. Copies of this thesis, either in full or in extracts and whether in hard or electronic copy, may be made only in accordance with the Copyright, Designs and Patents Act 1988 (as amended) and regulations issued under it or, where appropriate, in accordance with licensing agreements which the University has from time to time.This page must form part of any such copies made.

III. The ownership of certain copyright, patents, designs, trademarks and other intellectual property (the “Intellectual Property”) and any reproductions of copyright works in the thesis, for example graphs and tables (“Reproductions”), which may be described in this thesis, may not be owned by the author and may be owned by third parties. Such Intellectual Property and Reproductions cannot and must not be made available for use without the prior written permission of the owner(s) of the relevant Intellectual Property and /or Reproductions.

IV. Further information on the conditions under which disclosure, publication and commercialisation of this thesis, the Copyright and any Intellectual Property and /or Reproductions described in it may take place is available in the University IP Policy (see http://www.campus.manchester.ac.uk/medialibrary/policies/intellectualproperty.pdf) , in any relevant Thesis declarations deposited in the University Library, The University Library’s regulations (see http://www.manchester.ac.uk/library/aboutus/regulations) and in The University’s policy on presentation of Theses.

Dedication

This dissertation is dedicated to my late mother **Turkan Atar**. Thank you, Mom, for always believing in my potential to achieve academic excellence. You are no longer with us, but your blessings and memories will live on in our hearts forever. I will always miss you.

Acknowledgements

First and first, in the name of Allah, the Most Gracious and Merciful Alhamdulillah, I would like to thank the Almighty Allah (subhana wa taala) for bestowing upon me good health, courage, and the intellect to complete my thesis. Because of Allah's forgiveness, I have the strength to seize every opportunity and the persevere to complete my dissertation despite all obstacles through hard work.

I would like to express my heartfelt thanks to Dr. Keith Davey, my PhD supervisor at the University of Manchester, for his invaluable advice and support throughout my study. His real passion for the research, as well as his innovative suggestions, improved my vision and analytical skills. His prompt counsel, thorough inspection, and astute attitude to challenges have undeniably contributed to the completion of this work.

I owe Dr. Roohoolamin Darvizeh a great debt of gratitude for his guidance, which has helped me intellectually to become the person I am today. I shall be eternally grateful for his readiness to assist me at any moment, for the countless hours he spent educating, leading, pushing, and inspiring me to become the researcher I am today.

My heartfelt gratitude goes to the Turkish government, particularly the Ministry of National Education, for believing in me and awarding me a scholarship to pursue a Doctor of Philosophy degree in the United Kingdom. May Allah continue to bless my cherished motherland.

All my family members and close friends deserve my heartfelt appreciation. Without their unwavering support and inspiration, I would not have been able to complete this thesis. I want to express my gratitude to my father, Halim Atar, my sisters, Ebru Sahin and Esra Atar, and my brother, Emrah Atar, for inspiring me to pursue my PhD and other endeavors. I sincerely thank each and every one of them.

Chapter ONE

Introduction

1.1 Motivation

Population growth in cities and rapid urbanisation worldwide has necessitated a continuous increase in demand for high-rise buildings for satisfying commercial and residential needs. The cities like New York and London, where the population density is very high, can be shown as an example of the origin of high-rise buildings [1, 2]. Accordingly, some important regulations have been drawn to protect human lives at the same time ensuring the safety and reliability of structures. In order to ensure the reliability of such buildings in terms of human life and their reliable operation under certain loads, especially under lateral loads such as earthquake and wind loads, it is compulsory to study the behaviour of such buildings. Considering future increment in population and significance of the residential buildings, it becomes essential to detect and determine the characteristic behaviour of such structures. Under the light of the obtained information related to buildings could play a crucial role in designing future buildings. Those investigations require various type of analysis such as analytical, numerical or experimental. However, the rapid increment in engineering systems and complex structures makes it difficult to conduct required analyses, especially in the structural dynamics field. Indeed, physical experimentations might be costly, time-consuming and challenging to conduct analysis when the model is too large or small; on the other hand, analytical and numerical studies might be computationally expensive. One of the most common research types in the case of earthquake field is laboratory tests, particularly for massive and high-rise structures that spread worldwide. However, these types of analyses are more challenging and harder to apply. Therefore, scaled experimentation can be defined as a more convenient approach for such structures

since this type of tests are more applicable and cost-effective compared to full-scale laboratory tests. Sized tests are particularly advised as one of the few experimental methods in cases where testing an actual prototype is impractical [3]. In the last few years, similitude theory has been used to provide useful tools, which can derive laws for designing a scaled-up or down model of a prototype. These similarity laws allow reconstructing the full-scale model's behaviour from that of the scaled model (or vice versa). As a result of applying these sets of criteria and scaling rules, it is possible to construct a more convenient model to test and progress towards analytical or numerical domains with more computationally sufficient resolution. Because testing facilities are restricted and small-scale models are more economically practical, scaled-down models are routinely employed to examine the seismic performance of structures.

Scaled experimentation for parts and products continues to play an important role in process, product development, and assessment, but it is realised that it has considerable limitations. One of the major obstacles to scaling is the nonlinear relationships between full-scale and scaled processes, which cause changes in physical behaviour with scale. With geometric measurements of length, area, and volume scaling linearly, quadratically, and cubically, geometric scale relationships are easily obvious. Surface forces and body forces are important changes affected by changes in geometric measurements in structural analysis, with the latter dropping at a quicker pace than the former increasing scale. The occurrence of scale effects, combined with the growing complexity of computational modelling, has lowered the value of scaled testing in recent years, has invariably hastened this reduction.

Understanding the challenge early in the design process aids in the embedding of the most appropriate simulation technology for the task. When a problem can be solved analytically, for example, a mathematical model can be employed and constructed. The characteristic equations that characterise and implement the system must be established. Often, this necessitates the use of simplifying assumptions in order to resolve the mathematical models describing the system's behaviour. The fact that this procedure does not necessitate any experimental labour is a significant advantage However, if the solution requires a significant number of simplifying assumptions, the mathematical method can be challenging. Also, due to the complexity of the mathematical equations, complications can develop when the

analytical solution believed essential cannot be followed [3]. Simplicated models, of course, need experimental confirmation to verify the numerous simplifying assumptions that are considered in practical modelling [4].

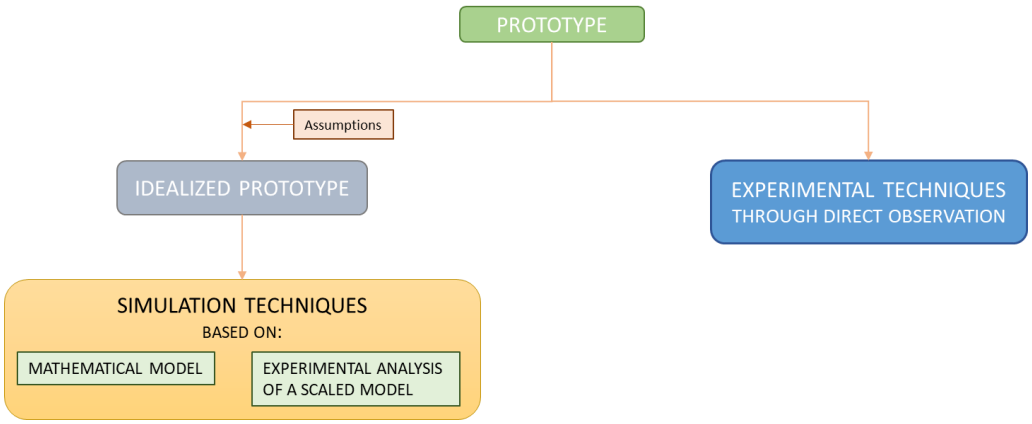

Figure 1.1: Flowchart for analysing a problem using experimental or simulated techniques [3].

The advent and widespread usage of very powerful digital computer hardware and software has had a significant influence on design skills and methods [5]. Computer simulation enables sensitivity analysis by examining system reaction to changes in starting and boundary conditions, as well as system characteristics [6][7]. When a discrete system is thought to give a realistic representation of a physical system, experimental validation is required to justify the numerous simplifications that are sometimes required for practical modelling [4]. Due of various simplifications on microstructure and boundary conditions, it is frequently insufficiently accurate and always necessitates post-process analysis, i.e. correction of boundary conditions and constitutive models.

Scaling, which reduces buildings to a fraction of their original size for testing purposes, is a theoretical solution to the size limitation imposed by laboratory research. In a broad sense, scaled experimentation is primarily concerned with the development of scaling rules that allow for the transfer of data from the scaled experiment to the full size. Although the focus is on earthquake seismic testing, scaling constraints are also acknowledged. Practical restrictions might include the lack of materials with the desired characteristics, as well as the availability of appropriate experimental equipment. A shaking table is a crucial piece of equipment for seismic testing and is used often. Because perfect similarity is rare, well-

researched scaling restrictions are frequently enforced when using shake-table experiments. To better understand the behaviour of buildings during seismic excitations, several scaled experiments have been done and papers have been published. In order to transmit information from the scaled model to the full-scale model, similarity laws between full-scale and trial models are necessary prior to the shaking table test. Similarity rules can be classified either directly from the equations defining a system, which define the relationships between the system's key variables and parameters, or indirectly using dimensional analysis [8]. The problem with most scaled experimental investigations is that they are all restricted by dimensional analysis' inability to account for improvised scaling rules that are required to accommodate scale effects in order for the scaled experiment to be meaningful. Weight and body forces are one example, as is the scaling need for mass to be added to the scaled model [9]. Masses are typically provided in the form of blocks attached to slabs, however solving one problem almost always leads to another, as it is expected that the supporting frame's behaviour would be incorrect during collapse. Under deformation situations, the mass blocks might move and even clash, resulting in atypical behaviour. When it comes to shrinking dimensions while keeping the prototype's material characteristics, extra mass is frequently required. However, the additional bulk has disadvantages since it makes movement and control more difficult [10,11]. Because increased mass has the potential to cause overturning moments, controlling the simulator becomes more challenging. This frequently necessitates the use of larger scaling factors and control methods in specimen design in order to handle the foregoing disadvantages to some extent, depending on the payload capacities of the shaking table [10]. It is obvious that adding mass causes issues, therefore another approach is to use similarity laws to enhance acceleration. Unfortunately, this approach has a flaw in that it requires huge accelerations to simulate the behaviour of high-rise structures. Because of the limitations of laboratory shake tables, this is a tough task to do. All of these studies are constrained by dimensional analysis' inability to account for scale effects and the ad hoc nature of the scaling rules required to expand the study.

This thesis investigates finite similitude, a novel concept for scaled experimentation that aims to systematise the integration of trials at two scales for the first time. The current research builds on prior work on scaling (now referred to as zeroth-order

finite similitude) that has been applied to impact mechanics, powder compaction, biomechanics, and metal forming, and includes only one scaled experiment. The study described here uses a more sophisticated version of the finite-similitude theory and two scaled experiments to apply finite similitude to seismic research. The finite similitude theory begins with a notion that cannot be physically implemented: space scaling. The theory demonstrates how metaphysical-space scaling is the foundation theory for scaling theory, providing an intuitive view of scaling. Space scaling mathematics is quite straightforward, and it eventually enables us to investigate scaled structural mechanics. The projection of transport equations developed on the trial space (where the scaled experiment is located) onto the physical space is the most important step in the finite similitude theory (where the full-scale structure resides).

1.2 Aims and objectives.

The primary aim of this research is to examine the application of first-order finite similitude theory, which enables more accurate reconstruction of full-scale behaviour using two scaled experiments, and to examine the limitations of zeroth-order finite similitude in the field of structural dynamics and earthquake engineering. This assertion will be supported by the introduction of a novel first-order methodology that replicates the full-scale model using two trial models. The trial's physical behaviour and physical spaces are connected via a new innovative scaling methodology based on transport equations.

A set of equations called transport equations describes the transport of variables such as displacement, mass, entropy, energy, and momentum. Transport equations can be used to determine the physics and behaviour of any scaled model and, more importantly, the dynamics of the full-scale process. Both transitioning from a small to a full scale and vice versa reveal information about how the model should be at the former stage in order to demonstrate the latter stage more accurately. While the literature establishes that scaled processes are not identical, it is established that good scaled designs can be created through the selection of appropriate materials, boundary conditions, and precise simulation. In the field of structural dynamics, the reality of scaled experimentation is that the scaled processes are not identical and

require additional techniques to extract information from scaled models. A sufficient scaled model can be designed using zeroth or first order finite similitude in accordance with finite similitude theory. Several of the primary objectives in relation to the study's primary objective are as follows:

1. On the basis of two scaled experiments, a new form of finite similitude has been established and introduced as first-order similitude theory. Prior to applying first-order finite similitude, the limitations of zeroth-order finite similitude theory, also known as classical dimensional analysis with additional advantages, were examined and evaluated. These analyses were conducted on equivalent models and structural elements when subjected to dynamic loads such as cyclic, ground motion, and so on.
2. The first-order theory is evaluated using practical structural and earthquake engineering applications by combining two independent zeroth-order scaled designs that accurately capture the physical model behaviour. These methods have been validated using equivalent models and then applied to high-rise buildings to determine the proposed design's capability.
3. Apply the first-order finite similitude equations to create a second trial model design, keeping the first model as created by the zeroth order untouched. In addition, different materials have been selected for trial models in order to show the ability of the proposed novel theory. This objective has been formed by application of the zeroth and first-order similitude in discrete dynamic systems in order to obtain scaling parameters for a physical problem to set physical experimental set up.
4. Two trial models are created from scratch independently from the first order similitude equations. This method was investigated numerically because it allows for simultaneous fixation of the young's modulus and yield stress values, which is not possible with zeroth-order or dimensional analysis. This novel similitude approach has been developed in differential form, allowing the results of two scaled experiments to be combined to predict the behaviour of a full-scale model. As a result, it enables the use of additional material properties for matching between virtual and physical full-scale models, as explained previously.

5. To demonstrate the finite similitude's ability to deviate from the traditional definition of geometric similarity, the theory was applied to a thin-walled beam model, where the theory successfully captured the exact global behaviour of the full-scale despite the wall thickness not following geometric scaling. Analytical and numerical analysis were performed using similarity rules based on first-order finite similitude.

1.3 Thesis outline

The following seven chapters make up this thesis:

The rationale for the research is presented in **Chapter 1**, as well as the research's aims and objectives.

Chapter 2 discusses the historical evolution of dimensional analysis, which is the foundation of similitude methods, as well as the similitude model's concept. It also includes a thorough literature analysis that summarises prior research that has used a scaled model in seismic testing models. This chapter also discusses the limitations of dimensional analysis and why it is necessary to develop a new similitude theory.

Chapter 3 details the reconstruction of physical model behaviour by means of two distinct scaled experiments of a selected beam, column and multi-storey frame when exposed to various loading conditions. This chapter consists of the first-time publication of a new approach to finite similitude theory, which demonstrates the merits of the proposed method. For the first time, a theory is able to fix the material properties, which have the same dimensions, and enables us to set the scaling parameters accordingly.

Chapter 4 consists of another publication discussing the scaling of discrete elements and the change of their behaviour with scaling. Single and two scaled experimentations have been shown for the different case studies numerically and analytically. Linear spring and fluid viscous damper have been investigated and the system exposed to friction force is demonstrated in order to present the ability of two distinct scaled experimentation.

Chapter 5 presents the scaling of nonlinear structural dynamic systems. This publication illustrates the benefits of the finite similitude theory when the nonlinear springs, dashpots and friction system are exposed to scaled experimentations for a range of loading conditions.

Chapter 6 considers the application of first-order finite similitude in structural mechanics and earthquake engineering. This publication demonstrates the practical applicability of the proposed theory for high-rise buildings and presents another ability of the approach in the case of breaking geometric similarity for scaled experimentation.

The relative benefits of the finite similitude method are summarised in **Chapter 7**, along with recommendations for further research.

It's critical to emphasise how each publication's coherent body is connected to and complements one another. The first journal publication (chapter 3) looked at the importance of current scaling theories and their limits, as well as offering a novel scaling theory approach. Scaled experimentation has been used for the design of earthquake-resistant (aseismic) structures since it was discovered. This chapter proposes a new theory based on the metaphysical idea of space scaling for the analysis of earthquake-resistant constructions (beams, substructures, or buildings). The benefits of the new scaling theory were detailed in the first article. After recognising the benefits and advantages of the new scaling theory in Chapter 3, it was decided to investigate the benefits of the new concept further in Chapter 4 using discrete mechanical dynamic systems that are commonly used in structural engineering, such as equivalent models consisting of mass-spring-damper systems. These systems are thought to be used to establish the applicability of first-order finite similitude for situations where existing scaling theories are insufficient, as well as to commence scaling parameters in a new scaling theory. It was thought that if a discrete system accurately represents a physical system, experimental verification is always required to support the various simplifications that are common in practical modelling. As a result, this research (Chapter 4) investigates discrete elements and how their behaviour changes as they scale. Following the publication of chapter 4, more research into nonlinear discrete systems and their behaviour under nonlinear loading conditions was required in chapter 5. The use of single and two-scaled experimentations to nonlinear structure dynamics was the motivation for this journal publication. Nonlinear behaviours are always an issue, and this is a study and application topic that poses significant challenges to scaled testing, as demonstrated by seismic experiments. Because the behaviour of such systems is complex and sophisticated, very comprehensive scaled-model designs that may yield practical

results are required. By considering nonlinear damper, spring, and friction all together, as well as gravitational acceleration, which has a significant impact on friction, the article shows how the new exact similarity rules provided by the new theory provide necessary precision for the prediction of full-scale model behaviour. For the implementation of physical modelling under earthquake loadings, Chapter 5 recommends several scaling rules based on nonlinear discrete dynamics models. The research was finished in the final publications by applying scaling rules discovered in earlier chapters to develop an optimal scaling design to use in this paper for buildings subjected to seismic loads. The new idea of scaling suggests new means of planning and testing buildings and structures, which is also the subject of Chapter 6. The selected complicated case studies demonstrated that the suggested scaling theory is simple to apply, and that full-scale model behaviour may be reconstructed with greater accuracy. In this chapter, the capability of the finite similitude theory has been demonstrated by examining structural elements under various loadings and high-rise buildings under earthquake excitation. In the example of breaking geometric similarity for a thin-walled beam, another key aspect of the first-order finite similitude is provided, where the first-order theory caught the global behaviour of the full-scale model with an exact match.

Chapter TWO

Literature review

2.1 Introduction

Along with its application in other sectors, the principle of similitude is used in structural engineering, seismic engineering, and contact concerns. The continued use of sub-scale testing models benefits engineers because it enables them to accurately estimate the performance of larger prototypes using scaling rules applied to the test results. According to Chambers [12], NASA's forerunner, the NACA, has been a pioneer in model testing for over 80 years. NACA and NASA used specialised models to improve aeronautical vehicles in nearly every technological subject examined, including aerodynamics, structures, and materials. Indeed, Chambers asserts that almost all advancements in recent technology have been documented in reports or publications that were either written on contract or as part of authorised research projects. NASA's Technical Reports Server (NTRS) has seen an increase in the number of reports submitted over the last year, the majority of which are related to scale models, structural similitude, and/or scale design studies [13]. Several of the studies described in this case study have reached a level of complexity that far exceeds the vast majority of the current literature.

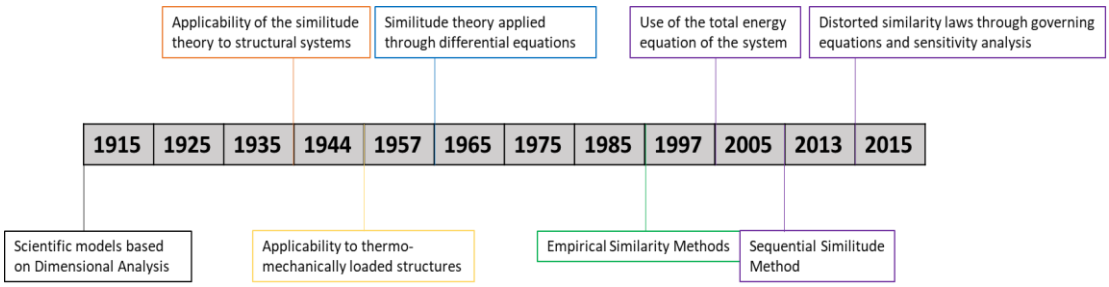

Figure 2.1: A chronological review of the most important developments, techniques, and case studies involving the application of scale models [13].

Complex technological issues can be solved by using model tests that employ scaling methods and related rules. Development time and expenses for the manufacturing of prototypes can be greatly reduced if the use of such approaches is applied. Full-scale complex systems are modelled using the physical modelling approach in the engineering sector in order to investigate their basic processes and behaviour. More precisely, earthquake engineering employs physical modelling techniques commonly referred to as shaking table and centrifuge tests. This method entails the construction of a full-scale model and a scaled model, with the full-scale model referred to as the "prototype." A "scaled model" is a laboratory-built representation of the "prototype" in a reduced size. Laboratory scale model testing enables greater control over model features and a faster response time than full-scale testing [14].

Physical modelling is well-suited for analysing seismic engineering challenges, such as [14]:

• Under controlled parameters, highly complicated, unusual, and three-dimensional issues can be modelled.

• Modelling full-scale systems is frequently a cost-effective and relatively rapid method of analysing them.

• The physical modelling approach provides a highly regulated database in which high-quality cases and prototype testing are uncommon for engineering issues.

• Scale model experimentation may be utilised for analytical procedures, or the response of a prototype construction may be predicted by use of calibration benchmarks.

Despite these advantages, physical modelling techniques have significant limitations:

• "Prototype" characteristics of the soil (i.e., shear modulus and shear wave speed) or the gravity of a tiny laboratory model might be challenging to measure correctly.

• In some cases, measurement scale effects can be relevant (i.e., accelerometers, pressure transducers, displacement monitors)

The similarity between laboratory scale model and prototype and the sets of scaling relations (i.e. similarity laws) should be determined between material properties in the model and the prototype for the physical modelling approach to give high quality and relevant findings.

2.2 Similarity Theory and its applications

A similarity or similitude theory, which may be applied in several sectors, including vibrational issues, impact, and structural design or damage, is recognised as part of engineering science. In particular, when phenomena are novel and requires thorough experimental verification that enables engineers to comprehend a new concept [15]. This hypothesis is based on the notion that in principle the results of the scaled model parameters may properly anticipate all the boundary conditions and mechanical characteristics of a full-scale process. The relationship between two models is termed a similarity that is determined by multiplying the physical amount of the model by a scaling factor to transfer it to the scale model [16]. The relationship between the models is defined as full and scaled models. Similar processes are produced by physics however, in practise, it is not simple to scale the complicated processes and the dimensionless quantities can seldom be perfectly matched. Two techniques allow for the resemblance between the two systems; direct analysis and dimensional analysis [17]. A mathematical model is used for direct analysis to analyse the model when any variables and factors impacting the system can be found. The limits and conduct of the systems are obtained directly from the system's governing equations. A variety of scaling approaches [4], [18] have also been implemented during the course of the year, including energy methods (EM), resemblances and asymptotic modelling for structural acoustic research applications (SAMSARA), sensitivity analysis (SA) and empirical similarity method (ESM). Each has its own benefits and demerits, but none corresponds to the simplicity and predominant of the dimension analysis and under the table the major aspects of the methods presented are demonstrated [19].

Table 2:1: An overview of scaling approaches, including how they take into account size effects and nonlinearity [19].

Method	**Description**	**Main scope**	**Size effects**	**Nonlinearity**
Dimensional analysis	Dimensionless key ratios are derived from a dimension matrix based on a relevance list with system-specific variables.	Many fields of engineering, from fluid mechanics up to structural engineering. Systems with unknown behavior	No	No
Differential Equations	Based on the definition of scale factors which are inserted into the governing differential equations to derive similarity conditions	Similar to dimensional analysis (more physical meaning). Any system with available governing equations	No	For simple case studies
Empirical Similitude	Transformation matrices are used to merge the empirically determined data of the geometrical and material changes. Separate scaling of material properties and geometric properties	Rapid Prototyping of models.	Partially	No
Energetic Approach	Using energy equations. Potential total energy of a similarly scaled model has to be proportional to that of a full-size structure and corresponds to the	Linear Static deflection and free vibration. Use of relationships between mode shapes, natural	Partially	No

	principle of energy conservation	frequencies and damping loss factors.		
Statistical Size Effect	Transfer of fatigue life data with the statistical size effect and the Basquin equation to predict lifetime of scaled components	Reliability Engineering	Yes	Yes
Artificial Intelligence	Parameter reduction and associated simplification of equations and contexts that result from the dimensional analysis	Genetic algorithms, case-based-reasoning, design evaluation, neural networks and pattern recognition.	No	No
Sequential Similitude Method	Similarity conditions can be established for a structure subjected to different loading situations, provided that each loading event is simulated independently.	Structures subjected to sequentially loading situations.	Yes	Yes
Sensitivity Analysis	Combining the governing equation and sensitivity analysis to derive similitude conditions for distorted models	Linear static and frequency analysis	No	No

The second condition is dimensional analysis, used to reorganise the models variables into independent dimensionless variables, with the same dimensions for all the terms of full scale and the scaled models. This approach is based on dimensional homogeneity in order to achieve similarity requirements. A suitable scaling law

relates the prototype structure to a physical model as crucial to success in physical modelling. Dimensional analysis and similarity theory are two key approaches utilised for deriving the proper scaling law [20]. Dimensional analysis is a way to produce dimensional groups that are examined for physical phenomena. This approach involves identifying all major variables that influence the physical phenomena and obtain non-dimensional groupings. The idea of similarity first specifies forces acting in system and system geometric characteristics. In addition, it uses dimensionless analysis in order for model and prototype to create and link dimensional terms [21].

2.2.1 Dimensional Analysis

Dimensional analysis is a significant tool in the design and brief explanation of the experimental data for scientists and engineers [22]. The genesis of current dimensional analysis theory goes back to the notion of geometric similarity employed for the first time by Galileo, which Euler first explored in 1765 with the significance of quantity, units and dimensional homogeneity. In 1822, Fourier laid the foundations for dimension analysis, one of the first to be recognised for the existence of dimensional groups [23], on the basis of the Euler work, and Lagrange and Laplace articulated the principles of dimensional analysis. Carvalho, Vashi and Riabouchinsky did a great deal of work before the pi-theorem was created in 1914 by Buckingham [24]. In fact, some writers claim that the pi-theorem is best credited to Vashy when he issued a paper in 1892 extremely similar to the pi-theorem in its structure [25]. In this theorem, the physical relations are investigated in the context of similarities [24], Bridgman, Brickhoff, Langhaar, Van Driest, and Brand analysed and updated this theorem [26]. Several publications, such as the book by Sonin [27], give a thorough understanding of the procedure, providing further explanation and examples of the dimension analysis process. The simplest dimensional analysis is founded on the basic assumption "Mother Nature is consistent in dimensions."

The simplest type of dimensional analysis incorporates four fundamental dimensions: length [L], time [T], mass [M], and force [F] [22]. Newton's second law is concerned with force, mass, time, and length. Force [F] can be substituted for [M][L]/[T]. Thus, the three fundamental independent dimensions of length [L], time [T], and mass [M] may be used to derive the dimensionless physical phenomenon

terms. The application of the Buckingham Pi theorem entails a more complicated form of dimension analysis. The Buckingham (Pi) theorem is a formalisation of Rayleigh's approach of dimensional analysis and is a crucial theorem in dimensional analysis. Buckingham proved in 1941 that the number of (Pi) quantities left after dimensional analysis is equal to the difference between the number of quantities entering the problem and the greatest number of these that are dimensionally independent [74]. The number of fundamental dimensions required to express all dimensional equations will always be equal to or less than the maximum number of dimensionally independent quantities [74].

As a general rule, the Buckingham Pi theorem can be broken down into the following steps [74]:

1. The Buckingham Pi theorem is a formula for calculating the number of dimensionless numbers (also known as's) to predict. The number of independent dimensionless groups equals the difference between the number of variables that make them up and the number of individual dimensions involved, according to the theorem. From a practical standpoint, the theorem's flaw is that it is based on the least number of dimensions that might have been employed rather than the actual number.

2. The first step is to determine which variables are involved in the situation. A dimensional analysis may occasionally reveal that one of the selected variables should not be there because it involves a dimension not shared by any of the other variables; however, most of the time, if the wrong variables are entered, the erroneous dimensionless numbers are produced.

3. Including variables whose influence is already implicitly accounted for is a error to avoid when choosing variables. One may claim that the liquid temperature is a significant variable in studying the dynamics of a liquid flow. It is significant only in terms of its influence on other qualities, such as viscosity, and thus should not be included alongside them.

4. When applied to the actual number of dimensions used, the Buckingham Pi theorem merely states that at least a certain number of dimensionless integers must be involved. Unless one employs one of the time-consuming methods for determining the minimum number of dimensions required, the theorem provides

little assurance that all dimensionless numbers have been discovered - assurance that can be obtained quickly using the step-by-step approach.

5. The dimensional analysis method is based on the evident truth that each term in an equation involving any system must have the same dimension.

These concepts are embodied in the Buckingham Pi theorem, which covers the construction of dimensional groups based on a number of dependent and distinct variables deemed significant to the occurrence of a given event [22]. Where P_1, P_2,...,P_n are physical factors affecting the specific physical phenomena, P_n may be written as

$$f_1 (P_1, P_2,...,P_n)= 0 \quad (2.1)$$

while f_1 is describing involved parameters and even it can describe a governing equation. It is believed that a list (P) of (n) variables (P_1, P_2,...,P_n) may characterise the phenomena examined. P_n as indicated in Eq.(2.1) is possible to build using Buckingham Pi's total inspection technique (m) independent physical quantities dimensionless products P_1, P_2,...,P_n [22]. Then, this physical relation may be expressed as a relation of (n-k) dimensionless products (called Π product) and is presented as follows:

$$f_2 (\Pi_1, \Pi_2,\ldots, \Pi_{n-k}) = 0 \quad (2.2)$$

where each Π product is a non-dimensional product of a set of k physical variables plus one other physical variable. Let k equals the number of essential dimensions necessary to describe the physical variables (e.g., mechanics: mass, length, and time; thus k=3) [74]. Let P_1, P_2,...,P_k be the selected set of k physical variables, Then different Π groups can be set as

$\Pi_1= f_3 (P_1, P_2,...,P_{k+1})$
$\Pi_2= f_4 (P_1, P_2,...,P_{k+2})$
.
.
.
.
$\Pi_{n-k}= f_5 (P_1, P_2,...,P_{k,} P_n)$

The selection of the repeating variables P_1, P_2,...,P_k should be in a way that they involve all the k dimensions used in the physical problem. In addition, the dependent variable should found in only one of the Π products [74].

There is no single Pi term applicable to a particular problem. It is critical to recognise the relevant variables and generate the Pi terms correctly for scale modelling challenges [21]. Each dimension in Eq. 2.2 must be identical between the model and prototype in order to achieve full dimensional similarity.

The similarities rules developed by Kim et al. [28] are included in Table 2.2 to facilitate the application of dimensional analysis or the Buckingham pi theorem to seismic technology applications such as shake table testing. To accurately recreate the gravity and inertia force of a structure in detail, the acceleration factor for dynamic issues must be unity, as the authors state. However, because weight and time scale factors are proportional to s2 and s0.5, additional weight is required for dynamic trials in a small-scale model, and test time should be reduced. Another example to demonstrate the non-uniqueness of setting scaling rules is that scaling relationships have been devised for investigating the seismic reactions of tunnels, and gravity distortion models are frequently utilised because adding extra weights is difficult [72]. Table 2.3 has been incorporated to set the experimentation based on the dimensions of the model box and the depth of the tunnel. As illustrated in Table 2.3, the applied acceleration must be increased, and material selection is critical due to the fact that the stress-strain curve and young's modulus must be scaled according to defined similarity rules.

Table 2:2: Derived Similitude Laws [28]

Quantity	Dimensions	Scale factor
Length	L	s
Mass	M	s^2
Time	T	$s^{0.5}$
Stress	$ML^{-1}T^{-2}$	1
Velocity	LT^{-1}	$s^{0.5}$
Acceleration	LT^{-2}	1
Force	MLT^{-2}	s^2
Stiffness	MT^{-2}	s
Damping	MT^{-1}	$s^{3/2}$
Added mass	-	$s^2.(m_p-m_s)$

Table 2:3: Similarity relations and similarity constants [72]

Physical parameters	Similarity relations
Length	C_l
Density	$C_\rho = 1$
Elastic modulus	C_E
Stress	$C_\sigma = C_E C_\varepsilon$
Strain	C_ε=1
Poisson's ratio	$C_\mu = 1$
Internal friction angle	$C_\emptyset = 1$
Time	$C_t = {C_\rho}^{0.5} {C_E}^{-0.5} C_l$
Displacement	$C_D = C_l$
Velocity	$C_v = {C_\rho}^{0.5} {C_E}^{-0.5}$
Acceleration	$C_a = {C_\rho}^{-1} {C_l}^{-1} C_E$

2.2.2 Theory of Similarity Principles

The concept of similarity emphasises the importance of defining similarity variables between model and prototype. While similar processes provide adequate physics, scaling complicated processes is not straightforward, and dimensional quantities are rarely precisely matched. Three conditions for similarity can be identified that, when satisfied, result in complete similarity between the full model and the scaled model [15, 20]. Langhaar [29] and Westine et al. [73] emphasised the importance of scaled-down models being geometrically, dynamically, kinematically, and constitutively similar to the full-scale model.

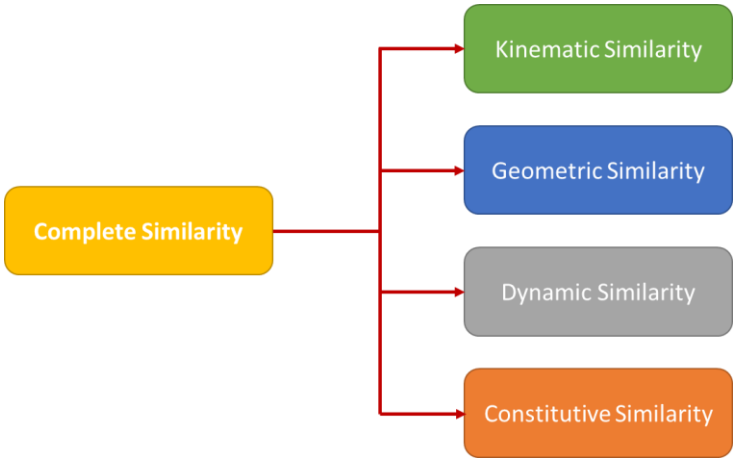

Figure 2.2: Schematic representation of complete similarity

Geometric Similarity: Two systems are considered geometrically similar if all matching lengths and angles are identical [30]. The ratio = L_m/L_p is constant across all dimensions of the systems. Where L denotes any dimension in a system and m and p denote models and prototypes, respectively [29].

Kinematic Similarity: The two system movements (model and prototype) are comparable when there is kinematic similitude. Kinematic similitude means that in the model and prototype systems the respective speed and accelerate components are comparable [29].

Dynamic similarity: The dynamic similarity exists if the acting forces on the system have the same ratio in full-scale and trial systems. This similarity imposes the acting forces at all corresponding points, and the duration, which is affecting both models, have the same ratio [31]. When systems exhibit kinematic similarity with identical mass distributions, this can serve as evidence for dynamic similarity [25].

Constitutive Similarity: What does "constitutive similarity" mean? That is, the constitutive properties of model and prototype materials, such as their stress-strain curves, are identical. While the majority of modellers define similarity in geometric, kinematic, and dynamic terms, other similarities may exist. For instance, homologous constitutive properties can be defined for materials [73]. Models need not be constructed from the same material as the prototype. A model composed of homologous materials at homologous locations in corresponding structures can be created for structural response studies. As with the drop test, a dissimilar material

model can be created if the materials' non-dimensional stress-strain curves are similar, a concept referred to as constitutive similarity [73]. Constitutive similarity refers to the similarity of materials' stress-strain curves or constitutive properties, which is especially important in soil dynamics.

2.2.3 The use in earthquake engineering of dimension analysis and theory of similarity in the model scale

Given that replica models have been used as supplements and substitutes for design and analysis in civil engineering for many years, this review of the literature is limited to articles deemed extremely helpful in the research effort. It focuses on identifying prior research on construction structures and materials, particularly those that deal with or contain information that could be used in dynamic model studies.
The intricacy and transitory nature of earthquakes' mathematical models need testing of entire buildings. Historically, these effects could only be tested by utilising building size models. These model scale tests were subsequently contrasted with analytical simulations. Scale models of building structures subject to diverse loads are facing the same challenges as those under static stresses. They also employ the same sort of methods to get the characteristics of prototypes-like materials like micro-concrete. The following can be summarised in [32]:

- Dead loads are lowered linearly in functioning, undistorted models and hence dead load stresses are considerably lower than in their reference prototypes. Additional loads are conceivable in models of scale to prevent this inconvenience.

- Scale models have lower tolerance values than equivalent prototypes and thus achieve a higher level of construction quality control, except when the scale ratio is large, as in a centrifuge test where the scale ratio is 1:100.
- Concrete behaves differently at various scales. In particular, with the decrease in size the perceived strength of the concrete rises. This is a result of the scaling of the combined substance or the use of micro concrete. However, when the concrete is not scaled, strength increases owing to the microscopic internal fractures of the scale model are less likely, such that, according to Keith, the existence of vulnerabilities is proportionate to the volume [32]. When the strength is increased relative to loads, their rigidity will rise in consideration of reinforced concrete structures in scale

models. Since rigidity is one of the major seismic calculus problems, this should be taken into account in seismic testing.

- Typically, curled reinforcing bars are replicated in scale models using plain wires to minimise internal fractures.
- With increased moisture transmission and scale models, shrinkage and creep have a greater volume of transfer surfaces available [33]. According to White and Chowdhury [34], the absence of fractures in scale models does not result in detectable changes in moments and deflections.

In 1959, previsions of precision through small-scale testing were addressed at the RILEM [35] Symposium in Madrid that dealt with broad elements of dynamic theory of modelling and material behaviour. Similar techniques were provided for motion testing like high mercury tanks for water simulation, brass simulation of steel, hanging loads or springs for simulation of wall stiffness. Techniques such as the 'shaken tables' example had been used until 1968 to perform scale models under load movements.

Grant used shake tables in conjunction with electrical equipment to more accurately replicate seismic movements in his PhD thesis [32]. UC Berkeley's Istituto Sperimentale modelli, Bergama's Istituto Sperimentale Strutture (Strutture), Lisbon's Laboratorio Nacional de Engenharia Civil, and Ljubljana, Yugoslavia's Materials Research and Testing Institute all conduct shaking table tests [35]. When the gravitational effect is negligible, the model without additional gravity forces will be adequate in comparison to the seismic effects. A perfect analogy should be obtained in cases where the influence of gravity and inertia are both significant [35]. In such situations, when the physical phenomena is complicated, dimensional analysis offers an alternative to matching model and prototype [32]. Dimensional analysis provides similitude and the performance of the criterion of identical pi-parameters is the perfect match between prototype and scale model. When any of them are not satisfied, the modification of other pi-parameters should be considered in order to preserve the similarity, which causes model distortion. The inertial and restoring force is critical in seismic testing for dynamic answers [36]. The reaction would be the similar if the ratio between the two is identical in the prototype and the scale model. Two techniques may be used by the use of dimensional analysis: either to utilise Cauchy's likeness or Froude's similitude [32]. The similarity with the Cauchy

means the usage of the free factor of mass scale, but the temporal variability affects the acceleration of the model in scale. It therefore affects:

- Horizontal acceleration, which may very readily be increased by applied horizontal acceleration.
- Vertical (gravitational) acceleration: difficult to apply. Certain techniques create additional loads, though not exactly as gravity does. If the floor is made of steel, a magnetic field can be used to increase the weight of the model by a small amount. Additionally, a centrifuge rotating force may be applied, although this is difficult to accomplish [32]. The issue with all of the above-mentioned scaled experimental investigations is that they are unable to account for precise scaling restrictions necessary to accommodate scale effects and make the scaled experiment beneficial. One example is weight and physical strength, as well as the scaling requirement to add mass to the scale model [37]. Masses are normally introduced as blocks attached to a platform, however the solving of one problem always generates another since it can be predicted that the behaviour. Under situations of deformation, the mass blocks can move and even clash and the outcome may be non-representative behaviour. When the dimensions are reduced while the prototype material characteristics are preserved, more mass is frequently needed. However, the additional bulk has disadvantages since it increases the complexity of movement and control [38, 39]. Control of the simulator gets harder since the extra mass might generate revolutionary moments. In many cases, this means that specimens must be conceived by utilising larger factors of scaling and must include control mechanisms so that the aforementioned disadvantages may be handled to a certain amount in accordance with the payload capacity of an operated shaking table [37]. The system was designed to enable the mass movement of the wires up to the maximum displacement limit at which point it stopped the further motion. The scaled system cannot unfortunately be described as genuinely realistic and was especially impacted by the load and overall stiffness of the scaled model [40]. Additional mass was needed in another study [41] concerning the seismic performance of a high bridge utilising a shaking table test. By use of repeated numerical tests, the accurate distribution of the mass may be established by a pier height in order to complete the mass location. The increased bulk is obviously caused by issues and there is an alternate way to boost the speed via matching legislation. However, this approach

has its own deficiency because it is necessary to use large structures to ensure their representational behaviour. This approach comes with a significant drawback in that huge accelerations are required for high-rise building representative behaviours. It is nearly impossible to put together, as there are only a certain number of laboratories shaking tables to work with.

Figure 2.3: The scaled model produced for shake table test in laboratory environment [49].

To examine a three-story scale model, researchers such as Sharma et al. [42] applied scaling rules and dimensional analysis theory to identify model behaviour. Likewise, Guerrero et al. [43] created a scaled model for their study, which had dimensions

that were 10% of the full-size construction due to size restrictions and equipment costs. According to Guerrero et al., the prototype structure is located in Mexico City. It was also done on a single-story, single-bay steel building, by Nader and Astaneh-Asl [44], using shake-table testing and experiments. Another example can be given as it can be seen from the figure above, a 34-storey 1:20 scale micro-concrete high-rise building [49]. The engineers also conducted experiments on steel structures to see how they would perform when subjected to various seismic loadings, which could only be tested at lower sizes.

As demonstrated by the preceding data, dimensional analysis has provided information in the past by examining other approaches previously discussed. According to Pawelski's [45] findings, the problem of approaching but not quite matching complete and perfect similarity solutions occurs fairly frequently. Due to the limitations of dimensional analysis in accounting for scale effects, all of these studies suffer from a fundamental scaling issue: the ad hoc nature of the scaling rules required to expand the study.

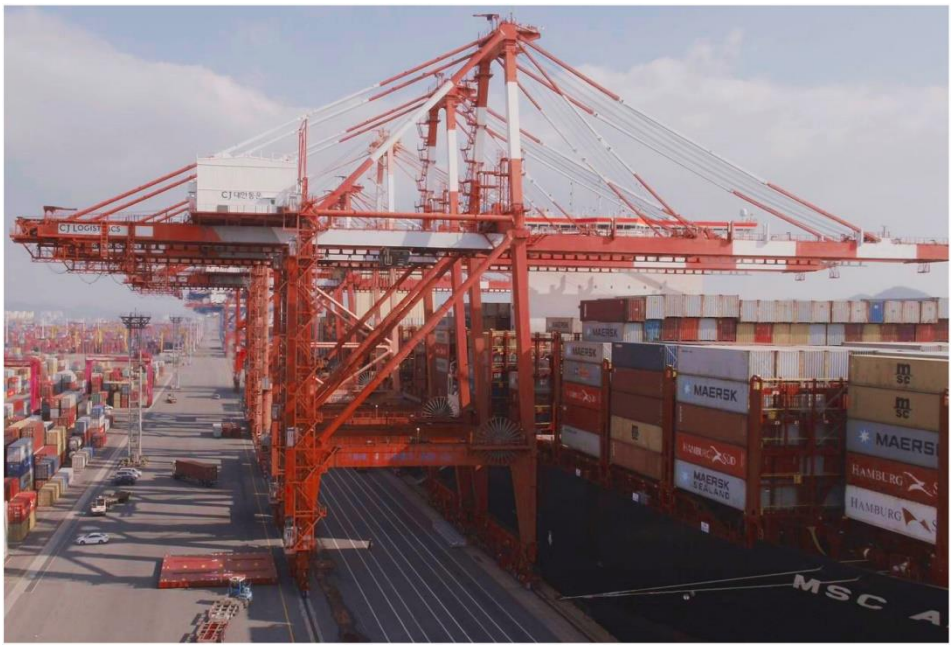

(a)

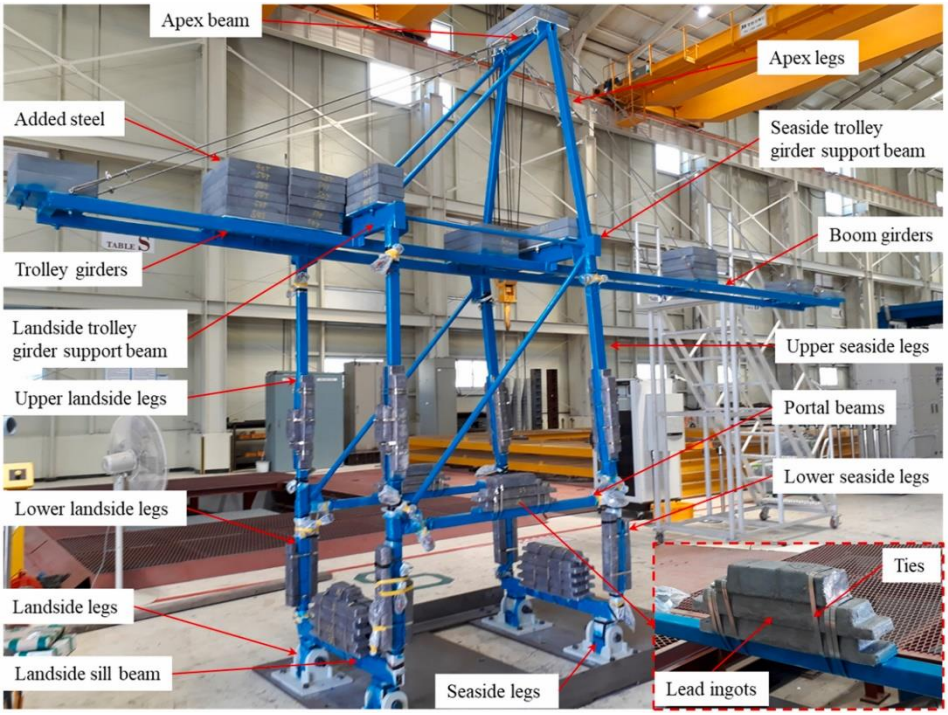

(b)

Figure 2.4: (a) Full-scale container crane (Gwangyang port in South Korea) (b) Overall photo of scaled-down model with a scale factor of 1/20 [46].

2.3 Limitations of Dimension Analysis and the need for a new similitude method

One of the difficulties with dimensional analysis is its incompatibility with modern simulation methods [47]. On one level, it is considered independent from the analytical process, as the generation of dimensionless quantities occurs independently of direct analysis. There are, however, several alternative approaches, one of which is straightforward rescaling of the governing partial differential equations. It is possible to rewrite these equations in such a way that critical non-dimensional quantities become coefficients. While the technique provides information about the functional relationship between non-dimensional variables, it makes no significant improvements to numerical analysis. Scaled studies, including dimensional analysis, are critical, though their applications are limited (for the reasons stated below). Following are the advantages and disadvantages of performing dimensional analysis [22, 48]:

- Dimensional analysis has the potential to significantly reduce the number of identities that must be counted in an empirical study.
- It can assist in the development of experimental models.
- It can deliver scaling rules and relationships for test models
- It is effective in checking dimensional consistency of equations
- It is useful for "generalising" dimensionless equations and converting them to dimensionless form.
- It is not capable of establishing relationships between variables.
- Variables cannot be distinguished by their relative significance.
- It is unable to determine the most useful type of dimensionless variables.
- It is trial-and-error technique, as non-dimensional groupings are non-unique.
- A highly trained analyst with a thorough understanding of the problem is required.

2.4 Summary

To determine a mathematical model, the equations derived through dimensional analysis have been applied to models subjected to various types of seismic motion. To begin, it must be recognised that replicating all of the characteristics that influence the behaviour of structures during dynamic operations is nearly impossible. The emphasis of this work is on the identification of critical factors and feasible model test types that allow for the most precise replication.

With the primary objective of universal applicability in mind, attention was given to prototype investigations of uniform isotropic materials, such as steel. One might conclude from the findings of this study that a wide variety of steel constructions can be successfully simulated. Only through a series of model tests, which can be directly compared to prototype investigations, can an answer be achieved. The fundamental objective of a model analyst is to choose the correct sort of model for the project and to accept the required level of approximation. In the major general case of a complex 3D structure, where gravity and inertia have equivalent effects of importance, the optimum choice in this instance is a real replica model, if a suitable model material can be obtained. When precision in model testing is not attainable, it

is frequently possible to get the same level of accuracy by using model tests with additional mass technique.

Scaling theory recently developed, dubbed 'Finite similitude,' introduces an entirely new approach to scaled experiments. It enables us to determine the scaling factors for desired experiments in relation to the transport equations and space scaling. The proposed theory was initially discovered in single experimentation called zeroth-order finite similitude; it has since been successfully applied in a variety of fields, as detailed in the references [50-56]. While the initial theory of finite similitude provides scaling factors comparable to those found in dimensional analysis, it is not based on dimensionless forms. Additionally, it demonstrates how scaling can be viewed as an imagined process accomplished by contracting or expanding the space itself. Since the zeroth-order finite similitude comes across similar issues when gravity and inertia are important for the test model, there appear similar limitations and it requires additional degree of freedoms to capture scale effects. Therefore, the following chapters examine both zeroth-order and first-order finite similitude, a novel approach to applications of finite similitude theory in structural mechanics and dynamics.

Chapter

THREE

Paper one: A first order finite similitude approach to scaled aseismic structures

Overview

After exploring numerous investigations, it was inferred that dimensional analysis was the vital hypothesis for scaled experimentations up until now. For many decades, scaled experimentation has been used for the design of earthquake-resistant (aseismic) structures, and those experiments have been conducted under the light of the theory of dimensional analysis. Although scaled experiments still have a significant impact, they are considered to have limitations, specifically when the scale ratio is large. This article discusses a new theory for the analysis of earthquake-resistant structures (beams, substructures, or buildings) that is founded on the metaphysical concept of space scaling. Those structures are contracted through the concept of space contraction with the evaluation of a new scaling theory. The new scaling theory has some advantages, which are explained in detail in this article.

Authors Contribution: K. Davey contributed to conceptualization, methodology, writing - review & editing of the paper while R. Darvizeh was mostly took place on supervision and methodology. **M. Atar** designed and performed the analytical and numerical analysis, contributed to methodology, validation, writing - review & editing the journal paper.

Details: Engineering Structures. Received 12 April 2020, Revised 28 November 2020, Accepted 14 December 2020, Available online 13 January 2021. **Publication date:** 12 March 2021

Paper DOI: https://doi.org/10.1016/j.engstruct.2020.111739

A first order finite similitude approach to scaled aseismic structures

K. Davey, R. Darvizeh, M. Atar

School of Mechanical, Aerospace and Civil Engineering,
The University of Manchester, ManchesterM13 9PL, UK

Abstract

For many decades the designs of earthquake-resistant (aseismic) structures have been influenced by scaled experiments, underpinned by the theory of dimensional analysis. Although scaled experiments still play an important role, they are recognised to suffer shortcomings, which are particularly severe when scaling ratios are pronounced. The issue is one of *scale effects* and the inability of dimensional analysis to offer any solution in their presence.

This paper is concerned with a new theory for the analysis of aseismic structures that is founded on the metaphysical concept of space scaling, where beams, substructures or buildings etc. are contracted through the mechanism of space contraction. Although space contraction is evidently practically impossible the theory describes the effects of such a process on the underpinning governing mechanics involved. Unlike dimensional analysis the approach which is termed *finite similitude* embraces scale effects and accounts for them by linking experiments at more than one scale.

It is demonstrated in this work how it is possible to reconstruct full-scale behaviour by means of two scaled experiments of a selected beam, column and multi-storey structure when subjected to dynamic loading conditions.

Keywords: finite similitude, aseismic structures, dimensional analysis, earthquakes, scaled experimentation.

1. Introduction

For massive structures like sturdy long bridges and skyscrapers, earthquake testing methods such as spot tests or indoor tests have become more challenging and less feasible. In such cases, testing scaled models is more practical, easier to implement and is a cost-effective option and can often be the only solution where testing the real-life prototype is impossible. Scaled experimentation continues to play a significant role in process, product design and testing for components and products but is recognized to suffer from severe limitations. The difficulty with scaling rises mainly from the non-linear relationships between the physical constraints imposed on any scaled physical system. The most readily observable changes that take place are those associated with geometric measures with length changing linearly, area quadratically and volume cubically with scale. This means for example that under a scaled contraction, the body forces will lessen at a much faster rate than the forces on the surface. The complexity of the multitude of changes involved cast a significant shadow over the reliability of scaled experimentation and this issue along with the rise of computational modelling has undoubtedly led to a diminution of scaled physical modelling trials in recent times.

The issue is well appreciated by the academic and industrial communities and the founding bedrock of modern-scaled experimentation is dimensional analysis and the concept of similarity. Similar structures behave identically and through the application of dimensional analysis, similarity can be sought [2]. Rather unfortunately similarity is seldom possible and dimensional analysis provides no solution when any two structures are not similar. In some respects, the theory that underpins scaled experimentation has not changed fundamentally for over a century and dimensional analysis remains the only ubiquitous scaling theory. Dimensional analysis is underpinned by the Buckingham Pi theorem [3] and should the dimensionless quantities (Pi groups) coincide for the full-scale and scaled systems, then the two processes are denoted similar. However, this seldom happens in practice [4] and the approach has to-date had little success in complex structural applications. Although structural engineering has been a field of study for many of hundreds if not over a thousand years, earliest attempts at scaled experimentation prior to the adoption of scaling rules were somewhat rudimentary and highly inaccurate. The work of Buckingham [2] provided the foundation for more realistic

scaled models and the first application of the scaled method can again be attributed to him [5], although for a purely theoretically study. A significant increase in the number of publications about scaled methods followed the seminal work of Buckingham [2].

A number of scaling approaches [6,7] have materialised over the year and these include: energy methods (EM), similitude and asymptotic models for structural acoustic research applications (SAMSARA), empirical similarity method (ESM) and sensitivity analysis (SA). Each has their own merits and demerits, but none match the simplicity and ubiquity of dimensional analysis. Moreover, a fundamental concern with all these approaches is that they cannot accommodate to any significant degree *scale effects*. Scale effects are those changes in behaviour that take place with scale. and recent attempts (e.g. empirical similarity [7], model variation [8], sensitivity analysis [9]) to address the problem of scale effects are to a large extent unsatisfactory being founded on perturbations around the standard definition of similarity [6]. The difficulty associated with scale effects has meant modern-day researchers adopting altogether different methodologies with the application and development of sophisticated computational approaches. Computation however does not altogether bypass experimentation and for those processes involving complex material behaviour, uncertainties, unknown behaviour etc., experimentation still plays a critical role. As noted by Simitses and Rezaeepazhand [10], some systems are so complex making it almost impossible to make simplifying assumptions for direct simulation. Complex material behaviour has led to the emergence of a plethora of constitutive models and multi-scale approaches [11–13]. It is beyond contention that computational approaches have led to significant advances but solving the problem of scale effects should provide alternative complementary approaches.

Full-scale structural experiments have the advantage of being able to replicate to good accuracy the exact environment and realistic conditions of any situation and represent a very direct approach for the analysis of physical phenomena. Thus, despite the complexities of the physics involved, experiments at full scale can provide precise and valuable data. However, with every increasing advances taking place in engineering and technology, the requirements for most experiments are becoming more involved with financial and time requirements increasing

accordingly. This is particularly acute in the case of damage-test experiments, which for any realistic structure can be expensive to perform as repetition is often required.

In the case of seismic structural testing the transfer of information from the scaled model to the structure is required to follow scaling rules if results are to be meaningful. Scaling however has its own limitations, where several aspects of the structure cannot always be scaled as a result of constraints on testing equipment (e.g. shake table) or unavailability of materials with the required properties etc. In order to understand the behaviour of the structure under earthquake loading, present-day tests are carried out and interpreted with the application of well-researched scaling relationships. There exist many interesting seismic structural studies involving shake tables, the application of scaling rules and dimensional analysis. Sharma et al. [14] for example analysed a three-storey scaled model by applying scaling laws and dimensional analysis theory to investigate the behaviour of the model. Similarly, a scaled model was constructed by Guerrero et al. [15], which was limited to 1/10 of the full-size structure due to size limitations and the cost of the experimental equipment. The prototype structure analysed in this reference is located in Mexico City as stated by Guerrero et al. [16]. Similarly, shake-table testing and studies have been carried out on a one-storey, single-bay steel frame by Nader and Astaneh-Asl [17]. They analysed the performance of steel structures under varying earthquake loadings simulated at smaller scales experimentally. In reference [10] an investigation into the effects of various material and section-level parameters on the structural response metrics was achieved by utilising the financial and logistical benefits offered by small-scale testing (1/8-scale factor). Other studies involving shake table testing are those done on: one-bay, two-storey steel frames, investigating such things as second-order inelastic behaviours [18]; scaling guidelines for modern unreinforced masonry buildings with hollow clay brick units (1/2 scale factor) [19] and; testing of a 1/50 scaled model under one and two dimensional base excitations and gradually increased amplitudes [20]. The main difficulty with all these studies is that they are limited by the inability of dimensional analysis to account for scale effects and the ad hoc nature of the scaling rules needed to extend the analysis.

This paper is concerned with a completely new concept for scaled experimentation termed *finite similitude* [21–26] and attempts for the first time to link experiments at

more than one scale in a systematic manner. The work here builds on earlier work on scaling (now termed *zeroth-order finite similitude*) that has been applied in the areas of impact mechanics [25], powder compaction [21], biomechanics [24] and metal forming [23], and involves only one scaled experiment. The work presented here is the first application of finite similitude to seismic studies with a more advanced version of the finite-similitude theory involving two scaled experiments.

The finite similitude theory is founded on the metaphysical concept of space scaling which is introduced in Section 2. The focus on space leads to an analysis method that is innately tied to the effects of space contraction, i.e. it naturally leads to control volume concepts in Section 2.2. At first sight the focus on control volumes and transport equations might appear somewhat removed from structural analysis but it is simply a consequence of the path the theory takes to move from space, to a moving region of space (control volume) to transport equations (laws of nature) to field identities and ultimately to structural analysis. The most critical step in the finite-similitude approach as discussed in Section 2.3 for structural mechanics is the projection of the trial-space (where the scaled experiment resides) physics onto the physical space (where the full-scale structure resides). This projection reveals in one form or another, scale dependences, explicitly for geometric measures such as area and volume but implicitly for scalar, vector and tensor fields such as density, displacement and stress, respectively. The problem of scaling becomes one of finding these dependencies, which is achieved in this paper through a new form of similarity (*first-order finite similitude*) as described in Section 3. The solving of the new differential similarity identity is shown in Section 3.1, where physically intuitive field relationships are revealed. One of the features of finite similitude is that it does not concern itself with constitutive equations as it reconstructs all fields in the physical space; this along with application practicalities for the theory are presented in Section 3.1 and Appendix A. Sections 4, 5 and 6 examine the behaviours of a beam, column and three-storey structure, respectively when subject to dynamic excitation to illustrate how the theory can replicate full-scale behaviours. Introduced in Section 5.2 and Appendix B is a new proportional-fields assumption for the determination of similitude parameters. The paper ends with a conclusions section.

2. The theoretical foundation of finite similitude

The finite similitude theory is founded on a metaphysical concept that cannot be physically enacted. However, the purpose of metaphysical space scaling is threefold; firstly it is to provide a physically intuitive approach to scaled experimentation, where it is possible to imagine the structure of interest being contracted or expanded by the contraction or expansion of space. Secondly, it facilitates the precise mathematical description of scaling, where its effect can be precisely relayed to the underpinning physics of a structure. Thirdly, since in principle, space can be metaphysically distorted in different ways, it introduces a high degree of flexibility, which is simply absent from competing methods.

2.1. The metaphysics of space scaling

The analysis of any structure begins with the identification of the inertial frame but at least two inertial frames are involved with scaling, one for the physical and another for the trial space. The starting point therefore is the specification of the trial-space coordinate system (denoted by $\boldsymbol{x}_{ts}$) along with a physical-space coordinate system (denoted by $\boldsymbol{x}_{ps}$), where the subscripts "ts" and "ps" refer to trial and physical space, respectively. It is assumed here that the coordinate frames, linked to these systems, are orthonormal. It should be appreciated however that structures in the scaled space are viewed from the viewpoint of an external observer, i.e. one unaffected by the scaling process and the choice of coordinate frame is therefore essentially a matter of choice. The overall concept of space scaling is presented in Fig. 1, where the orthonormal coordinate frames for the physical space $\{\underline{G}_i\}$ and the trial space $\{\underline{g}_i\}$ are depicted. Shown in the figure are two measures of time t_{ps} and t_{ts} for the physical and trial spaces, respectively. Since Newtonian mechanics is the focus here the existence of absolute time is assumed and it is assumed further that t_{ps} and t_{ts} are related, i.e. a function relationship $t_{ps} \mapsto t_{ts}$ exists, which in differential terms is of the form $dt_{ts} = g dt_{ps}$, where g is a positive parameter. As indicated in the figure, metaphysical scaling is quantified mathematical by a temporally invariant affine map of the form $\boldsymbol{x}_{ps} \mapsto \boldsymbol{x}_{ts}$, which can be represented in differential terms by $d\boldsymbol{x}_{ts} = F \cdot d\boldsymbol{x}_{ps}$, where in suffix notation this is

$dx_{ts}^{i} = F^{i}{}_{j} dx_{ps}^{j}$. Here the matrix F is both spatially and temporally invariant to reflect the focus on scaled experimentation.

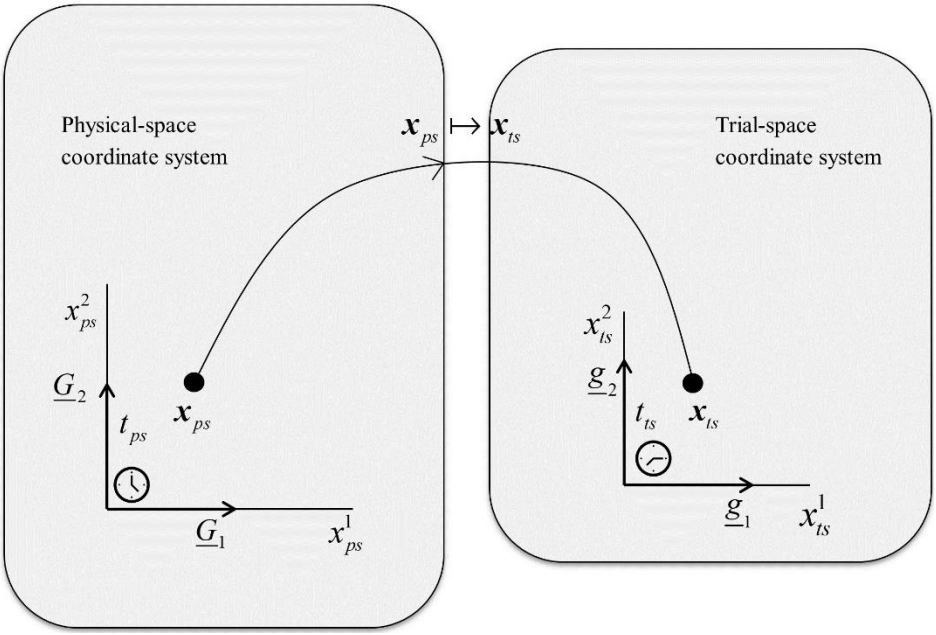

Figure 1: Metaphysical space-scaling concept and inertial coordinate systems

The nature of the space scaling is dictated by the matrix F and anisotropic scaling is indeed possible where geometric similarity as it is traditionally known can be broken. The focus here however is on isotropic scaling with $F = \beta I$, where I is a unit matrix and β is a positive parameter that dictates the extent of linear scaling taking place. The effect of β on the physical space is illustrated in Fig. 2, with $0 < \beta < 1$ indicating contraction, $\beta = 1$ for no scaling and $1 < \beta$ for expansion.

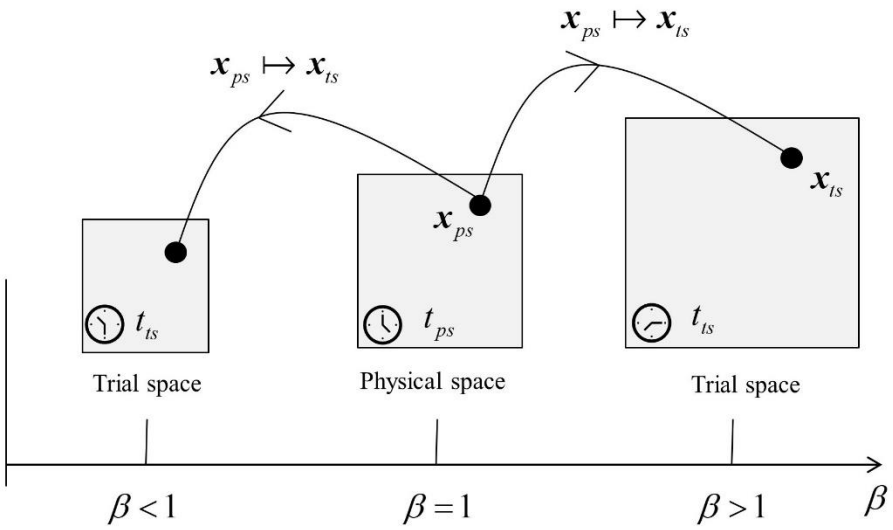

Figure 2: The role played by β in space scaling.

With the establishment and quantification of space scaling it is now possibly to relate the differential-geometric measures of volume and area, i.e. $dV_{ts} = \beta^3 dV_{ps}$ and $\boldsymbol{n}_{ts} d\Gamma_{ts} = \beta^2 \boldsymbol{n}_{ps} d\Gamma_{ps}$, where, dV_{ts} $d\Gamma_{ts}$ and $\boldsymbol{n}_{ts}$ refer to volume and area measures, and a unit normal vector, respectively in the trial space; subscript "ps" identifies like quantities in the physical space.

2.2. The mathematics of control volume motion

To relate analyses of structures in the trial and physical spaces it is first necessary to be able to identify connections between two regions of space. This can be achieved by means of control volumes, which are regions of space that are allowed to move and distort. Control volumes invariably lead to transport equations which at first sight may appear somewhat remote from traditional structural analysis, which is the focus of study here. However, transport equations provide the correct description of the underlying laws of nature as they incorporate directly the changes in geometric measures. The motion of a trial-space control volume Ω_{ts}^{*} can be described mathematically using a velocity field $\boldsymbol{v}_{ts}^{*}$ and by contrasting its location with to a reference control volume Ω_{ts}^{*ref}. The basic idea is depicted in Fig. 3 and also shown is the map $\boldsymbol{\chi}_{ts} \mapsto \boldsymbol{x}_{ts}^{*}$ with $\boldsymbol{\chi}_{ts} \in \Omega_{ts}^{*ref}$ and $\boldsymbol{x}_{ts}^{*} \in \Omega_{ts}^{*}$.

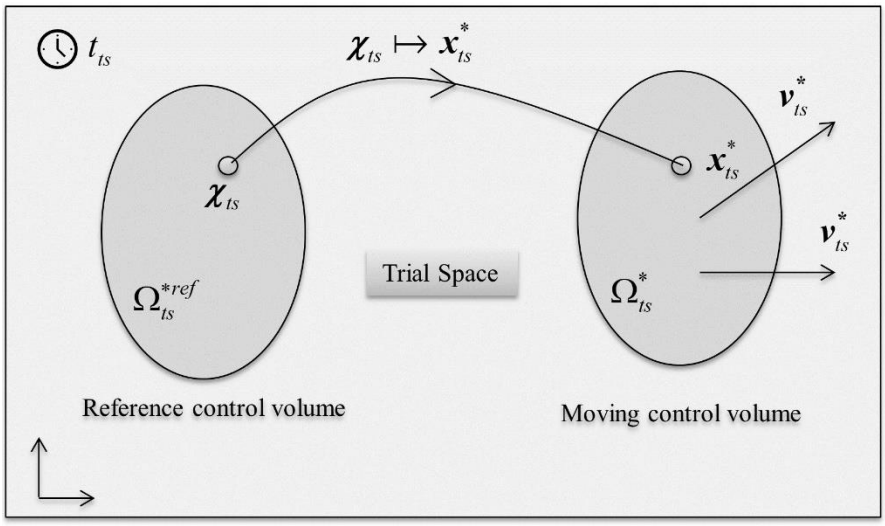

Figure 3: The kinematics of a moving control volume Ω^*_{ts}.

The idea presented here is very similar to that employed to describe the motion of a body of mass but in this case mass is not involved and the body is a moving region of space. The coordinate point $\boldsymbol{x}^*_{ts}$ is attached to Ω^*_{ts} and its velocity $\boldsymbol{v}^*_{ts}$ is defined by the partial derivative

$$\boldsymbol{v}^*_{ts} = \frac{D^*\boldsymbol{x}^*_{ts}}{D^*t_{ts}} = \left.\frac{\partial \boldsymbol{x}^*_{ts}}{\partial t_{ts}}\right|_{\boldsymbol{\chi}_{ts}} \qquad (1)$$

where the derivative $\frac{D^*}{D^*t_{ts}}$ is used here to signify a temporal derivative with the reference coordinate $\boldsymbol{\chi}_{ts}$ held constant.

Since a control volume is nothing more than a region of space it is affected in precisely the same manner as the accompanying scaled space and the identity $d\boldsymbol{x}^*_{ts} = \beta d\boldsymbol{x}^*_{ps}$ is assumed to apply. Moreover, in view of the temporal relationship $dt_{ts} = g dt_{ps}$ it follows that control-volume velocity fields are related by

$$\boldsymbol{v}^*_{ts} = g^{-1}\beta \boldsymbol{v}^*_{ps} \qquad (2)$$

which provides synchronous motion of the control volumes Ω^*_{ts} and Ω^*_{ps}.

The overall picture displaying the connectivity between reference and moving control volumes in the two spaces along with the synchronous motion is depicted in Fig. 4. Note that the identity $d\boldsymbol{x}^*_{ts} = \beta d\boldsymbol{x}^*_{ps}$ can be contrasted again the space-scaling

identity $d\boldsymbol{x}_{ts} = \beta d\boldsymbol{x}_{ps}$ where it is appreciated that the former unlike the latter is relating moving points.

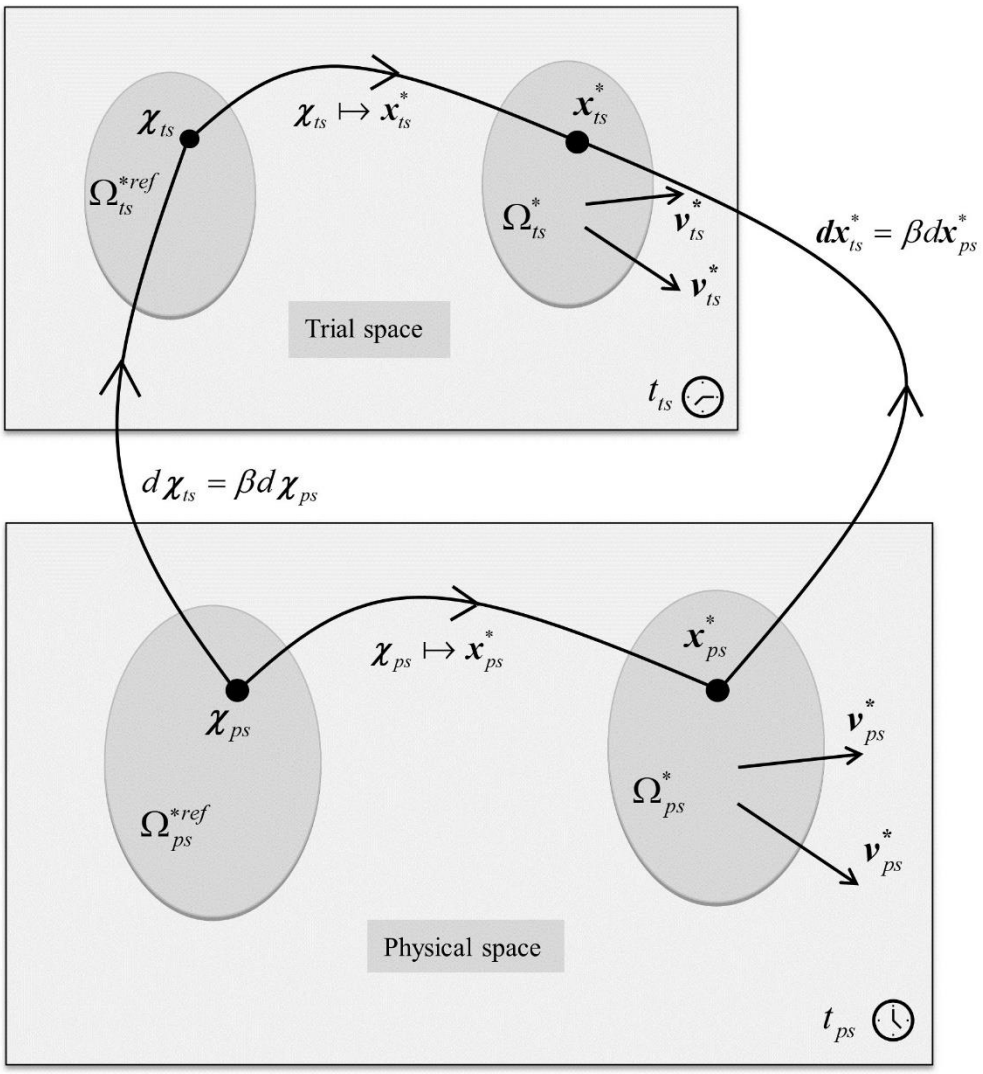

Figure 4: Synchronous motion of control volumes Ω^*_{ts} and Ω^*_{ps}.

Eq. (2) is closely related to the *law-of-volume* identity

$$\frac{D^*}{D^* t_{ts}} \int_{\Omega^*_{ts}} dV^*_{ts} - \int_{\Gamma^*_{ts}} \boldsymbol{v}^*_{ts} \cdot \boldsymbol{n}_{ts} d\Gamma^*_{ts} = 0 \qquad (3)$$

which is an equation not considered in structural mechanics as it has no field associated with it but nevertheless plays a significant role in finite similitude theory. It is relatively straightforward to prove that this equation is proportional to the physical space equation

$$\frac{D^*}{D^* t_{ps}} \int_{\Omega^*_{ps}} dV^*_{ps} - \int_{\Gamma^*_{ps}} \boldsymbol{v}^*_{ps} \cdot \boldsymbol{n}_{ps} d\Gamma^*_{ps} = 0 \qquad (4)$$

on substitution of $dV^*_{ts} = \beta^3 dV^*_{ps}$ and $\boldsymbol{n}_{ts} d\Gamma^*_{ts} = \beta^2 \boldsymbol{n}_{ps} d\Gamma^*_{ps}$ (which follows from $d\boldsymbol{x}^*_{ts} = \beta d\boldsymbol{x}^*_{ps}$) and $dt_{ts} = g dt_{ps}$ along with Eq. (2) to give

$$\frac{D^*}{D^* t_{ts}} \int_{\Omega^*_{ts}} dV^*_{ts} - \int_{\Gamma^*_{ts}} \boldsymbol{v}^*_{ts} \cdot \boldsymbol{n}_{ts} d\Gamma^*_{ts} = \frac{\beta^3}{g} \left(\frac{D^*}{D^* t_{ps}} \int_{\Omega^*_{ps}} dV^*_{ps} - \int_{\Gamma^*_{ps}} \boldsymbol{v}^*_{ps} \cdot \boldsymbol{n}_{ps} d\Gamma^*_{ps} \right) = 0 \qquad (5)$$

which evidently confirms proportionality.

The whole idea of the metaphysical space-scaling approach is encapsulated by Eq. (5), where the solution of an equation in one space confirms the solution of the corresponding equation in another.

2.3. Scaled structural mechanics in transport form

The transport equations important to structural mechanics for finite similitude are those concerned with continuity, momentum and movement and take the form

$$\frac{D^*}{D^* t_{ts}} \int_{\Omega^*_{ts}} \rho_{ts} dV^*_{ts} + \int_{\Gamma^*_{ts}} \rho_{ts} \left(\boldsymbol{v}_{ts} - \boldsymbol{v}^*_{ts} \right) \cdot \boldsymbol{n}_{ts} d\Gamma^*_{ts} = 0 \qquad (6a)$$

$$\frac{D^*}{D^* t_{ts}} \int_{\Omega^*_{ts}} \rho_{ts} \boldsymbol{v}_{ts} dV^*_{ts} + \int_{\Gamma^*_{ts}} \rho_{ts} \boldsymbol{v}_{ts} \left(\boldsymbol{v}_{ts} - \boldsymbol{v}^*_{ts} \right) \cdot \boldsymbol{n}_{ts} d\Gamma^*_{ts} - \int_{\Gamma^*_{ts}} \boldsymbol{\sigma}_{ts} \cdot \boldsymbol{n}_{ts} d\Gamma^*_{ts} - \int_{\Omega^*_{ts}} \rho_{ts} \boldsymbol{b}_{ts} dV^*_{ts} = 0 \qquad (6b)$$

$$\frac{D^*}{D^* t_{ts}} \int_{\Omega^*_{ts}} \rho_{ts} \boldsymbol{u}_{ts} dV^*_{ts} + \int_{\Gamma^*_{ts}} \rho_{ts} \boldsymbol{u}_{ts} \left(\boldsymbol{v}_{ts} - \boldsymbol{v}^*_{ts} \right) \cdot \boldsymbol{n}_{ts} d\Gamma^*_{ts} - \int_{\Omega^*_{ts}} \rho_{ts} \boldsymbol{v}_{ts} dV^*_{ts} = 0 \qquad (6c)$$

where ρ_{ts} is mass density, $\boldsymbol{v}_{ts}$ is material velocity, $\boldsymbol{u}_{ts}$ is material displacement, $\boldsymbol{\sigma}_{ts}$ is Cauchy stress and $\boldsymbol{b}_{ts}$ is specific-body force (i.e. force per unit mass).

It is usual not to involve the continuity equation in structural mechanics as density is often assumed fixed but in the context of scaling and physical modelling, materials can be substituted and it is necessary to understand what substitutions are allowable hence the reason for its inclusion here. Likewise a separate equation for movement is generally not a feature and this was introduced in reference [27] to bring displacement into the family of transport equations and it is particularly convenient to include this here as displacement is central to describing structural deformation.

The next step and most critically important along the path to scaling identities is the projection of Eqs. (6) onto the physical space, as it is through this mathematical operation that scale dependencies are exposed. Consider then the substitution of $dV_{ts}^{*}=\beta^{3}dV_{ps}^{*}$, $\boldsymbol{n}_{ts}d\Gamma_{ts}^{*}=\beta^{2}\boldsymbol{n}_{ps}d\Gamma_{ps}^{*}$, $dt_{ts}=gdt_{ps}$ and Eq. (2) into Eq. (6) (and Eq. (3) for completeness) and multiplication throughout by g. In addition, Eq. (3) and each of Eqs. (6) are multiplied throughout by non-zero scaling parameters α_0^1, α_0^ρ, α_0^ν and α_0^u, respectively; the role of which will be made clear. These operations provide the following four equations:

$$\alpha_0^1 T_0^1(\beta)=\frac{D^*}{D^* t_{ps}}\int_{\Omega_{ps}^*}\alpha_0^1\beta^3 dV_{ps}^*-\int_{\Gamma_{ps}^*}\alpha_0^1\beta^3\boldsymbol{v}_{ps}^*\cdot\boldsymbol{n}_{ps}d\Gamma_{ps}^*=0 \tag{7a}$$

$$\alpha_0^\rho T_0^\rho(\beta)=\frac{D^*}{D^* t_{ps}}\int_{\Omega_{ps}^*}\alpha_0^\rho\beta^3\rho_{ts}dV_{ps}^*+\int_{\Gamma_{ps}^*}\alpha_0^\rho\beta^3\rho_{ts}\left(\boldsymbol{V}_{ps}-\boldsymbol{v}_{ps}^*\right)\cdot\boldsymbol{n}_{ps}d\Gamma_{ps}^*=0 \tag{7b}$$

$$\alpha_0^\nu T_0^\nu(\beta)=\frac{D^*}{D^* t_{ps}}\int_{\Omega_{ts}^*}\left(\alpha_0^\nu g^{-1}\beta\right)\beta^3\rho_{ts}\boldsymbol{V}_{ps}dV_{ts}^*+\int_{\Gamma_{ps}^*}\left(\alpha_0^\nu g^{-1}\beta\right)\beta^3\rho_{ts}\boldsymbol{V}_{ps}\left(\boldsymbol{V}_{ts}-\boldsymbol{v}_{ps}^*\right)\cdot\boldsymbol{n}_{ps}d\Gamma_{ps}^*$$
$$-\int_{\Gamma_{ps}^*}\alpha_0^\nu g\beta^2\boldsymbol{\sigma}_{ts}\cdot\boldsymbol{n}_{ps}d\Gamma_{ps}^*-\int_{\Omega_{ps}^*}\alpha_0^\nu g\beta^3\rho_{ts}\boldsymbol{b}_{ts}dV_{ps}^*=0 \tag{7c}$$

$$\alpha_0^u T_0^u(\beta)=\frac{D^*}{D^* t_{ps}}\int_{\Omega_{ps}^*}\left(\alpha_0^u\beta\right)\beta^3\rho_{ts}\boldsymbol{U}_{ts}dV_{ps}^*+\int_{\Gamma_{ts}^*}\left(\alpha_0^u\beta\right)\beta^3\rho_{ts}\boldsymbol{U}_{ps}\left(\boldsymbol{V}_{ps}-\boldsymbol{v}_{ps}^*\right)\cdot\boldsymbol{n}_{ps}d\Gamma_{ps}^*$$
$$-\int_{\Omega_{ps}^*}\left(\alpha_0^u\beta\right)\beta^3\rho_{ts}\boldsymbol{V}_{ps}dV_{ps}^*=0 \tag{7d}$$

where $\boldsymbol{V}_{ps}=\beta^{-1}g\boldsymbol{v}_{ts}$ and $\boldsymbol{U}_{ps}=\beta^{-1}\boldsymbol{u}_{ts}$.

The importance of Eqs. (7) should not be understated as they capture all scale dependencies that are a feature of scaled structural mechanics. The appearance of β^3 and β^2 are explicit and are recognised to arise from the change in geometric measures of volume and area. Other dependencies are hidden, which include the fields $\boldsymbol{V}_{ps}(\beta)$ and $\boldsymbol{U}_{ps}(\beta)$ along with other fields. In this context scaling has been transformed into a problem of revealing the behaviour of hidden fields and unlike dimensional analysis embraces the changes that take place in scaled experimentation. The process for revealing hidden dependencies can take one of

two routes, with one requiring additional information (i.e. scale effects, boundary condition etc.) about the specific problem under consideration and the other effectively assuming how things behaviour in a global sense on application of a scale invariance. This latter approach is the focus here and is particularly well suited to physical modelling where the idea is to design physical-trial experiments to satisfy the scale invariance imposed.

3. The mathematics of scale invariances

The transport Eqs. (7) are of the general form $\alpha_0^{\psi} T_0^{\psi} = 0$, with ψ set to 1, ρ, v and u. An obvious β–invariance for scaling is that $\alpha_0^{\psi} T_0^{\psi}(\beta)$ does not depend on β, which in mathematical terms is

$$\frac{d}{d\beta}\left(\alpha_0^{\psi} T_0^{\psi}\right) \equiv 0 \qquad (8)$$

where the equality sign "$\equiv$" signifies that the derivative is identically zero.

Zeroth-order finite similitude refers to a system of transport equations that satisfies this particular identity and details on its application can be found in reference [21–23,25,26]. The "initial conditions" for Eq. (8) are taken to be the physical system at $\beta = \beta_0 = 1$. Note for Eqs. (7) that the requirement for $\alpha_0^{\psi} T_0^{\psi}(1) = 0$ to match the physical system imposes the following constraints on the scaling parameters: $\alpha_0^1(1) = \alpha_0^{\rho}(1) = \alpha_0^{\nu}(1) = \alpha_0^{u}(1) = 1$ along with $g(1) = 1$ since $dt_{ts}(1) = g(1)\, dt_{ps} = dt_{ps}$. Similarly the fields are required to satisfy: $\rho_{ts}(1) = \rho_{ps}$, $\boldsymbol{V}_{ps}(1) = \boldsymbol{v}_{ps}$, $\boldsymbol{U}_{ps}(1) = \boldsymbol{u}_{ps}$, and $\boldsymbol{\sigma}_{ts}(1) = \boldsymbol{\sigma}_{ps}$ and so on for other fields. In the presence of scale effects, Eq. (8) will not be satisfied and $\alpha_0^{\psi} T_0^{\psi}(\beta)$ will therefore depend on β but prior to examining this situation it is important to examine how attempting to satisfy this equation impacts on the scaling parameters $\alpha_0^{\psi}(\beta)$. Note that integration of Eq. (8) between β_1 and $\beta_0 = 1$ provides $\alpha_0^{\psi} T_0^{\psi}(\beta_1) \equiv \alpha_0^{\psi} T_0^{\psi}(\beta_0) = T_0^{\psi}(1)$, i.e. the transport equations at any arbitrary scale β_1 match the full-scale system, which of course is very similar to the invariance offered in dimensional analysis where dimensionless-governing equations do not change

with scale. Note also that β is eliminated from Eq. (7a) on setting $\alpha_0^1(\beta)=\beta^{-3}$, which satisfies as required $\alpha_0^1(1)=1$. The condition $\alpha_0^1(\beta)=\beta^{-3}$ is a necessary and sufficient requirement for the law of volume to be satisfied at any scale. Turning attention now to Eq. (7b) it is apparent that a necessary but not sufficient condition for satisfying Eq. (8) with $\psi=\rho$ is that $\rho_{ps}=\alpha_0^{\rho}\beta^3\rho_{ts}$. This condition is not sufficient as Eq. (8) additionally requires $\boldsymbol{V}_{ps}=\boldsymbol{v}_{ps}$, which is assumed not to be satisfied here. Examination of Eqs. (7c) and (7d) provide the necessary (but not sufficient) relationships $\alpha_0^{v}=g\beta^{-1}\alpha_0^{\rho}$ and $\alpha_0^{u}=\beta^{-1}\alpha_0^{\rho}$.

The identities $\rho_{ps}=\alpha_0^{\rho}\beta^3\rho_{ts}$, $\alpha_0^{v}=g\beta^{-1}\alpha_0^{\rho}$ and $\alpha_0^{u}=\beta^{-1}\alpha_0^{\rho}$ are to be taken forward to the next level of finite similitude termed *first-order finite similitude*. The observation that the scaling parameters $\alpha_0^{\psi}(\beta)$ have the role of attempting to eliminate β from $\alpha_0^{\psi}T_0^{\psi}(\beta)=0$ suggests that a way forward is to consider the scaling of the identity

$$T_1^{\psi}=\frac{d}{d\beta}\left(\alpha_0^{\psi}T_0^{\psi}\right) \tag{9}$$

with new scaling parameters $\alpha_1^{\psi}(\beta)$ (satisfying $\alpha_1^{\psi}(1)=1$) and consider then

$$\frac{d}{d\beta}\left(\alpha_1^{\psi}T_1^{\psi}\right)=\frac{d}{d\beta}\left(\alpha_1^{\psi}\frac{d}{d\beta}\left(\alpha_0^{\psi}T_0^{\psi}\right)\right)\equiv 0 \tag{10}$$

which is the scaled invariance for *first-order finite similitude* and was first introduced in reference [28] for impact mechanics.

This approach can lead to higher forms with

$$T_2^{\psi}=\frac{d}{d\beta}\left(\alpha_1^{\psi}T_1^{\psi}\right) \tag{11}$$

etc. but it will become clear that Eq. (10) leads to the requirement of two scaled structural experiments, so is sufficient for our purposes here.

It is important to note that should Eq. (8) be satisfied (i.e. zeroth-order finite similitude), then Eq. (10) is automatically satisfied which is a desirable feature. Also expanding the derivative on the left hand side of Eq. (10) gives

$$\frac{d}{d\beta}\left(\alpha_1^{\psi} T_1^{\psi}\right) = \frac{d\alpha_1^{\psi}}{d\beta} T_1^{\psi} + \alpha_1^{\psi} \frac{dT_1^{\psi}}{d\beta} \equiv 0 \tag{12}$$

which is an expansion of the derivatives of $\alpha_0^{\psi} T_0^{\psi}$, which at any arbitrary $\beta = \beta_1$ can represent (by means of osculation) any other linear combination of the derivatives of $\alpha_0^{\psi} T_0^{\psi}$ (up to the same order), which is sufficient for scaling purposes and illustrates that there is no better alternative to Eq. (10).

The form of Eq. (10) happens to be ideal for integration by means of divided differences as discussed in the following section, which provides added justification for its form.

3.1. First-order solutions

Prior to examining the solution to Eq. (10) for transport Eqs. (7) it is judicious to substitute the constraints $\rho_{ps} = \alpha_0^{\rho} \beta^3 \rho_{ts}$, $\alpha_0^{\nu} = g\beta^{-1}\alpha_0^{\rho}$ and $\alpha_0^{u} = \beta^{-1}\alpha_0^{\rho}$ to provide

$$\alpha_0^{\rho} T_0^{\rho}(\beta) = \frac{D^*}{D^* t_{ps}} \int_{\Omega_{ps}^*} \rho_{ps} dV_{ps}^* + \int_{\Gamma_{ps}^*} \rho_{ps} \left(\boldsymbol{V}_{ps} - \boldsymbol{v}_{ps}^*\right) \cdot \boldsymbol{n}_{ps} d\Gamma_{ps}^* = 0 \tag{13a}$$

$$\alpha_0^{\nu} T_0^{\nu}(\beta) = \frac{D^*}{D^* t_{ps}} \int_{\Omega_{ts}^*} \rho_{ps} \boldsymbol{V}_{ps} dV_{ts}^* + \int_{\Gamma_{ps}^*} \rho_{ps} \boldsymbol{V}_{ps} \left(\boldsymbol{v}_{ts} - \boldsymbol{v}_{ps}^*\right) \cdot \boldsymbol{n}_{ps} d\Gamma_{ps}^*$$
$$- \int_{\Gamma_{ps}^*} \boldsymbol{\Sigma}_{ts} \cdot \boldsymbol{n}_{ps} d\Gamma_{ps}^* - \int_{\Omega_{ps}^*} \boldsymbol{B}_{ts} dV_{ps}^* = 0 \tag{13b}$$

$$\alpha_0^{u} T_0^{u}(\beta) = \frac{D^*}{D^* t_{ps}} \int_{\Omega_{ps}^*} \rho_{ps} \boldsymbol{U}_{ts} dV_{ps}^* + \int_{\Gamma_{ts}^*} \rho_{ps} \boldsymbol{U}_{ps} \left(\boldsymbol{v}_{ps} - \boldsymbol{v}_{ps}^*\right) \cdot \boldsymbol{n}_{ps} d\Gamma_{ps}^* - \int_{\Omega_{ps}^*} \rho_{ps} \boldsymbol{V}_{ps} dV_{ps}^* = 0 \tag{13c}$$

where $\boldsymbol{\Sigma}_{ps} = \alpha_0^{\nu} g\beta^2 \boldsymbol{\sigma}_{ts}$, $\boldsymbol{B}_{ts} = \alpha_0^{\nu} g\beta^3 \rho_{ts} \boldsymbol{b}_{ts} = g^2 \beta^{-1} \boldsymbol{b}_{ts}$ and where the transfer $\left(\boldsymbol{V}_{ps} - \boldsymbol{v}_{ps}^*\right) \cdot \boldsymbol{n}_{ps}$ in the momentum and movement equations is approximated by the zeroth-order expression $\left(\boldsymbol{v}_{ps} - \boldsymbol{v}_{ps}^*\right) \cdot \boldsymbol{n}_{ps}$ to reflect the fact that the term $\boldsymbol{V}_{ps}\left(\boldsymbol{V}_{ps} \cdot \boldsymbol{n}_{ps}\right)$ is negligible in structural mechanics but also to avoid the necessity to consider higher forms of similitude.

The approach to solving Eq. (10) is to apply divided differences first to Eq. (9) along with a mean-value theorem for integration to provide

$$\alpha_1^{\psi} \mathbb{T}_1^{\psi}\left(\beta_2^1\right) \equiv \alpha_1^{\psi}\left(\beta_2^1\right) \frac{\alpha_0^{\psi} \mathbb{T}_0^{\psi}(\beta_1) - \alpha_0^{\psi} \mathbb{T}_0^{\psi}(\beta_2)}{\beta_1 - \beta_2} \tag{14a}$$

$$\alpha_1^{\psi}\mathbb{T}_1^{\psi}\left(\beta_1^0\right)\equiv\alpha_1^{\psi}\left(\beta_1^0\right)\frac{\alpha_0^{\psi}\mathbb{T}_0^{\psi}\left(\beta_0\right)-\alpha_0^{\psi}\mathbb{T}_0^{\psi}\left(\beta_1\right)}{\beta_0-\beta_1} \tag{14b}$$

where $\beta_2\le\beta_2^1\le\beta_1$ and $\beta_1\le\beta_1^0\le\beta_0$ with β_2 and β_1 being scales for trial-space experimentation and $\beta_0=1$ being at full scale.

In view of Eq. (10) the next divided difference gives zero or equivalently $\alpha_1^{\psi}T_1^{\psi}\left(\beta_1^0\right)\equiv\alpha_1^{\psi}T_1^{\psi}\left(\beta_2^1\right)$, which on substitution of Eqs. (14) provides after some manipulation

$$\alpha_0^{\psi}\mathbb{T}_0^{\psi}\left(\beta_0\right)\equiv\alpha_0^{\psi}\mathbb{T}_0^{\psi}\left(\beta_1\right)+R_1^{\psi}\left(\alpha_0^{\psi}\mathbb{T}_0^{\psi}\left(\beta_1\right)-\alpha_0^{\psi}\mathbb{T}_0^{\psi}\left(\beta_2\right)\right) \tag{15}$$

where

$$R_1^{\psi}=\left(\frac{\alpha_1^{\psi}\left(\beta_2^1\right)}{\alpha_1^{\psi}\left(\beta_1^0\right)}\right)\left(\frac{\beta_0-\beta_1}{\beta_1-\beta_2}\right) \tag{16}$$

with Eq. (15) providing the sought expression for relating trial-space experiments to the full-scale structure, and where R_1^{ψ} takes on the form of a parameter due to indeterminacy of α_1^{ψ}.

Application of Eq. (15) to Eqs. (13) provides the following field identities:

$$\boldsymbol{v}_{ps}=\boldsymbol{V}_{ps}\left(\beta_1\right)+R_1^{\rho}\left(\boldsymbol{V}_{ps}\left(\beta_1\right)-\boldsymbol{V}_{ps}\left(\beta_2\right)\right) \tag{17a}$$

$$\boldsymbol{v}_{ps}=\boldsymbol{V}_{ps}\left(\beta_1\right)+R_1^{v}\left(\boldsymbol{V}_{ps}\left(\beta_1\right)-\boldsymbol{V}_{ps}\left(\beta_2\right)\right) \tag{17b}$$

$$\boldsymbol{\sigma}_{ps}=\boldsymbol{\Sigma}_{ps}\left(\beta_1\right)+R_1^{v}\left(\boldsymbol{\Sigma}_{ps}\left(\beta_1\right)-\boldsymbol{\Sigma}_{ps}\left(\beta_2\right)\right) \tag{17c}$$

$$\boldsymbol{b}_{ps}=\boldsymbol{B}_{ps}\left(\beta_1\right)+R_1^{v}\left(\boldsymbol{B}_{ps}\left(\beta_1\right)-\boldsymbol{B}_{ps}\left(\beta_2\right)\right) \tag{17d}$$

$$\boldsymbol{u}_{ps}=\boldsymbol{U}_{ps}\left(\beta_1\right)+R_1^{u}\left(\boldsymbol{U}_{ps}\left(\beta_1\right)-\boldsymbol{U}_{ps}\left(\beta_2\right)\right) \tag{17e}$$

$$\boldsymbol{v}_{ps}=\boldsymbol{V}_{ps}\left(\beta_1\right)+R_1^{u}\left(\boldsymbol{V}_{ps}\left(\beta_1\right)-\boldsymbol{V}_{ps}\left(\beta_2\right)\right) \tag{17f}$$

where to arrive at a consistent velocity expression it is required that $R_1=R_1^{\rho}=R_1^{v}=R_1^{u}$, which is achieved on setting $\alpha_1^{\rho}=\alpha_1^{v}=\alpha_1^{u}$, and where as mentioned above $\boldsymbol{V}_{ps}=\beta^{-1}g\boldsymbol{v}_{ts}$, $\boldsymbol{U}_{ps}=\beta^{-1}\boldsymbol{u}_{ts}$, $\boldsymbol{\Sigma}_{ps}=\alpha_0^{v}g\beta^2\boldsymbol{\sigma}_{ts}$ and $\boldsymbol{B}_{ts}=g^2\beta^{-1}\boldsymbol{b}_{ts}$.

The condition $R_1^{\rho} = R_1^{v} = R_1^{u}$ provides a physically-intuitive solution for Eq. (15) in that it indicates that the differences between the experiments as described by transport Eqs. (7) are proportional. The theory provides the fields in Eqs. (17) whose differences are also proportional. The final solution to the scaling problem is rather elegant in its simplicity and all that remains is the details of its application.

3.2. Consistency and applicability

One of the features of the transport approach is that it does not depend on nor utilise constitutive laws as it provides all the physical fields needed for the physical space. In small deflection theory for example the identities $dx^i_{ps} = \beta_1^{-1} dx^i_{ps}\left(\beta_1\right) = \beta_2^{-1} dx^i_{ps}\left(\beta_2\right)$ and Eq. (17e) provide the strain relationship

$$\boldsymbol{\varepsilon}_{ps} = \boldsymbol{\varepsilon}_{ts}\left(\beta_1\right) + R_1\left(\boldsymbol{\varepsilon}_{ts}\left(\beta_1\right) - \boldsymbol{\varepsilon}_{ts}\left(\beta_2\right)\right) \tag{18}$$

which confirms that with first-order finite similitude, strains are not required to be identical, which is a feature of dimensional analysis.

Note also that Eq. (17f) and (17e) are consistent since division of the latter by $Dt_{ps} = g_1^{-1} Dt_{ps1} = g_2^{-1} Dt_{ps2}$, with $g_i = g\left(\beta_i\right)$ and $t_{ts\,i} = t_{ts}\left(\beta_i\right)$ gives

$$\frac{D\boldsymbol{u}_{ps}}{Dt_{ps}} = g_1 \frac{D\boldsymbol{U}_{ps1}}{Dt_{ts1}} + R_1\left(g_1 \frac{D\boldsymbol{U}_{ps1}}{Dt_{ts1}} - g_1 \frac{D\boldsymbol{U}_{ps}}{Dt_{ts1}}\right) = \boldsymbol{V}_{ps}\left(\beta_1\right) + R_1\left(\boldsymbol{V}_{ps}\left(\beta_1\right) - \boldsymbol{V}_{ps}\left(\beta_2\right)\right) \tag{19}$$

as expected, where $\frac{D}{Dt_{ts}}$ and $\frac{D}{Dt_{ps}}$ means material derivatives.

Before discussing the practical application of the theory, it is useful at this point to tabulate for both zeroth and first-order theories the important relationships, which are brought together in Table 1. It is worth noting that despite the relative complexity involved in the derivation of the field relationships in Table 1, their application transpires to be relatively straightforward. A detailed set of instructions for the application of both zeroth and first order finite similitude is presented in Appendix A. A particularly nice feature of the proposed similitude approach is that it can be applied directly to theoretical, numerical, and experimental results. The examples presented in the next three sections are purposely chosen to illustrate this

point but also to demonstrate the relative ease of applicability for problems of increasing complexity.

Table 3:1: Important zeroth and first-order finite similitude identities.

Finite similitude relationships		
Density	0^{th}-order	$\rho_{ps} = \alpha_{01}^{\rho}\rho_{ts1}\beta_1^3$
	1^{st}-order*	$\rho_{ps} = \alpha_{01}^{\rho}\rho_{ts1}\beta_1^3 + R_1\left(\alpha_{01}^{\rho}\rho_{ts1}\beta_1^3 - \alpha_{02}^{\rho}\rho_{ts2}\beta_2^3\right)$
Displacement	0^{th}-order	$\boldsymbol{u}_{ps} = \beta_1^{-1}\boldsymbol{u}_{ts1}$
	1^{st}-order	$\boldsymbol{u}_{ps} = \beta_1^{-1}\boldsymbol{u}_{ts1} + R_1\left(\beta_1^{-1}\boldsymbol{u}_{ts1} - \beta_2^{-1}\boldsymbol{u}_{ts2}\right)$
Strain	0^{th}-order	$\boldsymbol{\varepsilon}_{ps} = \boldsymbol{\varepsilon}_{ts1}$
	1^{st}-order	$\boldsymbol{\varepsilon}_{ps} = \boldsymbol{\varepsilon}_{ts1} + R_1\left(\boldsymbol{\varepsilon}_{ts1} - \boldsymbol{\varepsilon}_{ts2}\right)$
Stress	0^{th}-order	$\boldsymbol{\sigma}_{ps} = \alpha_{01}^{\rho}g_1^2\beta_1\boldsymbol{\sigma}_{ts1}$
	1^{st}-order	$\boldsymbol{\sigma}_{ps} = \alpha_{01}^{\rho}g_1^2\beta_1\boldsymbol{\sigma}_{ts1} + R_1\left(\alpha_{01}^{\rho}g_1^2\beta_1\boldsymbol{\sigma}_{ts1} - \alpha_{02}^{\rho}g_2^2\beta_2\boldsymbol{\sigma}_{ts2}\right)$

* Not derived in this work

4. The scaling of a beam: an analytical study

This section serves to provide an initial test on a problem of some simplicity to illustrate the practical implementation of the zeroth and first-order finite similitude theory by the scaling of a cantilever beam. The cantilever beam is depicted in Fig.5 and the goal here is to ascertain whether it is possible to capture the dynamic response of the beam using either one (zeroth-order) or two (first-order) trial-space tests. The behaviour of the cantilever beam in the physical space is assumed to be known in this analysis although in practice this might not be the case. It is assumed

here that the free vibration response of the cantilever is described by the well-known Euler-Bernoulli solution [29]:

$$w(x,t)=\sum_{n=1}^{\infty} a_n \cos(\omega_n t)\phi(x;\gamma_n,L) \tag{20a}$$

where the eigenfunctions $\phi(x;\gamma_n,L)$ are

$$\phi(x;\gamma_n,L)=\left[\cosh(\gamma_n x)-\cos(\gamma_n x)\right]-\left(\frac{\sinh(\gamma_n L)-\sin(\gamma_n L)}{\cosh(\gamma_n L)+\cos(\gamma_n L)}\right)\left[\sinh(\gamma_n x)-\sin(\gamma_n x)\right] \tag{20b}$$

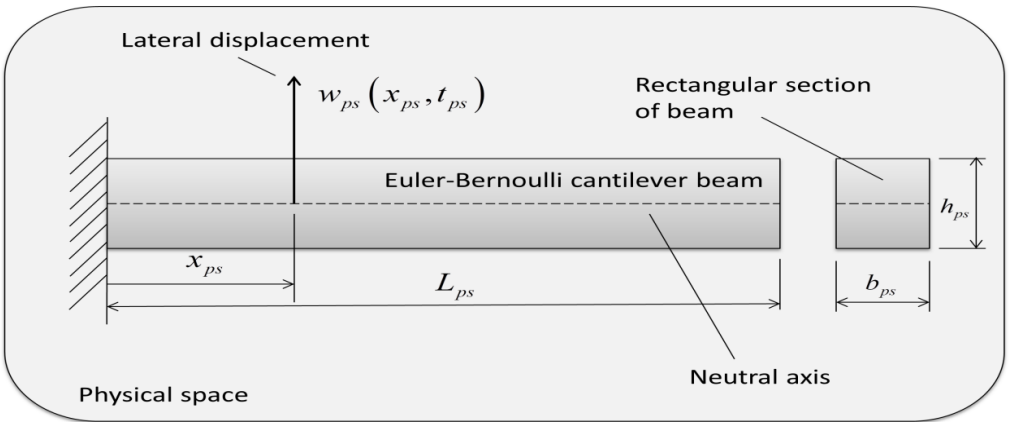

Figure 5: Uniform cantilever beam in the physical space

and where $\gamma_n L$ represents the frequency coefficient [29], $\omega_n=(\gamma_n L)^2\sqrt{EI/(\rho AL^4)}$ are natural frequencies, with Young's modulus E, second moment of area $I=\frac{1}{12}bh^3$, cross sectional area $A=bh$, mass density ρ and a_n are set to capture the initial configuration.

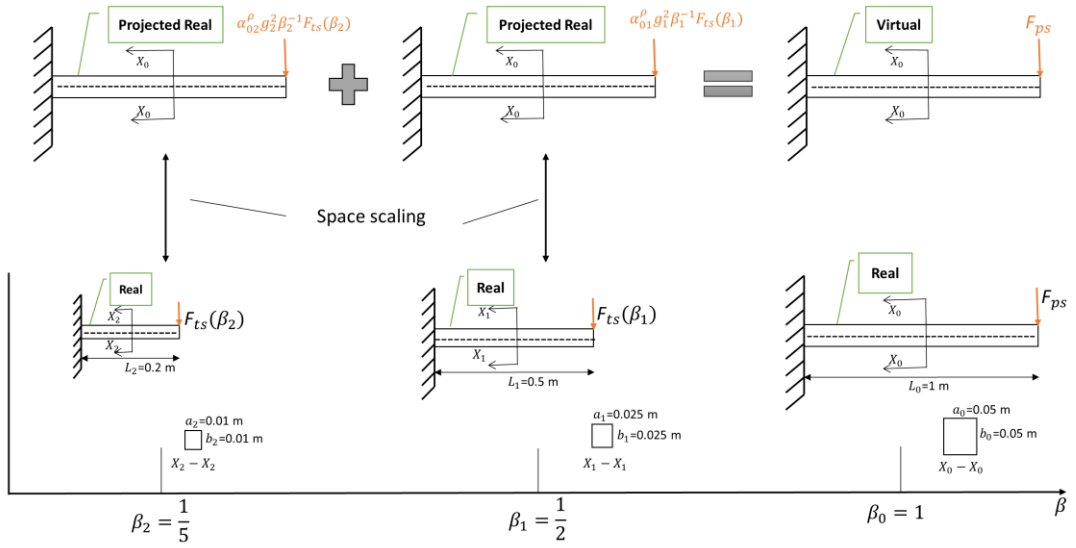

Figure 3.6: Projected trial and physical space models for the cantilever beam.

An overall view of the scaling process with one or two trial experiments involved is presented in Fig. 6. Shown in the figure is how space scaling is used to project the "real" trial-space experiments into the physical space and their subsequent combination using Eq. (15). Shown also is the effect of space scaling on the load at the free end of the beam with the aim that on combination of the projected beams the force F_{ps} is returned. In the tests that follow three designs are considered at selected scales $\beta_2 = \frac{1}{5}$ and $\beta_1 = \frac{1}{2}$, and are labelled Designs I, II and III. Design I is limited zeroth-order finite similitude with the same material used for both physical and trial space. Design II is also for identical materials but applies first-order scaling with Design III looking at alternative materials typical to physical modelling.

4.1. Design I: Zeroth-order with identical beam materials

Applying the zeroth-order procedure presented in Appendix A provides:

(i) The physical space cantilever is made of steel with properties listed at Table 2 and has dimensions $a_{ps} = b_{ps} = 0.05\ m$ and $L_{ps} = 1\ m$ (see Fig. 6.). The initial condition assumed to apply is obtained on setting $a_n = \text{constant}$ for all $n \geq 1$ with the constant specified so that $w_{ps}\left(L_{ps}, 0\right) = 0.1\text{m}$ and consequently the transient response is described by

$$w_{ps}\left(x_{ps},t_{ps}\right)=0.1\frac{\sum_{n=1}^{\infty}\cos\left(\left(\omega_{ps}\right)_n t_{ps}\right)\phi\left(x_{ps};\left(\gamma_{ps}\right)_n,L_{ps}\right)}{\sum_{n=1}^{\infty}\phi\left(L_{ps};\left(\gamma_{ps}\right)_n,L_{ps}\right)} \tag{21}$$

where the function ϕ is given in Eq. (19).

(ii) The dimensional scaling factor $\beta_1=\frac{1}{2}$ and consequently the steel (properties in Table 2) trial-space cantilever beam has dimensions $a_{ts1}=b_{ts1}=0.025\,\text{m}$ and $L_{ts1}=0.50\,\text{m}$ as shown in Fig. 6.

(iii) The density and elastic modulus are chosen to be fixed.

(iv) The density and time scaling factors are determined and equate to $\alpha_{01}^{\rho}=8.0$ and $g_1=0.5$ so that the identities $\rho_{ps}=\alpha_{01}^{\rho}\rho_{ts1}\beta_1^3$ and $E_{ps}=\alpha_{01}^{\rho}g_1^{\,2}\beta_1 E_{ts1}$ are satisfied. (see Table 1),

(v) The initial deflection of the beam at the free end is set to $w_{ts1}\left(L_{ts1},0\right)=0.05\,\text{m}$ in accordance with the displacement identity in Table 1.

(vi) By testing the trial model, its deflection-time behaviour satisfies

$$w_{ts1}\left(x_{ts1},t_{ts1}\right)=0.05\frac{\sum_{n=1}^{\infty}\cos\left(\left(\omega_{ts1}\right)_n t_{ts1}\right)\phi\left(x_{ts1};\left(\gamma_{ts1}\right)_n,L_{ts1}\right)}{\sum_{n=1}^{\infty}\phi\left(L_{ts1};\left(\gamma_{ts1}\right)_n,L_{ts1}\right)} \tag{22}$$

(vii) The final procedure is the lifting of the trial model response to predict the physical model (e.g. $w_{ps}=\beta_1^{-1}w_{ts1}$).

The results of this study are presented in Fig. 7 with the deflection at the free end captured as function of time; there is perfect match between the projected trial and physical results.

4.2. Design II: First-order with identical beam materials

Applying the zeroth-order procedure presented in Appendix B provides:

(i) The steel cantilever beam (properties in Table 2) in the physical space is again considered as in Section 4.1 with initial deflection satisfying Eq. (22) at time $t_{ps}=0$.

(ii) The dimensional scaling factors for the two trial-spaces are set to be $\beta_1=\frac{1}{2}$ and $\beta_2=\frac{1}{5}$ making the dimensions of the two steel cantilevers (properties listed in

Table 2) to be $a_{ts1} = b_{ts1} = 0.025\ m$, $L_{ts1} = 0.50\ m$, $a_{ts2} = b_{ts2} = 0.01\ m$ and $L_{ts2} = 0.20\ m$, as illustrated in Fig. 6.

(iii) The density scaling factors α_{01}^{ρ} and α_{02}^{ρ} are set on the basis of zeroth-order assumptions and equate to $\alpha_{01}^{\rho} = 8$ and $\alpha_{02}^{\rho} = 125$ so that the relationships $\rho_{ps} = \alpha_{01}^{\rho}\beta_1^3\rho_{ts1}$ and $\rho_{ps} = \alpha_{02}^{\rho}\beta_2^3\rho_{ts2}$ are satisfied.

(iv) The elastic modulus and the initial (or loading) conditions, which are displacement and the force required to cause this displacement are selected to be fixed.

(v) The temporal and first-order scaling factor g_1, g_2 and R_1 are found to equate to $g_1 = 0.5$, $g_2 = 0.2$ $R_1 = -0.12$. These are arrived by solving the following three algebraic equations:

$$E_{ps} = \alpha_{01}^{\rho} g_1^{\,2}\beta_1 E_{ts1} + R_1\left(\alpha_{01}^{\rho} g_1^{\,2}\beta_1 E_{ts1} - \alpha_{02}^{\rho} g_2^{\,2}\beta_2 E_{ts2}\right)$$

(23a)

$$F_{ps} = \alpha_{01}^{\rho} g_1^{\,2}\beta_1^{-1} F_{ts1} + R_1\left(\alpha_{01}^{\rho} g_1^{\,2}\beta_1^{-1} F_{ts1} - \alpha_{02}^{\rho} g_2^{\,2}\beta_2^{-2} F_{ts2}\right) \qquad (23b)$$

$$w_{ps}^{end} = \beta_1^{-1} w_{ts1}^{end} + R_1\left(\beta_1^{-1} w_{ts1}^{end} - \beta_2^{-1} w_{ts2}^{end}\right) \qquad (23c)$$

where the end forces are set to $F_{ts2} = 0.10F_{ps}$, $F_{ts1} = 0.20F_{ps}$ (see Fig. 6) and the initial end displacements w_{ts2}^{end} and w_{ts1}^{end} are determined on the basis of these forces at static equilibrium.

(vi) The initial conditions for the first and second trial models are set on the basis of end deflections w_{ts2}^{end} and w_{ts1}^{end}, i.e. $w_{ts2}\left(L_{ts2}, 0\right) = w_{ts2}^{end}$ and $w_{ts1}\left(L_{ts1}, 0\right) = w_{ts1}^{end}$.

(vii) Transient deflection of the beams in the trial space satisfy similar looking equations to Eq. (22) and explicitly are

$$w_{tsi}\left(x_{tsi}, t_{tsi}\right) = w_{tsi}^{end}\,\frac{\sum_{n=1}^{\infty}\cos\left(\left(\omega_{tsi}\right)_n t_{tsi}\right)\phi\left(x_{tsi};\left(\gamma_{tsi}\right)_n, L_{tsi}\right)}{\sum_{n=1}^{\infty}\phi\left(L_{tsi};\left(\gamma_{tsi}\right)_n, L_{tsi}\right)} \qquad (24)$$

where $i = 1$ or 2.

(viii) The final step is the combining of the trial-model prediction to produce a virtual model for comparison with the response of the beam in the physical space (e.g. $w_{ps} = \beta_1^{-1} w_{ts1} + R_1 \left(\beta_1^{-1} w_{ts1} - \beta_2^{-1} w_{ts2} \right)$) in accordance with Table 1.

The results of this study are presented in Fig. 7 with the deflection at the free end captured as function of time; there is perfect match between the virtual and physical results.

4.3. Design III: First-order with different beam materials

The results of Design-III are depicted in Fig. 7 for the situation of completely different materials used for physical (steel) and trial-models 1 (aluminium) and 2 (copper); see Table 2 for properties. In Design-III, the applied forces at the free end in the physical and trial spaces are determined on the basis of the maximum yield stress in the outer fibres of each beam, i.e. on the basis of $F^{end} = 2YI/Lh$, where Y is yield stress. These forces are used for initiation purposes and the determination of initial end deflections at static equilibrium. Following an identical procedure as discussed for Design II the following results are obtained: $g_1 = 0.51$, $g_2 = 0.27$ and $R_1 = -0.78$. The results of the Design III study are presented in Fig. 7 with the deflection at the free end captured as function of time; there is again a perfect match between projected trial and physical results.

Table 3:2: Material properties of steel, aluminum and copper [29],[30],[31].

Material	Density: ρ (kg/m^3)	Young Modulus: E (GPa)
Steel (S355)	7850	210
Aluminium	2700	70
Copper	8920	130

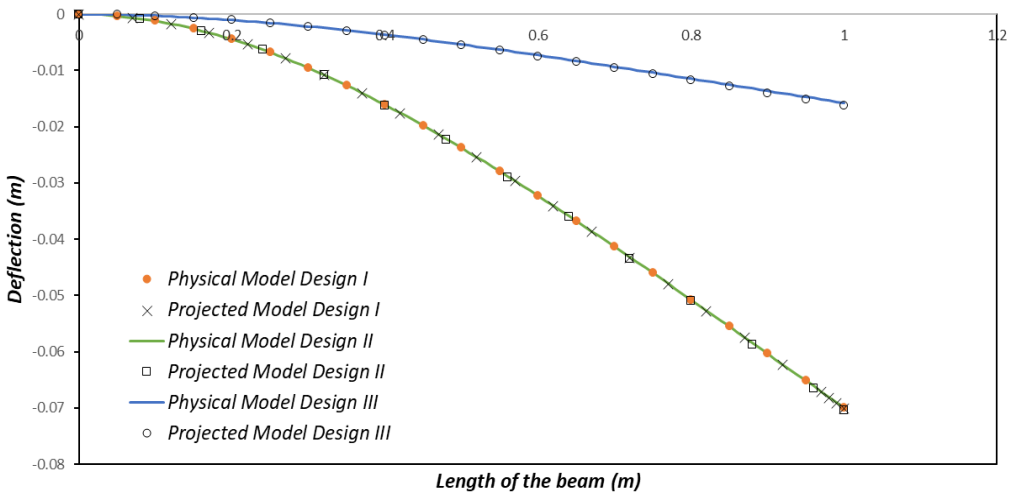

(a)

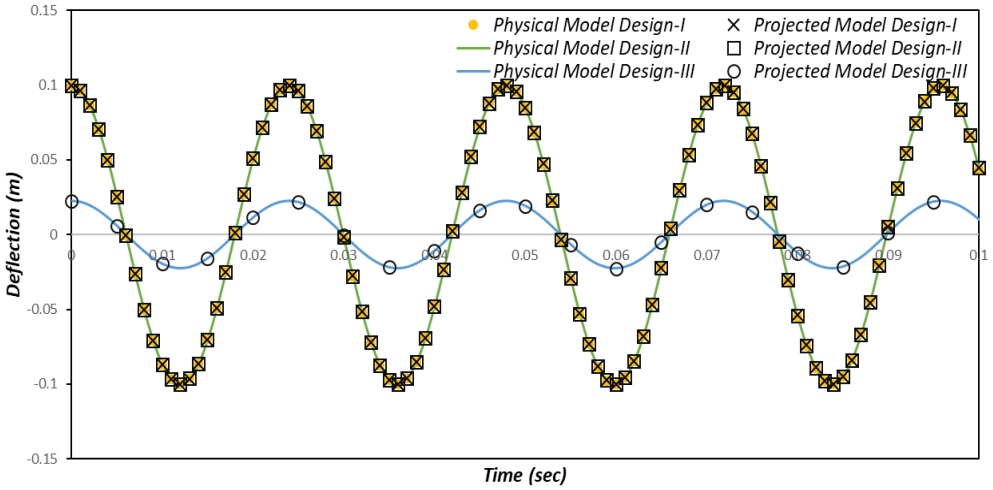

(b)

Figure 7: Predicting the (a) spatial ($t_{ps} = 0.015$ s) and (b) temporal response of the physical model using zeroth and first-order finite similitude theories in three designs.

5. Seismic loading of a column: numerical study

This section investigates the application of zeroth and first-order finite similitude to the earthquake loading of a relatively simple structure. A column is selected as the case study in order to focus the analysis on how the finite-similitude theory can be applied in seismic situations. Three possible column designs are considered for first-order and two for zeroth-order; each design is discussed in the subsections below. In order to give the study a degree of realism the Kocaeli Earthquake (1999)

is applied in this study as the time-acceleration ground motion, which is depicted in Fig.8 [30].

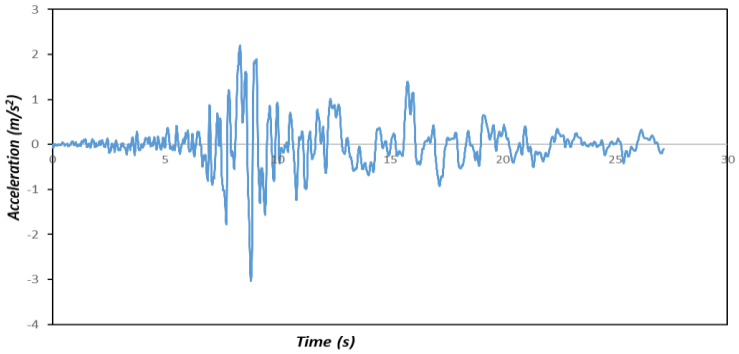

Figure 8: Acceleration – Time graph for Kocaeli earthquake.

5.1. First-order Finite Similitude: steel column

The application of the first-order finite similitude theory to a steel column housed in the physical space, where three combinations of different materials for trial models are examined. The purpose is to reveal how well the selected trial experiments capture the behaviour of the steel column. The dimensions of the steel column are provided in Fig. 9 and consist of a square section $a_{ps} = b_{ps} = 0.1\text{m}$ and height $l_{ps} = 4$ m. Geometric dimensions of the trial models for both zeroth and first-order finite similitude depend on β_1 and β_2, which are set to $\beta_1 = \frac{1}{4}$ and $\beta_2 = \frac{1}{10}$. It is possible to let β_1 and β_2 remain unknown and determine them as part of the analysis but this aspect is not featured here as reasonable order-of-magnitude results are found possible on the basis of the selections made. As alluded in Appendix B, the determination of scaling parameters is on the basis of what physical quantities are considered important to be targeted (e.g. stress, acceleration etc.) In seismic case studies the applied acceleration is an important physical quantity and matching applied acceleration (i.e. $\boldsymbol{A}_{ps} = \boldsymbol{A}_{ts1} = \boldsymbol{A}_{ts2}$) is often considered [31] as it can provide realistic and practical designs. Laboratories and devices for the application of seismic loads are of course limited in both size and load capacity and consequently constrain what is possible.

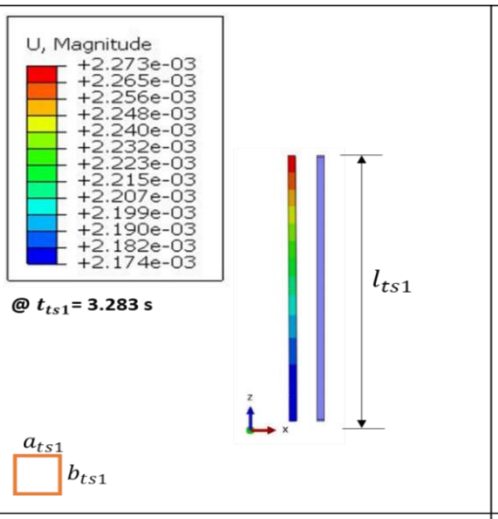

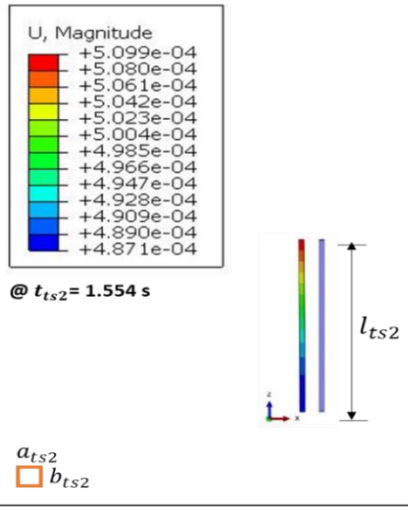

Trial-1 Model ($\beta_1 = \frac{1}{4}$)	**Trial-2 Model ($\beta_1 = \frac{1}{10}$)**
• Dimensions: l_{ts1}=1 m, a_{ts1}=0.25 m, b_{ts1}=0.25m • BCs: bottom fixed in x,y, and z directions. • Loading: earthquake acceleration-time. • Element: 3-D, 8-node element (C3D8R). • Number of elements: 1000.	• Dimensions: l_{ts2}=0.4 m, a_{ts2}=0.01 m, b_{ts2}=0.01m • BCs: bottom fixed in x,y, and z directions. • Loading: earthquake acceleration-time. • Element: 3-D, 8-node element (C3D8R). • Number of elements: 1000.

(a)

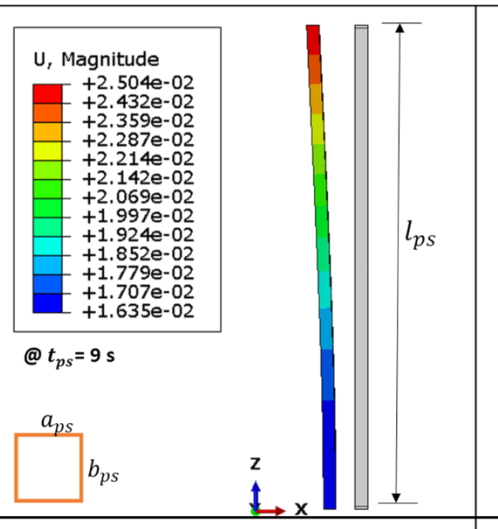

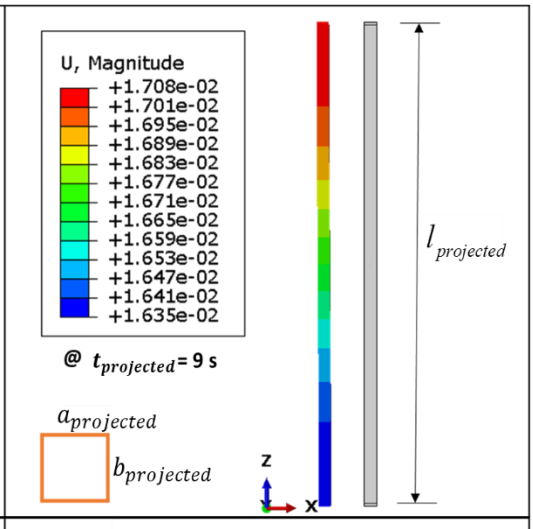

Physical (Full-Scale) Model ($\beta_0 = 1$)	**Projected Virtual Model**

• Dimensions: l_{ps}= $l_{projected}$=4 m, a_{ps}= $a_{projected}$=0.1 m, b_{ps}= $b_{projected}$=0.1 m
• BCs: bottom fixed in x,y, and z directions.
• Loading: earthquake acceleration-time.
• Element: 3-D, 8-node element (C3D8R).
• Number of elements: 1000.

(b)

Figure 9: Deformed shapes in (a) trial space and (b) physical at synchronised times for Design II.

As in Section 4, the problem reduces to finding the temporal scaling parameters g_1 and g_2 along with the first-order parameter R_1. Three equations are selected for this purpose which are:

$$\boldsymbol{A}_{ps} = g_1^2 \beta_1^{-1} \boldsymbol{A}_{ts1} + R_1 (g_1^2 \beta_1^{-1} \boldsymbol{A}_{ts1} - g_2^2 \beta_2^{-1} \boldsymbol{A}_{ts2}) \tag{25a}$$

$$\boldsymbol{\sigma}_{ps} = \alpha_{01}^{\rho} g_1^2 \beta_1 \boldsymbol{\sigma}_{ts1} + R_1 (\alpha_{01}^{\rho} g_1^2 \beta_1 \boldsymbol{\sigma}_{ts1} - \alpha_{02}^{\rho} g_2^2 \beta_2 \boldsymbol{\sigma}_{ts2}) \tag{25b}$$

$$\boldsymbol{\varepsilon}_{ps} = \boldsymbol{\varepsilon}_{ts1} + R_1 (\boldsymbol{\varepsilon}_{ts1} - \boldsymbol{\varepsilon}_{ts2}) \tag{25c}$$

which are first-order approximations for acceleration, stress and strain, and where the expression for acceleration is readily derived by temporal differentiation of velocity in Eq. (17) and noting that $dt_{ps} = g_1^{-1} dt_{ts1} = g_2^{-1} dt_{ts2}$.

In all the tests considered the zeroth-order density is applied, i.e. $\rho_{ps} = \alpha_{01}^{\rho} \rho_{ts1} \beta_1^3 = \alpha_{02}^{\rho} \rho_{ts2} \beta_2^3$, where α_{01}^{ρ} and α_{02}^{ρ} are set to match the density of the selected trial-space materials. The behaviour of both trial and physical-space columns is achieved numerically by means of the commercial finite-element software ABAQUS [32]; meshes and element type are depicted in Fig. 9. In practice of course, physical experiments would be undertaken but trialling the similitude theory is the focus here and numerical results are sufficient for this purpose.

5.2. The proportional fields assumption

In order to run scaled experiments in the trial space it is first necessary to specify g_1 and g_2, yet according to Eqs. (25), their solution is dependent on fields that are only available once the experiments have been run. To avoid the need for a time-consuming and somewhat impractical iterative approach to resolve this issue, a proportional-fields assumption is made. Recall that both dimensional analysis and zeroth-order finite similitude involve proportional fields, assumed ab initio for dimensional analysis and obtained as an output from finite similitude. The first-order theory on the other hand involves proportional differences as apparent in Table 1 for particular fields. With the knowledge that zeroth-order solutions are contained

in first order (see Appendix B), it is a reasonable assumption therefore that the fields in Eqs. (25) are all proportional in the sense:

$$\boldsymbol{A}_{ts1} = \hat{a}_1 \boldsymbol{A}_{ps} \tag{26a}$$

$$\boldsymbol{A}_{ts2} = \hat{a}_2 \boldsymbol{A}_{ps} \tag{26b}$$

$$\boldsymbol{\sigma}_{ts1} = \hat{b}_1 \boldsymbol{\sigma}_{ps} \tag{26c}$$

$$\boldsymbol{\sigma}_{ts2} = \hat{b}_2 \boldsymbol{\sigma}_{ps} \tag{26d}$$

$$\boldsymbol{\varepsilon}_{ts1} = \hat{c}_1 \boldsymbol{\varepsilon}_{ps} \tag{26e}$$

$$\boldsymbol{\varepsilon}_{ts2} = \hat{c}_2 \boldsymbol{\varepsilon}_{ps}\,, \tag{26f}$$

where it is understood that these relationships do not constrain the fields in Eqs. (25) as their purpose is only to aid the determination of g_1, g_2 and R_1, and where the hat "^" terms are non-zero dimensionless parameters.

Substitution of Eqs. (26) into Eqs. (25) provides

$$1 = g_1^2 \beta_1^{-1} \hat{a}_1 + R_1 (g_1^2 \beta_1^{-1} \hat{a}_1 - g_2^2 \beta_2^{-1} \hat{a}_2) \tag{27a}$$

$$1 = \alpha_{01}^{\rho} g_1^2 \beta_1 \hat{b}_1 + R_1 (\alpha_{01}^{\rho} g_1^2 \beta_1 \hat{b}_1 - \alpha_{02}^{\rho} g_2^2 \beta_2 \hat{b}_1) \tag{27b}$$

$$1 = \hat{c}_1 + R_1 (\hat{c}_1 - \hat{c}_2) \tag{27c}$$

which can in principle be solved for g_1, g_2 and R_1 on specifying $\hat{a}_i$, $\hat{b}_i$ and $\hat{c}_i$, $i = 1, 2$.

To set the parameters $\hat{a}_i$, $\hat{b}_i$ and $\hat{c}_i$, considered here is the situation of a uniaxial rod in each space subjected to the same uniform acceleration and stretched to attain yield stress (i.e. Y_{ps}, Y_{ts1} and Y_{ts2}) and yield strain (i.e. $\varepsilon_{ps}^{Y} = \frac{Y_{ps}}{E_{ps}}$, $\varepsilon_{ts1}^{Y} = \frac{Y_{ts1}}{E_{ts1}}$ and $\varepsilon_{ts2}^{Y} = \frac{Y_{ts2}}{E_{ts2}}$). This situation is possibly one of the simplest but substitution into Eqs. (26) for this case gives $\hat{a}_1 = \hat{a}_2 = 1$, $\hat{b}_1 = \frac{Y_{ts1}}{Y_{ps}}$, $\hat{b}_2 = \frac{Y_{ts2}}{Y_{ps}}$, $\hat{c}_1 = \frac{\varepsilon_{ts1}^{Y}}{\varepsilon_{ps}^{Y}}$ and $\hat{c}_2 = \frac{\varepsilon_{ts2}^{Y}}{\varepsilon_{ps}^{Y}}$.

5.3. Application of the theory

Three designs are considered, where are labelled Design I, Design II and Design III, the details of which are provided in Table 3. Design I is the case where the same

grade of steel (i.e. S355 [26]) is used in all spaces for the columns. Design II applies different grades of steel (see [28] and [29]) in each space as indicated in Table 3. Design III on the other hand again uses different materials with different grades of steel in the physical and trial-space one but aluminium for trial-space two.

For all three designs the applied acceleration A_1 in x-direction is the same and the yield stresses (Y_{ps}, Y_{ts1} and Y_{ts2}) and yield strains (ε_{ps}^{Y}, ε_{ts1}^{Y} and ε_{ts2}^{Y}) for the three designs can be found in Table 3. A feature of Design I is that $\hat{c}_1 = \hat{c}_2$, which removes Eq. (27c). The two remaining equations Eq. (27a) and Eq. (27a) have too many unknowns and to resolve the situation, so the zeroth-order condition $1 = g_1^2 \beta_1^{-1}$ (i.e. first two terms in Eq. (27a)) is assumed to apply, which gives $g_1 = \sqrt{\beta_1} = \frac{1}{2}$. The remaining values (i.e. g_2 and R_1), calculated using Eq. (27a) and (27b), can be found in Table 3. Qualitative results for the distribution of the displacement magnitude are provided in Fig. 9. along with a detailed model description. Design II involves three grades of steel [28] provides values $g_1 = 0.365$, $g_2 = 0.173$ and $R_1 = 2$ on solution of Eqs. (27). Design III on the other hand did not provide a solution to Eqs. (27), so was resolved in the same manner as Design I, i.e. by setting $g_1 = \sqrt{\beta_1} = \frac{1}{2}$ and solving for g_2 and R_1, which provided $g_2 = 0.316$, and $R_1 = 0.5$ as recorded in Table 3. With the determination of g_1, g_2 and scaling parameters, the trial models result results were obtained, projected to the full scale and combined by means of the first-order theory. The results for the top-story drift of the column for all three designs are presented in Fig. 10. Show in the figure are the virtual results obtained on application of the first-order theory along with those determined by virtue of direct simulation of the full-scale model in the physical space.

Table 3:3: Material properties of three models and calculated time scaling and values.

Designs	**Models**	**Material**	**Density (kg/m^3)**	**Young's Modulus (10^{11} Pa)**	**Yield Stress (10^8 Pa)**	**Yield Strain (10^{-3})**	g_1	g_2	R_1
Design I	Full-scale Model	S355	7850	2.1	3.55	1.69	0.5	0.316	0.5
	Trial-1 Model	S355	7850	2.1	3.55	1.69			
	Trial-2 Model	S355	7850	2.1	3.55	1.69			

Design II	Full-scale Model	S355	7850	2.1	3.55	1.69	0.365	0.173	2
	Trial-1 Model	S275	7850	2.1	2.75	1.31			
	Trial-2 Model	S235	7850	2.1	2.35	1.12			
Design III	Full-scale Model	S355	7850	2.1	3.55	1.69	0.5	0.316	0.0882
	Trial-1 Model	S275	7850	2.1	2.75	1.31			
	Trial-2 Model	Al	2770	0.7	3.37	4.814			

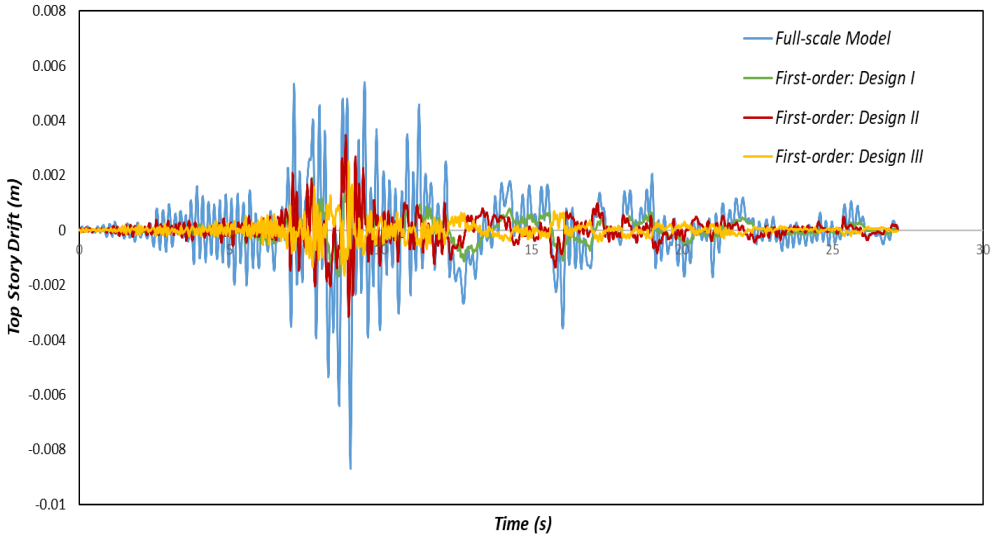

Figure 10: First-order predicts and direct-full scale simulation.

It is apparent on examination of Fig. 10 that the different designs provide different outputs and there are also in place significant differences between the virtual-model predictions and the direct full-scale simulation. It is possibly not too surprising that the scaled models were unable to fully capture the precise full-scale behaviour of an earthquake event. However, considered in the next section, are single-trial space models to better highlight the significant improvement achieved by the new theory.

5.4. Zeroth-order finite similitude design

Each of the trial models at scales $\beta_1 = \frac{1}{4}$ and $\beta_2 = \frac{1}{10}$ (introduced in Section 5.3) are reconsidered here using the zeroth-order theory, hence only one trial model per analysis. The zeroth order relationship $\boldsymbol{A}_{ps} = g^2 \beta^{-1} \boldsymbol{A}_{ts}$ with proportionality gives $1 = g^2 \beta^{-1} \hat{a}$ and on setting $\hat{a} = 1$ provides $g = \sqrt{\beta}$. Other zeroth-order scaling identities are provided in Table. 1. For the trial models that same materials as in Section 5.3 are used and details are provided in Table 5. Note that two test cases are

considered (test cases I and II) with each consisting of two trial models (trial models I and II) corresponding to the two scales (i.e. $\beta_1 = \frac{1}{4}$ and $\beta_2 = \frac{1}{10}$). The projected models correspond to the projection of the trial models into the physical space and the salient projected material properties are tabulated in Table 4. Shown in Fig. 11 is the temporal response of top displacement, which is recognised to be important for the comparison of building models under seismic loading.

Table 3:4: Zeroth-order Finite Similitude scaling parameters and material properties.

Test Cases	**Models**		**Density (kg/m^3)**	**Young's Modulus (10^{11} Pa)**	**Yield Stress (10^8 Pa)**	β	α_{01}^{ρ}	$g = \sqrt{\beta}$
Test Case I	Trial Model 1	S355	7850	2.1	3.55	1/4	64	2
	Trial Model 2	S355	7850	2.1	3.55	1/10	1000	$\sqrt{10}$
	Projected Model-1		7850	8.4	14.2			
	Projected Model-2		7850	210	35.5			
Test Case II	Trial Model 1	S275	7850	2.1	2.75	1/4	64	2
	Trial Model 2	S235	7850	2.1	2.35	1/10	1000	$\sqrt{10}$
	Projected Model 1		7850	8.4	11			
	Projected Model 2		7850	210	23.5			

The graphs in Fig. 11(b) illustrate the marked improvement achievable on application of the first-order finite similitude theory. The results for first-order Design I are much improved over those corresponding to Case I for both trial modes. Likewise first-order Design II outperforms all case and although fails to capture all aspects of the full-scale simulation it is vastly superior to single-space trial models. The advantage offered by first-order finite similitude theory in seismic studies is that it provides an ability to fix not only acceleration but also other material properties. Zeroth-order is limited in only enabling the fixing of acceleration and as revealed in Table 4, with other material properties not matched.

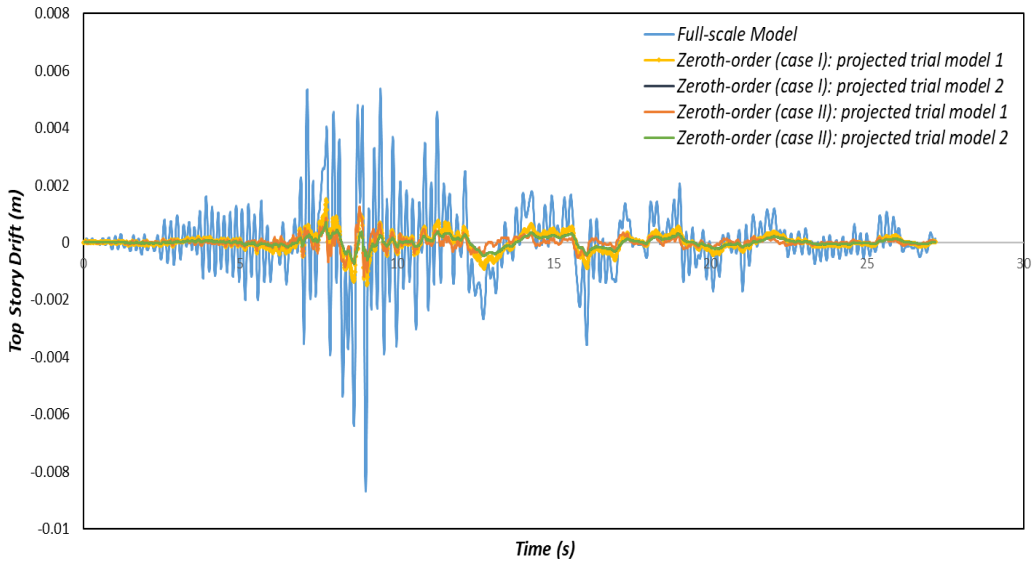

(a)

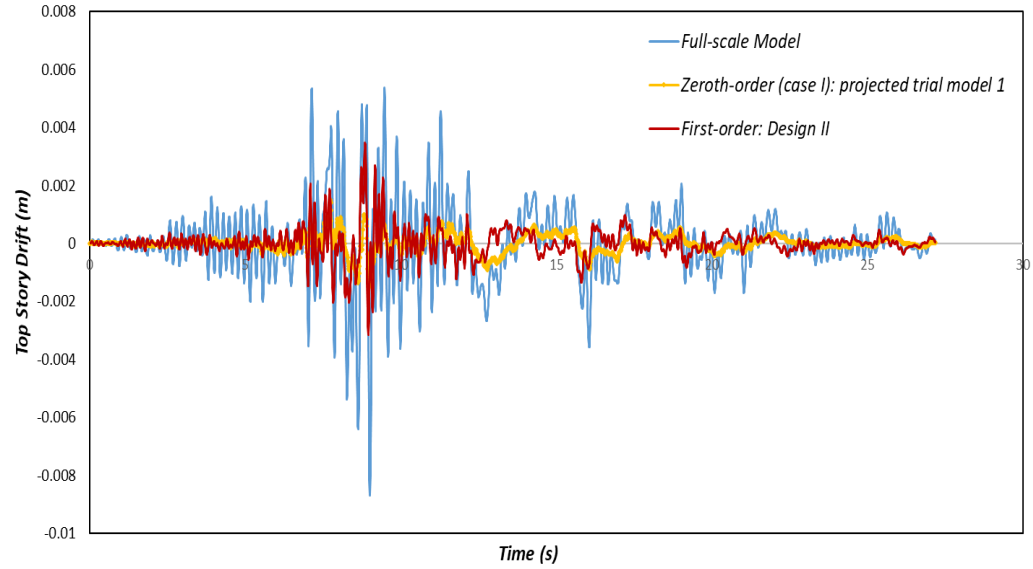

(b)

Figure 11: Performance of zeroth and first-order finite similitude designs.

To demonstrate the practical applicability of the new theory a more realistic structure is examined in the next section.

6. Multi-storey frame exposed to cyclic loading: a numerical study

Different forms of seismic or environmental loading can impact on the performance of a structure. Because of the inherent uncertainty associated with these types of load it is common practice in models to load systems quasi-statically with

consistently increasing loads. Although recognising that this approach does have its limitations [34] engineering structures must have the capacity to resist thousands of loading cycles to withstand disasters such as earthquakes [33]. Cyclic thermal and mechanical loads can push systems past the elastic region wherein plastic straining occurs [34] and it is important therefore that systems remain safe and serviceable under such conditions.

It is of interest therefore to examine the behaviour of structures under cyclic loading and for this reason, a steel frame consisting of two bays and three storey is modelled and the analysis executed by applying cyclic displacement loads at the top corner of the structure. The beam and column cross-sections are HSS 127 mm × 127 mm × 9.5 mm and the storey height is 0.8m while the bay is 1.25 m [35]. Scaled models are also created to test out the ability of scaling to capture in this case the effects of cyclic loading on a building structure. A schematic diagram is presented in Fig. 12 showing the real full-scale and trial models along with the projected trial models and their combination to form the full-scale virtual model. The scales selected for the study are $\beta_1 = \frac{1}{4}$ and $\beta_2 = \frac{1}{6}$ as indicated in Fig. 12. Both zeroth and first-order theory is applied and details are presented in Tables 5 and 6, respectively. Analysis of the full-scale and trial models is performed model using Abaqus explicit and for consistency a transient-cyclic analysis is performed.

Table 3:5: Zeroth-order material properties and scaling parameters.

Design	**Model**	**Mat.**	**Density (kg/m^3)**	**Young's Modulus (10^{11} Pa)**	**Yield Stress (10^8 Pa)**	β	α^{ρ}	g
Design I	Trial Model 1	S235	7850	2.1	2.35	1/4	64	0.30727
	Trial Model 2	Al	2770	0.7	3.37	1/4	181	0.15242
	Projected Model 1		7850	3.17	3.55			
	Projected Model 2		7850	0.737	3.55			
Design II	Trial Model 1	S235	7850	2.1	2.35	1/4	64	0.25
	Trial Model 2	Al	2770	0.7	3.37	1/4	181	0.257
	Projected Model 1		7850	2.1	2.35			
	Projected							

	Model 2		7850	2.1	10.1			

The material used in the full-scale structure is steel S355 and the targeted-physical quantities for the projected trial models are density and yield stress and/or Young's modulus. For zeroth order this involves the relationships $\rho_{ps} = \alpha_{01}^{\rho}\rho_{ts1}\beta_1^3$ and $Y_{ps} = \alpha_{01}^{\rho} g_1^2 \beta_1 Y_{ts1}$ or $E_{ps} = \alpha_{01}^{\rho} g_1^2 \beta_1 E_{ts1}$, respectively. With $\beta_1 = \frac{1}{4}$ the values of α_{01}^{ρ} and g_1 can be determined and their values are provided in Table 5 for the different material combinations. As regards first-order, the proportional method of Section 5.1 is applied leading to the equations

$$1 = \alpha_{01}^{\rho} g_1^2 \beta_1 \hat{b}_1 + R_1(\alpha_{01}^{\rho} g_1^2 \beta_1 \hat{b}_1 - \alpha_{02}^{\rho} g_2^2 \beta_2 \hat{b}_1) \quad (28a)$$

$$1 = \alpha_{01}^{\rho} g_1^2 \beta_1 \hat{e}_1 + R_1(\alpha_{01}^{\rho} g_1^2 \beta_1 \hat{e}_1 - \alpha_{02}^{\rho} g_2^2 \beta_2 \hat{e}_2) \quad (28b)$$

arising for stress and stiffness considerations with $\hat{b}_1 = \frac{Y_{ts1}}{Y_{ps}}$, $\hat{b}_2 = \frac{Y_{ts2}}{Y_{ps}}$, $\hat{e}_1 = \frac{E_{ts1}}{E_{ps}}$ and $\hat{e}_2 = \frac{E_{ts2}}{E_{ps}}$, and in order to solve these two equations for g_2 and R_1, it is necessary to set g_1.

This is done by means of zeroth-order theory and the consequential values of g_2 and R_1 obtained from Eqs. (28) are provided in Table 6. Note the common values of g_1 in Tables 5 and 6 indicating that Design I is the design taken forward to first-order analysis. The boundary and loading for each of the full scale and trial models are presented in Fig. 13 along with mesh details for the analysis.

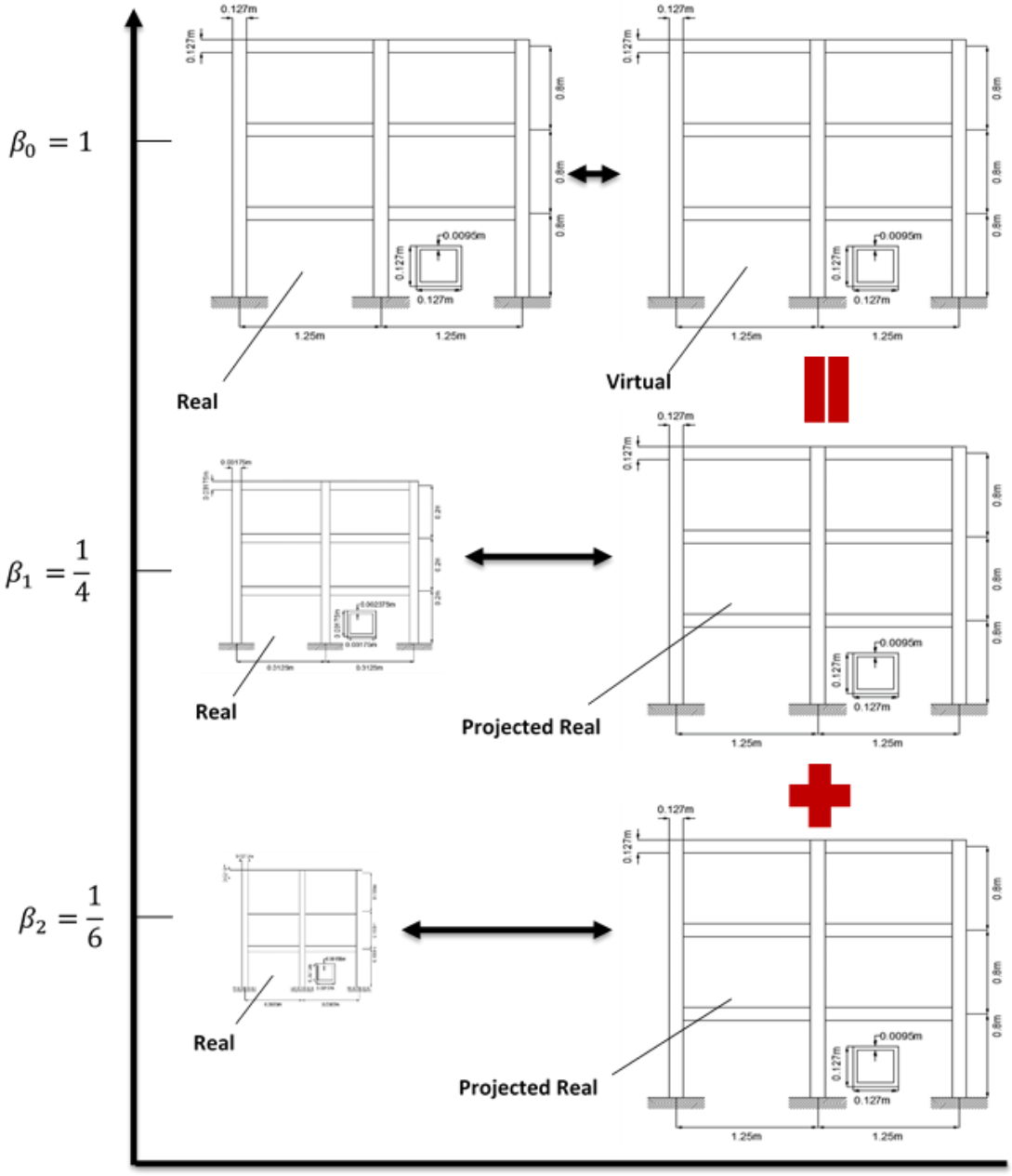

Figure 12: Scaled models for a two-bay, three-storey structure.

Table 3:6: First-order material properties and scaling parameters.

Designs		**Mat.**	**Density (kg/m^3)**	**Young's Modulus (10^{11} Pa)**	**Yield Stress (10^6 Pa)**	g_1	g_2	R_1
Design I	Full-scale Model	S355	7850	2.1	3.55	0.3073	0.1894	-2.324
	Trial Model 1	S235	7850	2.1	2.35			
	Trial Model 2	S275	7850	2.1	2.75			
Design II	Full-scale Model	S355	7850	2.1	3.55	0.153	0.205	-0.845
	Trial Model 1	Al	2770	0.7	3.37			
	Trial Model 2	S235	7850	2.1	2.35			

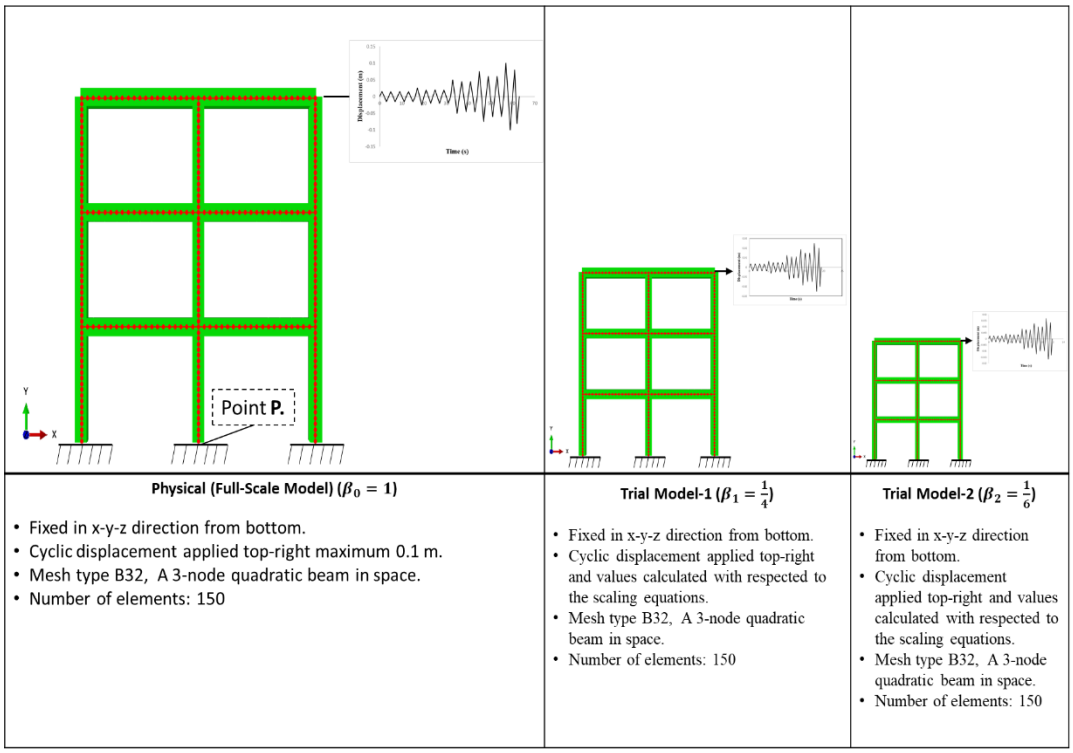

Figure 13: Boundary and loading for physical and trial models.

The mesh densities are those obtained from a mesh-sensitivity study and provide converged solutions. The loading applied in this study consists of a cyclically load generally increasing with amplitude as time progresses as shown in Figs. 13 and 14 (see references [36] and [37] for details). The results from the mesh-sensitivity study under the loading depicted in Fig. 14 are presented in Fig. 15. It is clear that the mesh size/number of elements had negligible influence on the results obtained. Note that the choice of loading is similar to that of an earthquake with increasing amplitudes with time. It can be seen from Fig. 15 that the loading consists of a form of generally increasing sharp waves punctuated by periods of constant amplitudes.

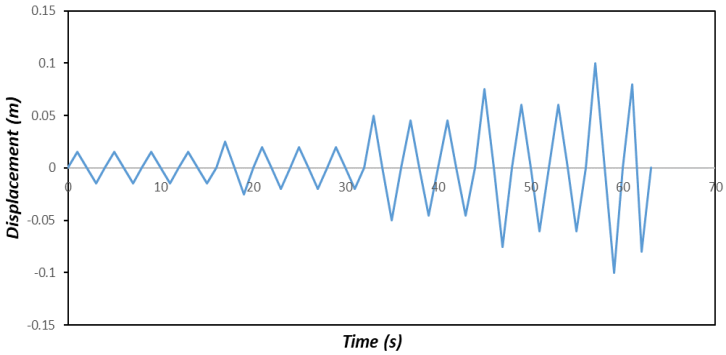

Figure 14: Applied cyclic displacement-time graph (based on [38]).

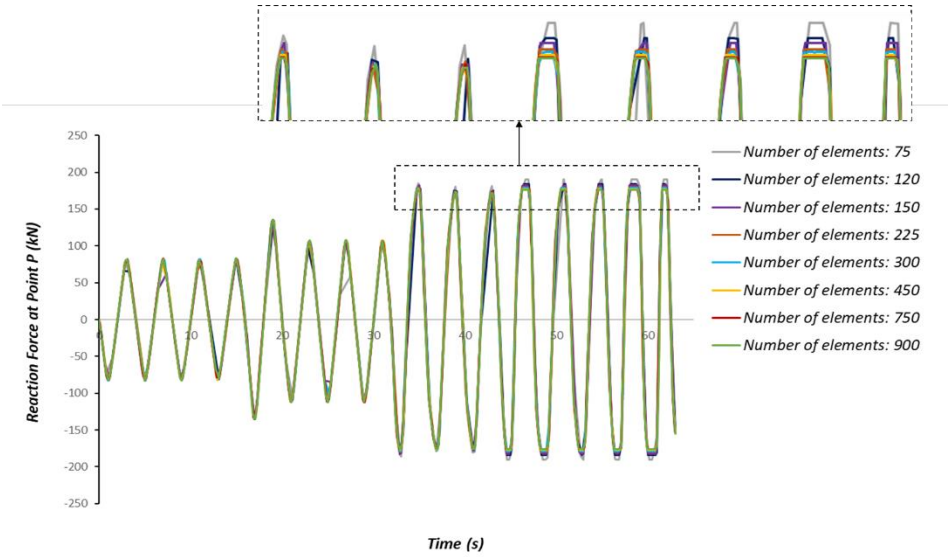

Figure 15: Mesh sensitivity analysis at point P shown in Fig. 13.

The results of the study are presented in Figs. 16 to 19, with zeroth-order results presented in Figs. 16 and 17. The results of Figs. 16 and 17 indicate that Design I (Trial 1) as defined in Table 6 provides the best approximation from the cases

considered. Examination of the values for yield stress, density and Young's modulus for the projected model indicate the reason for this, since these are closest to those of the full-scale model. However, the match is not perfect as indicated by the inclined portion of the graph which does not coincide.

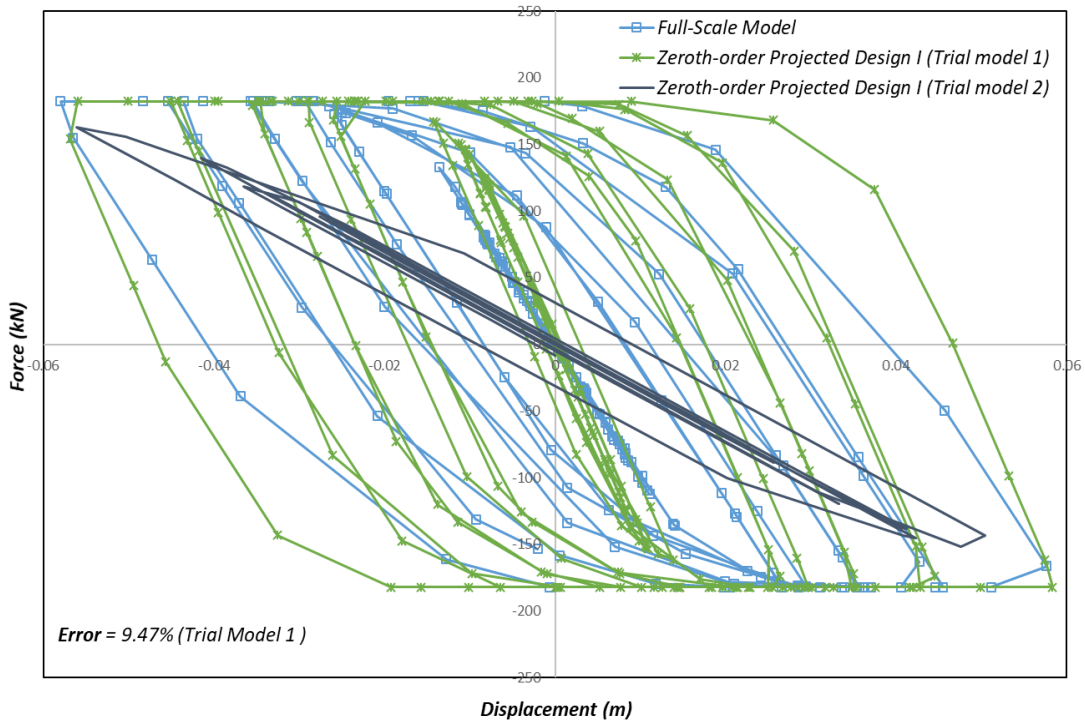

Figure 16: Zeroth order cyclic analysis of Design I models.

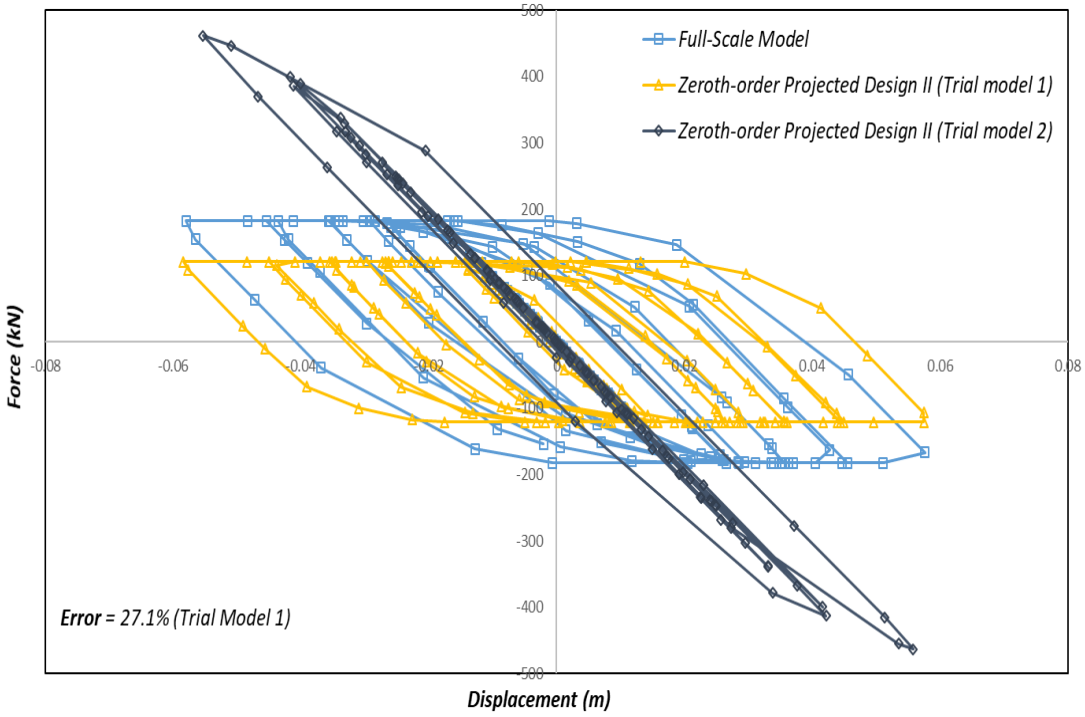

Figure 17: Zeroth order cyclic analysis of Design II models.

The percentage errors indicated in these figures refers to the differences in the areas enclosed by the last complete loop between the virtual and full-scale models. In view of the failure of the zeroth-order theory to provide a sufficiently close-enough match first-order theory is applied to both Designs I and II and the results presented in Fig. 18. A marked improvement is revealed in this figure with both designs providing an improved level of accuracy. This result provides good evidence for the benefits of two scaled experiments over one and confirms that the finite similitude theory is able to interpret the information arising from the two experiments.

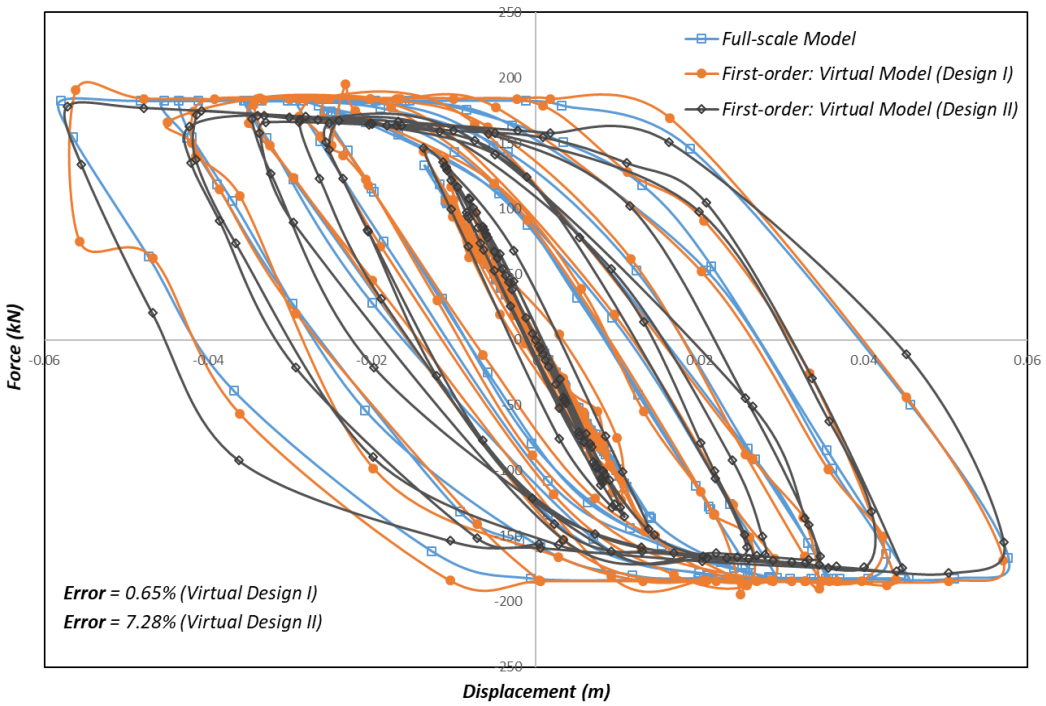

Figure 18: First-order cyclic analysis of Design I and II models.

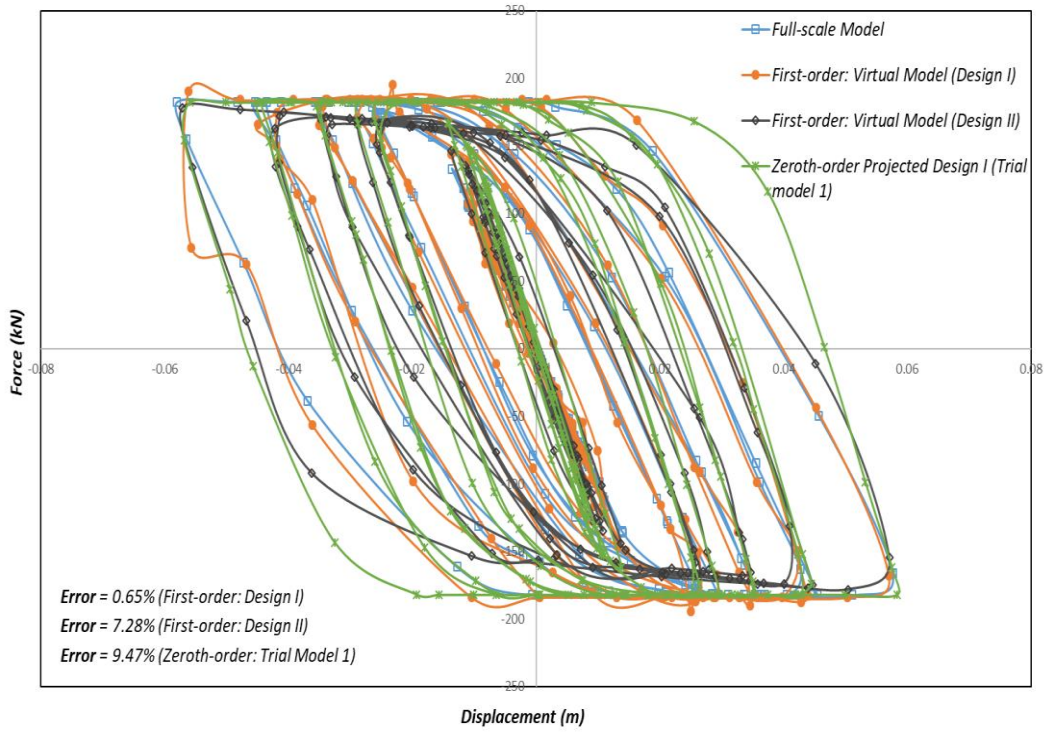

Figure 19: Zeroth and first-order cyclic analysis of Design I and models.

A final comparison between the best zeroth-order and first-order finite similitude designs is provided in Fig. 19. The figure confirms that the first-order theory provides better predictions than zeroth order and the differences can be marked.

7. Conclusion

The paper is concerned with the assessment of a new scaling theory for the investigation of the aseismic behaviour of structures. The new approach involves two scaled experiments and is founded on the metaphysical concept of space scaling. The following conclusions can be drawn from the work presented in the paper:

1. A new scaling theory has been established that captures either explicitly or implicitly all scale dependencies that arise in structural mechanics.
2. A new form of similarity has been established (termed first-order finite similitude) in differential form (see Eq. 10), which can be integrated exactly using finite differences to combine results from two scaled-trial experiments to predict full-scale structural behaviour.
3. The new theory has been trialled on analytical and numerical models and provides predictions (sometimes markedly) superior to a single-scale trial experiment.
4. Scale effects as previously defined by dimensional analysis can up to a limited degree be accommodated (e.g. dimensionless strain need not be constant).
5. A new proportional theory has been established that has been shown to provide an efficient means to determine scaling parameters and avoid the need for expensive iterative procedures.

More specifically for the trial experiments performed it has been show that:

1. The first-order scaling theory was able to target more material properties for matching between the virtual and physical full-scale model (e.g. yield stress, Young's modulus and density were matched in earthquake resistant structures).
2. The benefit of matching yield stress and Young's modulus for the cyclic loading of a two bay, three story structure was significant and confirmed the improvements possible with the new approach.
3. The investigation of aseismic structures is improved using two scaled experiments as opposed to a single scaled experiment. For a cyclically loaded three-storey building, the proposed methodology reduced an overall error of 9.47% with a single scaled experiment to 0.65% with the combination of two scaled experiments.

Acknowledgements

The authors would like to acknowledge The Ministry of National Education in Turkey and the Department of Civil Engineering at Firat University for providing support for Muhammed Atar to facilitate his doctoral research at the University of Manchester.

8. References

[1] Nayak S, Dutta SC. Failure of masonry structures in earthquake: A few simple cost effective techniques as possible solutions. Eng Struct 2016;106:53–67. https://doi.org/10.1016/j.engstruct.2015.10.014.

[2] Sedov LI, Friedman M, Holt M, Cole JD. Similarity and Dimensional Methods in Mechanics. J Appl Mech 1961. https://doi.org/10.1115/1.3640458.

[3] Buckingham E. On physically similar systems; Illustrations of the use of dimensional equations. Phys Rev 1914;4:345–76. https://doi.org/10.1103/PhysRev.4.345.

[4] Kline SJ, Radbill JR. Similitude and Approximation Theory. J Appl Mech 1966;33:238–238. https://doi.org/10.1115/1.3625015.

[5] Buckingham E. The principle of similitude . Nature 1915;96:396–7. https://doi.org/10.1038/096396d0.

[6] Casaburo A, Petrone G, Franco F, De Rosa S. A Review of Similitude Methods for Structural Engineering. Appl Mech Rev 2019;71. https://doi.org/10.1115/1.4043787.

[7] Dutson AJ, Wood KL. Using rapid prototypes for functional evaluation of evolutionary product designs. Rapid Prototyp J 2005;11:125–31. https://doi.org/10.1108/13552540510601246.

[8] Wissmunn JW. Dynamic Stability of Space Vehicles. Structural Dynamics Model Testing. KIRTLAND AFB: 1968.

[9] Luo Z, Wang Y, Zhu Y, Zhao X, Wang D. The similitude design method of thin-walled annular plates and determination of structural size intervals. Proc Inst Mech Eng Part C J Mech Eng Sci 2016;230:2158–68. https://doi.org/10.1177/0954406215592055.

[10] Simitses GJ, Rezaeepazhand J. Structural similitude and scaling laws for laminated beam-plates. Am. Soc. Mech. Eng. Aerosp. Div. AD, 1992.

[11] Budarapu PR, Zhuang X, Rabczuk T, Bordas SPA. Multiscale modeling of material failure: Theory and computational methods. Adv Appl Mech 2019;52:1–103. https://doi.org/10.1016/bs.aams.2019.04.002.

[12] Chen WQ. The renaissance of continuum mechanics. J Zhejiang Univ Sci A 2014;15:231–40. https://doi.org/10.1631/jzus.A1400079.

[13] Chen Y, Shabanov S, McDowell DL. Concurrent atomistic-continuum modeling of crystalline materials. J Appl Phys 2019;126:101101. https://doi.org/10.1063/1.5099653.

[14] Sharma A, Reddy GR, Vaze KK. Shake table tests on a non-seismically detailed RC frame structure. Struct Eng Mech 2012;41:1–24. https://doi.org/10.12989/sem.2012.41.1.001.

[15] Guerrero Bobadilla H, Ji T, Escobar JA. Experimental studies of a steel frame model with and without buckling-restrained braces. Rev Ing Sísmica 2016:33–52.

https://doi.org/10.18867/ris.95.338.

[16] Guerrero H, Ji T, Escobar JA, Teran-Gilmore A. Effects of Buckling-Restrained Braces on reinforced concrete precast models subjected to shaking table excitation. Eng Struct 2018;163:294–310. https://doi.org/10.1016/j.engstruct.2018.02.055.

[17] Nader MN, Astaneh-Asl A. Shaking Table Tests of Rigid, Semirigid, and Flexible Steel Frames. J Struct Eng 1996;122:589–96. https://doi.org/10.1061/(ASCE)0733-9445(1996)122:6(589).

[18] Kim SE, Lee DH, Ngo-Huu C. Shaking table tests of a two-story unbraced steel frame. J Constr Steel Res 2007;63:412–21. https://doi.org/10.1016/j.jcsr.2006.04.009.

[19] Petry S, Beyer K. Scaling unreinforced masonry for reduced-scale seismic testing. Bull Earthq Eng 2014;12:2557–81. https://doi.org/10.1007/s10518-014-9605-1.

[20] Zou Y, Lu XL. Shaking table model test on Shanghai World Financial Center. World Inf Earthq Eng 2007.

[21] Moghaddam M, Darvizeh R, Davey K, Darvizeh A. Scaling of the powder compaction process. Int J Solids Struct 2018;144–145:192–212. https://doi.org/10.1016/j.ijsolstr.2018.05.002.

[22] Sadeghi H, Davey K, Darvizeh R, Darvizeh A. A scaled framework for strain rate sensitive structures subjected to high rate impact loading. Int J Impact Eng 2019;125:229–45. https://doi.org/10.1016/j.ijimpeng.2018.11.008.

[23] Al-Tamimi A, Darvizeh R, Davey K. Experimental investigation into finite similitude for metal forming processes. J Mater Process Technol 2018;262:622–37. https://doi.org/10.1016/j.jmatprotec.2018.07.028.

[24] Ochoa-Cabrero R, Alonso-Rasgado T, Davey K. Scaling in biomechanical experimentation: A finite similitude approach. J R Soc Interface 2018. https://doi.org/10.1098/rsif.2018.0254.

[25] Sadeghi H, Davey K, Darvizeh R, Darvizeh A. Scaled models for failure under impact loading. Int J Impact Eng 2019;129:36–56. https://doi.org/10.1016/j.ijimpeng.2019.02.010.

[26] Davey K, Darvizeh R, Al-Tamimi A. Scaled metal forming experiments: A transport equation approach. Int J Solids Struct 2017;125:184–205. https://doi.org/10.1016/j.ijsolstr.2017.07.006.

[27] Davey K, Darvizeh R. Neglected transport equations: extended Rankine–Hugoniot conditions and J -integrals for fracture. Contin Mech Thermodyn 2016;28:1525–52. https://doi.org/10.1007/s00161-016-0493-2.

[28] Davey K, Sadeghi H, Darvizeh R, Golbaf A, Darvizeh A. A Finite Similitude Approach to Scaled Impact Mechanics. Int J Impact Eng 2021;148. https://doi.org/10.1016/j.ijimpeng.2020.103744.

[29] Wu JS. Analytical and Numerical Methods for Vibration Analyses. 2015. https://doi.org/10.1002/9781119137207.

[30] PEER Ground Motion Database - PEER Center n.d. https://ngawest2.berkeley.edu/spectras/273010/searches/251041/edit?fbclid=IwAR1xu

9ySZ4HcvctPnKqU-rDzgeawvghlwaPRWOQIVCgwJPd7gp5ObcMveUA (accessed March 22, 2020).

[31] Kim NS, Lee JH, Chang SP. Equivalent multi-phase similitude law for pseudodynamic test on small scale reinforced concrete models. Eng Struct 2009;31:834–46. https://doi.org/10.1016/j.engstruct.2008.06.008.

[32] Abaqus U manual. Version 6.14. Dassault Systèmes Simulia Corp, Provid RI 2014.

[33] Anbuchezian A, Baskar G. Behaviour of Cold-Formed Steel Beams Under Cyclic Load Reversal. Int J Eng Sci 2013:22–30.

[34] Spiliopoulos K V., Panagiotou KD. A numerical procedure for the shakedown analysis of structures under cyclic thermomechanical loading. Arch Appl Mech 2015;85:1499–511. https://doi.org/10.1007/s00419-014-0947-6.

[35] Kauffman A, Memari A. Performance Evaluation of Different Masonry Infill Walls with Structural Fuse Elements Based on In-Plane Cyclic Load Testing. Buildings 2014;4:605–34. https://doi.org/10.3390/buildings4040605.

[36] Casaburo A, Petrone G, Meruane V, Franco F, De Rosa S. Support of Dynamic Measurements Through Similitude Formulations. Exp Tech 2021. https://doi.org/10.1007/s40799-021-00457-1.

[37] Lirola JM, Castañeda E, Lauret B, Khayet M. A review on experimental research using scale models for buildings: Application and methodologies. Energy Build 2017;142:72–110. https://doi.org/10.1016/j.enbuild.2017.02.060.

[38] Langhaar H. Dimensional analysis and theory of models. Robert E. Krieger publishing company; 1980.

[39] Jones N. Structural Impact. 2nd ed. Cambridge University Press; 2012.

[40] Altun O, Wolniak P, Mozgova I, Lachmayer R. AN ANALYSIS OF SCALING METHODS FOR STRUCTURAL COMPONENTS IN THE CONTEXT OF SIZE EFFECTS AND NONLINEAR PHENOMENA. Proc Des Soc Des Conf 2020;1:797–806. https://doi.org/10.1017/dsd.2020.320.

[41] Davey K, Darvizeh R, Atar M. A first order finite similitude approach to scaled aseismic structures. Eng Struct 2021;231:111739. https://doi.org/10.1016/j.engstruct.2020.111739.

[42] Nature LR-, 1915. The principle of similitude. CiNiiAcJp n.d.:66–8.

[43] Oshiro RE, Alves M. Predicting the behaviour of structures under impact loads using geometrically distorted scaled models. J Mech Phys Solids 2012;60:1330–49. https://doi.org/10.1016/j.jmps.2012.03.005.

[44] Mazzariol LM, Alves M. Experimental verification of similarity laws for impacted structures made of different materials. Int J Impact Eng 2019;133:103364. https://doi.org/10.1016/j.ijimpeng.2019.103364.

[45] Mascolo I. Recent Developments in the Dynamic Stability of Elastic Structures. Front Appl Math Stat 2019;5:51. https://doi.org/10.3389/fams.2019.00051.

[46] Evkin A, Krasovsky V, Lykhachova O, Marchenko V. Local buckling of axially

compressed cylindrical shells with different boundary conditions. Thin-Walled Struct 2019;141:374–88. https://doi.org/10.1016/j.tws.2019.04.039.

[47] Stuart AM. Numerical analysis of dynamical systems. Acta Numer 1994;3:467–572. https://doi.org/10.1017/S0962492900002488.

[48] Jog CS, Agrawal M, Nandy A. The time finite element as a robust general scheme for solving nonlinear dynamic equations including chaotic systems. Appl Math Comput 2016;279:43–61. https://doi.org/10.1016/j.amc.2015.12.007.

[49] Mazzariol LM, Alves M. Similarity laws of structures under impact load: Geometric and material distortion. Int J Mech Sci 2019;157–158:633–47. https://doi.org/10.1016/j.ijmecsci.2019.05.011.

[50] Riddoch DJ, Cicirello A, Hills DA. Response of a mass-spring system subject to Coulomb damping and harmonic base excitation. Int J Solids Struct 2020;193–194:527–34. https://doi.org/10.1016/j.ijsolstr.2020.02.037.

[51] Li C, Yuan Y, He P, Yuan J, Yu H. Improved equivalent mass-spring model for seismic response analysis of two-dimensional soil strata. Soil Dyn Earthq Eng 2018;112:198–202. https://doi.org/10.1016/j.soildyn.2018.05.001.

[52] De La Cruz ST, Rodríguez MA, Hernández V. Using Spring-Mass Models to Determine the Dynamic Response of Two-Story Buildings Subjected to Lateral Loads, 2012, p. 1–8.

[53] Marino L, Cicirello A. Experimental investigation of a single-degree-of-freedom system with Coulomb friction. Nonlinear Dyn 2020;99:1781–99. https://doi.org/10.1007/s11071-019-05443-2.

[54] Hou CY. Behavior explanation and a new model for nonlinear viscous fluid dampers with a simple annular orifice. Arch Appl Mech 2012;82:1–12. https://doi.org/10.1007/s00419-011-0534-z.

[55] Seleemah AA, Constantinou MC. Investigation of Seismic Response of Buildings with Linear and Nonlinear Fluid Viscous Dampers. 1997.

[56] Farahi Shahri S, Roohollah Mousavi S. Seismic behavior of beam-to-column connections with elliptic slit dampers. Steel Compos Struct 2018;26:289–301. https://doi.org/10.12989/scs.2018.26.3.289.

[57] Mousavi SA, Esfandiyari R, Zahrai SM. Experimental Study on Two Full Scale Iranian Viscous Dampers, 2018, p. 11–2.

[58] Ata AA, Kamel AG. Numerical evaluation of the effect of Combined Pendulum Tuned Mass Damper on a basic vibrating system. Int J Mechatronics Appl Mech 2018;4:270.

[59] Kasai K, Pu WC, Wada A. Response of Passively-Controlled Tall Buildings in Tokyo during 2011 Great East Japan Earthquake. iitk.ac.in, 2012.

[60] Esfandiyari R, Nejad SM, Marnani JA, Mousavi SA, Zahrai SM. Seismic behavior of structural and non-structural elements in RC building with bypass viscous dampers. Steel Compos Struct 2020;34:487–97. https://doi.org/10.12989/scs.2020.34.4.487.

[61] Pekcan G, Mander JB, Chen SS. Fundamental considerations for the design of non-linear viscous dampers. Earthq Eng Struct Dyn 1999;28:1405–25.

https://doi.org/10.1002/(SICI)1096-9845(199911)28:11<1405::AID-EQE875>3.0.CO;2-A.

[62] Symans MD, Constantinou MC. Passive Fluid Viscous Damping Systems for Seismic Energy Dissipation. J Earthq Technol 1998;35:185–206.

[63] Asher JW, Young RP, Ewing RD. Seismic isolation design of the San Bernardino County Medical Center replacement project. Struct Des Tall Build 1996;5:265–79. https://doi.org/10.1002/(SICI)1099-1794(199612)5:4<265::AID-TAL77>3.0.CO;2-X.

[64] Terenzi G. Dynamics of SDOF Systems with Nonlinear Viscous Damping. J Eng Mech 1999;125:956–63. https://doi.org/10.1061/(ASCE)0733-9399(1999)125:8(956).

[65] Awrejcewicz J, Olejnik P. Analysis of dynamic systems with various friction laws. Appl. Mech. Rev., vol. 58, American Society of Mechanical Engineers Digital Collection; 2005, p. 389–410. https://doi.org/10.1115/1.2048687.

[66] García Reyes LE. Stick-slip vibrations and chaos. J Chem Inf Model 2013;53:1689–99.

[67] Coutinho C. Structural reduced scale models based on similitude theory. 2017.

[68] Zohuri B. Dimensional analysis and self-similarity methods for engineers and scientists. 2015.

[69] Pawelski O. Ways and limits of the theory of similarity in application to problems of physics and metal forming. J Mater Process Tech 1992;34:19–30. https://doi.org/10.1016/0924-0136(92)90086-8.

[70] Barenblatt GI. Scaling, Self-similarity, and Intermediate Asymptotics - Google Books. 1996.

[71] Sadeghi H, Davey K, Darvizeh R, Rajabiehfard R, Darvizeh A. An investigation into finite similitude for high-rate loading processes: Advantages in comparison to dimensional analysis and its practical implementation. Int J Impact Eng 2020;140:103554. https://doi.org/10.1016/j.ijimpeng.2020.103554.

[72] Davey K, Darvizeh R, Atar M, Golbaf A. A Study of Scale Effects in Discrete Scaled Dynamic Systems. Int J Mech Sci 2021;199:106399. https://doi.org/10.1016/j.ijmecsci.2021.106399.

[73] Ochoa-Cabrero R, Alonso-Rasgado T, Davey K. Scaling in biomechanical experimentation: a finite similitude approach. J R Soc Interface 2018;15:20180254. https://doi.org/10.1098/rsif.2018.0254.

[74] Davey K, Mondragon R. A non-physical enthalpy method for the numerical solution of isothermal solidification. Int J Numer Methods Eng 2010;84:214–52. https://doi.org/10.1002/nme.2896.

[75] Davey K, Darvizeh R, Golbaf A, Sadeghi H. The breaking of geometric similarity. Int J Mech Sci 2020;187:105925. https://doi.org/10.1016/j.ijmecsci.2020.105925.

[76] Darvizeh R, Davey K. A transport approach for analysis of shock waves in cellular materials. Int J Impact Eng 2015;82:59–73. https://doi.org/10.1016/j.ijimpeng.2014.11.006.

[77] Lin WH, Chopra AK. Earthquake response of elastic SDF systems with non-linear fluid viscous dampers. Earthq Eng Struct Dyn 2002;31:1623–42. https://doi.org/10.1002/eqe.179.

[78] Rodríguez S, Seim C, US TI-P of the third, 1994 undefined. Earthquake protective systems for the seismic upgrade of the Golden Gate bridge. Proc. third US-Japan Work. Earthq. Prot. Syst. Bridg., 1994, p. 4–147.

[79] Hou C-Y. Fluid Dynamics and Behavior of Nonlinear Viscous Fluid Dampers. J Struct Eng 2008;134:56–63. https://doi.org/10.1061/(ASCE)0733-9445(2008)134:1(56).

[80] Hibbett, Karlsson, Sorensen. ABAQUS/standard: User's Manual. 1998.

[81] Syrakos A, Dimakopoulos Y, Tsamopoulos J. Theoretical study of the flow in a fluid damper containing high viscosity silicone oil: Effects of shear-thinning and viscoelasticity. Phys Fluids 2018;30:030708. https://doi.org/10.1063/1.5011755.

[82] Narkhede DI, Sinha R. Behavior of nonlinear fluid viscous dampers for control of shock vibrations. J Sound Vib 2014;333:80–98. https://doi.org/10.1016/j.jsv.2013.08.041.

[83] Taylor Devices I. Fluid Viscous Dampers Manual. 2020.

[84] Galvanetto U, Bishop SR. Characterisation of the dynamics of a four-dimensional stick-slip system by a scalar variable. Chaos, Solitons and Fractals 1995;5:2171–9. https://doi.org/10.1016/0960-0779(94)00226-G.

[85] Van De Vrande BL, Van Campen DH, De Kraker A. An approximate analysis of dry-friction-induced stick-slip vibratons by a smoothing procedure An Approximate Analysis of Dry-Friction-Induced Stick-Slip Vibrations by a Smoothing Procedure *. Nonlinear Dyn 1999;19:157–69. https://doi.org/10.1023/A:1008306327781.

[86] GALVANETTO U, BISHOP SR, BRISEGHELLA L. MECHANICAL STICK-SLIP VIBRATIONS. Int J Bifurc Chaos 1995;05:637–51. https://doi.org/10.1142/s0218127495000508.

[87] Xu H, Jin X, Huang Z. Random Response of Spring–Damper–Mass–Belt System with Coulomb Friction. J Vib Eng Technol 2020;8:685–93. https://doi.org/10.1007/s42417-019-00168-3.

[88] Jin X, Xu H, Wang Y, Huang Z. Approximately analytical procedure to evaluate random stick-slip vibration of Duffing system including dry friction. J Sound Vib 2019;443:520–36. https://doi.org/10.1016/j.jsv.2018.12.001.

[89] Paredes M, Rodriguez E, Sartor M, Paredes M, Rodriguez E, Sartor M, et al. Analytical Behavior Law for a Constant Pitch Conical Compression. J Mech Des Am Soc Mech Eng 2006;6.

[90] Garevski M, Hristovski V, Talaganov, Kosta; Stojmanovska M. Experimental Investigations of 1/3-Scale R/C Frame with Infill Walls Building Structures. Proc. 13th World Conf. Earthq. Eng., 2004, p. 772.

[91] Mohammed A, Hughes TG, Mustapha A. The effect of scale on the structural behaviour of masonry under compression. Constr Build Mater 2011;25:303–7. https://doi.org/10.1016/j.conbuildmat.2010.06.025.

[92] Knappett JA, Reid C, Kinmond S, O'Reilly K. Small-scale modeling of reinforced concrete structural elements for use in a geotechnical centrifuge. J Struct Eng 2011;137:1263–71. https://doi.org/10.1061/(ASCE)ST.1943-541X.0000371.

[93] Li S, Zuo Z, Zhai C, Xu S, Xie L. Shaking table test on the collapse process of a three-story reinforced concrete frame structure. Eng Struct 2016;118:156–66. https://doi.org/10.1016/j.engstruct.2016.03.032.

[94] Bairrao R, Vaz C. Shaking table testing of civil engineering structures-The LNEC 3D simulator experience. 2th World Conf Earthq Eng 2000;2129.

[95] Carrillo J, Gonzalez G, Llano L. Evaluation of mass-rig systems for shaking table experiments. DYNA 2012;79:159–67.

[96] Saiidi MS, Douglas B. Shake Table Testing of Flexure Dominated Reinforced Concrete Bridge Columns Report No . CCEER 99-13 Patrick Laplace Center for Earthquake Engineering Research. 1999.

[97] Chen X, Guan Z, Li J, Spencer BF. Shake Table Tests of Tall-Pier Bridges to Evaluate Seismic Performance. J Bridg Eng 2018;23. https://doi.org/10.1061/(ASCE)BE.1943-5592.0001264.

[98] Davey K, Darvizeh R, Atar M, Golbaf A. A Study of Scale Effects in Discrete Scaled Dynamic Systems. Int J Mech Sci 2021.

[99] Darvizeh R, Davey K. Non-physical finite element method: Multiple material discontinuities. Comput Struct 2016;164:145–60. https://doi.org/10.1016/j.compstruc.2015.11.010.

[100] Darvizeh R, Davey K. Non-physical finite element modelling of high speed normal crushing of cellular materials. Int J Impact Eng 2015;82:130–43. https://doi.org/10.1016/j.ijimpeng.2015.04.002.

[101] Szymczak C, Kujawa M. Flexural buckling and post-buckling of columns made of aluminium alloy. Eur J Mech A/Solids 2019;73:420–9. https://doi.org/10.1016/j.euromechsol.2018.10.006.

[102] Ramberg W, Osgood WR. Description of stress-strain curves by three parameters. Natl Advis Comm Aeronaut 1943.

[103] Szymczak C, Kujawa M. Local buckling of thin-walled channel member flange made of aluminum alloy. AIP Conf. Proc., 2017. https://doi.org/10.1063/1.4977688.

[104] Theofanous M, Gardner L. Testing and numerical modelling of lean duplex stainless steel hollow section columns. Eng Struct 2009;31:3047–58. https://doi.org/10.1016/j.engstruct.2009.08.004.

[105] Ahmed S, Ashraf M. Numerical investigation on buckling resistance of stainless steel hollow members. J Constr Steel Res 2017;136:193–203. https://doi.org/10.1016/j.jcsr.2017.05.017.

[106] Kasivitamnuay J, Singhatanadgid P. Scaling laws for displacement of elastic beam by energy method. Int J Mech Sci 2017;128–129:361–7. https://doi.org/10.1016/j.ijmecsci.2017.05.001.

[107] Alves M, Oshiro RE. Scaling the impact of a mass on a structure. Int J Impact Eng

2006;32:1158–73. https://doi.org/10.1016/j.ijimpeng.2004.09.009.

[108] Luo Z, Zhu Y, Zhao X, Wang D. Determining Dynamic Scaling Laws of Geometrically Distorted Scaled Models of a Cantilever Plate. J Eng Mech 2016;142:04015108. https://doi.org/10.1061/(asce)em.1943-7889.0001028.

[109] Wu W, Ge S, Yuan Y, Ding W, Anastasopoulos I. Seismic response of subway station in soft soil: Shaking table testing versus numerical analysis. Tunn Undergr Sp Technol n.d.;100:103389. https://doi.org/10.1016/j.tust.2020.103389.

[110] Rahnavard R, Fard FFZ, Hosseini A, Suleiman M. Nonlinear analysis on progressive collapse of tall steel composite buildings. Case Stud Constr Mater 2018;8:359–79. https://doi.org/10.1016/j.cscm.2018.03.001.

[111] Song Z, Su C. Computation of Rayleigh Damping Coefficients for the Seismic Analysis of a Hydro-Powerhouse. Shock Vib 2017;2017:1–11. https://doi.org/10.1155/2017/2046345.

[112] Chen XM, Duan J, Qi H, Li YG. Rayleigh Damping in Abaqus/Explicit Dynamic Analysis. Appl Mech Mater n.d.;627:288–94. https://doi.org/10.4028/www.scientific.net/amm.627.288.

[113] Cremer L, Heckl M. Structure-Borne Sound. 1988. https://doi.org/10.1007/978-3-662-10121-6.

[114] Vince Adams and Abraham Askenazi. Building Better Products with Finite Element Analysis. vol. 127. New York: American Society of Mechanical Engineers; n.d.

[115] Bachmann H, Ammann WJ, Deischl F, Eisenmann J, Floegl I, Hirsch GH, et al. Vibration Problems in Structures. 1995. https://doi.org/10.1007/978-3-0348-9231-5.

[116] Orban F. Damping of materials and members in structures. J Phys Conf Ser 2011;268. https://doi.org/10.1088/1742-6596/268/1/012022.

[117] Banazadeh M, Ghanbari A, Ghanbari R. Seismic performance assessment of steel moment-resisting frames equipped with linear and nonlinear fluid viscous dampers with the same damping ratio. J Constr Steel Res 2017;136:215–28. https://doi.org/10.1016/j.jcsr.2017.05.022.

[118] CSI. SAP2000. Analysis Reference Manual. CSI Berkeley (CA, USA) Comput Struct INC 2016.

[119] Ras A, Boumechra N. Seismic energy dissipation study of linear fluid viscous dampers in steel structure design. Alexandria Eng J 2016;55:1–12. https://doi.org/10.1016/j.aej.2016.07.012.

[120] Boksmati JI, Madabhushi GSP. Centrifuge modelling of structures with oil dampers under seismic loading. Earthq Eng Struct Dyn 2020;49:356–74. https://doi.org/10.1002/eqe.3243.

[121] Huneault J, Kamil J, Higgins A, Plant D. Dynamic tensile strength of silicone oils. AIP Conf. Proc., 2018. https://doi.org/10.1063/1.5044825.

9. Appendices

9.1. Appendix A: Procedures for application

Presented in this section are the procedures followed in Sections 4, 5 and 6 in order to apply zeroth and first order finite theories. The zeroth-order theories follows the instruction set:

(i) Determine the geometrical and material properties and also boundary and initial (i.e. loading) conditions of the physical model;

(ii) Determine the dimensional scaling factor β_1 (thus, geometrical properties), material properties and boundary conditions for the trial model;

(iii) Determine which properties must be fixed;

(iv) Determine the independent density and time scaling factors (i.e. α_{01}^{ρ} and g_1);

(v) Calculate the initial (i.e. loading) conditions for the trial model;

(vi) Conduct experimental tests on the trial model and;

(vii) Lift the trial model response to predict the physical model response.

A similar looking set of instruction apply for the first-order finite similitude theory and these are:

(i) Determine the geometrical and material properties and also boundary and initial (i.e. loading) conditions for the physical model;

(ii) Determine the dimensional scaling factors β_1 and β_2 (thus, geometrical properties), material properties and boundary conditions for the first and second trial models;

(iii) Determine the density scaling factors (i.e. α_{01}^{ρ} and α_{02}^{ρ}) using the zeroth order finite similitude relations (i.e. $\rho_{ps} = \alpha_{01}^{\rho}\beta_1^3\rho_{ts1}$ and $\rho_{ps} = \alpha_{02}^{\rho}\beta_2^3\rho_{ts2}$);

(iv) Determine which properties must be fixed;

(v) Determine the time scaling factors (i.e. g_1 and g_2) and also R_1 by restricting the intended properties and also initial (i.e. loading) conditions;

(vi) Calculate the initial (i.e. loading) conditions of the first and second trial models;

(vii) Conduct the experimental tests on the first and second trial models and;

(viii) Combine trial models to produce a virtual model to predict the physical model behaviour.

9.2. Appendix B: Field restrictions

In this section a general understanding is provided pertaining to the proportional-fields assumption of Section 5.2 and the various restrictions placed on the fields for zeroth and first-order theories. The solution spaces on which each depends are $\mathfrak{I}_{zo}$, $\mathfrak{I}_{lin}$, $\mathfrak{I}_{fo}$ and $\mathfrak{I}_{dp}$, where $\mathfrak{I}_{zo}$ is zeroth-order solutions, $\mathfrak{I}_{lin}$ is proportional solutions (e.g. Eq. (26)), $\mathfrak{I}_{fo}$ is first-order solutions (e.g. Eqs. (17)) and $\mathfrak{I}_{dp}$ is solutions with proportional differences (e.g. $\boldsymbol{\sigma}_{ps} - \boldsymbol{\sigma}_{ts1} = \hat{b}\left(\boldsymbol{\sigma}_{ts1} - \boldsymbol{\sigma}_{ts2}\right)$).

It is assumed here that the elements of these spaces are drawn from vector spaces over the real field $\Re$. More specifically for non-zero $\lambda \in \Re$, $\boldsymbol{h}_1 \in \mathfrak{I}_{zo} \Leftrightarrow \boldsymbol{h}_{ps} = \lambda \boldsymbol{h}_1$ with λ restricted to scalars provided by zeroth-order theory (see Table 1.) For the space $\mathfrak{I}_{lin}$ however, $\boldsymbol{h}_1 \in \mathfrak{I}_{zo} \Leftrightarrow \boldsymbol{h}_{ps} = \lambda \boldsymbol{h}_1$ for $\forall \lambda \neq 0 \in \Re$ and evidently $\mathfrak{I}_{zo} \subset \mathfrak{I}_{lin}$. Similarly for the space $\mathfrak{I}_{fo}$, $\boldsymbol{h}_1, \boldsymbol{h}_2 \in \mathfrak{I}_{fo} \Leftrightarrow \boldsymbol{h}_{ps} - \boldsymbol{h}_1 = \lambda\left(\boldsymbol{h}_1 - \boldsymbol{h}_2\right)$, and where $\boldsymbol{h}_{ps}$, $\boldsymbol{h}_1$, $\boldsymbol{h}_2$ and λ are restricted to be those common fields and scalars provided by first-order theory (see Eq. (17)). Finally $\boldsymbol{h}_1, \boldsymbol{h}_2 \in \mathfrak{I}_{dp} \Leftrightarrow \boldsymbol{h}_{ps} - \boldsymbol{h}_1 = \lambda\left(\boldsymbol{h}_1 - \boldsymbol{h}_2\right)$, $\forall \lambda \neq 0 \in \Re$ and any common field types $\boldsymbol{h}_{ps}$, $\boldsymbol{h}_1$ and $\boldsymbol{h}_2$; evidently $\mathfrak{I}_{fo} \subset \mathfrak{I}_{dp}$.

Proposition B.1

The solution spaces satisfy $\mathfrak{I}_{zo} \subset \mathfrak{I}_{lin} \subset \mathfrak{I}_{dp}$ and $\mathfrak{I}_{zo} \subset \mathfrak{I}_{fo} \subset \mathfrak{I}_{dp}$.

Proof B.1

$\mathfrak{I}_{zo}$ is a proper subset of $\mathfrak{I}_{lin}$ since for example $\boldsymbol{u}_{ps} = \beta_1^{-1}\boldsymbol{u}_{ts1}$ and $\boldsymbol{u}_{ps} = -\boldsymbol{u}_{ts1}$ are in $\mathfrak{I}_{lin}$ but only $\boldsymbol{u}_{ps} = \beta_1^{-1}\boldsymbol{u}_{ts1}$ is in $\mathfrak{I}_{zo}$. $\mathfrak{I}_{lin}$ is a subset of $\mathfrak{I}_{dp}$ since $\boldsymbol{\sigma}_{ts1} = \hat{b}_1\boldsymbol{\sigma}_{ps}$ and $\boldsymbol{\sigma}_{ts2} = \hat{b}_2\boldsymbol{\sigma}_{ps}$ provide $\boldsymbol{\sigma}_{ps} - \boldsymbol{\sigma}_{ts1} = \left(1 - \hat{b}_1\right)\boldsymbol{\sigma}_{ps}$ and $\boldsymbol{\sigma}_{ts1} - \boldsymbol{\sigma}_{ts2} = \left(\hat{b}_1 - \hat{b}_2\right)\boldsymbol{\sigma}_{ps}$. It is a proper subset since for any arbitrary non-zero $\boldsymbol{d}_{ps}$ not proportional to $\boldsymbol{\sigma}_{ps}$ the relationships $\boldsymbol{\sigma}_{ts1} = \boldsymbol{\sigma}_{ps} - \hat{b}\boldsymbol{d}_{ps}$ and $\boldsymbol{\sigma}_{ts2} = \left(1 - \hat{b}^{-1}\right)\boldsymbol{\sigma}_{ps} + \left(1 - \hat{b}\right)\boldsymbol{d}_{ps}$ are not in $\mathfrak{I}_{lin}$ but satisfy $\boldsymbol{\sigma}_{ps} - \boldsymbol{\sigma}_{ts1} = \hat{b}\left(\boldsymbol{\sigma}_{ts1} - \boldsymbol{\sigma}_{ts2}\right)$, so belongs to $\mathfrak{I}_{dp}$. In addition $\mathfrak{I}_{fo}$ is a proper subset of $\mathfrak{I}_{dp}$ since for example $\boldsymbol{u}_{ps} = \beta_1^{-1}\boldsymbol{u}_{ts1} + R_1\left(\beta_1^{-1}\boldsymbol{u}_{ts1} - \beta_2^{-1}\boldsymbol{u}_{ts2}\right)$ belongs to $\mathfrak{I}_{fo}$

but $\boldsymbol{u}_{ps} = -\boldsymbol{u}_{ts1} + R_1\left(\beta_1^{-1}\boldsymbol{u}_{ts1} - \beta_2^{-1}\boldsymbol{u}_{ts2}\right)$ does not.

A question remains about the relationship between $\mathfrak{I}_{lin}$ and $\mathfrak{I}_{fo}$ but solutions of $\mathfrak{I}_{lin}$ can belong to $\mathfrak{I}_{fo}$ since $\mathfrak{I}_{zo} \subset \mathfrak{I}_{lin}$ but also there exists solutions that do not. An example is $\boldsymbol{h}_{ps} = -\boldsymbol{h}_{ts1}$ and $\boldsymbol{h}_{ps} = -\boldsymbol{h}_{ts2}$ since $\boldsymbol{h}_{ps} - \boldsymbol{h}_{ts1} = 2\boldsymbol{h}_{ps}$ and $R_1\left(\boldsymbol{h}_{ts1} - \boldsymbol{h}_{ts2}\right) = \boldsymbol{0}$, so does no belong to $\mathfrak{I}_{fo}$ since $R_1 \neq 0$.

Chapter

FOUR

Paper two: A Study of Scale Effects in Discrete Scaled Dynamic Systems

Overview

Once the benefits and advantages of the new scaling theory were recognised, the following step was considered to show how discrete mechanical dynamic systems, which have common usage in structural engineering, for example, equivalent models consisting of mass-spring-damper systems. These systems can be utilised to initiate scaling parameters in a new scaling theory and to establish the appropriateness of first-order finite similitude for circumstances where traditional scaling theories are not sufficient. If a discrete system is considered to provide a true representation of the physical system, an experimental verification is always required to support the many simplifications generally required for practical modelling. Therefore, this article studies discrete elements and the change of their behaviour with scaling.

Authors Contribution: K. Davey made effort for the conceptualization, methodology, writing - review & editing of the research with the help of R. Darvizeh for supervising the project. **M. Atar** designed the models and the computational framework and analysed the data and carried out the implementations. In addition, validation, writing - review & editing the journal paper was performed by M. Atar. Ali Golbaf helped to verify numerical models via software.

Details: International Journal of Mechanical Sciences. Received 19 November 2020, Revised 15 March 2021, Accepted 15 March 2021, Available online 19 March 2021.
Publication date: 1 June 2021

Paper DOI: https://doi.org/10.1016/j.ijmecsci.2021.106399

A Study of Scale Effects in Discrete Scaled Dynamic Systems

Keith Davey[a,*], Rooholamin Darvizeh[a], Muhammed Atar[a], Ali Golbaf[b]

[a]School of Mechanical, Aerospace and Civil Engineering, The University of Manchester, ManchesterM13 9PL, UK
[b]Department of Mechanical Engineering, University of Guilan, Rasht, Iran.

Abstract

Scaled experimentation is an important experimental approach for the investigation of complex systems. Unfortunately, scaling suffers scale effects, where changes in behaviour with scale can be so significant to undermine any scaled investigation. The state-of-the-art in scaled experimentation remains dimensional analysis, which unfortunately offers no solution to scale effects and consequently scaled experiments although important provide only limited usefulness at the present time.

This paper is concerned with a new approach to scaled experimentation founded on the theory of *finite similitude* applied to discrete mechanical systems. The new theory applies the metaphysical concept of space scaling, where objects, prototypes, systems, experimental apparatus and facilities are scaled by the means of space contraction or expansion. Although space scaling is clearly practically impossible, what is possible is an assessment of the effects of space scaling on the governing physics and a comparison with real experimental behaviours. It is shown in the paper how the new theory accounts for all scale dependencies and unlike dimensional analysis is able to accommodate known scale effects. It provides also alternative scale-invariances that cater for the situation where scale effects are present but unknown. This aspect is the focus here with application of first-order *finite similitude* to simple mechanical-dynamic systems, an approach that requires two scaled experiments at two distinct scales. It is demonstrated how it is possible by means of two scaled experiments to represent behaviours at the full scaled that hitherto would have been deemed impossible with traditional dimensional analysis.

Keywords:

scaling, dynamics, finite similitude, trial experimentation

1. Introduction

Modern methods for the analysis of mechanical-based dynamic systems invariably at some point turn to computer simulation to investigate such things as kinematics, stability, long-term behaviour and control [1][2][3][4]. Computer simulation provides great scope for all manner of investigations and facilitates sensitivity analysis with the scrutinization of system response to changes in initial and boundary conditions but also system properties [5][6]. In cases where the discrete system is deemed to provide a realistic representation of a physical system, then experimental validation is invariably required to support the many simplifications that are often necessary for practical modelling to take place [7]. Discrete representations find common usage in structural engineering for example where equivalent models consisting of mass-spring-damper systems are used to approximate and investigate the overall response of structures under loading. Such studies include the response of passive control systems [8], the behaviour of the buildings exposed to the seismic or base excitations [9, 10, 11], and the determination of metal-metal contacts between two one-storey buildings exposed to seismic loading [12]. The literature is replete with such studies supported by experimental evidence in order to justify there use, involving what might appear at first sight to be somewhat controversial looking simplifications [13][14]. Experimental studies take three distinct forms depending of the nature of the problem under consideration. Whole-system investigations can be performed for example in situations where such an investigation is practical and available. This type of study can involve instrumentation and examination of inputs and outputs to the system. Subsystem analysis is a similar type of study that is particularly pertinent to situations where interest is more focused or where the complexity of the whole system is such that makes this approach unavoidable. Included in this type of investigation is single component analysis but beyond this is sub-component investigations possibly related to material characterisation and behaviour with the intended aim being the development of sophisticated constitutive equations. There exists however other forms of experimental investigation that involve the physical representation of a system but at a reduced scale. This approach although having the advantage of reduced cost can suffer uncertainties since it is recognised to be affected by scale effects, which can diminish the benefits offered. Design of scaled experiments is aided by the theory of dimensional analysis, which is founded on an

invariance principle, where it is assumed that the dimensionless governing equations do not change with scale [15]. A particular advantage of dimensional analysis is the characterisation of dominant physics by a pertinent subset of dimensionless parameters, i.e. the Pi groups [16][17]. A severe disadvantage however is the reliance on an invariance principle that in all but the most rudimentary of systems seldom applies [7][18]. In a situation where scale effects are significant then dimensional analysis provides no solution and it would appear also that scaled experimentation provides little benefit either [19]. This is presently the situation but recently a new theory has emerged that unlike dimensional analysis embraces scale effects in the sense that it assumes these are present and attempts to accommodate their presence. The new approach is called *finite similitude* and is founded on the metaphysical concept of space scaling [20][21][22][23][24][25]. The word ”metaphysical” is applied here in the sense that it cannot be achieved practically but can be imagined and mathematically defined. It is evident that space scaling cannot be done practically (hence metaphysical) but its effect on governing equations can be interrogated to reveal what scale dependencies are present. The focus on space naturally leads to a focus on physical descriptions that relate to a portion of space (i.e. a control volume). The basic idea is the representation of the governing physics pertaining to a trial space (where the scaled experiment resides) in the physical space (where the full-scale experiment resides). This representation has

the effect of qualifying scale dependencies either explicitly or implicitly. Geometrical measures such as vol- ume and area are explicitly revealed yet other scalar, vector and tensor fields are implicit. The problem of scaling in this formulation effectively reduces to finding a means to reveal the implicit scale dependencies. This paper focuses on an alternative scaled invariance for doing this, which involves scaled experimentation at two distinct scales. A particular novel aspect of the study is the modelling of the two scaled experiments with discrete elements which leads to connected continuous dynamical systems. Of principle interest is the lifting of information from these two scaled systems to the physical space along with the implications the process has on experimental design and process parameters. The focus here on discrete systems addresses two particular weaknesses with the application of the new similitude rules. Firstly, they provide a quick and convenient vehicle for setting free similitude parameters, which are required to be set in order to link scaled experiments. Secondly, they provide the

means to check the appropriateness of a particular similitude identity for a scaled experimental trial. A particular difficulty with the similitude approach is that there is no guarantee that the results obtained from a series of scaled experiments belong to a particular similitude identity. It is shown in the paper how discrete systems provide the means to investigate the fitness of a similitude rule prior to any experiments being performed. It is recognised that discrete systems are approximate representations but also it is clear from the open literature and the works mentioned above that they have a place in the analysis of continuous structural systems. The work presented here builds on the benefits offered by this approach to connect scaled experiments in an efficient manner. The concept of metaphysical space scaling is discussed in Sec. 2, where anisotropic scaling [26] is mentioned but the principal focus is on isotropic scaling. Coordinate systems are introduced pertaining to two inertial frames, one residing in the physical space and the other in the trial space. The focus on space naturally leads to the control volume concept, i.e. a moving/deforming region of space and the kinematics of a control volume is presented in Sec. 2.2. Mechanics in transport form is introduced in Sec. 2.3, where the important step of projecting trial-space transport equations onto the physical space is considered. This particular mathematical process has the effect of exposing scale dependencies and is critical to the whole approach. In Sec. 3 it is demonstrated how it is possible reveal hidden-scale dependencies by defining different forms of similarity (termed *zeroth-order* and *first-order finite similitude*). In Sec. 4 the theory is applied to a linear mass-spring-dashpot system to reveal that no improvement is provided by first-order for these relatively simple systems. Scale dependencies in springs and dashpots are investigated both analytically and numerically in Sec. 5; the difference between structural and viscous damping is revealed. Finally, first-order systems are examined in Sec. 6 to reveal the benefits of a second scaled experiment for systems involving friction forces. The paper ends with a list of conclusions.

2. Recapping the finite similitude theory

The theoretical foundations underpinning finite similitude were first introduced by Davey et al. in reference [20] and subsequently applied to impact mechanics [23][24][27], biomechanics [22][28], powder compaction [21] and metal forming [29] but it is convenient nonetheless to recap the ideas here prior to extending the approach to discrete mechanical systems. The theory of finite similitude begins with

the imagined concept of space scaling, which can be quantified by relating the coordinate coefficients in the physical space x^i_{ps} to those in the trial space x^i_{ts}. In essence an affine mapping of the form $\mathbf{x}_{ps} \mapsto \mathbf{x}_{ts}$ is assumed to exist, which in differential terms is of the form $\mathrm{d}\mathbf{x}_{ts} = \mathrm{F} \cdot \mathrm{d}\mathbf{x}_{ps}$ or equivalently $d\,x^i_{ts} = F^i_j\, d\,x^i_{ps}$, where $F^i_j = \partial x^i_{ts} \big/ \partial x^j_{ps}$. The basic idea is presented in a 2-D frame in Fig. 1, where allowance is also made for time running at a different rate in the two spaces. Formally, the map $t_{ps} \mapsto t_{ts}$ is assumed to exist, which in differential terms is $dt_{ts} = g dt_{ps}$, where g is assumed both temporally and spatially invariant. Shown in the figure is the unit vector basis associated with the inertial frames for the two spaces, i.e. $\{\underline{G}_i\}$ and $\{\underline{g}_i\}$. It is important to appreciate that scaled experimentation is from the viewpoint of an external observer, so scaling of the basis vectors is not a feature and it is assumed here that $\underline{G}_i = \underline{g}_i$.

2.1. Isotropic Scaling

Under the assumption that the two frames $\{\underline{G}_i\}$ and $\{\underline{g}_i\}$ are orthonormal, then the restriction $F = \beta I$ is termed isotropic space scaling with $\beta > 0$ and I a unit matrix. The parameter β as illustrated in Fig.1 quantifies the extent of the scaling involved with $\beta < 1$ for contraction, $\beta = 1$ indicating no scaling, and $\beta > 1$ for expansion. Shown in Fig. 1 is the effect space scaling has on a simply dynamic system and clocks are included to emphasise that time can run at different rates in the spaces. Note also that anisotropic space scaling is possible, where geometric similarity as it is traditional known is lost, but this aspect is not explored further here (further details can be found in reference [26]). It is apparent though that even at this early stage that space scaling provides certain advantages over dimensionless approaches as it made clear in an intuitive physical sense how scaling is being achieved be it isotropic or anisotropic.

The focus in this paper is on the situation involving two scaled experiments at distinct scales β_1 and β_2 as illustrated in Fig. 1. The idea being that by some means the behaviour of the two scaled experiments are to be combined to produce the expected behaviour of a full-scale system at $\beta = \beta_0 = 1$. The theory underpinning the

combination of scaled experimentation is presented in subsequent sections but first it is necessary to consider the effect scaling has on control-volume kinematics.

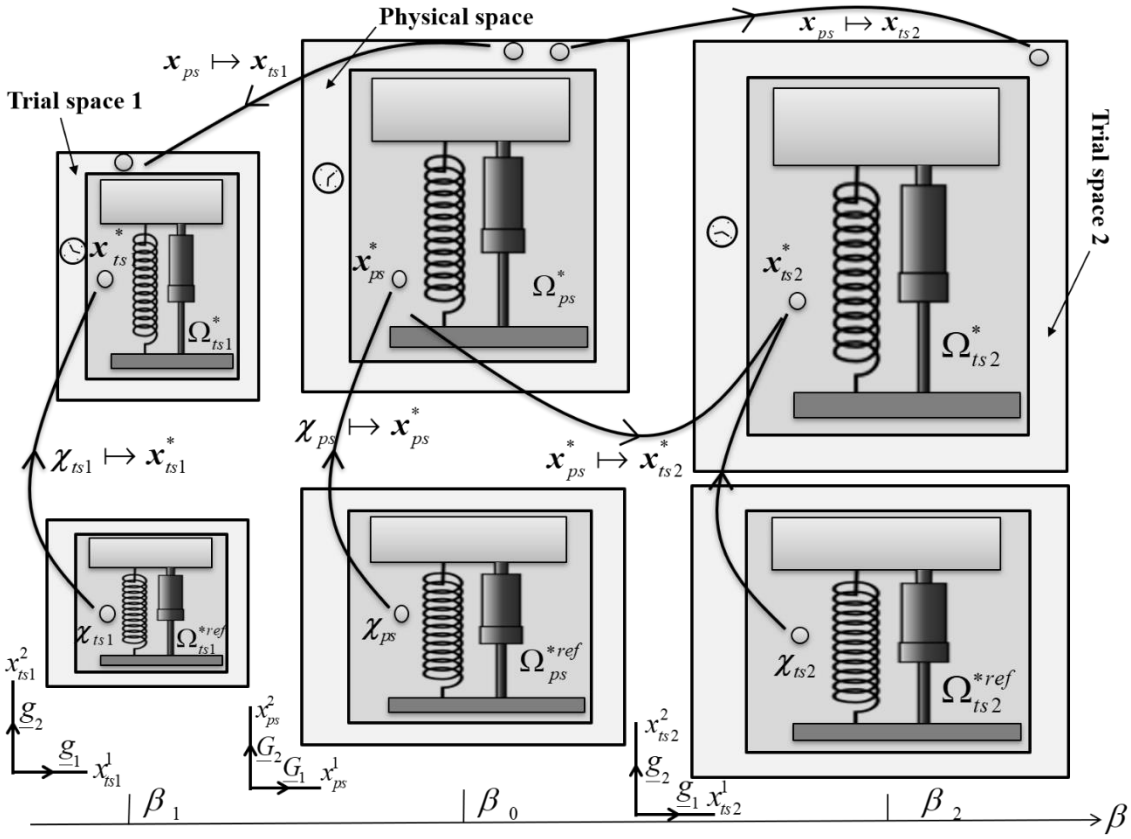

Figure 1: Inertial coordinate systems for physical and trial spaces where each space includes both reference and current moving control volumes, which here are tracking a moving and vibrating system. The geometric scaling factors and dictate the extent of the space scaling involved. The various maps depicted include maps between spatial points, and control volumes in different spaces along with reference

2.2. Kinematics of a moving control volume

To investigate the relationships between scaled experimentation and full-scale systems necessitates a description of the underpinning mechanics that is readily influenced by the act of scaling; in particular it must incorporate geometrical measures. A natural description therefore is a control-volume approach, where physical transfers are defined and related on a moving distorting region of space. The focus on space and control-volume descriptions may at first sight appear somewhat remote from the multi-body dynamics involving discrete elements that is the focus of this study. However, space considerations ultimately lead to point-based

identities and therefore to descriptions that are commonly applied in a Lagrangian frame of reference.

The motion of a control volume in the trial space is described here by means of the velocity field $\mathbf{v}_{ts}^{*}$, which itself is definable in terms of the temporal derivative $\frac{D^{*}}{D^{*}t_{ts}} = \left.\frac{\partial}{\partial t_{ts}}\right|_{\chi_{ts}}$ where χ_{ts} is a coordinate point in reference control volume Ω_{ts}^{*ref}. The basic idea is depicted in Fig. 1, where the motion of control volume Ω_{ts}^{*} is portrayed relative to the stationary reference control volume Ω_{ts}^{*ref}. The motion of the control volume Ω_{ts}^{*} is described by two equivalent means, first as the map $\left(\chi_{ts}, t_{ts}\right) \mapsto \mathbf{x}_{ts}^{*}$, where $\chi_{ts} \in \Omega_{ts}^{*ref}$, and second as the solution to the differential equation

$$\frac{D^{*}\mathbf{x}_{ts}^{*}}{D^{*}t_{ts}} = \mathbf{v}_{ts}^{*} \tag{1}$$

with $\mathbf{x}_{ts}^{*}$ being a point attached to the control volume and $\mathbf{v}_{ts}^{*}$ specified along with initial conditions. The unique solution to this differential equation for appropriate initial conditions is guaranteed by Frobenius's theorem. With the apparatus for the motion of a control volume in the trial space now defined, attention turns to its connectivity in the physical space. The control volume region effectively acts as a lens for that part of the trial space that is to be examined. It can be made as small or as large as required and can in principle be composed of many parts. The exact same apparatus can be defined for the physical space with

$$\frac{D^{*}\mathbf{x}_{ps}^{*}}{D^{*}t_{ps}} = \mathbf{v}_{ps}^{*} \tag{2}$$

where $\mathbf{x}_{ps}^{*}$ being a point attached to the control volume in the physical space and to reflect that fact that space scaling is involved the identity $d\mathbf{x}_{ts}^{*} = \beta d\mathbf{x}_{ps}^{*}$ is assumed to apply.

Note the similarity between the space identity $d\mathbf{x}_{ts} = \beta d\mathbf{x}_{ps}$ and that between the control volumes in the two spaces, where unlike the former the latter $d\mathbf{x}_{ts}^{*} = \beta d\mathbf{x}_{ps}^{*}$

relates moving points. Taking into consideration the two time scales involved and the identity $dt_{ts} = g dt_{ps}$ an important velocity field relationship

$$\mathbf{v}^*_{ts} = g^{-1}\beta \mathbf{v}^*_{ps} \tag{3}$$

is found to apply, which confers synchronous motion on the controls in the two spaces. Greater detail on this is available in reference [20] but with the kinematics of the two moving control volumes defined it is now possible to examine the critical equations in scaled dynamics.

2.3. Scaled mechanics in transport form

Particular transport equations pertinent to mechanics are introduced in this section. Volume conservation forms part of the discussion along with mass, although hardly critical to solid mechanics they do feature in finite similitude. Six additional equations are needed, three describing the critical conservation law of momentum and three concerned with the non-conserved concept of movement. Movement (first introduced in reference [30]) like volume is not common to classical work due to its elementary nature but included nonetheless to bring the displacement field into the family of transport equations. The transport equations of interest are:

$$\frac{D^*}{D^* t_{ts}} \int_{\Omega^*_{ts}} dV^*_{ts} = \int_{\Gamma^*_{ts}} \mathrm{v}^*_{ts} \cdot \mathbf{n}_{ts} d\Gamma^*_{ts} \tag{4a}$$

$$\frac{D^*}{D^* t_{ts}} \int_{\Omega^*_{ts}} \rho_{ts} dV^*_{ts} + \int_{\Gamma^*_{ts}} \rho_{ts} \left(\mathbf{v}_{ts} - \mathbf{v}^*_{ts} \right) \cdot \mathbf{n}_{ts} d\Gamma^*_{ts} = 0 \tag{4b}$$

$$\frac{D^*}{D^* t_{ts}} \int_{\Omega^*_{ts}} \rho_{ts} \mathbf{v}_{ts} dV^*_{ts} + \int_{\Gamma^*_{ts}} \rho_{ts} \mathbf{v}_{ts} \left(\mathbf{v}_{ts} - \mathbf{v}^*_{ts} \right) \cdot \mathbf{n}_{ts} d\Gamma^*_{ts} - \int_{\Gamma^*_{ts}} \sigma_{ts} \cdot \mathbf{n}_{ts} d\Gamma^*_{ts} - \int_{\Omega^*_{ts}} \rho_{ts} \mathbf{b}^{\nu}_{ts} dV^*_{ts} = 0 \tag{4c}$$

$$\frac{D^*}{D^* t_{ts}} \int_{\Omega^*_{ts}} \rho_{ts} \mathbf{u}_{ts} dV^*_{ts} + \int_{\Gamma^*_{ts}} \rho_{ts} \mathbf{u}_{ts} \left(\mathbf{v}_{ts} - \mathbf{v}^*_{ts} \right) \cdot \mathbf{n}_{ts} d\Gamma^*_{ts} - \int_{\Omega^*_{ts}} \rho_{ts} \mathbf{v}_{ts} dV^*_{ts} = 0 \tag{4d}$$

where ρ_{ts} is mass density, σ_{ts} is Cauchy stress, $\mathbf{u}_{ts}$ is displacement, $\mathbf{b}^{\nu}_{ts}$ represents specific-body force (i.e. force per unit mass), and $\mathbf{n}_{ts}$ is the outer pointing unit normal on the boundary Γ^*_{ts} of control volume Ω^*_{ts}. The basic idea is to project scaled versions of these equations into the physical space, which is achieved on

substitution of $dV_{ts}^{*}=\beta^{3}dV_{ps}^{*}$, $\mathbf{n}_{ts}d\Gamma_{ts}^{*}=\beta^{2}\mathbf{n}_{ps}d\Gamma_{ps}^{*}$ and and on multiplication by g and respectively $\alpha_0^1,\alpha_0^\rho,\alpha_0^\nu$ and α_0^u to provide

$$\alpha_0^1 T_0^1(\beta)=\frac{D^*}{D^* t_{ps}}\int_{\Omega_{ps}^*}\alpha_0^1\beta^3 dV_{ps}^*-\int_{\Gamma_{ps}^*}\alpha_0^1\beta^3\mathbf{v}_{ps}^*\cdot\mathbf{n}_{ps}d\Gamma_{ps}^*=0 \tag{5a}$$

$$\alpha_0^\rho T_0^\rho(\beta)=\frac{D^*}{D^* t_{ps}}\int_{\Omega_{ps}^*}\alpha_0^\rho\beta^3\rho_{ts}dV_{ps}^*+\int_{\Gamma_{ps}^*}\alpha_0^\rho\beta^3\rho_{ts}\left(\mathbf{V}_{ps}-\mathbf{v}_{ps}^*\right)\cdot\mathbf{n}_{ps}d\Gamma_{ps}^*=0 \tag{5b}$$

$$\alpha_0^\nu T_0^\nu(\beta)=\frac{D^*}{D^* t_{ps}}\int_{\Omega_{ps}^*}\left(\alpha_0^\nu g^{-1}\beta\right)\beta^3\rho_{ts}\mathbf{V}_{ps}dV_{ps}^*+\int_{\Gamma_{ps}^*}\left(\alpha_0^\nu g^{-1}\beta\right)\beta^3\rho_{ts}\mathbf{V}_{ps}\left(\mathbf{V}_{ps}-\mathbf{v}_{ps}^*\right)\cdot\mathbf{n}_{ps}d\Gamma_{ps}^*-$$
$$\int_{\Gamma_{ps}^*}\alpha_0^\nu g\beta^2\sigma_{ts}\cdot\mathbf{n}_{ps}d\Gamma_{ps}^*-\int_{\Omega_{ts}^*}\alpha_0^\nu g\beta^3\mathbf{b}_{ts}^\nu\mathbf{V}_{ps}dV_{ps}^*=0 \tag{5c}$$

$$\alpha_0^u T_0^u(\beta)=\frac{D^*}{D^* t_{ps}}\int_{\Omega_{ps}^*}\left(\alpha_0^u\beta\right)\beta^3\rho_{ts}\mathbf{U}_{ps}dV_{ps}^*+\int_{\Gamma_{ps}^*}\left(\alpha_0^u\beta\right)\beta^3\rho_{ts}\mathbf{U}_{ps}\left(\mathbf{V}_{ps}-\mathbf{v}_{ps}^*\right)\cdot\mathbf{n}_{ps}d\Gamma_{ps}^*-$$
$$-\int_{\Omega_{ts}^*}\left(\alpha_0^u\beta\right)\beta^3\rho_{ts}\mathbf{V}_{ps}dV_{ps}^*=0 \tag{5d}$$

where $\mathbf{V}_{ps}=\beta^{-1}g\mathbf{v}_{ts}$, $\mathbf{U}_{ps}=\beta^{-1}\mathbf{u}_{ts}$ and critically important scalars $\alpha_0^1,\alpha_0^\rho,\alpha_0^\nu$ and α_0^u (whose role is made clear below) along with g are assumed to be functions of β.

Eqs. (5) capture scaling from a somewhat different perspective, where the dependency on β is either explicitly or implicitly exposed. The presence of β^3 and β^2 is explicit arising from geometrical measures, but implicit is the behaviour of the fields, i.e. $\mathbf{V}_{ps}(\beta)$, $\mathbf{U}_{ps}(\beta)$, $\sigma_{ts}(\beta)$ and so on. The scaling problem has been transformed into one where the objective is to discover hidden $\beta-$dependencies. There are two routes to uncovering hidden behaviours, with one requiring additional information arising from the physics of the problem under study (i.e. size effects, boundary conditions etc.) or another with the application of scale invariances; this latter approach is the focus of this paper.

3. Finite similitude identities

The application of scale invariances to Eqs. (5) is in many respects about assuming how things are changing with β, which for an arbitrary problem will invariably be incorrect. A question of some interest however is whether it is possible to design scaled experiments to satisfy the scale invariance applied. The problem becomes one of design-of-experiments and the scaled invariance provides the vehicle for this design process.

The approach adopted here is the establishment of differential identities where Eqs. (5) are to be differentiated with respect to β. The" initial conditions" for this process are deemed to be at $\beta = \beta_0 = 1$, which immediately impacts on Eqs. (5), which must match the physical-space equations at β_0. The following identities follow on examination of these equations: $\alpha_0^1(1) = \alpha_0^\rho(1) = \alpha_0^\nu(1) = \alpha_0^u(1)$ along with $g(1) = 1$ since $dt_{ts}(1) = g(1)\,dt_{ps}$ and $\rho_{ts}(1) = \rho_{ps}$, $\mathbf{V}_{ps}(1) = \mathbf{v}_{ps}$, $\mathbf{U}_{ps}(1) = \mathbf{u}_{ps}$, $\sigma_{ts}(1) = \sigma_{ps}$ and so on for other fields. The first scale invariance of interest is the one that is the most obvious and is where Eqs. (5) have no variation with respect to β, which in mathematical terms is simply

$$\frac{d}{d\beta}\left(\alpha_0^\psi T_0^\psi\right) \equiv 0 \tag{6}$$

where ψ can be set to $1, \rho, \nu$ or u and the equality sign "≡" means that the transport equation is identically zero; the satisfaction of this identity is termed *zeroth-order finite similitude*.

Note that integration of this equation between the limits β_0 and $\beta_1 = 1$ provides $\alpha_0^\psi T_0^\psi(\beta_1) \equiv \alpha_0^\psi T_0^\psi(1) = T_0^\psi(1)$. This equality is essentially what dimensional analysis provides as it effectively confirms that the trial-space transport equations do not change with scale. Here, no attempt is made to form dimensionless equations as the scalars α_0^ψ are providing the means to treat all the transport equations in a unified manner. The significant advantage of the finite similitude approach is that it is not limited to a single invariance and Eqs. (5) are purposely of a form that embraces scale effects. Eq. (6) is the case were

scale effects are assumed absent but in most cases this is not satisfied and $\alpha_0^{\psi} T_0^{\psi}$ changes with β. A natural way forward in this case is to set $T_1^{\psi} = \frac{d}{d\beta}\left(\alpha_0^{\psi} T_0^{\psi}\right)$ and scale these equations with a new set of scalars α_1^{ψ} and consider the identity

$$\frac{d}{d\beta}\left(\alpha_1^{\psi} T_1^{\psi}\right) = \frac{d}{d\beta}\left(\alpha_1^{\psi} \frac{d}{d\beta}\left(\alpha_0^{\psi} T_0^{\psi}\right)\right) \equiv 0 \tag{7}$$

which when satisfied is termed *first-order finite similitude*.

Although higher-order forms are evidently possibly following the same pattern (i.e. setting $T_2^{\psi} = \frac{d}{d\beta}\left(\alpha_1^{\psi} T_1^{\psi}\right)$, etc.), focus here is limited Eq. (7) as it will become apparent that two scaled experiments are involved in this case. Two features are important to note and the first is that zeroth-order solutions are contained within the set of first-order ones since any solution of Eq. (6) automatically satisfies Eq. (7). Second, the form of Eq. (7) for arbitrary differentiable α_1^{ψ} (as a function of β) can represent any linear combination of the derivatives of the $\alpha_0^{\psi} T_0^{\psi}$ up to second order at any arbitrary point β_1. This is relatively easy to prove and its importance lies in the irrelevance of alternative identities that contain derivatives of $\alpha_0^{\psi} T_0^{\psi}$.

3.1. The first-order solution to scaling

As mentioned above in the context of Eqs. (5), scaling is solved once all $\beta-$ dependencies are revealed. The definition Eq. (7) is designed for the purpose of revealing said dependencies but in the absence of know behaviours (size effects, boundary changes) is unlikely to capture such changes. In the context of physical modelling, Eq. (7) has the potential to facilitate the design of these experiments. In order to do this however Eq. (7) is required to be replaced by a discrete form but prior to that it is prudent to consider first the outcomes from trying to satisfy Eq. (6).

Note then that Eq. (5a) satisfies identity Eq. (6) with $\psi = 1$ on setting uniquely $\alpha_0^1 = \beta^{-3}$, which evidently satisfies $\alpha_0^1(1) = 1$. In fact $\alpha_0^1 = \beta^{-3}$ is a necessary and sufficient solution for Eq. (6) and consequently Eq. (5a) is automatically satisfied in first-order theory. It is worth mentioning here that this result is

facilitated by Eq. (3) and in fact enforces this condition. Turning attention now to Eq. (5b) a necessary (although not sufficient) condition for satisfying Eq. (6) with $\psi = \rho$ is $\rho_{ps} = \alpha_0^{\rho}\beta^3\rho_{ts}$. Similarly for Eq. (5c) a necessary (but not sufficient) condition is $\alpha_0^{v} = g\beta^{-1}\alpha_0^{\rho}$. Likewise Eq. (5d) requires $\alpha^{u} = \beta^{-1}\alpha_0^{\rho}$ or alternatively $\alpha_0^{v} = g\alpha_0^{u}$. The identities: $\rho_{ps} = \alpha_0^{\rho}\beta^3\rho_{ts}$, $\alpha_0^{v} = g\beta^{-1}\alpha_0^{\rho}$ and $\alpha^{u} = \beta^{-1}\alpha_0^{\rho}$ are taken forward to first-order theory. Note that these scalars are set in an attempt to eliminate β from transport Eqs. (5b)

to (5d). Similarly, therefore, α_1^{ψ} has an identical role to play but for the transport equations $\alpha_1^{\psi}T_1^{\psi} = 0$ with $\alpha_1^{\psi}(1) = 1$, hence providing further justification for the form of identity Eq. (7).

The solving of first-order finite similitude requires the integration of Eq. (7), which happens to be of a form that is ideal for the application of divided differences. Note first the identity

$$\alpha_1^{\psi}T_1^{\psi}\left(\beta_2^1\right) = \alpha_1^{\psi}\frac{d}{d\beta}\left(\alpha_0^{\psi}T_0^{\psi}\right)\left(\beta_2^1\right) \equiv \alpha_1^{\psi}\left(\beta_2^1\right)\frac{\alpha_0^{\psi}T_0^{\psi}\left(\beta_1\right) - \alpha_0^{\psi}T_0^{\psi}\left(\beta_2\right)}{\beta_1 - \beta_2} \qquad (8a)$$

$$\alpha_1^{\psi}T_1^{\psi}\left(\beta_1^0\right) = \alpha_1^{\psi}\frac{d}{d\beta}\left(\alpha_0^{\psi}T_0^{\psi}\right)\left(\beta_1^0\right) \equiv \alpha_1^{\psi}\left(\beta_1^0\right)\frac{\alpha_0^{\psi}T_0^{\psi}\left(\beta_0\right) - \alpha_0^{\psi}T_0^{\psi}\left(\beta_1\right)}{\beta_0 - \beta_1} \qquad (8b)$$

with $\beta_2 \le \beta_2^1 \le \beta_1$, $\beta_1 \le \beta_1^0 \le \beta_0$, where a mean-value theorem is utilised to provide exact identities.

Note however that the first-order assumption means that $\alpha_1^{\psi}T_1^{\psi}\left(\beta_1^0\right) \equiv \alpha_1^{\psi}T_1^{\psi}\left(\beta_2^1\right)$, which on substitution of Eqs. (8) provides

$$\alpha_1^{\psi}\left(\beta_1^0\right)\frac{\alpha_0^{\psi}T_0^{\psi}\left(\beta_0\right) - \alpha_0^{\psi}T_0^{\psi}\left(\beta_1\right)}{\beta_0 - \beta_1} \equiv \alpha_1^{\psi}\left(\beta_2^1\right)\frac{\alpha_0^{\psi}T_0^{\psi}\left(\beta_1\right) - \alpha_0^{\psi}T_0^{\psi}\left(\beta_2\right)}{\beta_1 - \beta_2} \qquad (9)$$

which after some manipulation provides

$$\alpha_0^{\psi}T_0^{\psi}\left(\beta_0\right) \equiv \alpha_0^{\psi}T_0^{\psi}\left(\beta_1\right) + R_1^{\psi}\left(\alpha_0^{\psi}T_0^{\psi}\left(\beta_1\right) - \alpha_0^{\psi}T_0^{\psi}\left(\beta_2\right)\right) \qquad (10)$$

where

$$R_1^{\psi} = \left(\frac{\alpha_1^{\psi}\left(\beta_2^1\right)}{\alpha_1^{\psi}\left(\beta_1^0\right)} \right) \left(\frac{\beta_0 - \beta_1}{\beta_1 - \beta_2} \right) \tag{11}$$

And it is recognized that R_1^{ψ} takes the form of a parameter since α_1^{ψ} remains indeterminate.

3.2. First order field relationships

A feature of transport Eqs. (5c) to (5d) is a relative transfer flux of the form $\left(\mathbf{V}_{ps} - \mathbf{v}_{ps}^{*}\right) \cdot \mathbf{n}$ at the boundary of each equation. With focus on solid dynamics as opposed to fluid dynamics and in order to avoid higher forms of similitude it is reasonable to approximate this expression with $\left(\mathbf{v}_{ps} - \mathbf{v}_{ps}^{*}\right) \cdot \mathbf{n}$. With this approximation in place the application of Eq. (10) to transport Eqs. (5b) to (5d) provides relationships of the form

$$\mathbf{v}_{ps} = \mathbf{V}_{ps}\left(\beta_1\right) + R_1^{\rho}\left(\mathbf{V}_{ps}\left(\beta_1\right) - \mathbf{V}_{ps}\left(\beta_2\right)\right) \tag{12a}$$

$$\mathbf{v}_{ps} = \mathbf{V}_{ps}\left(\beta_1\right) + R_1^{v}\left(\mathbf{V}_{ps}\left(\beta_1\right) - \mathbf{V}_{ps}\left(\beta_2\right)\right) \tag{12b}$$

$$\sigma_{ps} = \mathbf{\Sigma}_{ps}\left(\beta_1\right) + R_1^{v}\left(\mathbf{\Sigma}_{ps}\left(\beta_1\right) - \mathbf{\Sigma}_{ps}\left(\beta_2\right)\right) \tag{12c}$$

$$\mathbf{b}_{ps} = \mathbf{B}_{ps}\left(\beta_1\right) + R_1^{v}\left(\mathbf{B}_{ps}\left(\beta_1\right) - \mathbf{B}_{ps}\left(\beta_2\right)\right) \tag{12d}$$

$$\mathbf{u}_{ps} = \mathbf{U}_{ps}\left(\beta_1\right) + R_1^{u}\left(\mathbf{U}_{ps}\left(\beta_1\right) - \mathbf{U}_{ps}\left(\beta_2\right)\right) \tag{12e}$$

$$\mathbf{v}_{ps} = \mathbf{V}_{ps}\left(\beta_1\right) + R_1^{u}\left(\mathbf{V}_{ps}\left(\beta_1\right) - \mathbf{V}_{ps}\left(\beta_2\right)\right) \tag{12f}$$

where $\mathbf{V}_{ps} = g\beta^{-1}\mathbf{v}_{ts}$, $\mathbf{U}_{ps} = \beta^{-1}\mathbf{u}_{ts}$, $\mathbf{\Sigma}_{ps} = \alpha_0^{v} g\beta^2 \sigma_{ts}$ and $\mathbf{B}_{ps} = g^2\beta^{-1}\mathbf{b}_{ts}$, and for a consistent expression of velocity it is required that $R_1 = R_1^{\rho} = R_1^{v} = R_1^{u}$.

Note how the displacement expression Eq. (12e) is consistent with velocity Eq. (12f), since differentiation of the former with respect to time (i.e. $\frac{D}{Dt_{ps}}$) and substitution of $\frac{D}{Dt_{ps}} = g_1 \frac{D}{Dt_{ts1}} = g_2 \frac{D}{Dt_{ts2}}$ gives the latter, where $g_i = g\left(\beta_i\right)$, $t_{tsi} = t_{ts}\left(\beta_i\right)$ and $\frac{D}{Dt_{ps}}$ means material derivative. The condition $R_1^{\rho} = R_1^{v} = R_1^{u}$ reveals the physical interpretation that Eqs. (10) and (12) infer, i.e. the

differences between transport equations and certain fields are proportional. The theory provides the fields, (i.e. $\mathbf{V}_{ps}$, $\mathbf{U}_{ps}$, $\mathbf{\Sigma}_{ps}$ and $\mathbf{B}_{ps}$) and the result is evidently a departure from dimensional analysis and zeroth-order finite similitude, which involve proportional fields only. Note additionally that all the differences in the right-hand bracket in Eqs. (12) are identically zero if zeroth-order happens to apply as is required.

4. Similitude for mass-spring-dashpot components

The important identities pertinent to dynamics are provided in Tab. 1, where included for completeness is the small strain relationship, which is derivable from the displacement identity (12e) on division by $dx^i_{ps} = \beta_1^{-1} dx^i_{ts1} = \beta_2^{-1} dx^i_{ts2}$.

Table 4:1: Important finite-similitude identities for zeroth and first-order.

Properties	Zeroth-order	First-order identities
Density	$\rho_{ps} = \alpha^{\rho}_{01} \rho_{ts1} \beta_1^3$	$\rho_{ps} = \alpha^{\rho}_{01} \rho_{ts1} \beta_1^3 + R_1 \left(\alpha^{\rho}_{01} \rho_{ts1} \beta_1^3 - \alpha^{\rho}_{02} \rho_{ts2} \beta_2^3 \right)$
Displacement	$\mathbf{u}_{ps} = \beta_1^{-1} \mathbf{u}_{ts1}$	$\mathbf{u}_{ps} = \beta_1^{-1} \mathbf{u}_{ts1} + R_1 \left(\beta_1^{-1} \mathbf{u}_{ts1} - \beta_2^{-1} \mathbf{u}_{ts2} \right)$
Velocity	$\mathbf{v}_{ps} = g_1 \beta_1^{-1} \mathbf{v}_{ts1}$	$\mathbf{v}_{ps} = \beta_1^{-1} g_1 \mathbf{v}_{ts1} + R_1 \left(\beta_1^{-1} g_1 \mathbf{v}_{ts1} - \beta_2^{-1} g_2 \mathbf{v}_{ts2} \right)$
Acceleration	$\mathbf{a}_{ps} = \beta_1^{-1} g_1^2 \mathbf{a}_{ts1}$	$\mathbf{a}_{ps} = \beta_1^{-1} g_1^2 \mathbf{a}_{ts1} + R_1 \left(\beta_1^{-1} g_1^2 \mathbf{a}_{ts1} - \beta_2^{-1} g_2^2 \mathbf{a}_{ts2} \right)$
Strain	$\varepsilon_{ps} = \varepsilon_{ts1}$	$\varepsilon_{ps} = \varepsilon_{ts1} + R_1 \left(\varepsilon_{ts1} - \varepsilon_{ts2} \right)$
Stress	$\sigma_{ps} = \alpha^{\rho}_{01} g_1^2 \beta_1 \sigma_{ts1}$	$\sigma_{ps} = \alpha^{\rho}_{01} g_1^2 \beta_1 \sigma_{ts1} + R_1 \left(\alpha^{\rho}_{01} g_1^2 \beta_1 \sigma_{ts1} - \alpha^{\rho}_{02} g_2^2 \beta_2 \sigma_{ts2} \right)$
Force	$\mathbf{F}_{ps} = \alpha^{v}_{01} g_1 \mathbf{F}_{ts1}$	$\mathbf{F}_{ps} = \alpha^{v}_{01} g_1 \mathbf{F}_{ts1} + R_1 \left(\alpha^{v}_{01} g_1 \mathbf{F}_{ts1} - \alpha^{v}_{02} g_2 \mathbf{F}_{ts2} \right)$

In a mass-spring-dashpot system (in the trial space) the damping force $\mathbf{F}^d_{ts} = -c_{ts} \mathbf{v}_{ts}$ and spring force $\mathbf{F}^s_{ts} = -k_{ts} \mathbf{u}_{ts}$ act along with the inertial "force" $\mathbf{F}^i_{ts} = m_{ts} \mathbf{a}_{ts}$. The scaling identity for force in Tab. 1 indicates how these forces should be treated. Multiplication throughout by $\alpha^v_0 g$ provides after some reorganisation $a^v_0 g \mathbf{F}^d_{ts} = -\left(a^v_0 \beta c_{ts} \right) \left(g \beta^{-1} \mathbf{v}_{ts} \right)$, $a^v_0 g \mathbf{F}^s_{ts} = -\left(a^v_0 g \beta k_{ts} \right) \left(\beta^{-1} \mathbf{u}_{ts} \right)$ and $a^v_0 g \mathbf{F}^i_{ts} = \left(a^v_0 g^{-1} \beta m_{ts} \right) \left(\beta^{-1} g^2 \mathbf{a}_{ts} \right)$ and recall that $a^v_0 g^{-1} \beta = a^{\rho}_0$ and consequentially

the inertial force equation reduces to $a_0^{\nu} g \mathbf{F}_{ts}^{i} = \left(a_0^{\rho} m_{ts}\right)\left(\beta^{-1} g^{2} \mathbf{a}_{ts}\right)$. The first-order theory endeavours (in this case) to combine the two equations

$$m_{ts1}\mathbf{a}_{ts1} + c_{ts}\mathbf{v}_{ts1} + k_{ts1}\mathbf{u}_{ts1} = 0 \tag{13a}$$

$$m_{ts1}\mathbf{a}_{ts2} + c_{ts}\mathbf{v}_{ts2} + k_{ts2}\mathbf{u}_{ts2} = 0 \tag{13b}$$

by first multiplying by $a_{01}^{\nu} g_1$ and $a_{02}^{\nu} g_2$, respectively and then forming

$$\begin{aligned}
&\left[\left(a_{01}^{\rho} m_{ts1}\right)\left(\beta_1^{-1} g_1^{2} \mathbf{a}_{ts1}\right) + R_1\left(\left(a_{01}^{\rho} m_{ts1}\right)\left(\beta_1^{-1} g_1^{2} \mathbf{a}_{ts1}\right) - \left(a_{02}^{\rho} m_{ts2}\right)\left(\beta_2^{-1} g_2^{2} \mathbf{a}_{ts2}\right)\right)\right] + \\
&\left[\left(a_{01}^{\nu} \beta_1 c_{ts1}\right)\left(\beta_1^{-1} g_1 \mathbf{v}_{ts1}\right) + R_1\left(\left(a_{01}^{\nu} \beta_1 c_{ts1}\right)\left(\beta_1^{-1} g_1 \mathbf{v}_{ts1}\right) - \left(a_{02}^{\nu} \beta_2 c_{ts2}\right)\left(\beta_2^{-1} g_2 \mathbf{v}_{ts2}\right)\right)\right] + \\
&\left[\left(a_{01}^{\nu} g_1 k_{ts1}\right)\left(\beta_1^{-1} \mathbf{u}_{ts1}\right) + R_1\left(\left(a_{01}^{\nu} g_1 k_{ts1}\right)\left(\beta_1^{-1} \mathbf{u}_{ts1}\right) - \left(a_{02}^{\nu} g_2 k_{ts2}\right)\left(\beta_2^{-1} \mathbf{u}_{ts2}\right)\right)\right] = 0
\end{aligned} \tag{14}$$

in an attempt to match the equation

$$m_{ps}\mathbf{a}_{ps} + c_{ps}\mathbf{v}_{ps} + k_{ps}\mathbf{u}_{ps} = 0 \tag{15}$$

Which provides the following identities

$$\mathbf{a}_{ps} = \left(\alpha_{01}^{\rho} \tfrac{m_{ts1}}{m_{ps}}\right)\left(\beta_1^{-1} g_1^{2} \mathbf{a}_{ts1}\right) + R_1\left(\left(\alpha_{01}^{\rho} \tfrac{m_{ts1}}{m_{ps}}\right)\left(\beta_1^{-1} g_1^{2} \mathbf{a}_{ts1}\right) - \left(\alpha_{02}^{\rho} \tfrac{m_{ts2}}{m_{ps}}\right)\left(\beta_2^{-1} g_2^{2} \mathbf{a}_{ts2}\right)\right) \tag{16a}$$

$$\mathbf{v}_{ps} = \left(\alpha_{01}^{\nu} \beta_1 \tfrac{c_{ts1}}{c_{ps}}\right)\left(\beta_1^{-1} g_1 \mathbf{v}_{ts1}\right) + R_1\left(\left(\alpha_{01}^{\nu} \beta_1 \tfrac{c_{ts1}}{c_{ps}}\right)\left(\beta_1^{-1} g_1 \mathbf{v}_{ts1}\right) - \left(\alpha_{02}^{\nu} \beta_2 \tfrac{c_{ts2}}{c_{ps}}\right)\left(\beta_2^{-1} g_2 \mathbf{v}_{ts2}\right)\right) \tag{16b}$$

$$\mathbf{u}_{ps} = \left(\alpha_{01}^{\nu} g_1 \beta_1 \tfrac{k_{ts1}}{k_{ps}}\right)\left(\beta_1^{-1} \mathbf{u}_{ts1}\right) + R_1\left(\left(\alpha_{01}^{\nu} g_1 \beta_1 \tfrac{k_{ts1}}{k_{ps}}\right)\left(\beta_1^{-1} \mathbf{u}_{ts1}\right) - \left(\alpha_{01}^{\nu} g_1 \beta_1 \tfrac{k_{ts1}}{k_{ps}}\right)\left(\beta_1^{-1} \mathbf{u}_{ts1}\right)\right) \tag{16c}$$

but comparison with the corresponding identities in Tab. 1 yields the zeroth-order identities in Tab. 2.

First-order identities for the material properties of the type presented in Tab. 2 offer little advantage for these linear systems as the satisfaction of zeroth-order identities (if possible) will lead to superior outcomes.

Table 4:2: Important material finite-similitude identities for mass-spring-dashpot systems

Properties	Zeroth-order	First-order identities
Mass	$m_{ps} = \alpha_{01}^{\rho} m_{ts1} = \alpha_{02}^{\rho} m_{ts2}$	$m_{ps} = \alpha_{01}^{\rho} m_{ts1} + R_1\left(\alpha_{01}^{\rho} m_{ts1} - \alpha_{02}^{\rho} m_{ts2}\right)$

Damping	$c_{ps} = \alpha_{01}^{v}\beta_1 c_{ts1} = \alpha_{02}^{v}\beta_2 c_{ts2}$	$c_{ps} = \alpha_{01}^{v}\beta_1 c_{ts1} + R_1\left(\alpha_{01}^{v}\beta_1 c_{ts1} - \alpha_{02}^{v}\beta_2 c_{ts2}\right)$
Stiffness	$k_{ps} = \alpha_{01}^{v} g_1 \beta_1 k_{ts1}$	$k_{ps} = \alpha_{01}^{v} g_1 \beta_1 k_{ts1} + R_1\left(\alpha_{01}^{v} g_1 \beta_1 k_{ts1} - \alpha_{02}^{v} g_2 \beta_2 k_{ts2}\right)$

In order to apply an appropriate level of approximation it is necessary to have some some understanding of the scale dependences of m_{ts}, c_{ts} and k_{ts}. In the section that follows it is shown that $c_{ts} = \beta^2 c_{ps}$ or $c_{ts} = \beta c_{ps}$ (or some combination of these two) and $k_{ts} = \beta k_{ps}$.

Consider then replica materials for all models and zeroth-order approximations for all material properties and set $a_0^{\rho} = \beta^{-3}$ to match densities in Tab. 1, which provides $m_{ts} = \beta^3 m_{ps}$, i.e. mass reduces in accordance with volume. Recall the zeroth-order identity $\alpha_0^{v} = g\beta^{-1}\alpha_0^{\rho}$, which becomes $\alpha_0^{v} = g\beta^{-4}$ and consequently $c_{ts} = g^{-1}\beta^3 c_{ps}$, which suggests $g = \beta$ or $g = \beta^2$ but since $k_{ts} = g^{-1}\beta^2 k_{ps}$, it is required therefore to set $g = \beta$. Thus zeroth order conditions are satisfied for $c_{ts} = \beta^2 c_{ps}$, which transpires to be pertinent to structural damping with $g = \beta$. The condition $c_{ts} = \beta c_{ps}$ is possibly countered with the added flexibility provided by using alternative materials (i.e. physical modelling). Application of the first-order approximation for the damping coefficient in Tab. 2 with $\alpha_0^{v} = g\beta^{-4} = \beta^{-3}$ provides

$$R_1 = \frac{1-\beta_1^{-1}}{\beta_1^{-1}-\beta_2^{-1}} \tag{17}$$

but such an approach is approximate and will not provide an exact match.

The reason for this is that zeroth-order conditions for the fields provides in Eq. (14)

$$\begin{aligned}&\left[\left(\alpha_{01}^{\rho} m_{ts1}\right) + R_1\left(\alpha_{01}^{\rho} m_{ts1} - \alpha_{02}^{\rho} m_{ts2}\right)\right]\mathbf{a}_{ps} + \\ &\qquad\left[\left(\alpha_{01}^{v}\beta_1 c_{ts}\right) + R_1\left(\alpha_{01}^{v}\beta_1 c_{ts} - \alpha_{02}^{v}\beta_2 c_{ts}\right)\right]\mathbf{v}_{ps} + \\ &\qquad\qquad\left[\left(\alpha_{01}^{v} g_1\beta_1 k_{ts1}\right) + R_1\left(\alpha_{01}^{v} g_1\beta_1 k_{ts1} - \alpha_{02}^{v} g_2\beta_2 k_{ts2}\right)\right]\mathbf{u}_{ps} = 0\end{aligned} \tag{18}$$

where the first-order identities in Tab. 2 would at first sight confirm the matching of Eqs. (15) and (18).

Unfortunately, zeroth-order conditions for the fields are dependent on zeroth-order conditions for the material properties, i.e. it is not possible to simply assume zeroth-order conditions for the fields as these are constrained by Eqs. (13). On the other hand, application of zeroth-order properties (see Tab. 2) is not constrained by these equations and reduce Eq. (14) to

$$\begin{aligned} m_{ps}\left(\beta_1^{-1}g_1^2\mathbf{a}_{ts1}+R_1\left(\beta_1^{-1}g_1^2\mathbf{a}_{ts1}-\beta_2^{-1}g_2^2\mathbf{a}_{ts2}\right)\right)+ \\ c_{ps}\left(\beta_1^{-1}g_1\mathbf{v}_{ts1}+R_1\left(\beta_1^{-1}g_1\mathbf{v}_{ts1}-\beta_2^{-1}g_2\mathbf{v}_{ts2}\right)\right)+ \\ k_{ps}\left(\beta_1^{-1}\mathbf{u}_{ts1}+R_1\left(\beta_1^{-1}\mathbf{u}_{ts1}-\beta_2^{-1}\mathbf{u}_{ts2}\right)\right) \end{aligned} \tag{19}$$

and the identities in Tab. 1 confirm the match with Eq. (15) and for this case the match is exact although the fields collapse further to zeroth order.

The key to successful scaling of these linear systems is an understanding of scale dependencies and good approximations for zeroth-order entities.

5. Scale dependencies of physical components

Despite the relative complexity involved in arriving at the identities in Tabs. 1 and 2, the application of the finite-similitude theory turns out to be relatively straightforward. However, prior to application of the theory to discrete-mechanical systems it is first necessary to acquire information on how the discrete elements change with scale. This section investigates both analytically and numerically how springs, materials and dashpots are affected by scale.

5.1. Spring dependencies

The zeroth-order finite similitude theory is applied to a mass-spring system consisting (separately) of cylindrical and conical springs with constant pitch and circular wire, which have widespread use in engineering systems. The stiffness k of a cylindrical spring is readily determined using the expression [31],

$$k=\frac{Gd^4}{8D^3n} \tag{20}$$

where G is the shear modulus, D is the mean diameter of the coil, *d* is the wire diameter and *n* is the number of active coils.

Note that unlike the cylindrical springs, which operate predominantly in a linear phase, conical-compression springs possess both linear and nonlinear phases. Stiffness pertaining to the linear phase is readily determined using [32],

$$k = \frac{Gd^4}{2n\left(D_1^2 + D_2^2\right)\left(D_1 + D_2\right)} \tag{21}$$

where D_1 and D_2 are the mean diameter of the smallest and largest active coils, respectively.

Although no analytical solution exists to describe the nonlinear phase precisely, Rodrigues et al. did manage to develop an approximate continuous analytical model to describe the nonlinear load-deflection response of conical-compression springs. In this study the load-deflection response of both spring types is examined using the commercial finite element software ABAQUS, and is compared against know solutions in Figs. 2 and 3. The geometrical dimensions and material proprieties of both springs are detailed in Table 3. The results show that the ABAQUS simulation of the load-deflections are in good agreement with the research of Rodrigues et al. and Yang et al. [31].

The validated finite-element model provides the means to assess the influence of scaling on spring stiffness. This is achieved here by loading the springs at full-size (full scale model) and then by comparing with springs scaled down by $\beta = 0.5$ and scaled up by $\beta = 2$ (see Fig. 5). It is revealed in Fig. 5 for cylindrical springs (and similarly for conical springs) that the stiffness is linearly proportional to β. For the linear phases of the cylindrical and conical springs, using expressions Eqs. (20) and (21), this relationship is immediately apparent on substitution of $d_{ts} = \beta d_{ps}$ and $D_{ts} = \beta D_{ps}$ for the diameters to obtain $k_{ts} = \beta k_{ps}$ (for $G_{ts} = G_{ps}$). Although a linear relationship with β is a convenient it is not sufficient relate the vibration of real mass-spring systems of different sizes; the problem is energy dissipation.

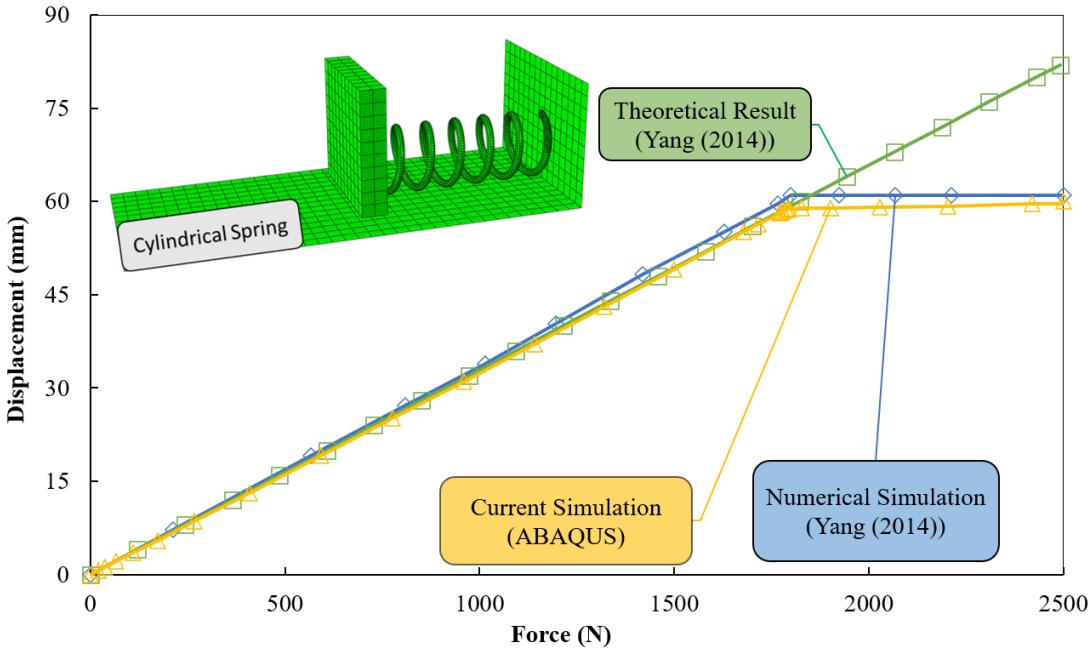

Figure 2: (colour online) Verification of the FE simulation results for the force-deflection of the linear cylindrical spring-mass system by comparison against numerical and analytical results presented in the literature. Based on the mesh sensitivity analysis, the spring CAD model has been discretised using 42777 linear hexahedral (C3D8R) and 19918 quadratic tetrahedral (C3D10) elements. The average number of the elements through the radius of the spring is 3 with average element size of 1 mm.

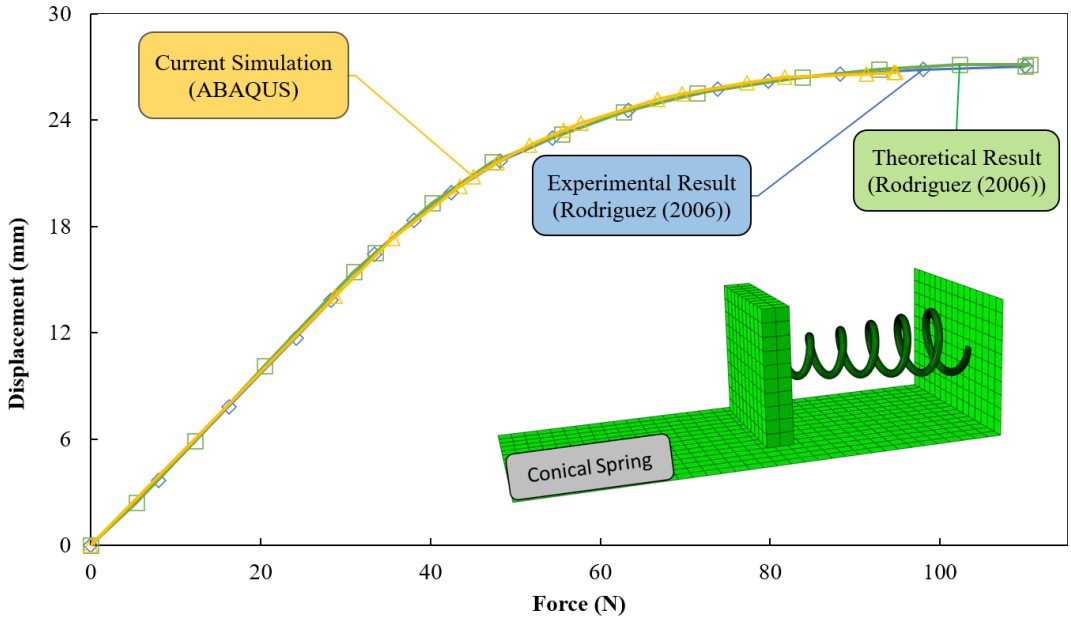

Figure 3: (colour online) Evaluation of the presented numerical results for the linear and nonlinear behaviour of the conical spring-mass system by comparison against numerical and analytical results presented in the literature. In order to guarantee the convergence of the numerical solution and avoid the mesh sensitivity of the results, the minimum number of elements for the discretised conical spring is 47839 with average size of 1 mm. The average number of elements in radial direction is 4 elements.

Table 4:3: Characteristics of both cylindrical and conical springs

Parameters	Cylindrical Spring	Conical Spring
D_1 (mm)	50	8.97
D_2 (mm)	50	13.3
d (mm)	6	1.2
L_0 (mm)	88	37.2
n_a	3.5	7.13
G (MPa)	82030	80000

5.1.1. Structural damping of springs

All engineering structures show some degree of energy dissipation during free vibration due to inherent losses arising from internal friction in structural materials. A convenient pragmatic approach to deal with the complex sources of energy loss is the inclusion of a viscous-type damper to simplify the mathematical treatment [33, 34]. Of interest here is the damping-size dependency of the mass-cylindrical spring system depicted in Fig. 4. For this purpose, ABAQUS analysis is implemented for the three sizes depicted, i.e. the full-size system, the scaled-down system ($\beta = 0.5$) and scaled-up system ($\beta = 2$). The geometrical dimensions, material proprieties and initial conditions of the systems are presented in Tab. 4. Prior to presenting the results of the numerical simulation, it is appropriate to briefly review the analytical framework of the damped free vibrations of a mass-spring system. To account for structural damping of the springs an external damper is added to the spring systems depicted in Fig. 4. The value of the damping coefficients *c* are unknown in these systems but for free vibration the equation of motion is

$$\left(M + \tfrac{m}{3}\right)\ddot{x} + c\dot{x} + kx = 0 \qquad (22)$$

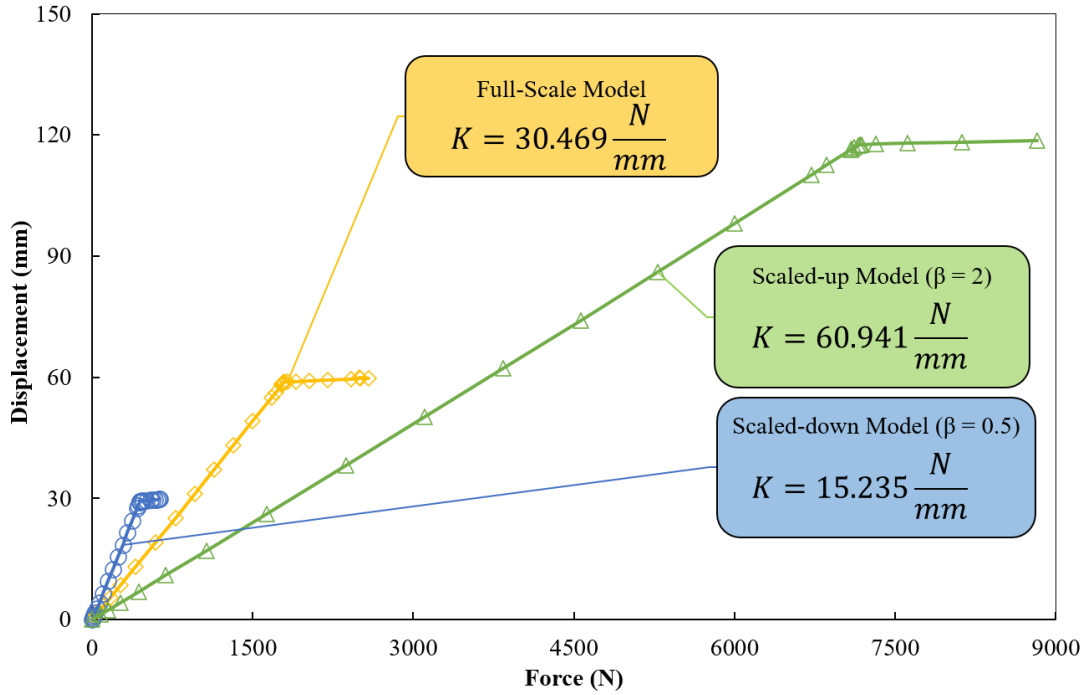

Figure 4: (colour online) Scale dependency of the stiffness of the linear helical spring. The orange, green and blue lines represent the FE numerical results for the displacement-force values of full-scale ($\beta_0 = 1$), scaled down ($\beta_1 = 1/2$) and scaled

up ($\beta_2 = 2$) models where the slope of the line parts is inverse of the stiffness value.

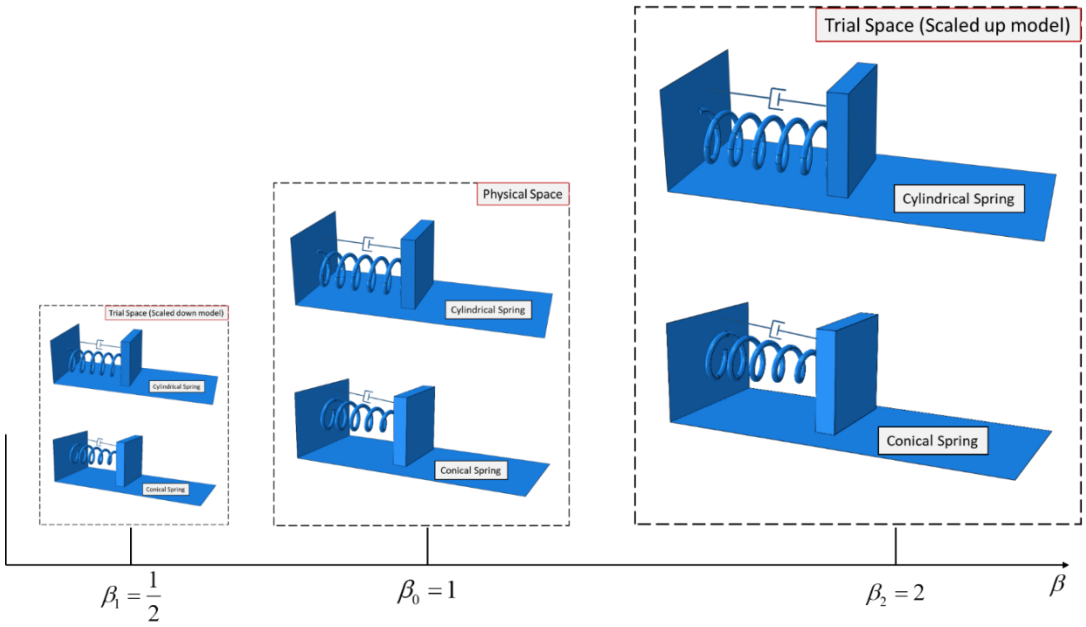

Figure 5: (colour online) Physical, trial 1 and trial 2 spaces which includes both cylindrical and conical spring-mass systems as scalable objects. The geometrical scaling factors for the trial 1 and trial 2 models are β_1 and β_2, respectively.

Table 4:4: Geometrical,material characteristics and initial condition of mass-cylindrical spring systems

Parameters	Full scale system	Scaled down system	Scaled up system
$D\,(mm)$	50	25	100
$d\,(mm)$	6	3	12
$L_0\,(mm)$	150	75	300
Initial Exitation (mm)	50	25	100
n_a	6	6	6
$E\,(MPa)$	210000	210000	210000
Poisson ratio (ν)	0.28	0.28	0.28
Density(kg/mm^3)	$7.8\cdot10^{-6}$	$7.8\cdot10^{-6}$	$7.8\cdot10^{-6}$
$Mass_{spring}\,(kg)$	0.206	0.0257	1.648
$Mass_{body}\,(kg)$	0.050	0.00625	0.400

where k is the spring stiffness, c is the viscous damping value, M is mass of the rigid body, and m is the mass of the spring. There are three critical quantities which are

necessary for describing the dynamic response of the system, i.e. the undamped natural frequency ω_n, obtained from the following expression [35],

$$\omega_n = \sqrt{\frac{k}{\frac{m}{3} + M}} \tag{23}$$

the critical damping constant $c_c = 2\left(\frac{m}{3} + M\right)\omega_n$, and the damping ratio $\zeta = \frac{c}{c_c}$, which is a dimensionless measure that is related to the logarithmic decrement δ describing how oscillations in a system decay following a disturbance and is observable in experiments.

For spring steel the damping ratio ξ can be assumed to be appropriately 0.0013, where it might vary between 0.001 and 0.002 [36]. Understanding how the damping ratio ζ (structural damping) changes with scale is of critical interest here. According to the book by Lazan [37], energy dissipation *D* can for the most part can be related to stress amplitude σ_a, through a relationship of the type $D = J\sigma_a^n$, where *J* and *n* are material properties. In the situation of a uniform rod (of modulus E) subjected to an axial stress σ, the elastic energy density $U = \frac{1}{2}\frac{\sigma^2}{E}$ and the damping ratio is

$$\zeta = \frac{1}{4\pi}\frac{D}{U} = \frac{1}{4\pi}\frac{J\sigma^n}{\frac{1}{2}\frac{\sigma^2}{E}} = \frac{JE}{2\pi}\sigma^{n-2} \tag{24}$$

where *n* takes up values between 2 and 4 [37, 38]; typically, *n* = 2.3 for spring steel.

It is clear that stress plays a critical role in the determination of the damping ratio and from Eq. (24), it can be deduced that for structural damping it will remain reasonably invariant for an identical material provided stress levels are also similar. The situation is presented in Tab. 5 for the cylindrical-spring systems depicted in Fig. 4 and note that although ζ is constant the damping coefficient *c* invariably changes. Note that the zeroth-order conditions $M_{ps} = \alpha_0^\rho M_{ts}$, $m_{ps} = \alpha_0^\rho m_{ts}$, $\omega_{ps} = g\omega_{ts}$ and consequently $\left(c_c\right)_{ps} = \alpha_0^\rho g\left(c_c\right)_{ts}$ from the relationship $c_c = 2\left(\frac{m}{3} + M\right)\omega_n$. Thus for $\zeta_{ps} = \zeta_{ts}$ to be satisfied it follows that $c_{ps} = \alpha_0^\rho g c_{ts}$ and for identical materials and identical stress levels it follows (from Tab. 1) that $\alpha_0^\rho = \beta^{-3}$ and $\alpha_0^\rho g^2\beta = 1$ and consequently $g = \beta$ and $c_{ps} = \beta^{-2}c_{ts}$ as observed in

Tab. 5. Note that a relationship between c_{ps} and c_{ts} can be obtained directly on consideration of force, since $c_{ps}\mathbf{v}_{ps} = \alpha_0^v g c_{ts}\mathbf{v}_{ts}$, which on substitution of $\mathbf{v}_{ps} = g\beta^{-1}\mathbf{v}_{ts}$ provides $c_{ps} = \alpha_0^v \beta c_{ts}$ and finally on substitution of $\alpha_0^v = \alpha_0^\rho g\beta^{-1}$ gives $c_{ps} = \alpha_0^\rho g c_{ts}$, which for $g = \beta$ and $\alpha_0^\rho = \beta^{-3}$ returns to $c_{ps} = \beta^{-2} c_{ts}$; see analysis in Sec. 4 and Tab. 2.

Table 4:5: Dynamic Characteristics of cylindrical mass-spring system

Parameters	Full scale system	Scaled down system (Trial model I)	Scaled up system (Trial model II)
Scaling Factor (β)	1	0.5	2
Time Scaling Factor (g)	1	0.5	2
Stiffness *(N/mm)*	17.718	8.859	35.436
ω_n *(1/s)*	386.413	772.826	193.206
$c_{cr}\left(N.s/mm\right)$	$91.7087\cdot10^{-3}$	$22.9272\cdot10^{-3}$	$366.8347\cdot10^{-3}$
ζ	0.0013	0.0013	0.0013
$c\left(N.s/mm\right)$	$0.1192\cdot10^{-3}$	$0.0298\cdot10^{-3}$	$0.4768\cdot10^{-3}$

5.1.2. Numerical spring-system analysis

In the following, the dynamic response characteristics of the full-scale and trial models for mass-cylindrical spring system are obtained using finite element analysis. The finite element software ABAQUS with dynamic solver [39] is used for the simulations comprising of 7056 linear hexahedral elements (C3D84) and 3011 quadratic tetrahedral elements (C3D10). In addition, 280 bilinear rigid-quadrilateral elements (R3D4) have been used for modelling the mass and additionally the damper is defined as a dashpot element. In Fig. 6 the scaled-down and scaled-up systems are termed trial models I and II, respectively. To predict dynamic response of the full scale model with a good accuracy, Young's modulus and density are considered as fixed parameters and satisfy the following zeroth-order relationships: $E_{ps} = \alpha_0^\rho g^2 \beta E_{ts}$ and $\rho_{ps} = \alpha_0^\rho \beta^3 \rho_{ts}$, which for identical materials returns $\alpha_0^\rho = \beta^{-3}$ and $g = \beta$ in accordance with Tab. 5. The Abaqus results presented in Figs. 6 and 7

provide a clear indication that the" projected" trial models predict the dynamic response of the full-scale model to good accuracy. Note that the trial model results in Fig. 6 are all projected onto the physical space to facilitate a direct comparison with the full-scale results.

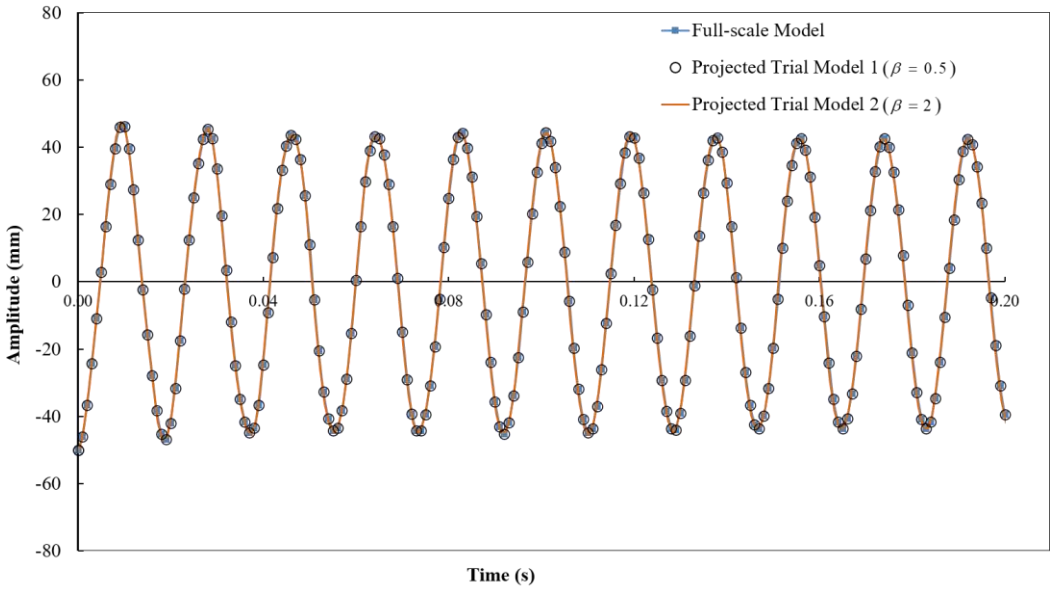

Figure 6: (colour online) Vibration amplitude of full-scale and projected trial mass-cylindrical spring system. The geometrical and temporal scaling factors for projecting the trial 1 and trial 2 model results onto the physical space are respectively ($\beta_1 = 1/2, g_1 = 1/2$) and ($\beta_2 = 2, g_2 = 2$) for the same materials.

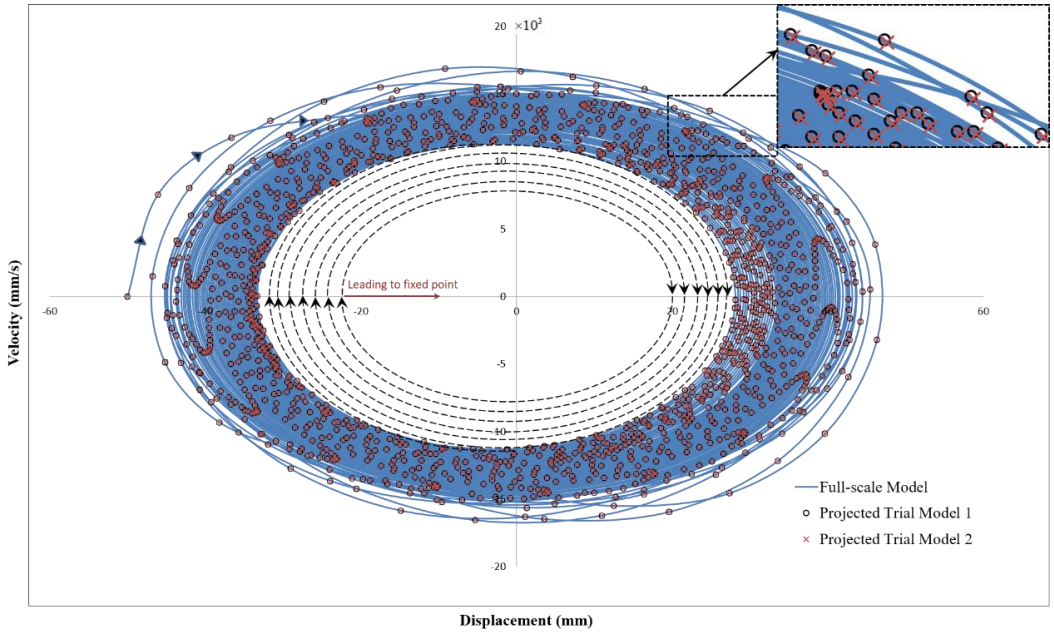

Figure 7:(colour online) Phase-space for full-scale and projected-trial models of the mass-cylindrical spring system. The blue line, black circular and cross pointers demonstrate that the velocity-displacement behaviour of the full-scale, projected trial model 1 and projected trial model 2, respectively, exactly follow the same path and set of data. For the sake of the clarity, the data from the three models is reduced and replaced by dashed lines that lead ultimately to a fixed point of attraction.

The exact same analysis is repeated for the dynamic response of the mass-conical spring. The conical spring is modelled in SOLIDWORKS software [40] and discretized with 31997 linear hexahedral elements (C3D8R) and 15842 quadratic tetrahedral elements (C3D10) in ABAQUS. Geometrical features for the full scale and trial models based on the scaling factors ($\beta = 0.5$ for trial Model I and $\beta = 2$ for trial model II), material properties and systems initial excitation are tabulated in Tab. 6. Fig. 4 shows the CAD models of the full-scale model, trial models I and II. As above Young's modulus and density are targeted and the dynamic response for the full scale and projected-trial models are presented in Figs. 8 and 9. Again good accuracy is returned providing good evidence that zeroth-order scaling is able to predict the scaled behaviour of linear mass-spring systems.

Table 4:6:Geometrical, material Characteristics and initial condition of mass-conical spring system

Parameters	Full-scale System	Scaled Down System (Trial Model I)	Scaled Up System (Trial Model II)
D_1 (mm)	50	25	100
D_2 (mm)	23.75	47.50	11.875
d (mm)	6	3	12
L_0 (mm)	150	75	300
Initial Exitation (mm)	50	25	100
n_a	6	6	6
E (MPa)	210000	210000	210000
Poisson ratio (ν)	0.28	0.28	0.28
Density(kg/mm^3)	$7.8\cdot10^{-6}$	$7.8\cdot10^{-6}$	$7.8\cdot10^{-6}$
$Mass_{spring}$ *(kg)*	0.155	0.019375	1.240
$Mass_{body}$ *(kg)*	0.050	0.00625	0.400

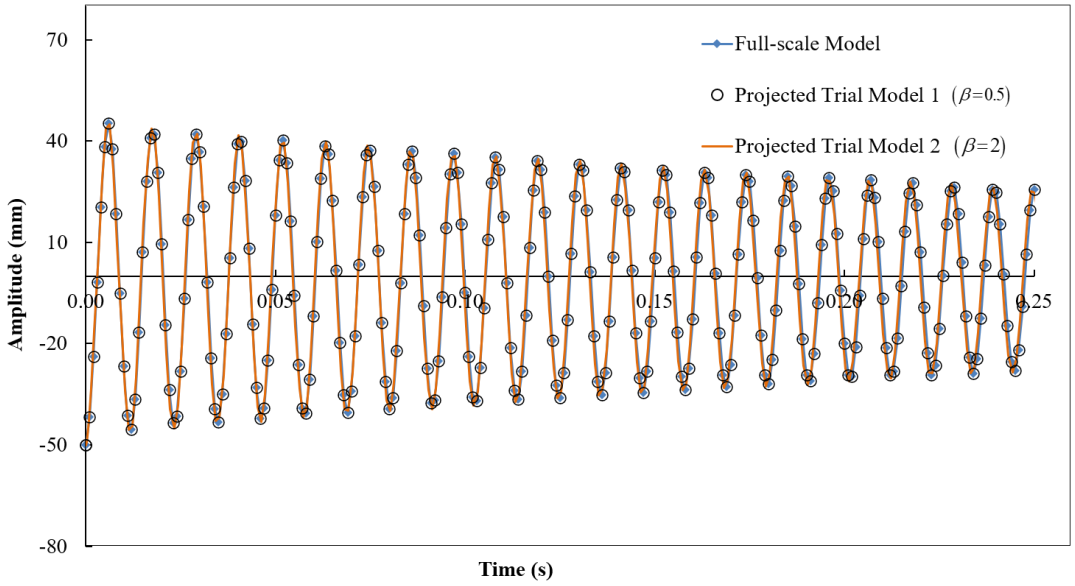

Figure 8: (colour online) Vibration amplitude of full-scale and projected trial models of the nonlinear conical spring system. The geometrical and temporal scaling factors for projecting the trial 1 and trial 2 model results onto the physical space are respectively ($\beta_1 = 1/2, g_1 = 1/2$) and ($\beta_2 = 2, g_2 = 2$) for the same materials.

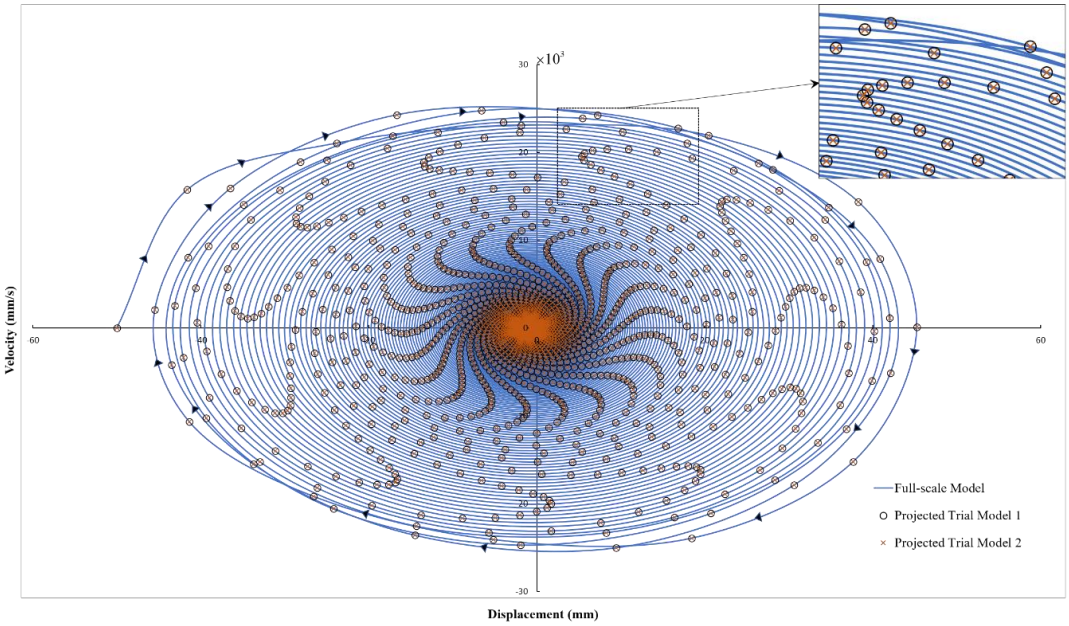

Figure 9: (colour online) Phase-space for full-scale and projected-trial models of mass-conical spring system. The blue line, black circular and cross pointers demonstrate that the velocity-displacement behaviour of the full-scale, projected trial model 1 and projected trial model 2, respectively follow exactly the same path towards the origin (point of attraction).

5.2. Viscous-Damper dependencies

In the previous subsection the scaled behaviour of structural damping was examined and it was revealed that for an identical material the relationship $c_{ts} = \beta^2 c_{ps}$ applied. The reality of scaling for a system involving a physical dashpot is something altogether different and scale dependencies are required. A particular design for the dashpot is depicted in Fig. 10, which consists of a viscous damper filled with Newtonian fluid of viscosity μ, which is allowed to move from one side of the chamber to the other with movement of the piston.

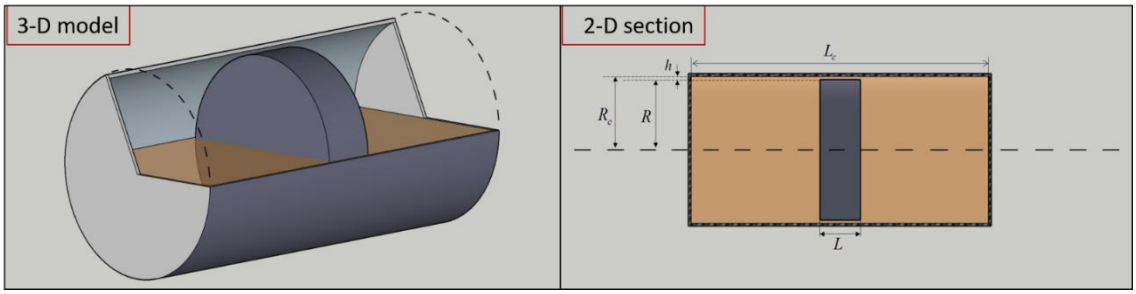

Figure 10: (colour online) 3-D and 2-D CAD models of the fluid viscous damper. The orange parts represent the viscous fluid while the grey parts depict the rigid piston and the rigid walls of the cylindrical container.

Note that ρ is the fluid density, L is piston head width, R_i is piston head radius, h is orifice width (which fluid passes through) and finally the cylinder velocity $\dot{x}$ [41]. The pressure drop across the piston under the assumption of laminar flow is.

$$\Delta P = \frac{6\mu L \dot{x} R_i}{h^3} \tag{25}$$

and on multiplication of ΔP by the piston cross-sectional area a relationship for damping force F^d is obtained, i.e.

$$F^d = \left(\frac{6\mu L \dot{x} R_i}{h^3} \right) \dot{x} = c\dot{x} \tag{26}$$

where c is the sort damping coefficient and observe from the quotient LR_i^3 / h^3 that $c_{ts} = \beta c_{ps}$ (for $\mu_{ts} = \mu_{ps}$)[41], which can be contrasted with the relationship for structural damping $c_{ts} = \beta^2 c_{ps}$. To confirm the veracity of Eq. (26) a numerical model (identical to that of Hou (2008) [41]) is created within the commercial finite element software ABAQUS/CFD [39]. The piston rod is not included (assumed small) and an outline of the model is presented in Fig. 10. The analysis approach adopted here is identical to that presented Hou (2008) [41] and involves a stationary piston head (none-slip boundary conditions applied) and the velocity of the fluid dictated by the cylinder motion. The maximum velocity of the flow is defined as $\dot{x}_{max} = \omega a$, where ω is the angular frequency and a is the oscillation amplitude [42]. The flow velocity is assumed to behave sinusoidally according to the equation $\dot{x} = \dot{x}_{max} \sin \omega t$. For this specific test case, the applied frequency is 10 Hz with 10 mm amplitude of displacement [41] [42]. The cylinder is filled with incompressible

silicon oil with properties: 970 kg/m3 density with 1 kg/ms dynamic viscosity (see Fig. 10) and the physical dimensions of the damper is defined in Tab. 7.

Table 4:7:Physical dimensions of damper models (mm).

Parameters	Full-scale System	Scaled-down System	Scaled-up System
Radius of piston head (R)	24.45	12.225	48.9
Width of piston head (L)	15	7.50	30
Width of orifice (h)	0.55	0.275	1.1
Radius of cylinder (R_c)	25	12.5	50
Length of cylinder (L_c)	110	55	220

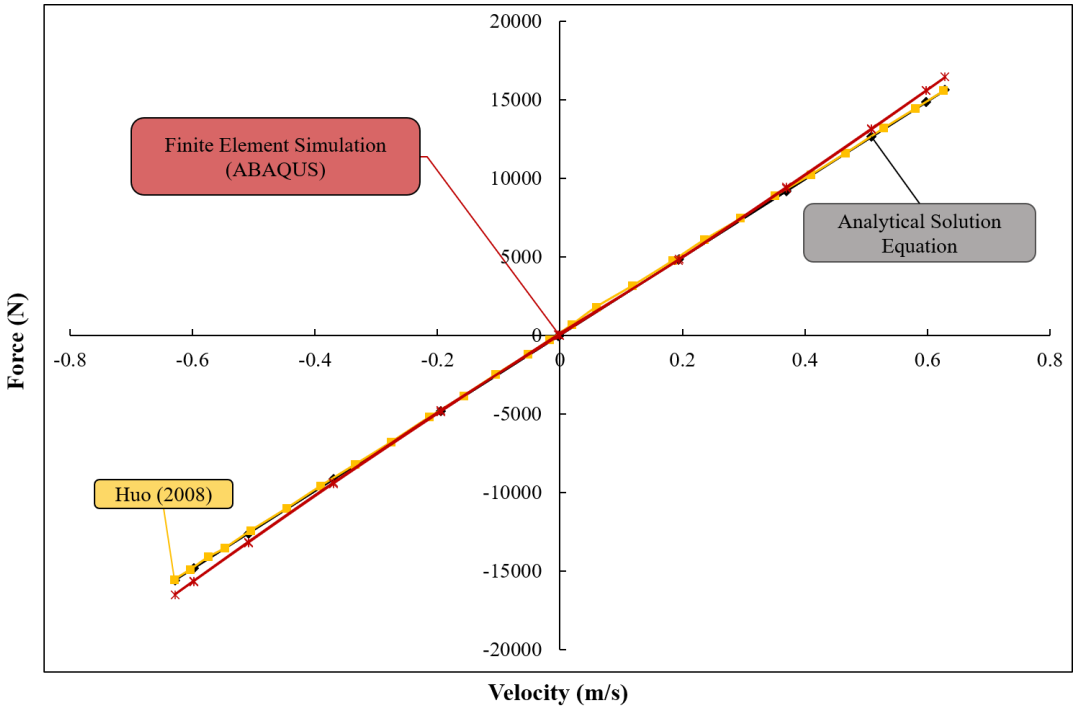

Figure 11: (colour online) Verification of the FE simulation results for the force-velocity of the linear fluid viscous dashpot by comparison against numerical and analytical results presented in the literature.

The finite-element results (see Fig. 11) show that the force-velocity relationship is linear and provides a good match with Eq. (26) and the results of Hou (2008). The verified finite-element model provides the means to investigate the effects of scaling

and dimension scaling parameter is therefore selected as $\beta = 1/2$ and $\beta = 2$ for scaled-down and scaled-up dampers, respectively. The physical parameters of both scaled models are depicted in Tab. 7 and same materials (liquid, steel etc.) were used for all three models. In this analysis $g = \beta^2$ in accordance with the discussion in Sec. 4, so as to ensure zeroth-order scaling is in force. The scaling parameters, boundary conditions, and the model designed in the ABAQUS software and a depiction is provided in Fig. 12. The finite element software results also confirm that the linear fluid viscous damper damping coefficient c changes with respect to β^{-1} as depicted in Fig. 13.

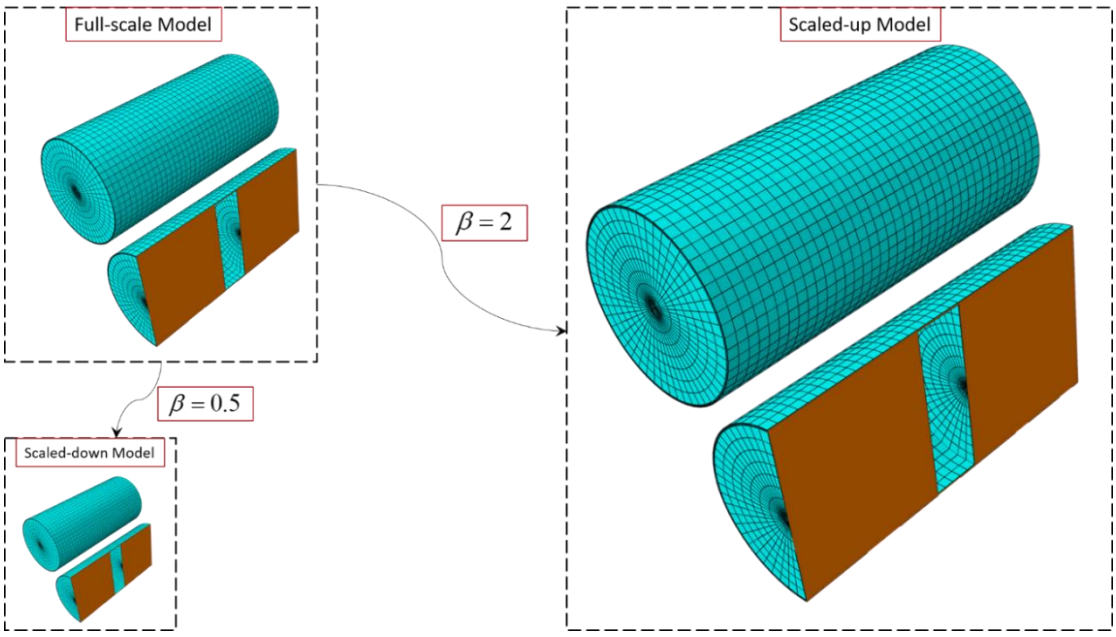

Figure 12: (colour online) Full and scaled down ($\beta_1 = 1/2$) and up ($\beta_2 = 2$) model of the dashpot models which includes both fluid (brown) and rigid parts (light blue).

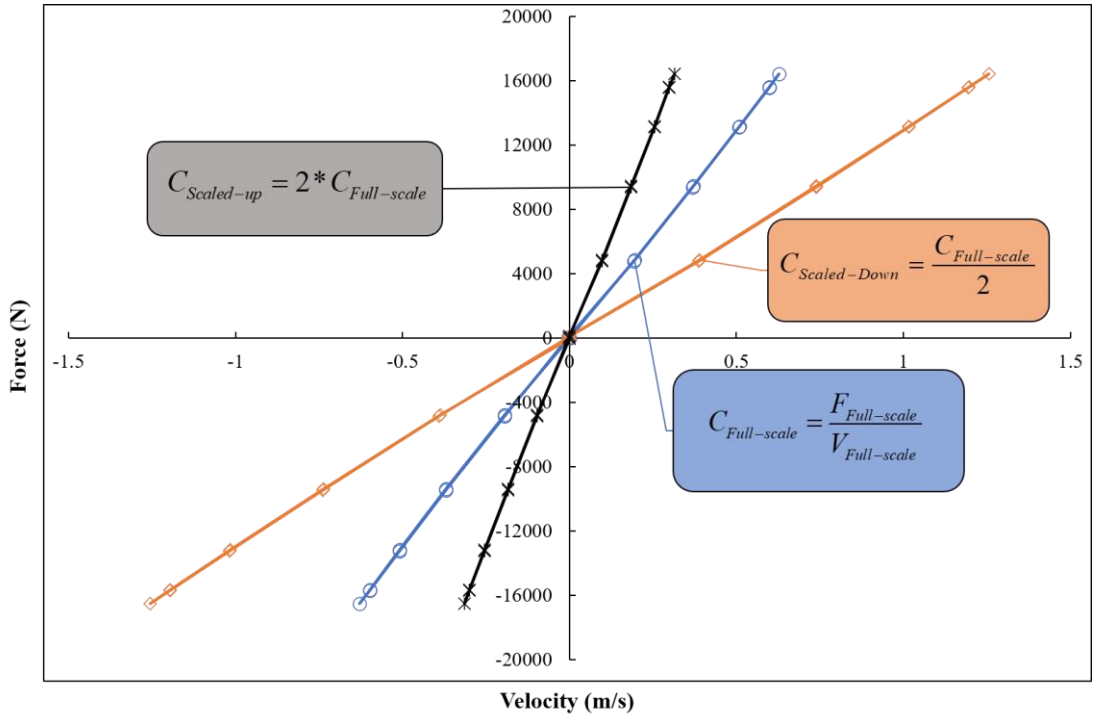

Figure 13: (colour online) Scale dependency of the damping coefficient of the linear fluid viscous damper. The blue, brown and grey lines represent the FE numerical results for the force-velocity values of full-scale ($\beta_0 = 1$), scaled down ($\beta_1 = 1/2$) and scaled up ($\beta_2 = 2$) models where the slope of the line parts is inverse of the damping coefficient value.

5.2.1. Numerical analysis of viscous-damper system

To investigate further the scaling behaviour of the linear fluid viscous damper, a mass-spring-damper system was designed [43], with $\beta = 1/2$ for the scaled-down model. The material properties of the full-scale and scaled-down models are tabulated in Tab. 8. As the scaling of spring stiffness and density was studied in the previous sections, the obtained material properties are defined in the same table.

Table 4:8: Physical properties of mass-spring-dashpot model for full-scale and scaled models

Parameters	Full Scale System	Scaled Down System (Trial Model)
Dimension scaling factor (β)	1	0.5
Time scaling factor (g)	1	0.5
Stiffness (N/m)	100	50

Damping coefficient $c\left(N.s/m\right)$	10	5
Mass (kg)	50	6.25
Applied displacement (m)	0.1	0.05

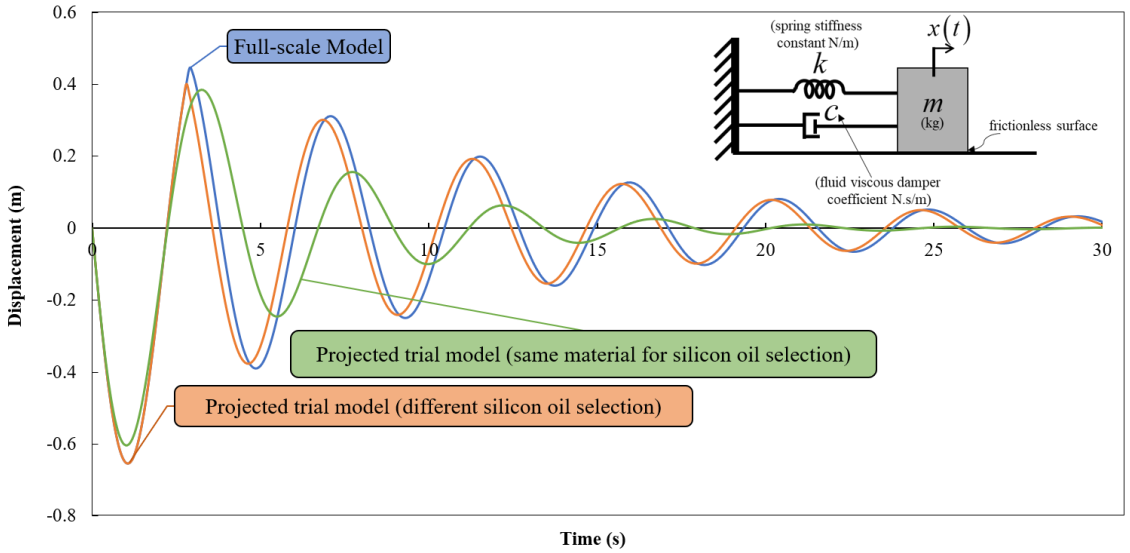

Figure 14:(colour online) Temporal displacement response of zeroth-order mass-spring dashpot system. The green line represents the projected trial model behaviour of the trial model scaled using identical materials including the damper fluid while the orange line represents the projected trial model with a different silicon oil.

The spring and damper are defined as dashpot elements in ABAQUS for the simplicity of the analysis. The spring stiffness and dashpot coefficients are numerically entered into the software. An initial displacement is applied to the mass and the results of the ABAQUS analysis are presented in Fig. 14. The displacement-time curve of the full-scale model and the projected-trial model do not match in this case. The issue was alluded in Sec. 4, where zeroth-order scaling of the spring and viscous dashpot requiring $g=\beta$ and $g=\beta^2$, respectively. Zeroth-order scaling has not been achieved for the whole system and exact replication from a single experiment is not therefore possible. With physical modelling in mind a relatively straightforward modification is the use of an alternative fluid in the scaled-down viscous damper. Consider then the same problem but with a different silicon oil with

970 (kg/m^3)density and 0.5 (kg/ms) viscosity [44] in the smaller model. In this case damping coefficient c_{ts1} is 2.5 Ns/m, which satisfies the relationship $c_{ts1} = \beta_1^2 c_{ps}$ (as opposed to $c_{ts1} = \beta_1 c_{ps}$). The obtained results are presented in the Fig. 14 and as expected replication between full-scale and projected trial-model results are achieved.

6. First-order systems

As alluded to in Sec. 4, the scaling of linear systems is best served using zeroth-order theory. The fundamental issue is the matching of first-order identities for $\frac{m_{ts}}{m_{ps}}\mathbf{a}_{ts}$, $\frac{c_{ts}}{c_{ps}}\mathbf{v}_{ts}$ and $\frac{k_{ts}}{k_{ps}}\mathbf{u}_{ts}$ (from force) and $\mathbf{a}_{ts}$, $\mathbf{v}_{ts}$, and $\mathbf{u}_{ts}$ (from kinematics), is only exact if and only if $\frac{m_{ts}}{m_{ps}}$, $\frac{c_{ts}}{c_{ps}}$, and $\frac{k_{ts}}{k_{ps}}$ satisfy zeroth-order relationships (see Tab. 2). In essence, the simple form of the force terms involved in linear dynamics provides a barrier to the application of first-order relationships. However, other types of force are involved in dynamics and one such force arises from sliding friction. To illustrate that exact first-order solutions exist the finite-similitude theory is applied to relatively simple systems involving friction.

6.1. Analysis of scaled-sliding systems

The system in Fig. 15 is investigated analytically using the Maple software package, where an algorithm similar to that presented in reference [45] is employed to solve the differential equations

$$m\ddot{x} = -kx + \mu mG \text{ where } \dot{x} < 0; \tag{27a}$$

$$m\ddot{x} = -kx - \mu mG \text{ where } \dot{x} > 0; \tag{27b}$$

where G is the acceleration in free-fall due to gravity and μ is the kinetic coefficient of friction.

The properties for system depicted in Fig. 15 are tabulated in Tab. 9, with verification results for the full-scale model presented in Fig. 15. Excellent replication of the results of Marchewka (2003) [45] is apparent from Fig. 15 and note from Tab. 9 that two scales ($\beta_1 = 0.5$ and $\beta_2 = 0.25$) and two designs (Design I and II) are trialled.

It is useful at this point to repeat the analysis on the friction force that was performed for the other forces in Sec. 4. Consider then the friction force $\mathbf{F}_{ts}^{f} = -\mu_{ts} m_{ts} G_{ts} \frac{\mathbf{v}_{ts}}{|\mathbf{v}_{ts}|}$ and the multiplication throughout by $\alpha_0^{v} g$, which provides after some reorganization

$$\alpha_0^{v} \mathrm{g} \mathbf{F}_{ts}^{f} = -\left(\mu_{ts}\right)\left(\alpha_0^{v} \mathrm{g}^{-1} \beta m_{ts}\right)\left(\beta^{-1} g^{2} G_{ts}\right) \frac{\mathrm{g}\beta^{-1}\mathbf{v}_{ts}}{|\mathrm{g}\beta^{-1}\mathbf{v}_{ts}|} \tag{28}$$

which for $g = \beta$ (needed for the spring) provides an immediate difficulty for zeroth-order scaling as $\beta^{-1} g^{2} G_{ts} \neq G_{ps}$, i.e. zeroth-order scaling requires gravitational force to change!

Table 4:9: Properties and conditions of scaled sliding-friction system

Geometrical/Material Parameters	Full-scale Model	Scaled Model	Trial model I	Trail Model II
Initial Exitation (m)	1	0.5	0.5	0.25
Mass of Body (kg)	2	0.25	0.25	0.0625
k (N/m)	50	25	25	12.5
G (m/s^2)	9.81	19.62	9.81	9.81
μ	0.11	0.11	0.11	0.11

Replica scaling is again trialled with Young's modulus and density targeted, which results in $g_{ts1} = \beta_1 = 0.5$ and $g_{ts2} = \beta_2 = 0.25$. Material properties, initial conditions of scaled and trial models provided in Tab. 9. The response of the full-scale model and the projected models I and II are presented in Fig. 15, where it is evident that full-scale model response is not captured with zeroth order, individually by the two scaled models. The issue is gravity and it would require mass to be added, the coefficient of friction to be changed or gravity to be increased for zeroth-order matching. Rather than changing the physical problem, first-order finite similitude is next considered. The first-order approach combines the two projected zeroth-order solutions as depicted in Fig. 17. This requires the determination of the parameters R_1, which is chosen to ensure gravity is correctly captured by the virtual model.

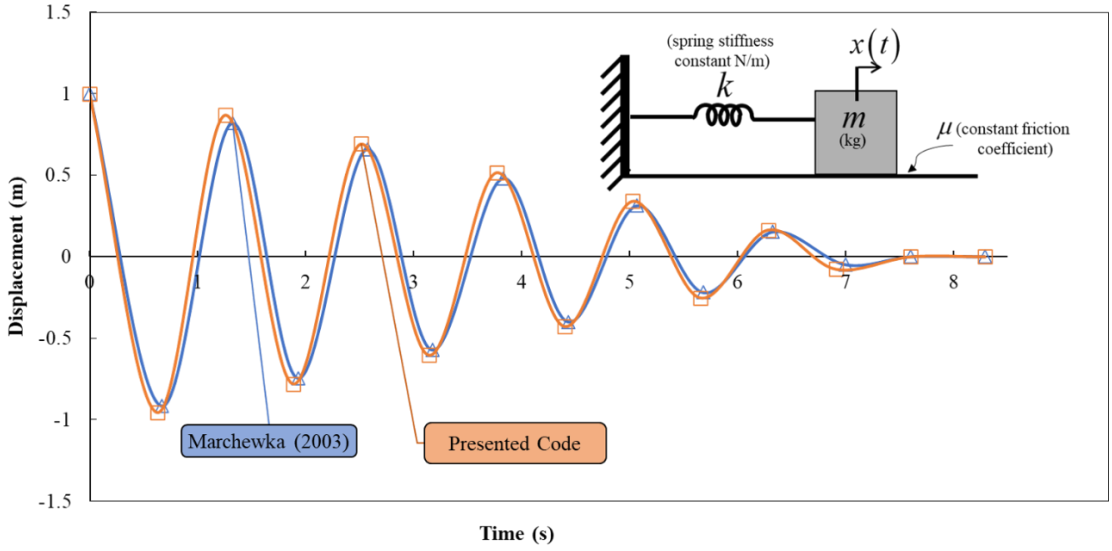

Figure 15: (colour online) Verification of the numerical results for the displacement-time of the mass-spring-friction system by comparison against numerical and analytical results presented in the literature. Here k, m and μ are spring stiffness, mass of the body and friction coefficient, respectively.

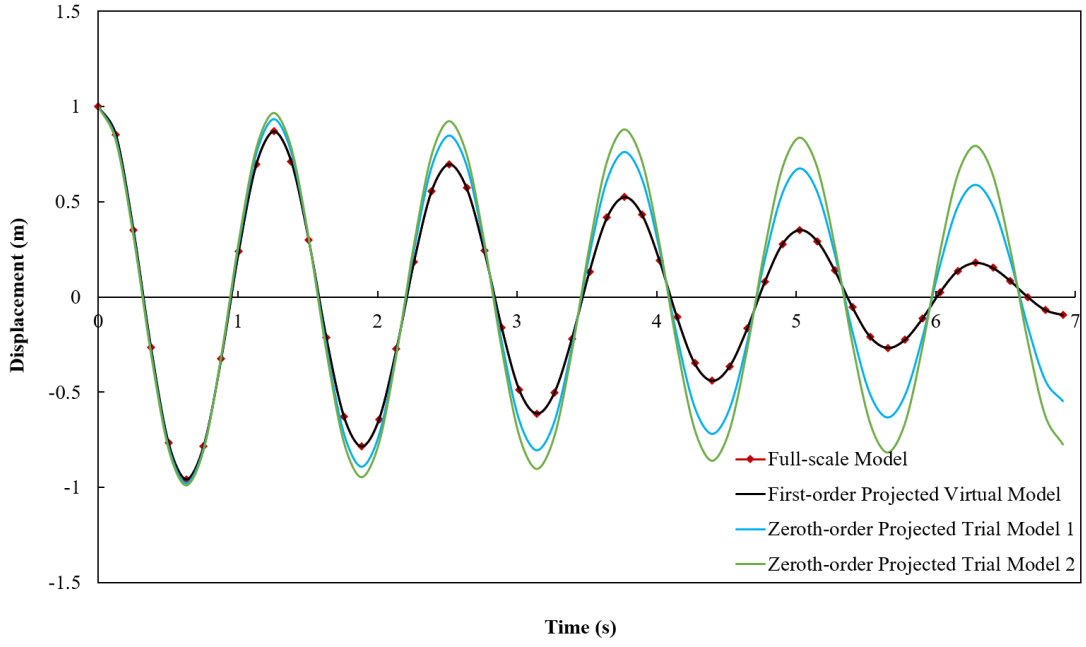

Figure 16: (colour online) Response of scaled mass-spring systems subjected to sliding friction forces. The first-order virtual model represents the combination of two trial models, which are trial 1 and trial 2, while the zeroth-order projected trial models are the results pertaining to the projection of the individual scaled models for trial 1 and 2.

The pertinent first-order equation is (see acceleration in Tab. 1)

$$G_{ps} = \beta_1^{-1} g_1^2 G_{ts1} + R_1 \left(\beta_1^{-1} g_1^2 G_{ts1} - \beta_2^{-1} g_2^2 G_{ts2} \right) \tag{29}$$

where of substitution of $g_{ts1} = \beta_1 = 0.5$ and $g_{ts2} = \beta_2 = 0.25$ provides

$$R_1 = \frac{1-\beta_1}{\beta_1 - \beta_2} = \frac{1-0.5}{0.5-0.25} = 2 \tag{30}$$

where it is appreciated that $G_{ps} = G_{ts1} = G_{ts2}$. The first-order results are presented in Fig. 16, which in line with expectations for the first-order theory, provides a perfect match for the full-scale system.

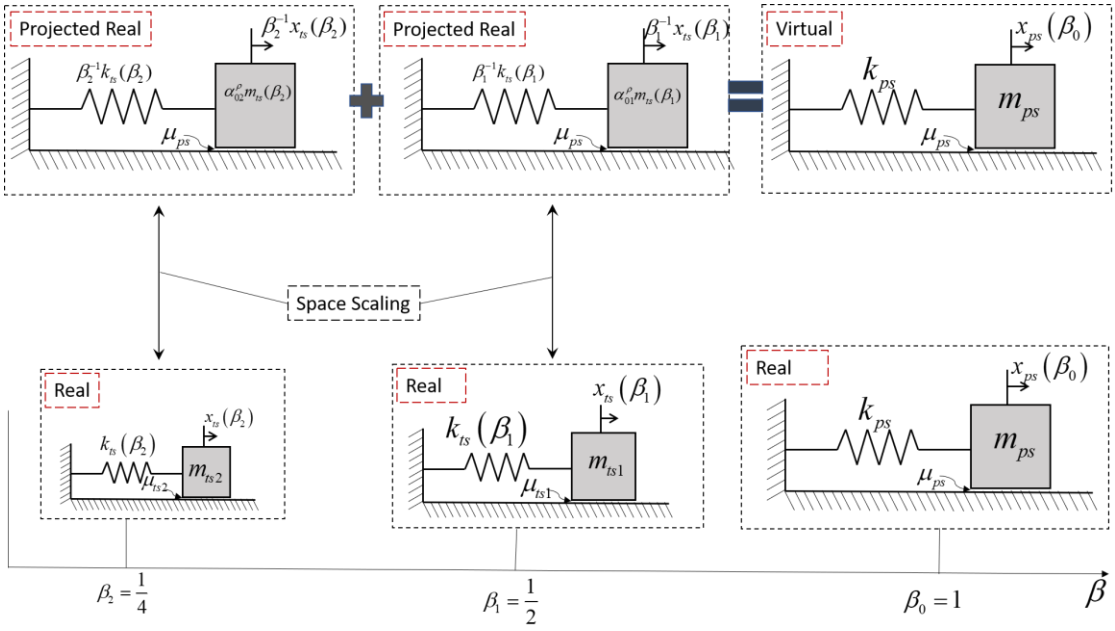

Figure 17:Projected trial and physical spaces models for the mass-spring-friction system. The vertical double arrows represent the scaling map between two trials and physical spaces which facilitate the projection of the trial model results into the physical space. The top row shows the combination of trial 1($\beta_1 = 1/2$) and trial 2 ($\beta_2 = 1/4$) projected models to form the virtual model, which can be compared with the real full-scale model ($\beta_0 = 1$).

6.2. Passive vibration absorber analysis

A slightly more involved application of the slider type is a passive vibration absorber [46], excited by a base motion $A\cos(\omega t)$, where ω is the angular frequency

and A is displacement amplitude. The system (along with scaled versions) is depicted in Fig. 18 and is assumed to be governed [46] by the differential equations

$$m_1\ddot{x}_1 = -c\left(\dot{x}_1 - \dot{x}_2\right) - k_1\left(x_1 - A\cos\left(\omega t\right)\right) - k_2\left(x_1 - x_2\right) \quad (31a)$$

$$m_2\ddot{x}_2 = -c\left(\dot{x}_2 - \dot{x}_1\right) - k_2\left(x_2 - x_1\right) - k_2\left(x_1 - x_2\right) - \mu m_2 G \quad (31b)$$

which are to be solved analytically using the Maple software; details are tabulated in Tab. 10.

Table : Properties and conditions for the passive-vibration absorber

Geometric/Material Properties	Full-scale Model	Trial Model I	Trial Model II
Mass of Body (kg)	8.5	1.06	0.13
k_1 *(N/m)*	670	335	167.5
k_2 *(N/m)*	670	335	167.5
c_2 *(N.s/m)*	37.7	9.425	2.36
A *(m)*	0.0025	0.00125	0.000625
ω *(1/s)*	8.878	17.756	35.513
G (m/s^2)	9.81	9.81	9.81
ζ	0.003	0.003	0.003
μ	0.15	0.15	0.15

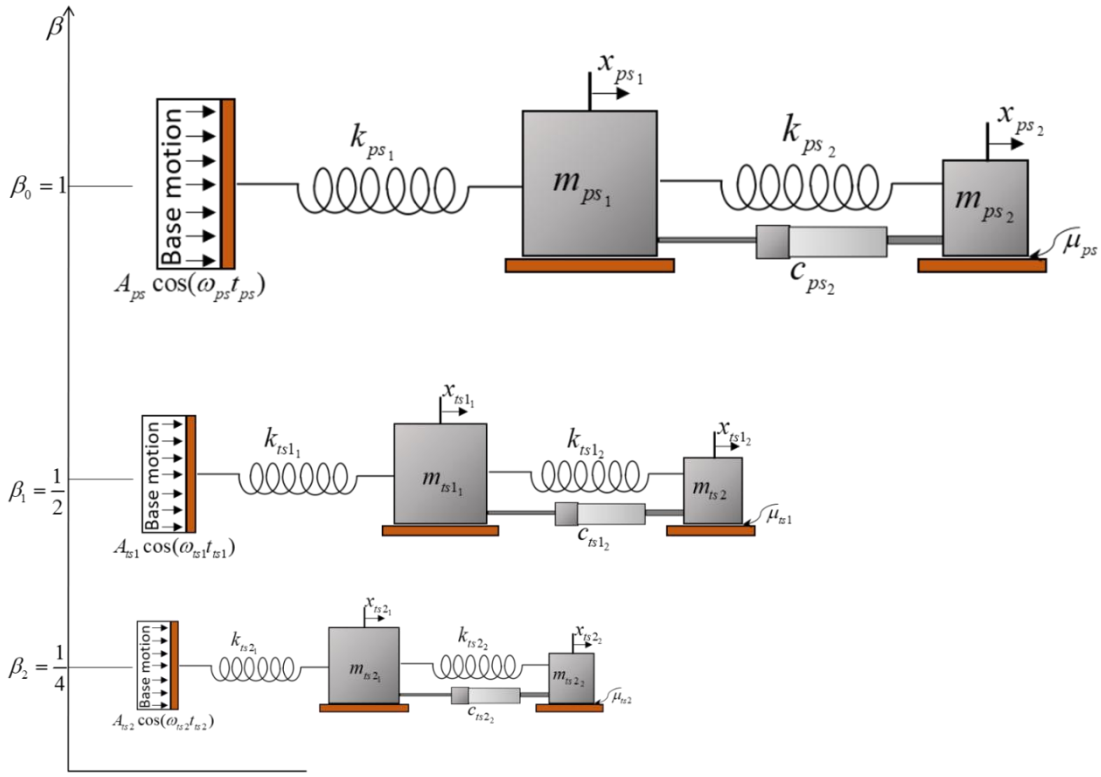

Figure 18: Physical and trial spaces models for the passive vibration-absorber system. The geometrical scaling factors of trial 1 and trial 2 models are set to $\beta_1 = 1/2$ and $\beta_2 = 1/4$, respectively.

The zeroth-order analysis (with $g_{ts1} = \beta_1 = 0.5$ and $g_{ts2} = \beta_2 = 0.25$) fails to provide a perfect match as illustrated in Fig. 19 for the exact same reasons described in Sec. 6.1. Eqs. (29) and (30) apply for the first-order analysis and the results are presented in Fig. 20, where it is apparent that perfect replication is attained.

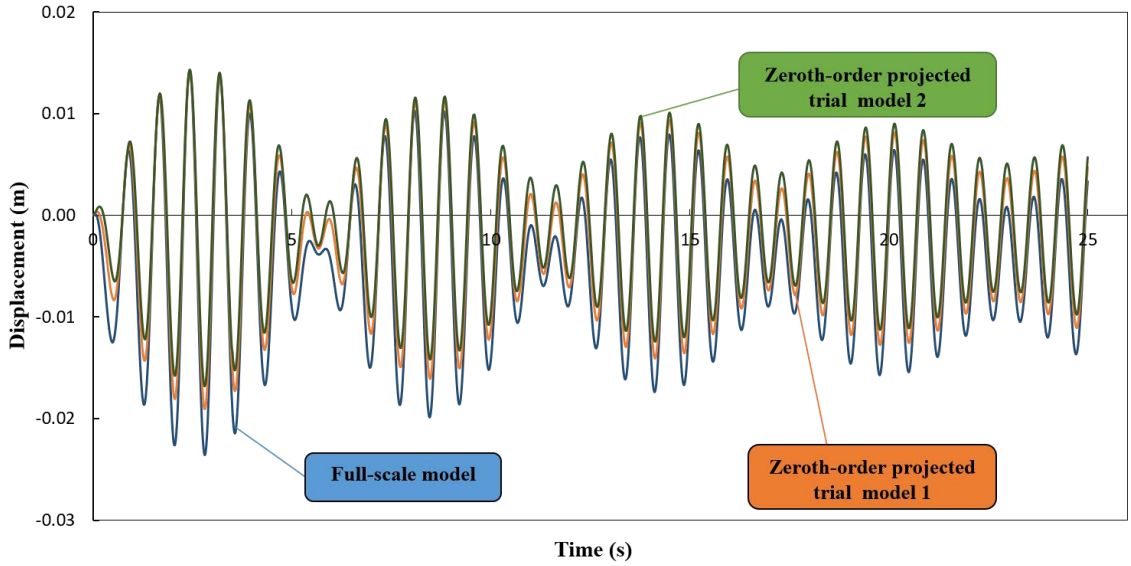

Figure 19: (colour online) Temporal response of mass m_1 described by zeroth-order finite similitude for trial model 1 ($\beta_1 = 1/2$) and trial model 2 ($\beta_1 = 1/4$). The maximum absolute error between the results of the projected trial 1(orange line), (green line) and the full-scale model (blue line) are 16.32% and 21.35%, respectively.

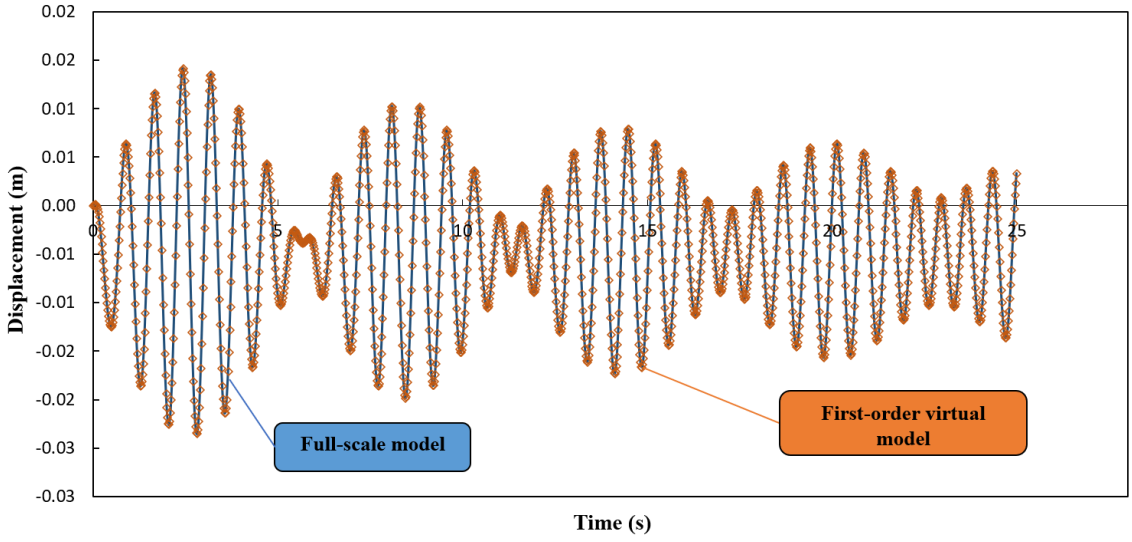

Figure 20: (colour online) Temporal response of mass m_1 described by first-order finite similitude. Comparison between results for the full-scale model (blue line) and the virtual model (orange diamond marker) is shown, where the latter model is a combination of trial model 1 ($\beta_1 = 1/2$) and trial model 2 ($\beta_1 = 1/4$).

7. Conclusion

The aim of the work presented in this paper is to show how discrete mechanical dynamic systems can be used to initiate scaling parameters in a new scaling theory and to establish the appropriateness of a similitude rule called first-order finite similitude for situations where classical scaling theories fail. In order to confirm the new concepts, relatively simple case studies have been considered that can be readily extended to more complicated dynamical systems by following the procedures established in the presented work. The new scaling theory in combination with the first-order finite similitude rule combines information from two scaled experiments instead of a single scaled experiment. The following conclusions can be drawn from the work presented in the paper:

- The theory of finite similitude has been further developed to capture all scale dependencies that arise in the fields describing the mechanics of discrete mechanical systems.
- Differential forms of similitude have been integrated to capture information across two scaled mechanical dynamic-system experiments.
- Proportional field differences feature in the new scaling, so scale effects as previously defined by dimensional analysis cease to be scale effects, under the new theory.
- The scaling theory is equally applicable to analytical, numerical and experimental data and reduces to zeroth-order scaling (single experiment) if this provides the best solution.

More specifically, from the simulations performed on the specific mechanical systems considered, it has been show that:

- Scaled dependencies for mass, springs, structural damping and viscous dashpots have been established and for replica scaling the following relationships, respectively apply: $m_{ts} = \beta^3 m_{ps}$, $k_{ts} = \beta k_{ps}$, $c_{ts} = \beta^2 c_{ps}$ and $c_{ts} = \beta c_{ps}$.
- Analysis and numerical simulation confirmed that zeroth-order scaling proved best for linear mass- spring-dashpot models if physically realisable and required a substitute fluid for the dashpot trials considered here.

- First-order theory proved to be critical in capturing the response of a discrete mechanical system involving friction and zeroth-order theory proved insufficient under replica scaling.

Acknowledgements

The authors would like to acknowledge The Ministry of National Education in Turkey and the Department of Civil Engineering at Firat University for providing support for Muhammed Atar to facilitate his doctoral research at the University of Manchester.

8. References

[1] E. N. Strømmen, Structural dynamics, 2014.

[2] A. Kundu, F. DiazDelaO, S. Adhikari, M. Friswell, A hybrid spectral and metamodeling approach for the stochastic finite element analysis of structural dynamic systems, Computer Methods in Applied Mechanics and Engineering 270 (2014) 201 – 219. doi:https://doi.org/10.1016/j.cma.2013.11.013. URL http://www.sciencedirect.com/science/article/pii/S0045782513003149

[3] I. Mascolo, Recent developments in the dynamic stability of elastic structures, Frontiers in Applied Mathematics and Statistics 5 (2019) 51. doi:10.3389/fams.2019.00051.

[4] A. Evkin, V. Krasovsky, O. Lykhachova, V. Marchenko, Local buckling of axially compressed cylindrical shells with different boundary conditions, Thin-Walled Structures 141 (2019) 374 – 388. doi:https://doi.org/10.1016/j.tws.2019.04.039. URL http://www.sciencedirect.com/science/article/pii/S026382311930014X

[5] A. M. Stuart, Numerical analysis of dynamical systems, Acta numerica 3 (1994) 467–572. doi:10.1017/ S0962492900002488.

[6] C. Jog, M. Agrawal, A. Nandy, The time finite element as a robust general scheme for solving nonlinear dynamic equations including chaotic systems, Applied Mathematics and Computation 279 (2016) 43 – 61. doi:https://doi.org/10.1016/j.amc.2015.12.007.

[7] A. Casaburo, G. Petrone, F. Franco, S. De Rosa, A review of similitude methods for structural engineer- ing, Applied Mechanics Reviews 71 (3). doi:https://doi.org/10.1115/1.4043787.

[8] N. D. Tiwari, A. Gogoi, B. Hazra, Q. Wang, A shape memory alloy-tuned mass damper inerter system for passive control of linked-sdof structural systems under seismic excitation, Journal of Sound and Vibration 494 (2021) 115893. doi:https://doi.org/10.1016/j.jsv.2020.115893.

[9] D. J. Riddoch, A. Cicirello, D. A. Hills, Response of a mass-spring system subject to coulomb damping and harmonic base excitation, International Journal of Solids and Structures 193 (2020) 527–534. doi: https://doi.org/10.1016/j.ijsolstr.2020.02.037.

[10] C. Li, Y. Yuan, P. He, J. Yuan, H. Yu, Improved equivalent mass-spring model for seismic response analysis of two-dimensional soil strata, Soil Dynamics and Earthquake Engineering 112 (2018) 198–202. doi:https://doi.org/10.1016/j.soildyn.2018.05.001.

[11] S. De la Cruz, M. Rodr´ıguez, V. Hern´andez, Using spring-mass models to determine the dynamic response of two-story buildings subjected to lateral loads, in: Proc. of 15 WCEE, 2012, pp. 1–8.

[12]L. Marino, A. Cicirello, Experimental investigation of a single-degree-of-freedom system with coulomb friction, Nonlinear Dynamics 99 (3) (2020) 1781–1799. doi:https://doi.org/10.1007/ s11071-019-05443-2.

[13] C. J. P. Coutinho, Structural reduced scale models based on similitude theory, Ph.D. thesis, Universidade do Porto (Portugal) (2017).

[14] J. M. Lirola, E. Castan˜eda, B. Lauret, M. Khayet, A review on experimental research using scale models for buildings: Application and methodologies, Energy and Buildings 142 (2017) 72 – 110. doi:https://doi.org/10.1016/j.enbuild.2017.02.060. URL http://www.sciencedirect.com/science/article/pii/S0378778817306928

[15] L. Rayleigh, The principle of similitude, Nature 95 (1915) 66.

[16] E. Buckingham, On physically similar systems; illustrations of the use of dimensional equations, Physical review 4 (1914) 345–376. doi:10.1103/PhysRev.4.345.

[17] B. Zohuri, Dimensional analysis and self-similarity methods for engineers and scientists, 2015.

[18] O. Pawelski, Ways and limits of the theory of similarity in application to problems of physics and metal forming, Journal of Materials Processing Technology 34 (1) (1992) 19 – 30. doi:https://doi.org/10. 1016/0924-0136(92)90086-8. URL http://www.sciencedirect.com/science/article/pii/0924013692900868

[19] G. I. Barenblatt, G. I. Barenblatt, B. G. Isaakovich, Scaling, self-similarity, and intermediate asymptotics: dimensional analysis and intermediate asymptotics, Vol. 14, 1996.

[20] K. Davey, R. Darvizeh, A. Al-Tamimi, Scaled metal forming experiments: A transport equation ap- proach, International Journal of Solids and Structures 125 (2017) 184 – 205. doi:https://doi.org/

10.1016/j.ijsolstr.2017.07.006. URL http://www.sciencedirect.com/science/article/pii/S0020768317303232

[21] M. Moghaddam, R. Darvizeh, K. Davey, A. Darvizeh, Scaling of the powder compaction process, Inter- national Journal of Solids and Structures 144-145 (2018) 192 – 212. doi:https://doi.org/10.1016/j.ijsolstr.2018.05.002. URL http://www.sciencedirect.com/science/article/pii/S0020768318301872

[22] R. Ochoa-Cabrero, T. Alonso-Rasgado, K. Davey, Scaling in biomechanical experimentation: a finite similitude approach, Journal of The Royal Society Interface 15 (143) (2018) 20180254. doi:https://doi.org/10.1098/rsif.2018.0254.

[23] H. Sadeghi, K. Davey, R. Darvizeh, A. Darvizeh, A scaled framework for strain rate sensitive structures subjected to high rate impact loading, International Journal of Impact Engineering 125 (2019) 229 – 245. doi:https://doi.org/10.1016/j.ijimpeng.2018.11.008. URL http://www.sciencedirect.com/science/article/pii/S0734743X18304123

[24] H. Sadeghi, K. Davey, R. Darvizeh, A. Darvizeh, Scaled models for failure under impact loading, Interna- tional Journal of Impact Engineering 129 (2019) 36 – 56. doi:https://doi.org/10.1016/j.ijimpeng. 2019.02.010. URL http://www.sciencedirect.com/science/article/pii/S0734743X18313137

[25] A. Al-Tamimi, R. Darvizeh, K. Davey, Experimental investigation into finite similitude for metal forming processes, Journal of Materials Processing Technology 262 (2018) 622 – 637. doi:https://doi.org/10.1016/j.jmatprotec.2018.07.028. URL http://www.sciencedirect.com/science/article/pii/S092401361830325X

[26] K. Davey, R. Darvizeh, A. Golbaf, H. Sadeghi, The breaking of geometric similarity, International Journal of Mechanical Sciences 187 (2020) 105925. doi:https://doi.org/10.1016/j.ijmecsci.2020.105925. URL http://www.sciencedirect.com/science/article/pii/S0020740320312558

[27] K. Davey, H. Sadeghi, R. Darvizeh, A. Golbaf, A. Darvizeh, A finite similitude approach to scaled impact mechanics, International Journal of Impact Engineering 148 (2021) 103744. doi:https://doi.org/10.1016/j.ijimpeng.2020.103744. URL http://www.sciencedirect.com/science/article/pii/S0734743X20308149

[28] R. Ochoa-Cabrero, T. Alonso-Rasgado, K. Davey, Zeroth-order finite similitude and scaling of complex geometries in biomechanical experimentation, Journal of the Royal Society interface 17 (167) (2020) 20190806–20190806. doi:https://doi.org/10.1098/rsif.2019.0806.

[29] K. Davey, O. Bylya, B. Krishnamurthy, Exact and inexact scaled models for hot forging, International Journal of Solids and Structures 203 (2020) 110 – 130. doi:https://doi.org/10.1016/j.ijsolstr. 2020.06.024. URL http://www.sciencedirect.com/science/article/pii/S0020768320302468

[30] K. Davey, R. Darvizeh, Neglected transport equations: extended rankine–hugoniot conditions and j-integrals for fracture, Continuum mechanics and thermodynamics 28 (5) (2016) 1525–1552. doi:https://doi-org.manchester.idm.oclc.org/10.1007/s00161-016-0493-2.

[31] C. Yang, W. Zhang, G. Ren, X. Liu, Modeling and dynamics analysis of helical spring under compression using a curved beam element with consideration on contact between its coils, Meccanica 49 (4) (2014) 907–917. doi:10.1007/s11012-013-9837-1.

[32] E. Rodriguez, M. Paredes, M. Sartor, Analytical behavior law for a constant pitch conical compression spring, Journal of Mechanical Design 128 (6) (2005) 1352–1356. doi:10.1115/1.2338580.

[33] F. A. Charney, Unintended consequences of modeling damping in structures, Journal of structural engi- neering 134 (4) (2008) 581–592. doi:https://doi-org.manchester.idm.oclc.org/10.1061/(ASCE) 0733-9445(2008)134:4(581.

[34] A. Kareem, K. Gurley, Damping in structures: its evaluation and treatment of uncertainty, Journal of wind engineering and industrial aerodynamics 59 (2) (1996) 131–157. doi:https://doi.org/10.1016/ 0167-6105(96)00004-9.

[35] L. Mei, J. Zhu, F. Liu, Discussion on vibration frequency of spring, in: AIP Conference Proceedings, Vol. 1834, 2017, p. 030006. doi:https://doi-org.manchester.idm.oclc.org/10.1063/1.4981571.

[36] H. Bachmann, et al., Vibration problems in structures : practical guidelines, Basel, 1995.

[37] B. J. Lazan, Damping of materials and members in structural mechanics, PERGAMON PRESS LTD, OXFORD, ENGLAND. 1968, 317.

[38] F. Orban, Damping of materials and members in structures, Vol. 268, 2011, p. 012022. doi:10.1088/ 1742-6596/268/1/012022. URL https://doi.org/10.1088%2F1742-6596%2F268%2F1%2F012022

[39] Abaqus, 6.14, online documentation help, theory manual: Dassault systms (2016).

[40] Solidworks 2016, Online help, Accessed (2015) 03–20.

[41] C. Y. Hou, Fluid dynamics and behavior of nonlinear viscous fluid dampers, Journal of Structural Engineering 134 (1) (2008) 56–63. doi:10.1061/(ASCE)0733-9445(2008)134:1(56).

[42] A. Syrakos, Y. Dimakopoulos, J. Tsamopoulos, Theoretical study of the flow in a fluid damper containing high viscosity silicone oil: Effects of shear-thinning and viscoelasticity, Physics of Fluids 30 (3) (2018) 030708. doi:10.1063/1.5011755.

[43] A. A. Ata, A. G. Kamel, Numerical evaluation of the effect of combined pendulum tuned mass damper on a basic vibrating system, International Journal (4) (2018) 270–279.

[44] J. Huneault, J. Kamil, A. Higgins, D. Plant, Dynamic tensile strength of silicone oils 1979 (1) (2018) 070016. doi:10.1063/1.5044825.

[45] A. Marchewka, D. S. Abbott, R. J. Beichner, Oscillator damped by a constant-magnitude friction force, American journal of physics 72 (4) (2004) 477–483. doi:10.1119/1.1624113.

[46] A. Hartung, H. Schmieg, P. Vielsack, Passive vibration absorber with dry friction, Archive of applied mechanics 71 (6) (2001) 463–472. doi:10.1007/s004190000149.

Chapter

FIVE

Paper three: The Scaling of Nonlinear Structural Dynamic Systems

Overview

Following the previous publication, it was necessary to investigate more about nonlinear discrete systems and their behaviour under nonlinear loading conditions. The motivation of this study is the application of single and two-scaled experimentations to nonlinear structural dynamics. It is obvious that nonlinear behaviours are always an issue, and this is a research and application field that brings major difficulties to scaled experimentation. Since the behaviour of such systems is complex and complicated, these systems require very detailed scaled-model designs that can practically achieve satisfactory outcomes. The article shows how the new exact similarity rules provided by the new theory provide necessary precision for the prediction of full-scale model behaviours. This study specifically considers the behaviour of nonlinear damper, spring, and friction all together and the gravitational acceleration which has a significant impact on friction was considered to be the same although the classical scaling theories imposed to be changed. Two scaled experimentation (first-order finite similitude) revealed exact similarity by providing exact replication of behaviours.

Authors Contribution: K. Davey devised the project, the main conceptual ideas and proof outline (conceptualization, methodology, writing - review & editing). R. Darvizeh for supervising the project. **M. Atar** worked out almost all of the technical details, and performed the numerical calculations for the research. He designed the models and the computational framework and carried out validation, writing - review & editing the journal paper. Hamed Sadeghi helped to perform simulations.

Details: International Journal of Mechanical Sciences. Received 16 May 2021, and 24 June 2021, Accepted 27 June 2021. **Publication date:** 15 September 2021

Paper DOI: https://doi.org/10.1016/j.ijmecsci.2021.106631

The Scaling of Nonlinear Structural Dynamic Systems

Keith Davey[a,*], Muhammed Atar[a], Hamed Sadeghi[b], Rooholamin Darvizeh[a]

[a]Department of Mechanical, Aerospace and Civil Engineering, The University of Manchester, UK.

[b]Department of Mechanical Engineering, University of Guilan, Rasht, Iran.

Abstract

A new scaling theory has appeared in the recent literature that has the potential to transform current approaches to scaled experimentation. The new theory introduces new similitude rules that hitherto did not exist and significantly extends the classical definition of similitude underpinned by dimensional analysis. Each new similitude rule is tied to the number of scaled experiments, and in theoretical terms there is no limit to the number of scaled experiments involved.

The focus of this paper is on one and two scaled experiments applied to nonlinear structural dynamics, which is a field of study and application that gives rise to significant difficulties for scaled experimentation. The highly nonlinear behaviour common to these systems means that only very precise scaled-model designs can feasibly achieve acceptable outcomes. It is shown in the paper how the new exact similitude rules provided by the new theory deliver the precision necessary for mathematically exact replication of behaviours. It is demonstrated further how the limited scope provided by a single scaled experiment can be significantly extended by application of two properly designed scaled experiments. Through the analysis of carefully selected structural systems of one and two degrees of freedom involving nonlinear springs, dashpots and friction, the benefits of two scaled experiments are demonstrable for a range of loading conditions. Exact similitude for two scaled experiments is confirmed providing exact replication of behaviours with conformity recorded over long timescales.

Keywords: scaling, finite similitude, trial experimentation, nonlinear dynamic systems.

1. Introduction

Modern structural dynamics makes use of a range of analysis and investigative approaches which in broad terms can be classified as analytical, numerical, experimental, along with combinations of the three. The interminable need to achieve greater accuracy and deal with increased complexity and sophistication of structural systems necessitates the need for new improved investigative and analysis approaches. A particular convenient type of investigation, where accuracy can readily be assured, is those performed under laboratory conditions. Rather unfortunately, however, laboratory experiments have limitations, and one concern is the constraint imposed by size, where for structural dynamics in particular, large structures are the norm. Dealing with large experimental structures can be time consuming and expensive when contrasted against direct analytical and numerical investigations. For complex systems however an overreliance on these direct approaches can itself be problematic and not recommended as uncertainties can make model predictions questionable and invariably some form of experimental support is often required [36–38].

In principle, the solution to the size constraint faced by laboratory experimentation is scaling, where structures are scaled to a fraction of their original size for testing purposes. This is the approach investigated in this paper, but the downside of scaled experimentation is well understood by academic and industrial communities. The issue is one of scale effects [39,40], where the behaviour of the scaled model fails to be representative of the full-scale system. This is certainly the situation prior to the arrival of finite similitude [23,41] but has the arrival of this theory significantly changed the situation? Questions about the usefulness of the new similitude identities remain and an objective of this work is to discover whether nonlinear systems can be assessed with this new approach. It is recognised of course that it is only through the application of the new similitude rules to realistic systems can the benefits be truly quantified.

Over the many decades, following on from the inspirational work of Buckingham [3] and Rayleigh [42], techniques have been developed to quantify the conditions needed to representatively scale down and up systems. These techniques are termed similitude methods, which facilitate (where possible) the accurate representation of a system by preserving dynamic behaviour with the help of scaling laws [6,37,43,44].

Most recent approaches for the analysis of mechanically based dynamic systems tend to rely heavily on computer-based simulation, as computational models can readily be applied over a range of scales [45,46]. Modern numerical approaches are advancing at pace, with robust approaches for analysis, with the ability to scrutinise the entire behaviour of dynamic systems, in response to changes in boundary conditions, properties, system properties, and so forth [47–49]. Despite the advances being made however, simplifications are required to make practicable complex models, and this can be achieved with discrete-element representations that can be employed effectively in investigative studies. It is recognised of course that simplified models require experimental validation to justify the many simplifying assumptions involved in practical modelling [6]. Discrete systems find commonplace usage in the study of structural engineering systems and take the appearance of a network of lumped masses, springs, and dashpots to capture complex dynamic and dissipative behaviours.

Spring-mass-damper discrete systems find common usage but an area of interest, where large-scale systems are involved, is earthquake mechanics [50–53]. Examining building behaviours subjected to seismic excitations is the focus here, where amongst the many possible options, dampers are often employed as part of a passive control system. One of the most commonly used energy dissipation devices in building and building related structures are fluid viscous dampers (FVDs) [54]. The reason behind their widespread adoption is due to their capacity to significantly dampen accelerations [55–59], and consequently increase the seismic operation of the many non-structural parts. Although the operating principles of viscous dampers are relatively straightforward, the design and fabrication of modern FVDs is a multidisciplinary task, requiring considerable expertise in a variety of fields of science [60]. The advantage of nonlinear force-velocity relationships is the focus of much research for FVDs [61–64], since best designs can limit the peak damper force at high structural velocities, but at the same time provide adequate supplementary damping. Understanding the details is very much needed in scaling to gauge the performance and behaviour of these in scaled experiments. In addition to dampers, the other significant energy dissipation mechanisms common to structures is friction and wear in the area where two bodies come into contact. The prevalence of friction in technology and everyday life justifies the extensive scientific research directed at it. A thorough understanding of friction [65] is a necessity, and the particular

behaviour of interest here is that arising from stick-slip systems [66]. The advantage of discrete systems in this regard is that dominant physics (such as friction) can be captured in an efficient manner but as mentioned above experimental evidence is needed to justify and support what might appear to be controversial simplifications [37,67]. With such discrete approaches, the fundamental nonlinear aspects can be captured, and consequently is it of interest to understand their response under scaling. Understanding the scaled nonlinear behaviour of the individual elements (e.g., FVDs, springs, contacting surfaces) is critical, but also in their entirety in relation to the systems under consideration.

The importance of the theory dimensional analysis in scaling is well recognised as it aids in the design of scaled experiments. The theory is founded on a well-known invariance principle, which basically states that dimensionless governing equations remain invariant with scale [5]. This statement confers importance on dimensionless forms, which have distinct advantages. In particular, they can be used to characterise dominant physics by means of a dominant subset of dimensionless parameters (i.e., the Pi groups) [3,5,68]. The biggest issue with dimensional analysis in scaling is connected to the underpinning invariance principle itself, as this is rarely applicable to all but the most basic of systems [6,69]. In the presence of scale effects, by definition, this invariance principle breaks down, and the importance of dimensional analysis and scaled experimentation is undoubtedly diminished by this [70].

To overcome these shortcomings with dimensional analysis a new theory has recently emerged called finite similitude [21,22,25,26,41,71–73]. This approach is not underpinned by dimensionless forms but assumes that scaling can be viewed as an imagined process in which space itself is contracted or expanded. The process is "metaphysical" in the sense that it cannot be achieved physically but nevertheless can be imagined and defined in very precise mathematical terms. Central to the new approach is the projection of the governing physics, described on a scaled space, onto the original full-scale space. This projection has the effect of exposing all possible scale dependencies (either explicitly or implicitly), transforming the scaling problem into one where the objective is to reveal hidden scale dependencies. The revealing of hidden dependencies is efficiently achieved with the application of scale invariances and unlike dimensional analysis there exists more than one invariance. There exists in fact a countable infinite number of scale invariances but with each

invariance linked to the number of scaled experiments involved there exists practical limits on the approach.

A novel aspect of the study presented in this paper is the examination of the application of the new approach to nonlinear structural systems. The focus on discrete element modelling is particularly advantageous to the finite similitude theory as it provides a means to set free variables that exist with the theory. It is very important to appreciate that similitude rules do not constrain behaviours in the scaled experiments but provide the means to connect experiments across the scales. It is necessary therefore to have a means to examine the systems involved prior to applying the similitude rules to the physical experiments. Discrete representations are shown to provide a highly efficient approach to achieve this and allow for the initial exploration of the benefits of similitude in any experimental study.

The finite similitude theory although explained elsewhere [28,41] is re-examined in brief in Sec. 2 for the sake of readability, but also to bring into focus the limitations of the theory. It is important to appreciate that scale dependencies as previously defined under dimensional analysis can cease to be scale dependencies under the new theory. Linear dynamic systems are briefly assessed in Sec. 3 to provide an illustration how the scaling theory is applied to confirm that replica scaling with a single scaled experiment is not representative. Examined in Sec. 4 are aspects relating to the scaling of nonlinear FVDs, which are critical items in structures where passive control is a requirement. Friction is the focus of Sec. 5 and on the stick-slip phenomenon and its analysis through scaled experimentation. Nonlinear springs are introduced in Sec. 6, where it is revealed just how flexible the invariance founded on two scaled experiments can be. Overall, the paper demonstrates that the new similitude rule can offer practical experimental solutions to problems that cannot be tackled by one scaled experiment. The paper ends with a set of conclusions.

2. Finite similitude in brief

The finite similitude theory brings together several concepts to provide a generic scaling theory that in principle can be applied to all physics. The starting point is space scaling and the idea that space itself can be distorted, and that through space distortion objects can be scaled. Such objects might include such things as cities,

buildings, laboratories, machinery, experimental rigs down to individual components and specimens. Once space scaling is quantified mathematically, attention turns to the effect such a process has on the underpinning physics of interest. The theory is a little unusual in this respect in that it requires that transport equations in their integral form [27] are considered. The reason for this is that this form immediately involves geometrical measures (e.g., volume and area), which are first and foremost central to any scaling effect that takes place. Point based formulations founded on partial or ordinary differential equations do not provide this feature and consequently are not suitable. Ultimately however the theory does provide point-based identities although imperceptibly connecting spatial points in scaled and unscaled spaces. The approach necessitates a very precise description of control volume movement and the formulation presented below follows the approach first formulated in reference [74]. With transport forms defined on a scaled space a critically important projection to the physical full-scale space is considered. This projection is key to the whole concept as it provides the means to describe all scale dependencies on the physical space. Scale invariances can then be applied and integrated to link scaled experiments, whose number depends on the invariance chosen. The whole approach is exact involving no approximations and provides new similitude rules for experimental design.

2.1. A brief recap on space scaling

As mentioned above the starting point of the finite similitude theory is the concept of space scaling, which happens to be a physically intuitive approach. The structural system of interest is tethered to the space it resides in, in the sense that it is immediately affected, i.e., is contracted/expanded by the contraction/expansion of space. The starting point of any analysis in structural dynamics is the stipulation of suitable inertial frames for both the physical and trial spaces. The full-scale system of interest sits in the physical space with the scaled experiment residing in the trial space. With subscripts "ts" and "ps" denoting trial and physical spaces, respectively the assumed orthogonal inertial coordinate systems are labelled by $\boldsymbol{x}_{ts}$ and $\boldsymbol{x}_{ps}$. With Newtonian physics assumed, two absolute temporal measures for time are introduced in each space and are labelled by t_{ps} and t_{ts}, and are related by the differential relationship $dt_{ts} = g dt_{ps}$, where g is a positive parameter. Space scaling is easy to define mathematically and for isotropic scaling and is defined by a

temporally invariant affine map $\boldsymbol{x}_{ps} \mapsto \boldsymbol{x}_{ts}$, which in differential terms takes the form $d\boldsymbol{x}_{ts} = \beta d\boldsymbol{x}_{ps}$ (i.e. $dx^i_{ts} = \beta dx^i_{ps}$), where β is a positive parameter. Space contraction, which tends to be of principle interest is provided by $0 < \beta < 1$, with no scaling if $\beta = 1$ and expansion for $1 < \beta$. Note from references [23,24,26,75] that the theory of finite similitude is underpinned by physics described on synchronised moving controls. Depicted in Fig. 1 is the motion of control volume Ω^*_{ts} in the trial-space described mathematically by a velocity field $\boldsymbol{v}^*_{ts}$. All motion is quantified with reference to something else and in this case the motion is relative to a reference control volume Ω^{*ref}_{ts} (the set of coordinate points χ_{ts}). The synchronised motion of the control volumes Ω^*_{ts} and Ω^*_{ps} in the trial and physical spaces are depicted in Fig. 1, where coordinate point $\boldsymbol{x}^*_{ts}$ moves with Ω^*_{ts} with velocity $\boldsymbol{v}^*_{ts}$ and coordinate point $\boldsymbol{x}^*_{ps}$ moves with Ω^*_{ps} with velocity $\boldsymbol{v}^*_{ps}$. The control volumes (being regions of space) are affected by space scaling and consequently are related by the map $d\boldsymbol{x}^*_{ts} = \beta d\boldsymbol{x}^*_{ps}$ and since $dt_{ts} = g dt_{ps}$, the field-velocity relationship $\boldsymbol{v}^*_{ts} = g^{-1}\beta \boldsymbol{v}^*_{ps}$ applies.

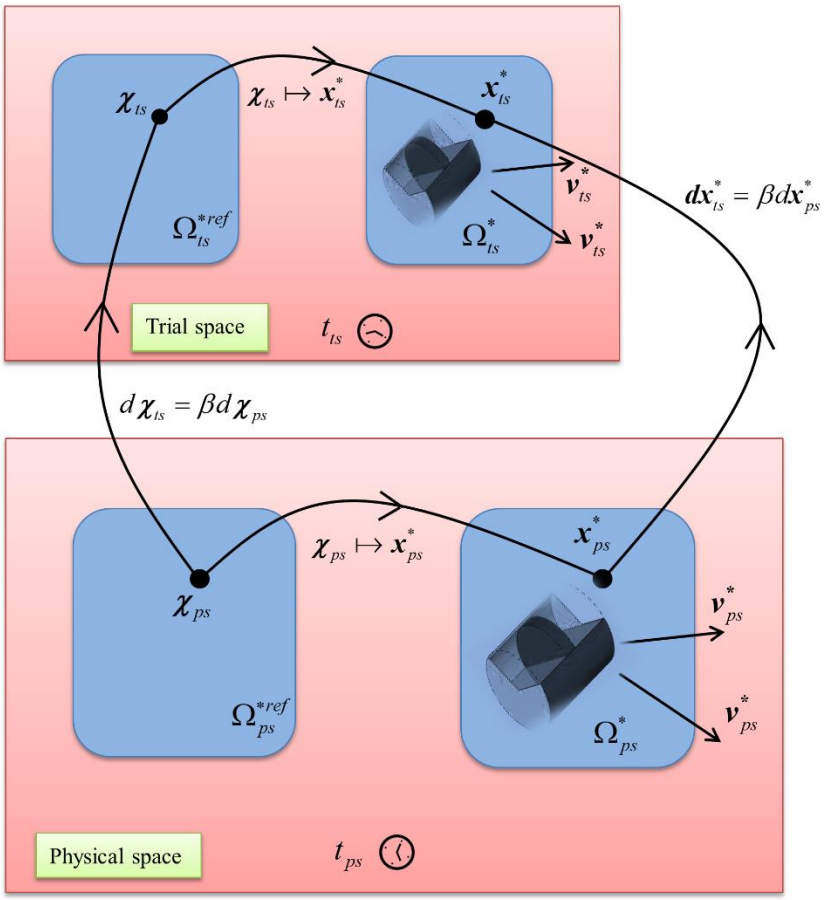

Figure 1: 2D schematic of synchronous control volumes Ω^*_{ts} and Ω^*_{ps} moving while containing a moving dashpot.

Figure 1: 2D schematic of synchronous control volumes Ω^*_{ts} and Ω^*_{ps} moving while containing a moving dashpot.

2.2. Projected structural dynamics in transport form

Four transport equations are of interest in finite similitude for structural dynamics, which are those for conservation of volume, mass and momentum, and the non-conserved movement equation introduced by Davey and Darvizeh [48],

$$\frac{D^*}{D^* t_{ts}} \int_{\Omega^*_{ts}} d\Omega^*_{ts} - \int_{\Gamma^*_{ts}} \boldsymbol{v}^*_{ts} \cdot \boldsymbol{n}_{ts} d\Gamma^*_{ts} = 0 \tag{1a}$$

$$\frac{D^*}{D^* t_{ts}} \int_{\Omega^*_{ts}} \rho_{ts} d\Omega^*_{ts} + \int_{\Gamma^*_{ts}} \rho_{ts} \left(\boldsymbol{v}_{ts} - \boldsymbol{v}^*_{ts} \right) \cdot \boldsymbol{n}_{ts} d\Gamma^*_{ts} = 0 \tag{1b}$$

$$\frac{D^*}{D^*t_{ts}}\int_{\Omega^*_{ts}}\rho_{ts}\boldsymbol{v}_{ts}d\Omega^*_{ts}+\int_{\Gamma^*_{ts}}\rho_{ts}\boldsymbol{v}_{ts}\left(\boldsymbol{v}_{ts}-\boldsymbol{v}^*_{ts}\right)\cdot\boldsymbol{n}_{ts}d\Gamma^*_{ts}-\int_{\Gamma^*_{ts}}\boldsymbol{\sigma}_{ts}\cdot\boldsymbol{n}_{ts}d\Gamma^*_{ts}-\int_{\Omega^*_{ts}}\rho_{ts}\boldsymbol{b}_{ts}d\Omega^*_{ts}=0 \tag{1c}$$

$$\frac{D^*}{D^*t_{ts}}\int_{\Omega^*_{ts}}\rho_{ts}\boldsymbol{u}_{ts}d\Omega^*_{ts}+\int_{\Gamma^*_{ts}}\rho_{ts}\boldsymbol{u}_{ts}\left(\boldsymbol{v}_{ts}-\boldsymbol{v}^*_{ts}\right)\cdot\boldsymbol{n}_{ts}d\Gamma^*_{ts}-\int_{\Omega^*_{ts}}\rho_{ts}\boldsymbol{v}_{ts}d\Omega^*_{ts}=0 \tag{1d}$$

where ρ_{ts} is mass density, $\boldsymbol{u}_{ts}$ is material displacement, $\boldsymbol{v}_{ts}$ is material velocity, $\boldsymbol{\sigma}_{ts}$ is the Cauchy stress tensor, $\boldsymbol{b}_{ts}$ is a body force (force per unit mass), and $\boldsymbol{n}_{ts}$ is an outward pointing unit normal on boundary Γ^*_{ts} of the control volume Ω^*_{ts}.

Note that the temporal derivative $\frac{D^*}{D^*t_{ts}}$ in Eq. (1) signifies that the control volume Ω^*_{ts} is moving relative to Ω^{*ref}_{ts} as depicted in Fig. 1, and this explains the presence of the velocity field $\boldsymbol{v}^*_{ts}$ appearing in these equations. The most significant equation is Eq. (1c), and for most practical problems in structural mechanics, this equation can be sufficient. However, other considerations necessitate the inclusion of additional equations with finite similitude. Eq. (1a) is somewhat unusual and never features in structural dynamics because it has no field associated with it but is considered here nevertheless to enforce the synchronous velocity field relationship $\boldsymbol{v}^*_{ts}=g^{-1}\beta\boldsymbol{v}^*_{ps}$. Similarly, Eq. (1b), the continuity equation, has little role to play in most practical structural problems as density is invariably set to a constant but with finite similitude and physical modelling there exists the possibility that materials could be changed in the scaled models and some account must be made to accommodate this possibility. The equation for non-conserved movement, Eq. (1d), was first introduced by Davey and Darvizeh in reference [27], and has the effect of making displacement explicit in solid-mechanics type analysis. It is important to appreciate that there is no barrier to including more equations (see reference [52] for inclusion of a transport equation for energy) as the physics dictates in the problems under study.

The most important transformation critical to the whole approach can now be applied with the projection of Eqs. (1) onto the physical space. This has the effect of exposing all scale dependencies and involves the substitution of $d\Omega^*_{ts}=\beta^3 d\Omega^*_{ps}$, $\boldsymbol{n}_{ts}d\Gamma^*_{ts}=\beta^2\boldsymbol{n}_{ps}d\Gamma^*_{ps}$, $dt_{ts}=gdt_{ps}$ into Eqs. (1). Additionally each equation is multiplied throughout by non-zero scaling parameters α_0^1, α_0^ρ, α_0^v and α_0^u,

respectively (whose role will be made clear) and time scalar g. This procedure produces the following equations:

$$\alpha_0^1 T_0^1(\beta) = \frac{D^*}{D^* t_{ps}} \int_{\Omega_{ps}^*} \alpha_0^1 \beta^3 d\Omega_{ps}^* - \int_{\Gamma_{ps}^*} \alpha_0^1 \beta^3 \boldsymbol{v}_{ps}^* \cdot \boldsymbol{n}_{ps} d\Gamma_{ps}^* = 0 \tag{2a}$$

$$\alpha_0^\rho T_0^\rho(\beta) = \frac{D^*}{D^* t_{ps}} \int_{\Omega_{ps}^*} \alpha_0^\rho \beta^3 \rho_{ts} d\Omega_{ps}^* + \int_{\Gamma_{ps}^*} \alpha_0^\rho \beta^3 \rho_{ts} \left(\boldsymbol{V}_{ps} - \boldsymbol{v}_{ps}^*\right) \cdot \boldsymbol{n}_{ps} d\Gamma_{ps}^* = 0 \tag{2b}$$

$$\alpha_0^\nu T_0^\nu(\beta) = \frac{D^*}{D^* t_{ps}} \int_{\Omega_{ps}^*} \left(\alpha_0^\nu g^{-1} \beta\right) \beta^3 \rho_{ts} \boldsymbol{V}_{ps} d\Omega_{ts}^* + \int_{\Gamma_{ps}^*} \left(\alpha_0^\nu g^{-1} \beta\right) \beta^3 \rho_{ts} \boldsymbol{V}_{ps} \left(\boldsymbol{V}_{ts} - \boldsymbol{v}_{ps}^*\right) \cdot \boldsymbol{n}_{ps} d\Gamma_{ps}^*$$

$$- \int_{\Gamma_{ps}^*} \boldsymbol{\Sigma}_{ps} \cdot \boldsymbol{n}_{ps} d\Gamma_{ps}^* - \int_{\Omega_{ps}^*} \boldsymbol{B}_{ts} d\Omega_{ps}^* = 0 \tag{2c}$$

$$\alpha_0^u T_0^u(\beta) = \frac{D^*}{D^* t_{ps}} \int_{\Omega_{ps}^*} \left(\alpha_0^u \beta\right) \beta^3 \rho_{ts} \boldsymbol{U}_{ps} d\Omega_{ps}^* + \int_{\Gamma_{ps}^*} \left(\alpha_0^u \beta\right) \beta^3 \rho_{ts} \boldsymbol{U}_{ps} \left(\boldsymbol{V}_{ps} - \boldsymbol{v}_{ps}^*\right) \cdot \boldsymbol{n}_{ps} d\Gamma_{ps}^*$$

$$- \int_{\Omega_{ps}^*} \left(\alpha_0^u \beta\right) \beta^3 \rho_{ts} \boldsymbol{V}_{ps} d\Omega_{ps}^* = 0 \tag{2d}$$

where $\boldsymbol{V}_{ps} = \beta^{-1} g \boldsymbol{v}_{ts}$, $\boldsymbol{U}_{ps} = \beta^{-1} \boldsymbol{u}_{ts}$, $\boldsymbol{\Sigma}_{ps} = \alpha_0^\nu g \beta^2 \boldsymbol{\sigma}_{ts}$ and $\boldsymbol{B}_{ts} = \alpha_0^\nu g \beta^3 \rho_{ts} \boldsymbol{b}_{ts}$.

The significance of these equations is that they expose all possible scale dependencies that can feature in scaled structural dynamics. Note the explicit exposure of geometrical measures with the appearance of β^3 and β^2, but also exposed are other hidden dependencies with the fields $\boldsymbol{V}_{ps}(\beta)$, $\boldsymbol{U}_{ps}(\beta)$, $\boldsymbol{\Sigma}_{ps}(\beta)$ and $\boldsymbol{B}_{ps}(\beta)$ being dependent on β. The ability to relate fields and measures to β on the physical space means that the scaling problem has effectively been transformed into one where discovering the behaviour of hidden-field dependencies is the principal focus. In this way the finite similitude theory embraces the presence of scale effects as opposed to ignoring them as in the theory of dimensional analysis (see refs. [23,26,41,72]). The revealing of hidden dependencies can be readily achieved by the application of scale invariances, which are similitude rules that connect information across scaled experiments.

2.3. Scale invariances

Eqs. (2) are of the form $\alpha_0^{\psi} T_0^{\psi} = 0$, with ψ set to 1, ρ, v and u, and where α_0^{ψ} are scalars that are functions of β. These scalars play a critical role and facilitate the unified application of invariances to all the transport equations, which would not be possible without their presence as is shown below. The simplest scale invariance possible is to assume that all the transport equations $\alpha_0^{\psi} T_0^{\psi}(\beta) = 0$ do not in fact depend on β, which of course is unlikely in practice. However, this assumption is readily captured by the identity,

$$\frac{d}{d\beta}\left(\alpha_0^{\psi} T_0^{\psi}\right) \equiv 0 \qquad (3)$$

where the equality sign "≡" means identically zero and infers that the transport equations vanish under the derivative.

The application details surrounding this identity termed *zeroth-order finite similitude* can be found in references [23,26,72]. The scaling parameters α_0^{ψ} are being set to eliminate β from $\alpha_0^{\psi} T_0^{\psi}(\beta) = 0$ to satisfy Eq. (3). In the volume transport equation Eq. (2a) for example this is achieved with $\alpha_0^1 = \beta^{-3}$ and note that $\alpha_0^1(1) = 1$, which is a requirement imposed on all the scalars α_0^{ψ} to ensure that $\alpha_0^{\psi} T_0^{\psi}(1) = T_{ps}^{\psi}$. The field identities arising out of this Eqs. (2) are presented in Table 1 but also [41,72], so are not considered further here.

Table 5:1: Zeroth-order relationships arising out of Eq. (3).

Quantity/ Equations	Scalar identities	Field relationships	Transfer terms	Source terms
Volume Eq. (2a)	$\alpha_0^1 = \beta^{-3}$	$\boldsymbol{v}_{ps}^{*} = g\beta^{-1}\boldsymbol{v}_{ts}^{*}$		

Mass Eq. (2b)		$\rho_{ps} = \alpha_0^{\rho}\beta^3\rho_{ts}$ $\boldsymbol{V}_{ps} = \boldsymbol{v}_{ps} = g\beta^{-1}\boldsymbol{v}_{ts}$		
Momentum Eq. (2c)	$\alpha_0^{v} = g\beta^{-1}\alpha_0^{\rho}$	$\boldsymbol{V}_{ps} = \boldsymbol{v}_{ps} = g\beta^{-1}\boldsymbol{v}_{ts}$	$\boldsymbol{\Sigma}_{ps} = \boldsymbol{\sigma}_{ps} = \alpha_0^{v} g\beta^2\boldsymbol{\sigma}_{ts}$	$\boldsymbol{B}_{ps} = \rho_{ps}\boldsymbol{b}_{ps} = \alpha_0^{v} g\beta^3\rho_{ts}\boldsymbol{b}_{ts}$
Movement Eq. (2d)	$\alpha_0^{u} = \beta^{-1}\alpha_0^{\rho}$	$\boldsymbol{U}_{ps} = \boldsymbol{u}_{ps} = \beta^{-1}\boldsymbol{u}_{ts}$		$\boldsymbol{V}_{ps} = \boldsymbol{v}_{ps} = g\beta^{-1}\boldsymbol{v}_{ts}$

The following definition provides a recursive relationship that facilitates the creation of higher forms of similitude rules:

2.4. Definition (High-order finite similitude)

The finite similitude rule of k[th] order is identified with the lowest order derivative that satisfies,

$$T_{k+1}^{\psi} = \frac{d}{d\beta}\left(\alpha_k^{\psi} T_k^{\psi}\right) \equiv 0 \qquad (4)$$

for all $\beta > 0$, and where $\alpha_0^{\psi} T_0^{\psi}$ is defined by Eqs. (2) and the scalars α_k^{ψ} are functions of β with $\alpha_k^{\psi}(1) = 1$, and where the symbol "≡" signifies identically zero in Eq. (4).

The motivation for definition 2.1 is the expectation that higher derivatives are involved in similitude rules involving more than one scaled experiment along with the requirement that lower order rules are contained in higher-order forms. If Eq. (3) is not satisfied, then consideration is given to the identity,

$$\alpha_1^{\psi} T_1^{\psi} = \alpha_1^{\psi}\frac{d}{d\beta}\left(\alpha_0^{\psi} T_0^{\psi}\right) \qquad (5)$$

where $\alpha_1^{\psi}(1) = 1$ and similarly in accordance with Eq. (4) the similitude condition

$$T_2^{\psi} = \frac{d}{d\beta}\left(\alpha_1^{\psi} T_1^{\psi}\right) = \frac{d}{d\beta}\left(\alpha_1^{\psi}\frac{d}{d\beta}\left(\alpha_0^{\psi} T_0^{\psi}\right)\right) \equiv 0 \qquad (6)$$

provides the identity for *first-order finite similitude* involving not one but two derivatives.

Since the similitude rules are nested it is possible to take forward the zeroth-order identities $\rho_{ps} = \alpha_0^{\rho}\beta^3\rho_{ts}$, $\alpha_0^{v} = g\beta^{-1}\alpha_0^{\rho}$ and $\alpha_0^{u} = \beta^{-1}\alpha_0^{\rho}$ and substitute them in Eqs. (3) to obtain

$$\alpha_0^{\rho}T_0^{\rho}(\beta) = \frac{D^*}{D^*t_{ps}}\int_{\Omega_{ps}^*}\rho_{ps}d\Omega_{ps}^* + \int_{\Gamma_{ps}^*}\rho_{ps}\left(\boldsymbol{V}_{ps} - \boldsymbol{v}_{ps}^*\right)\cdot\boldsymbol{n}_{ps}d\Gamma_{ps}^* = 0 \tag{7a}$$

$$\alpha_0^{v}T_0^{v}(\beta) = \frac{D^*}{D^*t_{ps}}\int_{\Omega_{ts}^*}\rho_{ps}\boldsymbol{V}_{ps}d\Omega_{ts}^* + \int_{\Gamma_{ps}^*}\rho_{ps}\boldsymbol{V}_{ps}\left(\boldsymbol{v}_{ts} - \boldsymbol{v}_{ps}^*\right)\cdot\boldsymbol{n}_{ps}d\Gamma_{ps}^* - \int_{\Gamma_{ps}^*}\boldsymbol{\Sigma}_{ts}\cdot\boldsymbol{n}_{ps}d\Gamma_{ps}^* - \int_{\Omega_{ps}^*}\boldsymbol{B}_{ts}d\Omega_{ps}^* = 0 \tag{7b}$$

$$\alpha_0^{u}T_0^{u}(\beta) = \frac{D^*}{D^*t_{ps}}\int_{\Omega_{ps}^*}\rho_{ps}\boldsymbol{U}_{ts}d\Omega_{ps}^* + \int_{\Gamma_{ps}^*}\rho_{ps}\boldsymbol{U}_{ps}\left(\boldsymbol{v}_{ps} - \boldsymbol{v}_{ps}^*\right)\cdot\boldsymbol{n}_{ps}d\Gamma_{ps}^* - \int_{\Omega_{ps}^*}\rho_{ps}\boldsymbol{V}_{ps}d\Omega_{ps}^* = 0 \tag{7c}$$

where $\boldsymbol{\Sigma}_{ps} = \alpha_0^{v}g\beta^2\boldsymbol{\sigma}_{ts}$, $\boldsymbol{B}_{ts} = \alpha_0^{v}g\beta^3\rho_{ts}\boldsymbol{b}_{ts} = g^2\beta^{-1}\boldsymbol{b}_{ts}$ and observe that Eq. (2a) satisfies Eq. (4), and therefore plays no part in first-order theory.

All the theory presented thus far is exact apart from the substitution of the zeroth-order term $\left(\boldsymbol{v}_{ps} - \boldsymbol{v}_{ps}^*\right)\cdot\boldsymbol{n}_{ps}$ in place of $\left(\boldsymbol{V}_{ps} - \boldsymbol{v}_{ps}^*\right)\cdot\boldsymbol{n}_{ps}$ in equations Eq. (7b) and Eq. (7c). This reflects the fact that the convective term $\boldsymbol{V}_{ps}\left(\boldsymbol{V}_{ps}\cdot\boldsymbol{n}_{ps}\right)$ is typically negligible in solid mechanics but also conveniently sidesteps the need to higher forms of similitude.

2.5. First-order fields

Exact integration of Eq. (6) can be readily achieved using divided differences with the application of a mean-value theorem, which provides:

$$\alpha_1^{\psi}\mathbf{T}_1^{\psi}\left(\beta_2^1\right) \equiv \alpha_1^{\psi}\left(\beta_2^1\right)\frac{\alpha_0^{\psi}\mathbf{T}_0^{\psi}(\beta_1) - \alpha_0^{\psi}\mathbf{T}_0^{\psi}(\beta_2)}{\beta_1 - \beta_2} \tag{8a}$$

$$\alpha_1^{\psi}\mathbf{T}_1^{\psi}\left(\beta_1^0\right) \equiv \alpha_1^{\psi}\left(\beta_1^0\right)\frac{\alpha_0^{\psi}\mathbf{T}_0^{\psi}(\beta_0) - \alpha_0^{\psi}\mathbf{T}_0^{\psi}(\beta_1)}{\beta_0 - \beta_1} \tag{8b}$$

where $\beta_2 \le \beta_2^1 \le \beta_1$ and $\beta_1 \le \beta_1^0 \le \beta_0$, and where β_2 and β_1 are the scales for the trial-space experiments with $\beta_0 = 1$ signifying the physical space (i.e., full scale experimentation).

Note that the direct integration of Eq. (6) between the limits β_2^1 and β_1^0 provides the identity $\alpha_1^{\psi} T_1^{\psi}\left(\beta_1^0\right) \equiv \alpha_1^{\psi} T_1^{\psi}\left(\beta_2^1\right)$, and consequently on substitution of Eqs. (8) gives rise to the key first-order similitude rule for scaled transport equation, which is

$$\alpha_0^{\psi} \mathbb{T}_0^{\psi}\left(\beta_0\right) \equiv \alpha_0^{\psi} \mathbb{T}_0^{\psi}\left(\beta_1\right) + R_1^{\psi}\left(\alpha_0^{\psi} \mathbb{T}_0^{\psi}\left(\beta_1\right) - \alpha_0^{\psi} \mathbb{T}_0^{\psi}\left(\beta_2\right)\right) \tag{9}$$

where

$$R_1^{\psi} = \left(\frac{\alpha_1^{\psi}\left(\beta_2^1\right)}{\alpha_1^{\psi}\left(\beta_1^0\right)}\right)\left(\frac{\beta_0 - \beta_1}{\beta_1 - \beta_2}\right) \tag{10}$$

which leads immediately to the field relationships listed in Table 2, but note that R_1^{ψ} is in the form of a parameter due to indeterminacy of α_1^{ψ} and consistent velocity expressions necessitates that $R_1 = R_1^{\rho} = R_1^{v} = R_1^{u}$ imposed by $\alpha_1^{\rho} = \alpha_1^{v} = \alpha_1^{u}$.

Table 5:2: Zeroth and first order field relationships.

Quantity/ Equations	Zeroth order field relationships	First order field relationships
Mass Eq.(7a)	$\rho_{ps} = \left(\alpha_0^{\rho} \beta^3 \rho_{ts}\right)\left(\beta_1\right)$ $\boldsymbol{V}_{ps} = \boldsymbol{v}_{ps} = \left(g\beta^{-1}\boldsymbol{v}_{ts}\right)\left(\beta_1\right)$	$\boldsymbol{v}_{ps} = \boldsymbol{V}_{ps}\left(\beta_1\right) + R_1^{\rho}\left(\boldsymbol{V}_{ps}\left(\beta_1\right) - \boldsymbol{V}_{ps}\left(\beta_2\right)\right)$
Momentum Eq.(7b)	$\boldsymbol{\Sigma}_{ps}\left(\beta_1\right) = \boldsymbol{\sigma}_{ps} = \left(\alpha_0^{v} g \beta^2 \boldsymbol{\sigma}_{ts}\right)\left(\beta_1\right),$ $\boldsymbol{V}_{ps}\left(\beta_1\right) = \boldsymbol{v}_{ps} = \left(g\beta^{-1}\boldsymbol{v}_{ts}\right)\left(\beta_1\right)$	$\boldsymbol{\sigma}_{ps} = \boldsymbol{\Sigma}_{ps}\left(\beta_1\right) + R_1^{v}\left(\boldsymbol{\Sigma}_{ps}\left(\beta_1\right) - \boldsymbol{\Sigma}_{ps}\left(\beta_2\right)\right)$ $\boldsymbol{b}_{ps} = \boldsymbol{B}_{ps}\left(\beta_1\right) + R_1^{v}\left(\boldsymbol{B}_{ps}\left(\beta_1\right) - \boldsymbol{B}_{ps}\left(\beta_2\right)\right)$ $\boldsymbol{v}_{ps} = \boldsymbol{V}_{ps}\left(\beta_1\right) + R_1^{v}\left(\boldsymbol{V}_{ps}\left(\beta_1\right) - \boldsymbol{V}_{ps}\left(\beta_2\right)\right)$
Movement Eq.(7c)	$\boldsymbol{U}_{ps}\left(\beta_1\right) = \boldsymbol{u}_{ps} = \left(\beta^{-1}\boldsymbol{u}_{ts}\right)\left(\beta_1\right)$ $\boldsymbol{V}_{ps}\left(\beta_1\right) = \boldsymbol{v}_{ps} = \left(g\beta^{-1}\boldsymbol{v}_{ts}\right)\left(\beta_1\right)$	$\boldsymbol{u}_{ps} = \boldsymbol{U}_{ps}\left(\beta_1\right) + R_1^{u}\left(\boldsymbol{U}_{ps}\left(\beta_1\right) - \boldsymbol{U}_{ps}\left(\beta_2\right)\right)$ $\boldsymbol{v}_{ps} = \boldsymbol{V}_{ps}\left(\beta_1\right) + R_1^{u}\left(\boldsymbol{V}_{ps}\left(\beta_1\right) - \boldsymbol{V}_{ps}\left(\beta_2\right)\right)$

A feature of the finite similitude approach is that constitutive laws do not feature in its formulation since all the fields required for the physical space can be obtained from existing fields. Shown in Table 3 are typical fields of interest in structural dynamics and note how relationships for both stress and strain exist for small strain

theory. Constitutive laws can play a role in the setting of free parameters g_1, g_2 and R_1 as required, but in order to apply the new theory to structural dynamics some understanding of the nonlinearities involved is required.

Table 5:3: Zeroth and first order field relationships for practical use.

Physical quantity	Zeroth order field relationships	First order field relationships
Density	$\rho_{ps} = \alpha_{01}^{\rho}\beta_1^3\rho_{ts1}$	
Velocity	$\boldsymbol{v}_{ps} = g_1\beta_1^{-1}\boldsymbol{v}_{ts1}$	$\boldsymbol{v}_{ps} = g_1\beta_1^{-1}\boldsymbol{v}_{ts1} + R_1\left(g_1\beta_1^{-1}\boldsymbol{v}_{ts1} - g_2\beta_2^{-1}\boldsymbol{v}_{ts2}\right)$
Displacement	$\boldsymbol{u}_{ps} = \beta_1^{-1}\boldsymbol{u}_{ts1}$	$\boldsymbol{u}_{ps} = \beta_1^{-1}\boldsymbol{u}_{ts1} + R_1\left(\beta_1^{-1}\boldsymbol{u}_{ts1} - \beta_2^{-1}\boldsymbol{u}_{ts2}\right)$
Acceleration	$\boldsymbol{a}_{ps} = g_1^2\beta_1^{-1}\boldsymbol{a}_{ts1}$	$\boldsymbol{a}_{ps} = g_1^2\beta_1^{-1}\boldsymbol{a}_{ts1} + R_1\left(g_1^2\beta_1^{-1}\boldsymbol{a}_{ts1} - g_2^2\beta_2^{-1}\boldsymbol{a}_{ts2}\right)$
Small strain	$\boldsymbol{\varepsilon}_{ps} = \boldsymbol{\varepsilon}_{ts1}$	$\boldsymbol{\varepsilon}_{ps} = \boldsymbol{\varepsilon}_{ts1} + R_1\left(\boldsymbol{\varepsilon}_{ts1} - \boldsymbol{\varepsilon}_{ts2}\right)$
Strain rate	$\dot{\boldsymbol{\varepsilon}}_{ps} = g_1\dot{\boldsymbol{\varepsilon}}_{ts1}$	$\dot{\boldsymbol{\varepsilon}}_{ps} = g_1\dot{\boldsymbol{\varepsilon}}_{ts1} + R_1\left(g_1\dot{\boldsymbol{\varepsilon}}_{ts1} - g_2\dot{\boldsymbol{\varepsilon}}_{ts2}\right)$
Stress	$\boldsymbol{\sigma}_{ps} = \alpha_{01}^{v}g_1\beta_1^2\boldsymbol{\sigma}_{ts1}$	$\boldsymbol{\sigma}_{ps} = \alpha_{01}^{v}g_1^2\beta_1\boldsymbol{\sigma}_{ts1} + R_1\left(\alpha_{01}^{v}g_1^2\beta_1\boldsymbol{\sigma}_{ts1} - \alpha_{02}^{v}g_2^2\beta_2\boldsymbol{\sigma}_{ts2}\right)$
Force	$\boldsymbol{F}_{ps} = \alpha_{01}^{v}g_1\boldsymbol{F}_{ts1}$	$\boldsymbol{F}_{ps} = \alpha_{01}^{v}g_1\boldsymbol{F}_{ts1} + R_1\left(\alpha_{01}^{v}g_1\boldsymbol{F}_{ts1} - \alpha_{02}^{v}g_2\boldsymbol{F}_{ts2}\right)$

3. Linear dynamic systems

Prior to the analysis of nonlinear systems, it is useful to examine in brief, a linear mass-spring-damper system [36]. Consider then the "forces" $\boldsymbol{F}_{ts}^{i} = m_{ts}\boldsymbol{a}_{ts}$, $\boldsymbol{F}_{ts}^{d} = -c_{ts}\boldsymbol{v}_{ts}$ and $\boldsymbol{F}_{ts}^{s} = -k_{ts}\boldsymbol{u}_{ts}$ in a series free-vibration arrangement satisfying the equation $\boldsymbol{F}_{ts}^{i} = \boldsymbol{F}_{ts}^{d} + \boldsymbol{F}_{ts}^{s}$, where in the trial space, m_{ts} is mass, c_{ts} is a damping coefficient and k_{ts} is a spring stiffness. To understand how this equation scales for a single scaled experiment it is necessary examine the zeroth-order relationship $\boldsymbol{F}_{ps} = \alpha_0^{v}g\boldsymbol{F}_{ts}$ in Table 3. The inertial relationship $\boldsymbol{F}_{ts}^{i} = m_{ts}\boldsymbol{a}_{ts}$ on application of the

identity $\boldsymbol{F}_{ps} = \alpha_0^v g \boldsymbol{F}_{ts}$ and substitution of $\boldsymbol{a}_{ps} = g^2 \beta^{-1} \boldsymbol{a}_{ts}$ (see Table 3) and $\alpha_0^v = g\beta^{-1}\alpha_0^\rho$ (see Table 1) gives,

$$\boldsymbol{F}_{ps}^i = m_{ps}\boldsymbol{a}_{ps} = m_{ps} g^2 \beta^{-1} \boldsymbol{a}_{ts} = \alpha_0^v g \boldsymbol{F}_{ts}^i = \alpha_0^v g m_{ts} \boldsymbol{a}_{ts} = \alpha_0^\rho g^2 \beta^{-1} m_{ts} \boldsymbol{a}_{ts} \tag{11}$$

which necessitates that $\alpha_0^\rho m_{ts} = m_{ps}$.

Similarly, the spring force relationship $\boldsymbol{F}_{ts}^s = -k_{ts}\boldsymbol{u}_{ts}$ on substitution of $\boldsymbol{u}_{ps} = \beta^{-1}\boldsymbol{u}_{ts}$ (see Table 3) gives,

$$\boldsymbol{F}_{ps}^s = -k_{ps}\boldsymbol{u}_{ps} = -k_{ps}\beta^{-1}\boldsymbol{u}_{ts} = \alpha_0^v g \boldsymbol{F}_{ts}^s = -\alpha_0^v g k_{ts} \boldsymbol{a}_{ts} = -\alpha_0^\rho g^2 \beta^{-1} k_{ts} \boldsymbol{u}_{ts}$$

(12)

which requires $\alpha_0^\rho g^2 k_{ts} = k_{ps}$ and finally $\boldsymbol{F}_{ts}^d = -c_{ts}\boldsymbol{v}_{ts}$ on substitution of $\boldsymbol{v}_{ps} = g\beta^{-1}\boldsymbol{v}_{ts}$ (see Table 3) gives,

$$\boldsymbol{F}_{ps}^d = -c_{ps}\boldsymbol{v}_{ps} = -c_{ps} g\beta^{-1}\boldsymbol{v}_{ts} = \alpha_0^v g \boldsymbol{F}_{ts}^d = -\alpha_0^v g c_{ts} \boldsymbol{v}_{ts} = -\alpha_0^\rho g^2 \beta^{-1} c_{ts} \boldsymbol{v}_{ts} \tag{13}$$

and the requirement $\alpha_0^\rho g c_{ts} = c_{ps}$.

In the situation where identical material used in the trial and physical models, then the zeroth-order relationship $\rho_{ps} = \alpha_0^\rho \beta^3 \rho_{ts}$ (see Table 2) with $\rho_{ps} = \rho_{ts}$ gives $\alpha_0^\rho = \beta^{-3}$ and therefore the relationships $\alpha_0^\rho m_{ts} = m_{ps}$, $\alpha_0^\rho g^2 k_{ts} = k_{ps}$ and $\alpha_0^\rho g c_{ts} = c_{ps}$ reduce to $m_{ts} = \beta^3 m_{ps}$, $k_{ts} = \beta^3 g^{-2} k_{ps}$ and $c_{ts} = \beta^3 g^{-1} c_{ps}$, respectively. To proceed further and determine the relationship between the time scalar g and β requires information about constitutive behaviour of the spring material and the damping fluid used in the dashpot. An elastic response is expected for the spring material satisfying a constitutive model of the form $\boldsymbol{\sigma}_{ts} = \boldsymbol{C}_{ts} : \boldsymbol{\varepsilon}_{ts}$ (Hooke's law), where $\boldsymbol{C}_{ts}$ is the elasticity tensor. Application of the identity $\boldsymbol{\sigma}_{ps} = \alpha_0^v g \beta^2 \boldsymbol{\sigma}_{ts}$ and $\boldsymbol{\varepsilon}_{ps} = \boldsymbol{\varepsilon}_{ts}$ from Table 3 provides,

$$\boldsymbol{\sigma}_{ps} = \boldsymbol{C}_{ps} : \boldsymbol{\varepsilon}_{ps} = \boldsymbol{C}_{ps} : \boldsymbol{\varepsilon}_{ts} = \alpha_0^v g \beta^2 \boldsymbol{\sigma}_{ts} = \alpha_0^v g \beta^2 \boldsymbol{C}_{ts} : \boldsymbol{\varepsilon}_{ts} = \alpha_0^\rho g^2 \beta \boldsymbol{C}_{ts} : \boldsymbol{\varepsilon}_{ts} = g^2 \beta^{-2} \boldsymbol{C}_{ts} : \boldsymbol{\varepsilon}_{ts} \tag{14}$$

which requires $g^2 \beta^{-2} \boldsymbol{C}_{ts} = \boldsymbol{C}_{ps}$, and for an identical material must satisfy $\boldsymbol{C}_{ts} = \boldsymbol{C}_{ps}$, and therefore $g = \beta$ and the stiffness relationship is $k_{ts} = \beta k_{ps}$.

Substitution of $g = \beta$ into the dashpot relationship $c_{ts} = \beta^3 g^{-1} c_{ps}$ gives $c_{ts} = \beta^2 c_{ps}$, but this relationship provides a conflict. The reason for this is because the damping

fluid might be anticipated to behave as a Newtonian fluid and satisfy a relationship of the form $\boldsymbol{\tau}'_{ts} = 2\mu_{ts}\dot{\boldsymbol{\varepsilon}}'_{ts}$, where the dash signifies a reduced tensor and with the assumption of incompressibility gives rise to $\tau_{ts} = 2\mu_{ts}\dot{\boldsymbol{\varepsilon}}_{ts}$, where $\boldsymbol{\sigma}_{ts} = -p_{ts}\boldsymbol{I} + \boldsymbol{\tau}_{ts}$, and where μ_{ts} is (shear) viscosity, p_{ts} is hydrostatic pressure, and $\boldsymbol{I}$ is a unit tensor. Application of the identity $\boldsymbol{\sigma}_{ps} = \alpha_0^{\nu} g\beta^2\boldsymbol{\sigma}_{ts}$ and $\dot{\boldsymbol{\varepsilon}}_{ps} = g\dot{\boldsymbol{\varepsilon}}_{ts}$ from Table 3 provides,

$$\boldsymbol{\tau}_{ps} = 2\mu_{ps}\dot{\boldsymbol{\varepsilon}}_{ps} = 2\mu_{ps}g\dot{\boldsymbol{\varepsilon}}_{ts} = \alpha_0^{\nu} g\beta^2\boldsymbol{\tau}_{ts} = \alpha_0^{\nu} g\beta^2 2\mu_{ts}\dot{\boldsymbol{\varepsilon}}_{ts} = 2\alpha_0^{\rho} g^2\beta\mu_{ts}\dot{\boldsymbol{\varepsilon}}_{ts} = 2g^2\beta^{-2}\mu_{ts}\dot{\boldsymbol{\varepsilon}}_{ts} \tag{15}$$

which requires $\alpha_0^{\rho} g\beta\mu_{ts} = g\beta^{-2}\mu_{ts} = \mu_{ps}$, and for an identical material with $\mu_{ts} = \mu_{ps}$ suggests that $g = \beta^2$, which reduces the expression $c_{ts} = \beta^3 g^{-1} c_{ps}$ to $c_{ts} = \beta c_{ps}$, confirming that a single experiment with identical materials will not provide representative behaviour for the mass-spring-damper system.

4. Scale dependencies of nonlinear fluid viscous dampers

Fluid viscous dampers are recognised as common energy dissipation devices that provide a level of protection to structures from damage inflicted by seismic excitations. The use of this form of damping system is universal and finds use in a multitude of constructions, which includes bridges, low rise buildings to skyscrapers. A damper typically consists of a steel cylinder filled with silicon oil (for dissipation) and a piston. The whole arrangement can be connected between floors and/or beams [77] and are designed according to need. The basic schematic for a fluid viscous damper (FVD) is depicted in Fig. 2, where only the cylinder and piston head arrangement are shown. The nonlinear behaviour of a FVD can be approximated by a simple fractional velocity power law such as,

$$f_D = c_\alpha \, sgn(v)|v|^{\alpha} \tag{16}$$

where f_D is force, v is piston velocity relative to the cylinder, c_α is an experimentally determined damping coefficient, α is the velocity exponent, and the signum function sgn is either plus or minus unity depending on the sign of the relative velocity v.

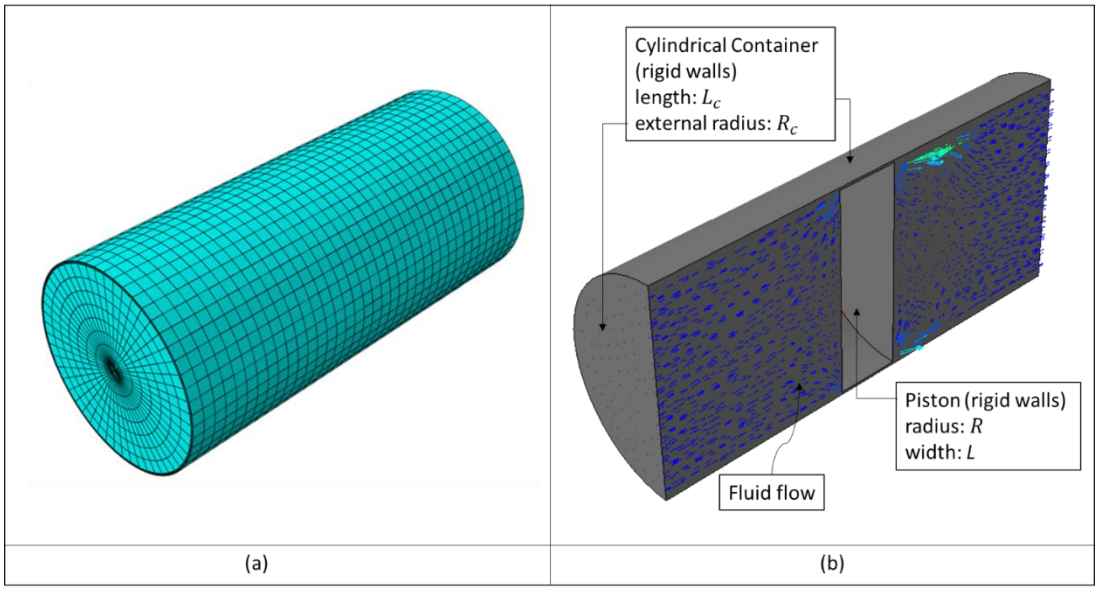

Figure 2: (colour online) 3-D configurations of fluid viscous damper (a) Discretised model using 4-noded linear tetrahedron element type (FC3D4) (b) Fluid flow inside the rigid body of dashpot modelled as rigid walls. The number of elements for full-scale and trial models are identically 44105 and follow the rules of space scaling.

The nonlinearity of the damper is dictated by the velocity exponent α, where linear behaviour is returned for $\alpha = 1$ and Eq. (10) in this case reduces to $f_D = c_1 v$. The velocity exponent α for seismic protection applications is usually in the range of 0.35 – 1 [63,78] with typical curves relating force f_D to velocity v depicted in Fig. 3.

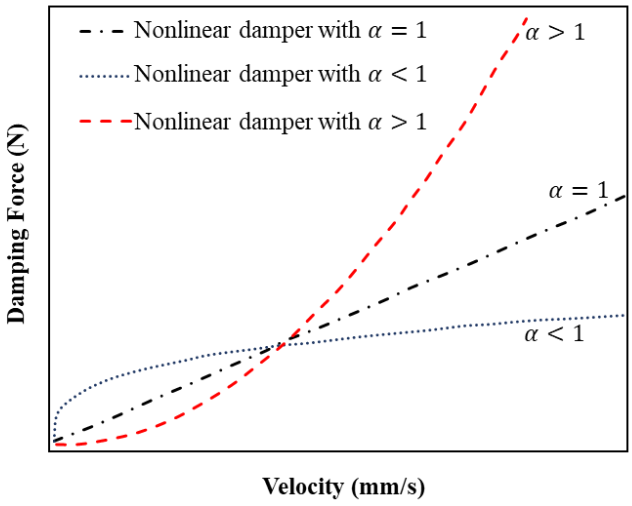

Figure 3: (colour online) Schematic representation of constitutive behaviour of fluid viscous damper. The red and grey curves represent two different nonlinear

behaviours of the FVD while the black curve is force-velocity curve for a linear FVD.

The curves in Fig. 3 display the behaviour of the damper subjected to a sinusoidal excitation $x = x_0 \sin \omega t$, for different values of α, where ω is angular frequency and $v = \dot{x}$. Note how the linear damper encounters high forces if exposed to large velocities, which can be an unwelcome feature. The damping force, for damper designs with velocity exponent in the range of $0 < \alpha < 1$, increases at a relatively lower rate than other conditions [77]. This is a desirable feature and makes nonlinear FVDs particularly attractive for the control and suppression of earthquake loads.

To investigate the scaling of a FVD and to capture more precisely nonlinear behaviours it is of interest to construct a numerical model. A previous study on FVDs detailed in Hou (2008) [79] is replicated here for scaling purposes and is performed in the commercial package ABAQUS/CFD [80]. A particular difficulty with this type of analysis is that it features fluid-solid interaction, which is recognised to be problematic for some solvers. To avoid these problems the analysis performed here considers the piston head to be stationary (also excludes the piston rod) and allows the fluid to flow around it being sourced by the cylinder motion. The detailed presentation is depicted in Fig. 2, and an initial analysis is conducted to verify the results in comparison with those provided by Hou (2008) [79], as confirmed in Fig. 4. The velocity of the flow is defined as sinusoidal with respect to the equation $v = v_{max} \sin \omega t$, where v_{max} is the maximum flow velocity, which is specified as $v_{max} = \omega A$, where ω and A present the angular frequency and oscillation amplitude [81], respectively. The damper is filled with incompressible silicon oil with oil properties selected to emphasise nonlinear behaviour. The density is set as 100,000 kg/m^3 and the dynamic viscosity is 1 kg/ms, with the overall dimensions of the damper tabulated in Table 4. The design of dashpot considered (as depicted in Fig. 2) permits the movement of the fluid from one side of the chamber to the other, and the constitutive behaviour of the fluid is assumed Newtonian (see Sec. 3). An initial analysis based on Eq. (16) and the relationships $\boldsymbol{F}_{ps} = \alpha_0^v g \boldsymbol{F}_{ts}$ and $\boldsymbol{v}_{ps} = g\beta^{-1}\boldsymbol{v}_{ts}$ in Table 3 provides,

$$f_{Dps} = c_{\alpha_{ps}} \operatorname{sgn}\left(v_{ps}\right)\left|v_{ps}\right|^{\alpha_{ps}} = c_{\alpha_{ps}} \operatorname{sgn}\left(g\beta^{-1}v_{ts}\right)\left|g\beta^{-1}v_{ts}\right|^{\alpha_{ps}} = c_{\alpha_{ps}}\left(g\beta^{-1}\right)^{\alpha_{ps}} \operatorname{sgn}\left(v_{ts}\right)\left|v_{ts}\right|^{\alpha_{ps}}$$

$$= \alpha_0^{v} g f_{Dts} = \alpha_0^{v} g c_{\alpha_{ts}} \operatorname{sgn}\left(v_{ts}\right)\left|v_{ts}\right|^{\alpha_{ts}} \tag{17}$$

which requires that,

$$c_{\alpha_{ps}} = \alpha_0^{v} g^{1-\alpha_{ps}} \beta^{\alpha_{ps}} c_{\alpha_{ts}} \left|v_{ts}\right|^{\alpha_{ts}-\alpha_{ps}} = \alpha_0^{\rho} g^{2-\alpha_{ps}} \beta^{\alpha_{ps}-1} c_{\alpha_{ts}} \left|v_{ts}\right|^{\alpha_{ts}-\alpha_{ps}} = g^{2-\alpha_{ps}} \beta^{\alpha_{ps}-4} c_{\alpha_{ts}} \left|v_{ts}\right|^{\alpha_{ts}-\alpha_{ps}} \tag{18}$$

on substitution of $\alpha_0^{v} = g\beta^{-1}\alpha_0^{\rho}$ (see Table 1) and on setting $\alpha_0^{\rho} = \beta^{-3}$ for an identical fluid.

Note additionally from Sec. 3 that a Newtonian fluid requires that $g = \beta^2$, which provides the simplification of Eq. (18) to $c_{\alpha_{ps}} = \beta^{-\alpha_{ps}} c_{\alpha_{ts}} \left|v_{ts}\right|^{\alpha_{ts}-\alpha_{ps}}$. This reduces to the relationship for a linear dashpot (i.e. $c_{\alpha_{ts}} = \beta c_{\alpha_{ps}}$) on setting $\alpha_{ts} = \alpha_{ps} = 1$, and further infers [41] that for a scaled model incorporating an identical damping fluid, it can be anticipated that the velocity exponents are equal, i.e., $\alpha_{ps} = \alpha_{ts}$. This provides a further simplification to the relationship $c_{\alpha_{ps}} = \beta^{-\alpha_{ps}} c_{\alpha_{ts}} \left|v_{ts}\right|^{\alpha_{ts}-\alpha_{ps}}$, which reduces to $c_{\alpha_{ps}} = \beta^{-\alpha_{ps}} c_{\alpha_{ts}}$ with $\alpha_{ps} = \alpha_{ts}$, and is readily confirmed below with numerical analysis. Note that the expectation that $\alpha_{ps} = \alpha_{ts}$ is a consequence of the behaviour of the dashpot being dominated by viscous flow being critically dependent on Reynolds number. Substitution of $\mu_{ps} = \alpha_0^{\rho} g \beta \mu_{ts}$ (to satisfy Eq. (15)), $\rho_{ps} = \alpha_0^{\rho} \beta^3 \rho_{ts}$, $V_{ps} = g\ \beta^{-1} V_{ts}$ (for some velocity) and $D_{ps} = \beta^{-1} D_{ts}$ (for some diameter/length) into Reynolds number Re gives not unexpectedly,

$$\mathrm{Re}_{ps} = \frac{\rho_{ps} V_{ps} D_{ps}}{\mu_{ps}} = \frac{\left(\alpha_0^{\rho}\beta^3\rho_{ts}\right)\left(g\beta^{-1}V_{ts}\right)\left(\beta^{-1}D_{ts}\right)}{\alpha_0^{\rho} g \beta \mu_{ts}} = \frac{\alpha_0^{\rho}\beta^3 g\beta^{-1}\beta^{-1}}{\alpha_0^{\rho} g\beta} \frac{\rho_{ts} V_{ts} D_{ts}}{\mu_{ts}} = \mathrm{Re}_{ts} \tag{19}$$

and note that kinematic viscosity,

$$\nu_{ps} = \frac{\mu_{ps}}{\rho_{ps}} = \frac{\alpha_0^{\rho} g \beta \mu_{ts}}{\alpha_0^{\rho}\beta^3\rho_{ts}} = g\beta^{-2}\nu_{ts} \tag{20}$$

which for $g = \beta^2$ reduces to $\nu_{ps} = \nu_{ts}$ and for $g = \beta$ gives $\nu_{ps} = \beta^{-1}\nu_{ts}$.

Therefore, scaling with an identical damping fluid with $g = \beta^2$ satisfies zeroth-order rules, so non-linear behaviours at full and at scale are expected to correspond, i.e., $\alpha_{ps} = \alpha_{ts}$.

Table 5:4: Physical dimensions of nonlinear damper model

Parameters	Full-scale system
Radius of piston head R (mm)	24.45
Width of piston head L (mm)	15
Width of orifice h (mm)	0.55
Radius of cylinder R_c (mm)	25
Length of cylinder L_c (mm)	110
Applied frequency ω (Hz)	10
Amplitude x_0 (mm)	10

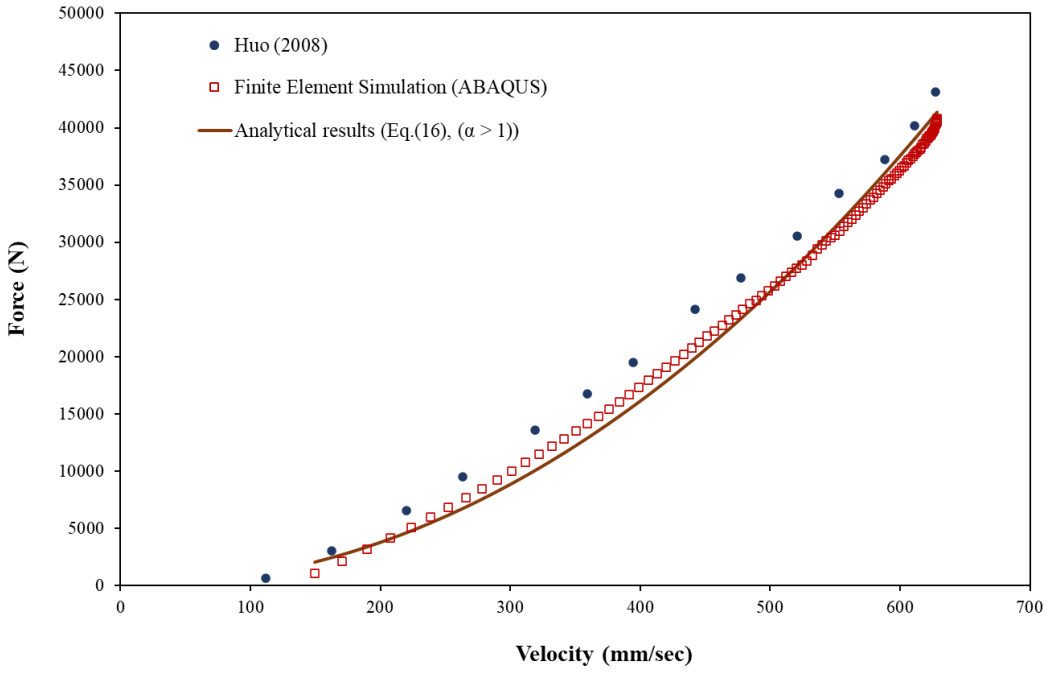

Figure 4: (colour online) Evaluation of the numerical results for the force-velocity of the nonlinear FVD by comparison against FE analytical results presented in the literature.

The results of the FVD simulation presented in Fig. 4 confirm the nonlinearity in the force-velocity relationship and confirm likewise good agreement with the results of Hou (2008). The verified finite-element model provides a convenient vehicle to investigate the effects of scaling on damping. Both contraction and expansion are considered with scaling parameter β taking on discrete values $1/2$ and 2. Identical materials are used in all scaled models and the time scalar g is set equal to β^2 in accordance with the analysis presented in Sec. 3. The damping coefficients and velocity exponents obtained from the nonlinear curve-fitting analysis at scale are tabulated in Table 5. The results confirm that the exponent components do not change with scale over the range of scales considered, i.e., $\alpha_{ps} = \alpha_{ts}$. Also confirmed by this table is the relationship $c_{\alpha_{ts}} = \beta^{\alpha_{ps}} c_{\alpha_{ps}}$ (with $\alpha_{ps} = \alpha_{ts}$) and reaffirmed by the curves in Fig. 5 conforming to good accuracy to the form expected from Eq. (16).

Table 5:5: Nonlinear fluid viscous damper damping coefficient and velocity exponent for full-scale and trial models.

Models	**Damping coefficients (N.s/mm)** (c_α)	α
Full-scale model $\beta_0 = 1$	0.0612	2.0834
Scale-down model $\beta_1 = \frac{1}{2}$	0.0144	2.0834
Scale-up model $\beta_1 = 2$	0.259	2.0834

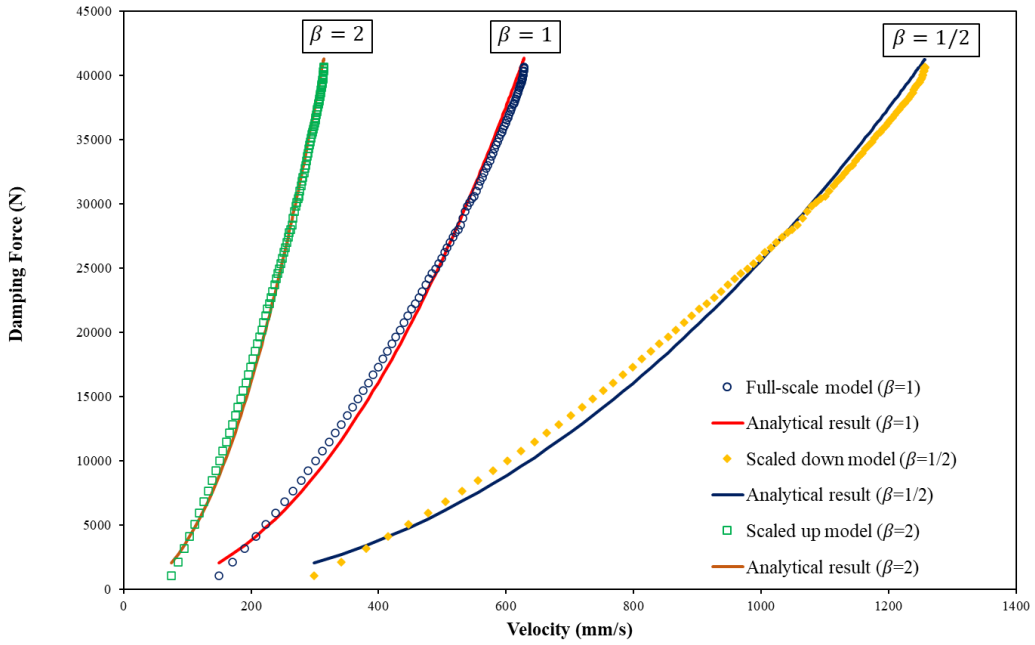

Figure 5: (colour online) Size dependency of the nonlinear FVD damping coefficient for identical material selection. The markers present the FE results while the continuous lines demonstrate the analytical solution.

The analysis performed thus far is for a FVD in isolation using identical materials, but no account is made of other structural elements. Considering elastic structural behaviour requires that the time scalar g is set equal to β (see Sec. 3) and consequently the FVD does not scale according to zeroth-order requirements. Substitution of $g=\beta$ into Eq. (18) provides $c_{\alpha_{ps}} = \beta^{-2} c_{\alpha_{ts}} \left|v_{ts}\right|^{\alpha_{ts}-\alpha_{ps}}$, which reduces further to $c_{\alpha_{ps}} = \beta^{-2} c_{\alpha_{ts}}$ under the assumption that $\alpha_{ps} = \alpha_{ts}$. This assumption (because of Eqs. (19) and (20)) requires a change in the damping fluid to ensure that zeroth-order scaling rules apply, with kinematic viscosity satisfying the relationship $\nu_{ps} = \beta^{-1} \nu_{ts}$. Numerical analysis supporting this assertion is shown in Fig. 6 with scaled FVDs conforming to the expected behaviours (i.e., $c_{\alpha_{ts}} = \beta^{2} c_{\alpha_{ps}}$ and $\alpha_{ps} = \alpha_{ts}$). This result is of practical value since, apart from giving special consideration to the properties of the damping fluid, it confirms that scaled FVDs can be readily incorporated into scaled models without major modification. It is demonstrated in reference [36] that structural damping follows the relationship $c_{ts}^{struc} = \beta^{2} c_{ps}^{struc}$ (with

$g = \beta$) and arranging for $c_{\alpha_{ts}} = \beta^2 c_{\alpha_{ps}}$ for FVDs also is evidently desirable in scaled experimentation.

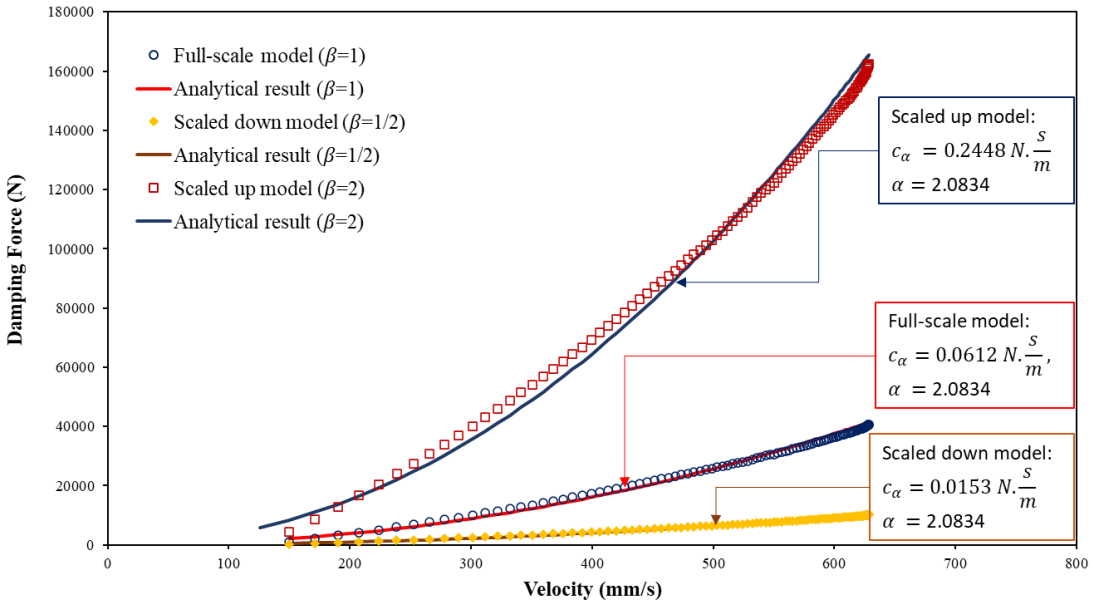

(a)

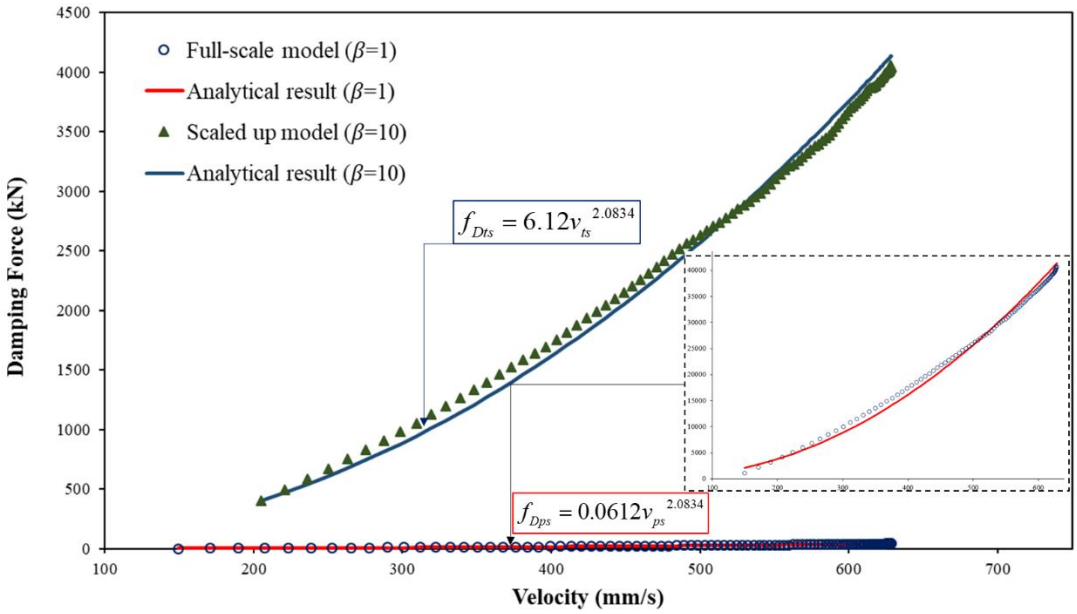

(b)

Figure 6: (colour online) Size dependency of the nonlinear FVD damping coefficient for different damper fluid selection ($\mu_{ts} = \beta\mu_{ps}$). The FE simulation and analytical results based on Eq. (16) are demonstrated for distinct scale models, i.e. (a) scaling with $\beta = \frac{1}{2}$ and $\beta = 2$ and (b) large-scale up with $\beta = 10$.

4.1. Scaling a single-story building incorporating a nonlinear FVD

To investigate further the practical value of scaling when featuring a nonlinear fluid viscous damper, a single-story building is considered. The main purpose of this case study is to investigate what scale effects arise (if any) for the situation when the structure and connected dampers are scaled down. Since the aim of using nonlinear dampers is to reduce structural vibration and peak loading, it is important to capture the nonlinear behaviour, so that adequate scaled models can be created. The case study here involves a nonlinear FVD with velocity exponent $\alpha = \frac{1}{2}$. The model is exposed to the half-cycle sine shock, which is detailed in the Fig. 7 [82].

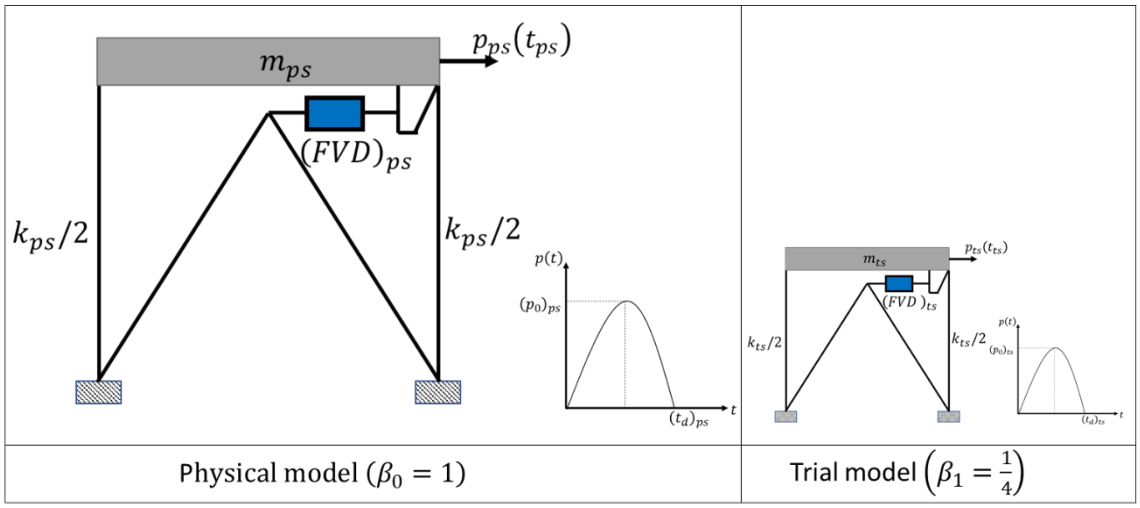

Figure 7: (colour online) Schematic and idealized representation of one-story structure equipped by nonlinear FVD under impulse loading. The curves depict the applied external impulse loads on the full-scale physical model ($\beta_0 = 1$) and the trial-space model ($\beta_1 = 1/4$).

The model parameters are detailed in Table 6, and the model behaviour is assumed to remain in the linear elastic region. The details of the model has been taken from reference [82], where the lump mass is 25,000 kg, the stiffness of the columns calculated with respect to the time period of 0.05 s (i.e., $T_n = 0.05\text{s}$). The inherent structural damping of the system is assumed to be 2%, and critical damping value is determined by $c_{cr} = 2m\omega_n$ and $\omega_n = \sqrt{\frac{k}{m}}$. The maximum acceleration is taken to be $60g$ (i.e., $\ddot{u}_0 = 60g$) with the total duration of 0.01s (i.e., $t_d = 0.01\text{s}$). As detailed in reference [40], the applied sine shock is a form of impulse load, where the ratio of the time-period to the impulse-load duration is smaller than 1/4. The structure

depicted in Fig. 7 can be represented therefore as a single degree of freedom (SDF) system with mass m, stiffness k, structural damping c, and nonlinear viscous-fluid damping c_α, being exposed to half-cycle sine shock. The mathematical model representing the SDF system is,

$$m\ddot{u} + c\dot{u} + ku + c_\alpha \, sgn(\dot{u})|\dot{u}|^\alpha = m\ddot{u}_0 \sin \omega t \tag{21}$$

where the nonlinear FDV is exposed to half-cycle sine shock $m\ddot{u}_0 \sin \omega t$.

In applying the similitude rules to this model, the time scalar g is required to be set equal to β (i.e., $g = \beta$) as dictated by the elastic members as discussed in Sec. 3. However, as also mentioned above, this setting poses some difficulty for the FVD, where an identical damping fluid is to be employed in both the full size and scaled FVDs. The significance of this is shown in Fig. 8, where the projected-trial model signifies results transferred to the physical space by the zeroth-order relationships $\boldsymbol{F}_{ps} = \alpha_{01}^{v} g_1 \boldsymbol{F}_{ts1}$ and $\boldsymbol{u}_{ps} = \beta_1^{-1} \boldsymbol{u}_{ts1}$ (see Table 3). It is evident that the transferred scaled behaviour is not representative of the full-scale behaviour. Replacing the damping fluid in the scaled model and noting the properties tabulated in Table 6, which are in accordance with the relationships (see Table 3) $g_1 = \beta_1$, $k_{ts1} = \beta_1 k_{ps}$, $c_{ts1} = \beta_1^2 c_{ps}$, $c_{\alpha_{ts1}} = \beta_1^2 c_{\alpha_{ps}}$, $m_{ts1} = \beta_1^3 m_{ps}$, and $a_{ps} = g_1^2 \beta_1^{-1} a_{ts1}$, new predictions are provided in Figs. 9 and 10. In complete accordance with theory exact replication is returned between full scale and projected trial-scale models. Note from a practical perspective, the Taylor-devices manual [83] confirms that it is indeed possible to obtain or design a damper with the required zeroth-order requirements, i.e. one which provides $c_{\alpha_{ts1}} = \beta_1^2 c_{\alpha_{ps}}$ and $\alpha_{ts1} = \alpha_{ps}$.

Table 5:6: Physical properties of equivalent 1-DoF model for full-scale and scaled models.

Parameters	Full-scale system	Scaled-down system (Trial Model)
Dimension scaling factor (β)	1	1/4
Time scaling factor (g)	1	1/4
Stiffness (N/m)	394784176	98696044

Damping coefficient $c\left(N.s/m\right)$	10125663	632854
Nonlinear Damping coefficient $c_{\alpha}\left(N.s/m\right)$	3760000	235000
Mass (kg)	25000	390.6
Peak acceleration (g)	60	240

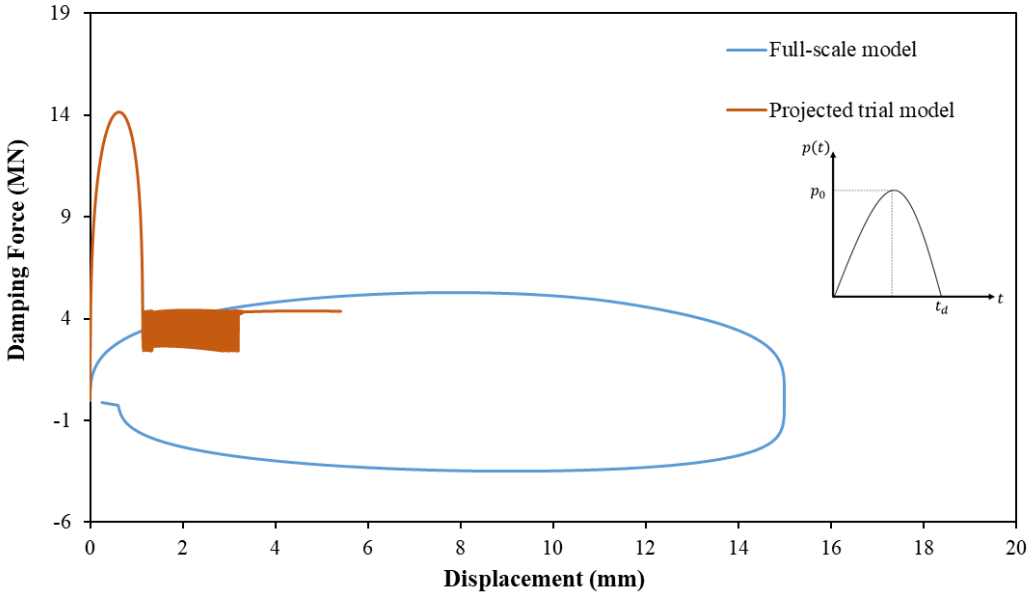

Figure 8: (colour online) The orange line illustrates the replication of damping force-displacement behaviour of the equivalent 1-DOF model of one-story structure equipped by nonlinear FVD based on zeroth-order finite similitude. The blue curve depicts the full- scale model behaviour.

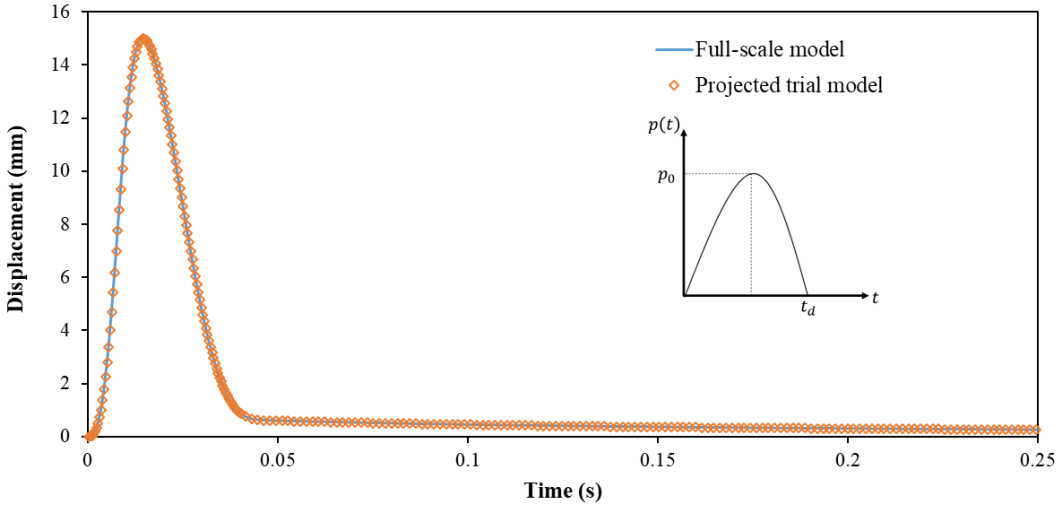

Figure 9: (colour online) The orange marker presents the replication of temporal behaviour of displacement of the projected trial-space equivalent model based on zeroth-order finite similitude, while the blue curve demonstrates the full-scale equivalent model behaviour.

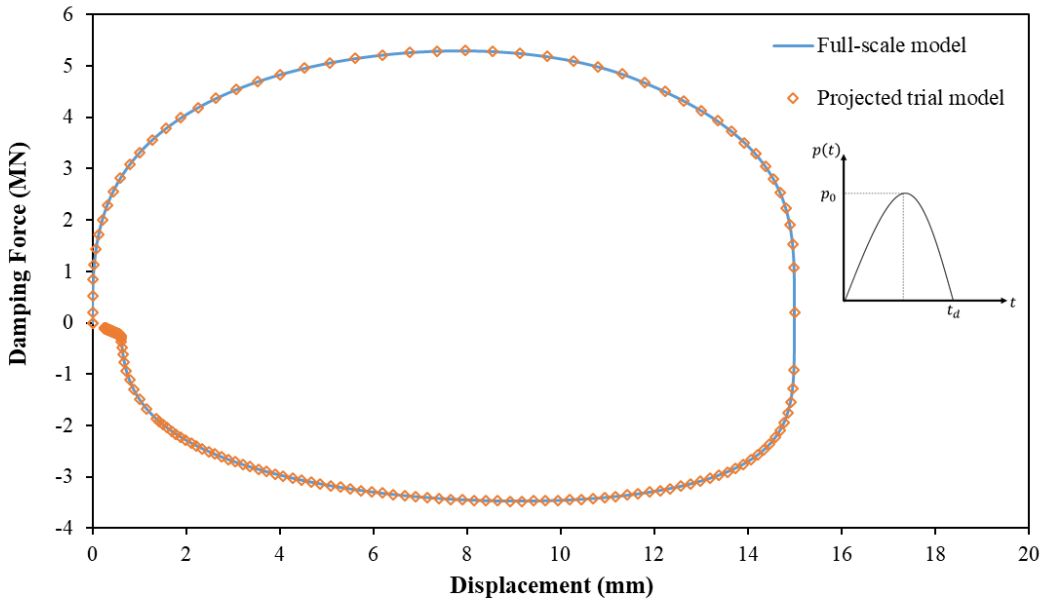

Figure 10: (colour online) The numerical results show the exact match between the behaviour of the real model (blue line) and projected model (orange marker) replicated by first-order finite similitude.

5. Scaling of friction induced stick-slip behaviour

A complex friction case study is considered in this section to ascertain whether it is possible to examine nonlinear friction behaviour via scaled experiments. The model

under scrutiny here is the Burridge-Knopoff earthquake model, which is commonly applied in the study of stick-slip vibration, being recognised to be a significant phenomenon [84]. The model of interest is depicted Fig. 11 and consists of two masses connected by spring elements on a moving belt. This model is assumed to represent the movement of stone blocks during seismic excitation by introducing friction between the components. The system features two forms of friction, which are static friction and dynamic friction. A rough surface is assumed to exist between the belt and masses to give rise to dry friction at the mass-belt interface. The blocks stick when the maximum force applied by the springs to a block happens to be less than the maximum static friction force. When the spring forces exceed the static friction forces, slipping motion starts and it slips until the velocity of the belt and masses are equal. The constant repetition of such movements creates a stick-slip oscillation.

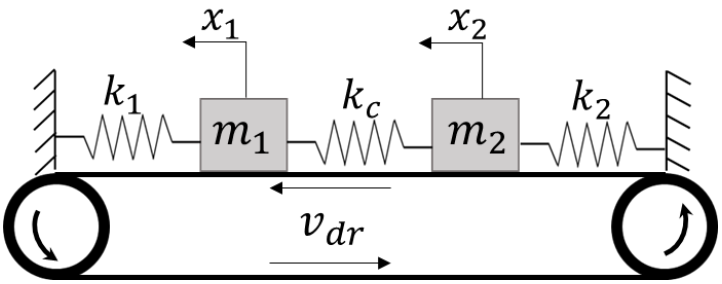

Figure 11: Schematic representation of the 2-DoF stick-slip vibrational system. k_1, k_2 and k_c represent spring stiffnesses, v_{dr} is the belt velocity and m_1, m_2 represent the mass of the blocks.

The system presented in Fig. 11 consists of two mass blocks m_1 and m_2 sitting on a moving belt which is traversing under the blocks with constant velocity v_{dr} [85]. The two mass blocks are connected by a spring of stiffness k_c and at the same time each block is connected individually to fixed constraints through springs of stiffness k_1 and k_2, respectively. The displacement of each mass block (m_1 and m_2) is quantified by x_1 and x_2, respectively. Since the blocks are in contact with the moving belt friction forces F_1 and F_2 are assumed to apply. The material properties and details relating to the full trial-scale models can be found in Table 7. The system with scaled models is depicted in Fig. 12 and are governed by the differential equations [46]

$$m_1\ddot{x}_1 + k_1 x_1 + k_c\left(x_1 - x_2\right) = F_1 \tag{21a}$$

$$m_2\ddot{x}_2 + k_2 x_2 + k_c\left(x_2 - x_1\right) = F_2 \tag{21b}$$

which can be readily solved with the assistance of the commercial Matlab software package, where smoothed analytical relationships for the frictional forces F_1 and F_2 are given by

$$\begin{cases} F_1 \le F_{s,1} & \text{if} \quad \dfrac{\sqrt{k_1 m_1}}{F_{s,1}}\left(\dot{x}_1 - v_{dr}\right) = 0 \\ F_1 = -F_{s,1}\dfrac{sgn\left(\dfrac{\sqrt{k_1 m_1}}{F_{s,1}}\left(\dot{x}_1 - v_{dr}\right)\right)}{1+\gamma\left|\dfrac{\sqrt{k_1 m_1}}{F_{s,1}}\left(\dot{x}_1 - v_{dr}\right)\right|} & \text{if} \quad \dfrac{\sqrt{k_1 m_1}}{F_{s,1}}\left(\dot{x}_1 - v_{dr}\right) \ne 0 \end{cases} \tag{22a}$$

$$\begin{cases} F_2 \le F_{s,2} & \text{if} \quad \dfrac{\sqrt{k_2 m_2}}{F_{s,2}}\left(\dot{x}_2 - v_{dr}\right) = 0 \\ F_2 = -F_{s,2}\dfrac{sgn\left(\dfrac{\sqrt{k_2 m_2}}{F_{s,2}}\left(\dot{x}_2 - v_{dr}\right)\right)}{1+\gamma\left|\dfrac{\sqrt{k_2 m_2}}{F_{s,2}}\left(\dot{x}_2 - v_{dr}\right)\right|} & \text{if} \quad \dfrac{\sqrt{k_2 m_2}}{F_{s,2}}\left(\dot{x}_2 - v_{dr}\right) \ne 0 \end{cases} \tag{22b}$$

where, γ is the shape coefficient of the dynamic friction law, $F_{s,1} = \mu_{s1} m_1 G$ and $F_{s,2} = \mu_{s2} m_2 G$, represent static frictional forces, and where μ_{s1} and μ_{s2} are Coulomb coefficients of friction pertaining to each block, and G is acceleration due to gravity (9.81m/s^2).

In order to solve the specified system, the initial conditions in reference [86], for the displacements and velocities are applied, i.e., $x_1 = \frac{0.9F_{s,1}}{k_1}$, $x_2 = \frac{F_{s,2}}{k_2}$ and $\dot{x}_1 = \dot{x}_2 = v_{dr}$. In addition, following again the suggestions of Galvanetto et al. [86], the following settings are also imposed: $k_c = 1.2k$, $\mu_{s1} = \mu_s = 0.22$, $\mu_{s2} = 1.3\mu_s$, $\gamma = 3$, and $v_{dr} = \frac{0.14F_{s,1}}{\sqrt{k_1 m_1}}$. Presented in Fig. 13 are validation results, where the solution to Eqs. (22) is contrasted against that provided in reference [44]; complete agreement is shown.

Table 5:7: Material parameters of stick-slip system for full-scale and trial models

Geometric/Material Properties	Full-scale Model	Trial Model I	Trial Model II
m_1 *(kg)*	80	10	1.25
m_2 *(kg)*	80	10	1.25
k_1 *(N/m)*	1000	500	250
k_2 *(N/m)*	1000	500	250
G (m/s^2)	9.81	9.81	9.81
μ_s	0.22	0.22	0.22

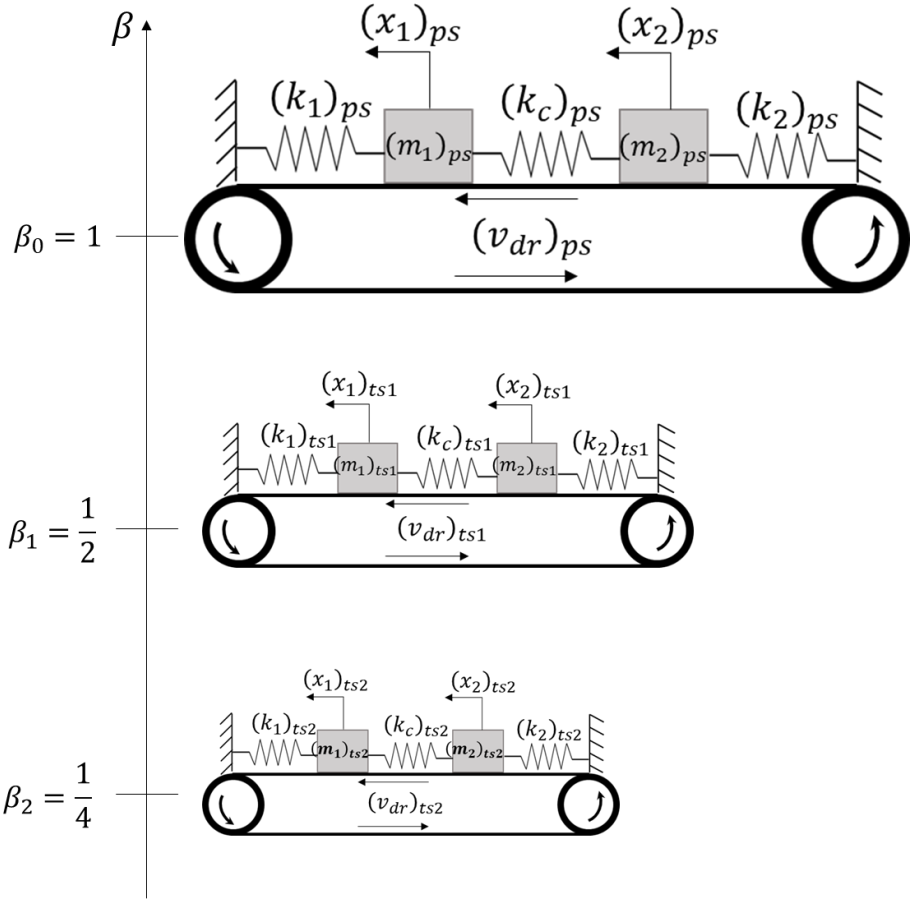

Figure 12: Full-scale $(\beta_0 = 1)$ and scaled models for the stick-slip vibrational system. The geometrical scaling factors of scaled models 1 and 2 are $\beta_1 = \frac{1}{2}$ and $\beta_2 = \frac{1}{4}$, respectively.

It is relatively easy to confirm for a scaled model consisting of identical materials as the full-scale system, that a single scaled model is insufficient to represent full-scale behaviour. To show this consider the zeroth-order force relationship in Table 3, i.e.,

$\boldsymbol{F}_{ps} = \alpha_0^{\nu} g\ \boldsymbol{F}_{ts}$ and consider further the static friction satisfying a relationship of the form $\left(\mathbf{F}_s\right)_{ts} = -\left(\mu_s\right)_{ts} m_{ts} G_{ts} \frac{\mathbf{v}_{ts}}{|\mathbf{v}_{ts}|}$. Multiplying both sides of this equation by $\alpha_0^{\nu} g$ provides after some manipulation,

$$\alpha_0^{\nu} \mathrm{g} \left(\mathbf{F}_s\right)_{ts} = -\left(\mu_s\right)_{ts} \left(\alpha_0^{\nu} \mathrm{g}^{-1} \beta m_{ts}\right) \left(\beta^{-1} g^2 G_{ts}\right) \frac{\mathrm{g}\beta^{-1}\mathbf{v}_{ts}}{|\mathrm{g}\beta^{-1}\mathbf{v}_{ts}|} \tag{23}$$

and recall that $\alpha_0^{\nu} \mathrm{g}^{-1} \beta m_{ts} = \alpha_0^{\rho} m_{ts} = m_{ps}$ and $g\beta^{-1}\boldsymbol{v}_{ts} = \boldsymbol{v}_{ps}$, so consequently to satisfy the relationship $\boldsymbol{F}_{ps} = \alpha_0^{\nu} g\ \boldsymbol{F}_{ts}$ with $\left(\boldsymbol{F}_s\right)_{ps} = -\left(\mu_s\right)_{ps} m_{ps} G_{ps} \frac{\boldsymbol{v}_{ps}}{|\boldsymbol{v}_{ps}|}$ requires that $\left(\mu_s\right)_{ps} = \left(\mu_s\right)_{ts}$, and somewhat problematically $\beta^{-1} g^2 G_{ts} = G_{ps}$.

The last expression is problematic because elastic structural members necessitate that $g = \beta$ (for identical spring materials), giving rise to a contradiction forcing the acceleration due to gravity to change!

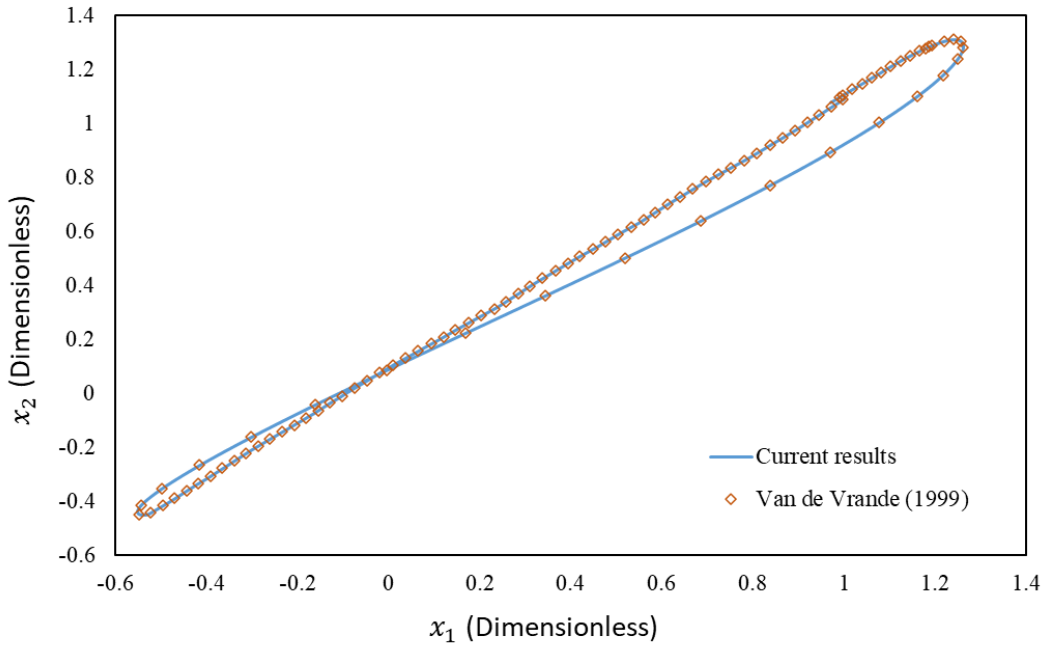

Figure 13: (colour online) The curves represent a comparison between two in-phase solutions, presented in this work (current results) and literature (orange marker) where both masses move in the same direction.

Because of this contradiction attention now turns to first-order finite similitude with selected geometric scaling factors set to $\beta_1 = \frac{1}{2}$ and $\beta_2 = \frac{1}{4}$ for trial-models 1 and 2, respectively. Under the assumption that identical materials are involved at full size and at scale the time scalars are required to be set as $g_1 = \beta_1 = \frac{1}{2}$ and $g_2 = \beta_2 = \frac{1}{4}$.

Prior to examining the first-order solution it is of interest to examine what is achieved with zeroth order. Presented in Fig. 14 therefore is the behaviour of the full-scale model and the projected trial models 1 and 2, where significant disparities are apparent. The main issue is gravity, and it would require an additional mass approach or alteration to friction conditions or gravitational acceleration, for zeroth-order theory to apply. Rather than amending the physical problem, the first-order theory is applied, which combines of two projected zeroth-order solutions in accordance with first-order relationships in Table 3. Since gravity is an issue with zeroth order the identity for acceleration in Table 3 is employed in the determination of the unknown parameter R_1, being selected to provide the correct acceleration due to gravity by the virtual model (i.e., the combined projected models).

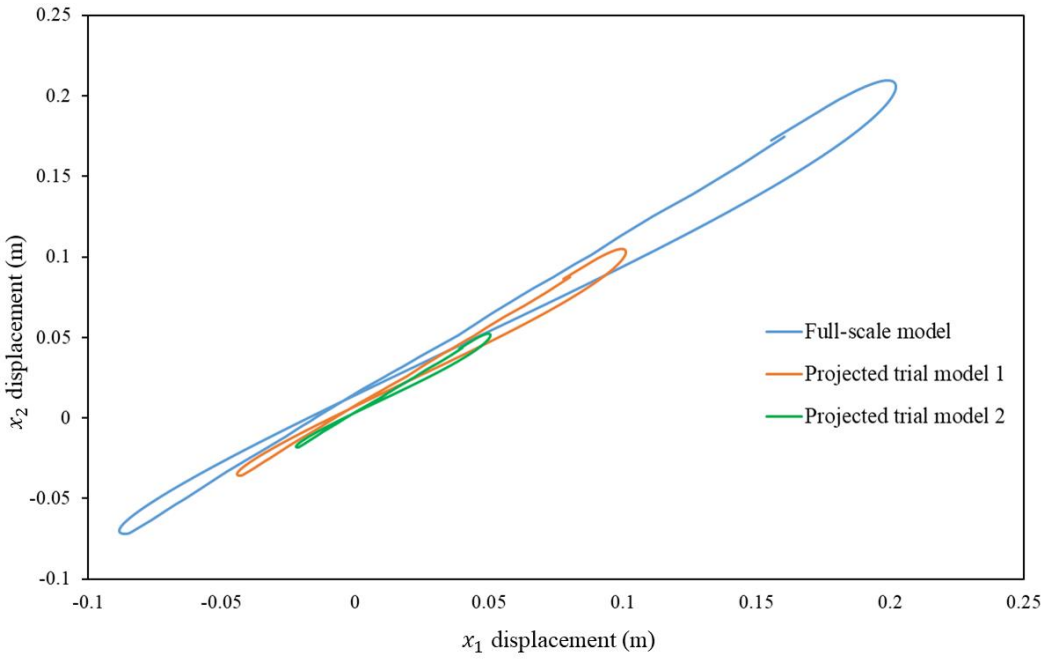

Figure 14: (colour online) The curves represent a comparison between the full-scale (blue curve) and two distinct trial models in-phase solutions. The response of masses m_1 and m_2 described by zeroth-order finite similitude for trial model 1 with $\beta_1 = \frac{1}{2}$ (orange curve) and trial model 2 with $\beta_1 = \frac{1}{4}$ (green curve).

The first-order equation of interest from Table 3 is acceleration in the form

$$G_{ps} = \beta_1^{-1} g_1^2 G_{ts1} + R_1 \left(\beta_1^{-1} g_1^2 G_{ts1} - \beta_2^{-1} g_2^2 G_{ts2} \right) \tag{24}$$

which on substitution of $g_1 = \beta_1 = \frac{1}{2}$, $g_2 = \beta_2 = \frac{1}{4}$ and on setting $G_{ps} = G_{ts1} = G_{ts2}$, provides after a little algebraic manipulation,

$$R_1 = \frac{1-\beta_1}{\beta_1-\beta_2} = \frac{1-0.5}{0.5-0.25} = 2 \tag{25}$$

The expression for displacement provided in Table 3, which for this case gives,

$$x_{1ps} = \beta_1^{-1} x_{1ts1} + R_1\left(\beta_1^{-1} x_{1ts1} - \beta_2^{-1} x_{1ts2}\right) \tag{26a}$$

$$x_{2ps} = \beta_1^{-1} x_{2ts1} + R_1\left(\beta_1^{-1} x_{2ts1} - \beta_2^{-1} x_{2ts2}\right) \tag{26b}$$

where x_{1ps} and x_{2ps} are the required displacements of the masses for the virtual model, and these are plotted in Fig. 15, where a perfect match with the full-scale model is obtained.

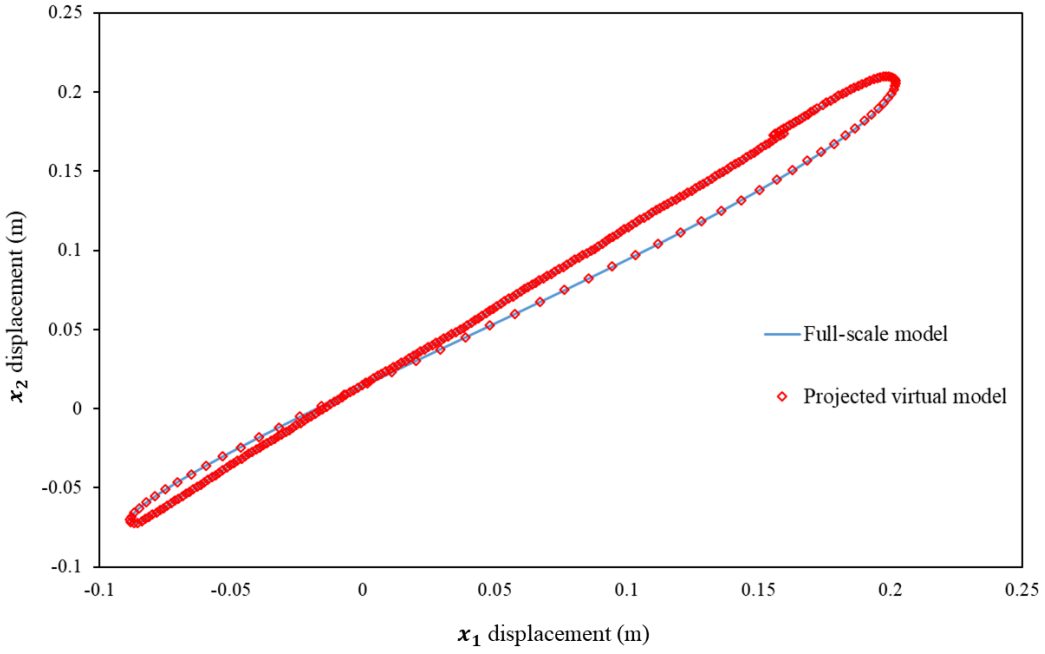

Figure 15: (colour online) The curves represent a comparison between the full-scale (blue curve) and first order projected virtual model (red marker) in-phase solutions. The response of the first-order virtual model is achieved by a linear combination of the result of two distinct trial models.

Further confirmation of the exactness of the predictions in provided in Fig. 16, where phase-space plots are provided for each of the lumped masses. Despite the complicated nature of the stick-slip behaviour, perfect replication is provided by the first-order theory.

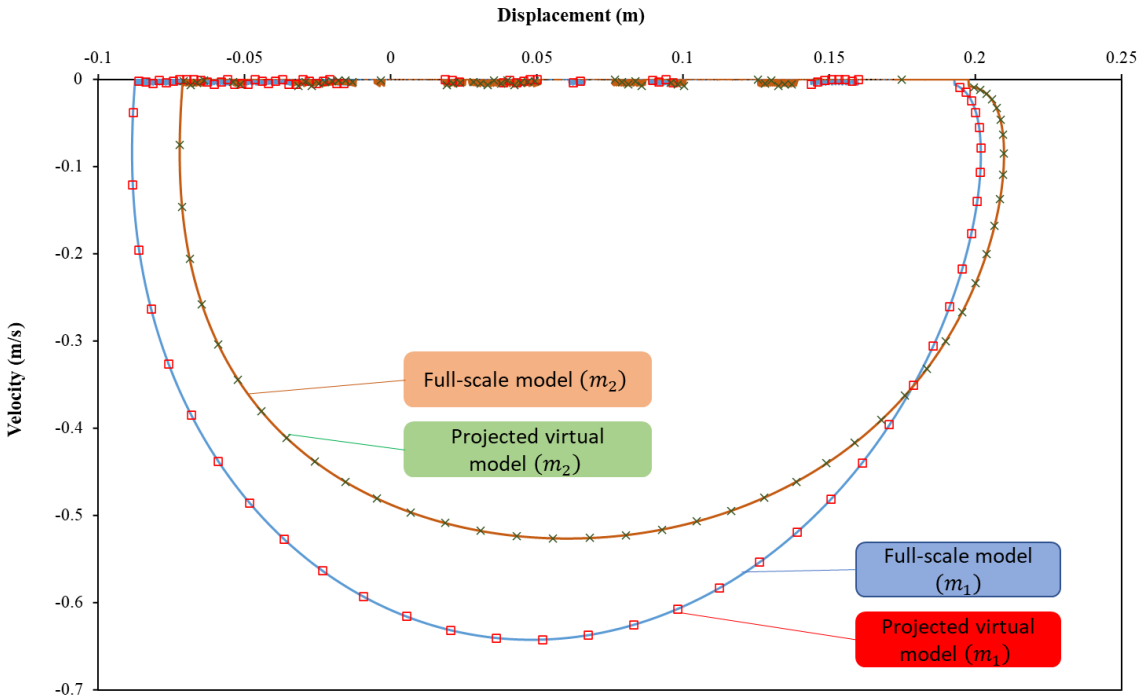

Figure 16: (colour online) The phase diagrams for masses m_1 and m_2 for full-scale (blue and orange curves) and first-order virtual models (red and green markers), respectively.

6. Scaling of a nonlinear spring-damper-friction system

In this section, another nonlinear feature is added in the form of a nonlinear spring to investigate whether scaled experimentation is still applicable in this case. Moreover, cyclic loading is applied to the mechanical system under scrutiny to exacerbate any disparities that might occur over a long timescale. The system under consideration is presented in Fig. 17 along with scaled versions, and features both nonlinear dampers and springs, and again features mass on a moving belt. As in the system considered in Section 5, the friction between the mass block and the belt induces a stick-slip behaviour, which in combination with the other nonlinearities provides a highly nonlinear system for scaled experimentation. There is little possibility that such a system could be represented by a single scaled experiment without significantly modifying the physical problem. It is of interest therefore to examine whether the first-order theory has the capability to accurately describe the response of the system, which is governed by equation [87,88]

$$m\ddot{x}+c\dot{x}+c_{\alpha}\,\mathrm{sgn}\left(\dot{x}\right)\left|\dot{x}\right|^{\alpha}+P\left(L_0-x\right)+\mu mG\,\mathrm{sgn}\left(\dot{x}-v_b\right)=F_0\sin\left(\frac{\pi t}{t_d}\right) \tag{27}$$

where for the full-scale model, the parameters of this equation are tabulated according to Table 8, and where the nonlinear function P is the force arising from a conical spring, v_b is belt velocity and t_d is the time period for the applied external force.

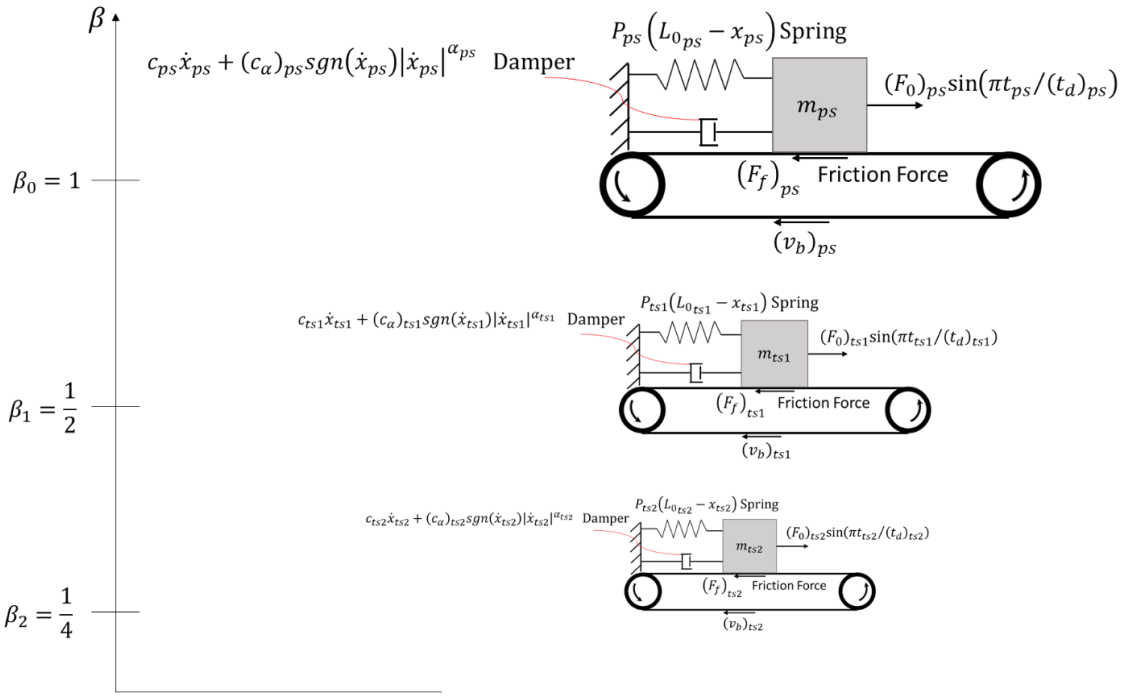

Figure 17: A schematic diagram of the full-scale and small-scale models of the 1-DoF vibrational system including nonlinear spring, nonlinear fluid viscous and Coulomb friction damper under cyclic loading.

Conical springs are in common usage [72,89] and present nonlinear behaviour arising from their geometry, so provide a good practical example of wide interest. The linear response of a conical spring under scaling is presented in ref [72] but the nonlinear response is of principal interest here and is reasonably well described by the relationship [89],

$$P\left(L\right)=\left(\frac{K_1}{2}\right)^{3/2}\left\{1-\left(1-2\left[1-\left(1+\frac{K_2}{K_1^2}\right)^{1/2}\right]\right)^{1/2}\right\}^3 \tag{28}$$

where $K_1 = K_3 - \frac{K_2}{3K_3}$, $K_2 = -\frac{K_6}{K_5}$, and where, $K_4 = \left(\frac{K_7 - L_0 + L}{K_5}\right)^2$ with

$$K_3 = \left\{ \frac{K_4}{16} + \left[\left(\frac{K_4}{16} \right)^2 + \left(\frac{K_2}{3} \right)^3 \right]^{1/2} \right\}^{1/3}$$

(29a)

$$K_5 = -\frac{2D_1^4 n_a}{Sd^4 \left(D_2 - D_1 \right)} \tag{29b}$$

$$K_6 = -\frac{3}{8\left(D_2 - D_1 \right)} \left(\frac{Sd^4 \left(L_a - L_s \right)^4}{n_a} \right)^{1/3} \tag{29c}$$

$$K_7 = \left(L_a - L_s \right) \frac{D_2}{D_2 - D_1} \tag{29d}$$

where $L_a = L_0 - n_i d$ is the initial active length, $L_s = \max\left\{0,\ \left(n_a d\right)^2 - \frac{1}{4}\left(D_2 - D_1\right)^2\right\}$ refers to the active coils solid length, and where the values considered are provided in the Table 9; it is readily confirmed that $P_{ts} = \beta^2 P_{ps}$ for an identical spring material.

Table 5:8: The parameters of the vibrational system including a nonlinear damper and a nonlinear spring for full-scale and trial models.

Parameters	Full-scale Model	Trial Model 1	Trial Model 2
β		1/2	1/4
g		1/2	1/4
m *(kg)*	1000	125	15.625
c *(N.s/m)*	189	47.25	11.8125
c_α $N\ (s/m)^\alpha$	200	50	12.5
α	0.50	0.5	0.5
μ	0.22	0.22	0.22
v_b *(m/s)*	0.5	0.5	0.5
F_0 *(N)*	45000	11250	2812.5
t_d *(s)*	0.05	0.025	0.0125

Table 5:9: Characteristics parameters of conical springs for full-scale and trial models

	Conical Spring		
Parameters	Full-scale model $\beta_0 = 1$	Scaled-down model $\beta_1 = 1/2$	Scaled-up model $\beta_2 = 8$
mean diameter of the smallest active coil: D_1 (mm)	8.97	4.485	71.76
mean diameter of the largest active coil: D_2 (mm)	13.3	6.65	106.4
wire diameter: d (mm)	1.2	0.6	9.6
free length: L_0 (mm)	37.2	18.6	297.6
parameter defining the influence of end coils on the difference between L_0 and L_s: n_i	1.5	1.5	1.5
total number of active coils: n_a	7.13	7.13	7.13
shear modulus: S (MPa)	80000	80000	80000

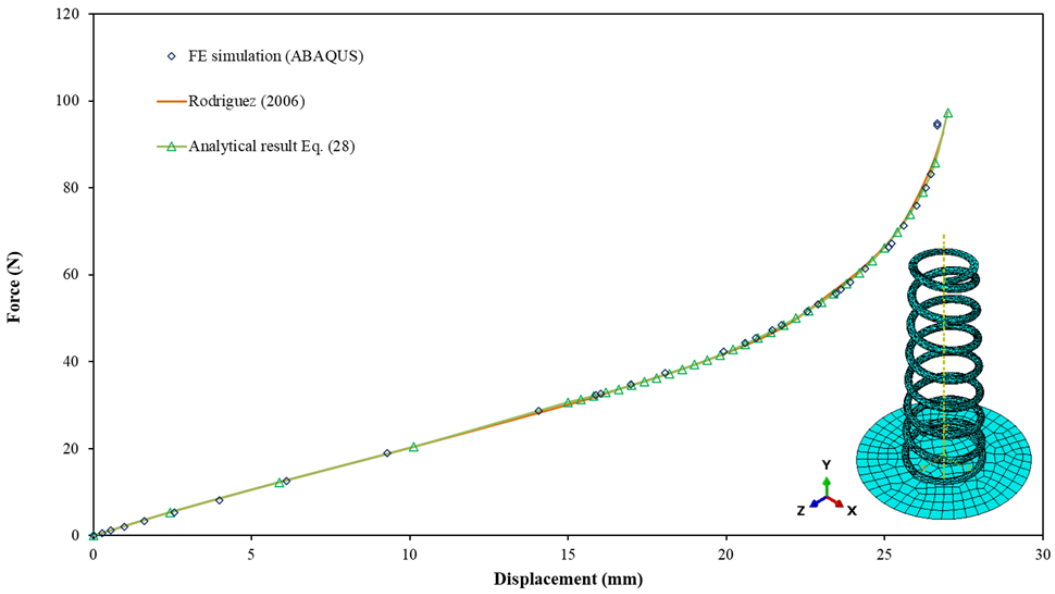

Figure 18: (colour online) Verification of the FE numerical results for the force-displacement of the nonlinear conical spring by comparison against experimental and analytical results presented in the literature. The FE (ABAQUS) model of spring modelled as a 10-node quadratic tetrahedron element (C3D10) including 9641 elements and 18601 nodes.

In addition to the analytical expression provided by Eq. (28) an ABAQUS model for the conical spring under scrutiny is presented in Fig. 18 along with the mesh used for analysis. Also shown in this figure is the predicted nonlinear behaviour in the force-displacement curve and confirmed is excellent agreement between the finite element results and those of Rodriguez (2006) [89] and Eq. (28). The validated finite element model provides a convenient vehicle to study the behaviour of the nonlinear conical spring with scaling. The selected geometric scaling parameters for the contraction and expansion are set to $\beta_1 = \frac{1}{2}$ and $\beta_2 = 8$ to provide a good range of scale. Identical material is used for both the scaled-down and up models and consequently in accordance with the theory presented in Sec. 3, the time scaling factor g is set equal to β. Note additionally that differentiation of Eq. (27) with respect to displacement $-x$ provides the nonlinear stiffness of the conical spring,

$$k = \frac{dP}{d(-x)} = \frac{dP}{dL}\frac{dL}{d(-x)} = \frac{dP}{dL} \tag{30}$$

but recall the scaling relationship $P_{ts} = \beta^2 P_{ps}$ and consequently $k_{ts} = \beta k_{ps}$, which as discussed in Sec. 3 is the expected zeroth-order relationship.

The validity of this analysis is confirmed in Figs. 19, where the figure compares the curves for force against displacement obtained on the trial space but projected onto the physical space using the relationships for force ($\boldsymbol{F}_{ps} = \alpha_0^v g \boldsymbol{F}_{ts} = \beta^2 \boldsymbol{F}_{ts}$) and displacement ($\boldsymbol{u}_{ps} = \beta^{-1} \boldsymbol{u}_{ts}$) from Table 3.

With the spring behaviour confirmed to be well described by Eq. (28), and structural damping and nonlinear damper taking the form presented in Sec. 5, i.e., $c\dot{x} + c_\alpha \operatorname{sgn}(\dot{x})|\dot{x}|^\alpha$, attention now turns to the solving of Eq. (27) and the application of first-order finite similitude.

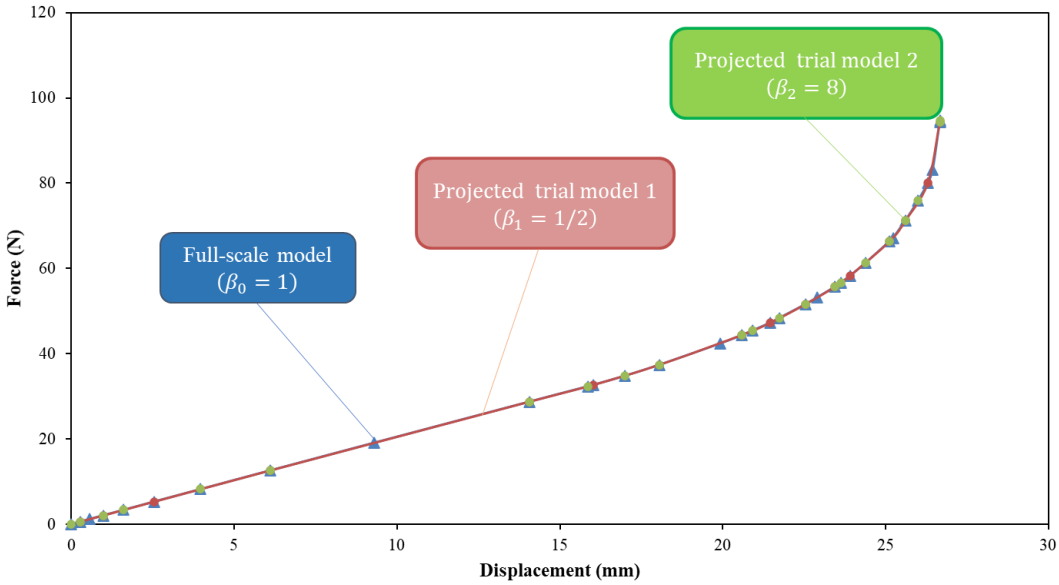

Figure 19: (colour online) Response of scaled nonlinear-spring system subjected to compression force. The blue markers represent the full-scale model behaviour, while the zeroth-order projected trial models are the results of the projection of the scaled models for trial 1 and 2, purple and green lines, respectively.

Note that the first-order rule for force in Table 3 with $\alpha_0^v g = \beta^{-2}$ provides the following combination of Eq. (27):

$$\beta_1^{-2} m_{ts1} \ddot{x}_{ts1} + R_1 \left(\beta_1^{-2} m_{ts1} \ddot{x}_{ts1} - \beta_2^{-2} m_{ts2} \ddot{x}_{ts2} \right) +$$
$$\beta_1^{-2} c_{ts1} \dot{x}_{ts1} + R_1 \left(\beta_1^{-2} c_{ts1} \dot{x}_{ts1} - \beta_2^{-2} m_{ts2} \dot{x}_{ts2} \right) +$$
$$\beta_1^{-2} c_{\alpha_{ts1}} \operatorname{sgn}\left(\dot{x}_{ts1} \right) \left| \dot{x}_{ts1} \right|^{\alpha_{ts1}} + R_1 \left(\beta_1^{-2} c_{\alpha_{ts1}} \operatorname{sgn}\left(\dot{x}_{ts1} \right) \left| \dot{x}_{ts1} \right|^{\alpha_{ts1}} - \beta_2^{-2} c_{\alpha_{ts2}} \operatorname{sgn}\left(\dot{x}_{ts2} \right) \left| \dot{x}_{ts2} \right|^{\alpha_{ts2}} \right)$$
$$\beta_1^{-2} P_{ts1} \left(L_{0ts1} - x_{ts1} \right) + R_1 \left(\beta_1^{-2} P_{ts1} \left(L_{0ts1} - x_{ts1} \right) - \beta_2^{-2} P_{ts2} \left(L_{0ts2} - x_{ts2} \right) \right) +$$
$$\beta_1^{-2} \mu_{ts1} m_{ts1} G \operatorname{sgn}\left(\dot{x}_{ts1} - v_{bts1} \right) + R_1 \left(\beta_1^{-2} \mu_{ts1} m_{ts1} G \operatorname{sgn}\left(\dot{x}_{ts1} - v_{bts1} \right) - \beta_2^{-2} \mu_{ts1} m_{ts1} G \operatorname{sgn}\left(\dot{x}_{ts1} - v_{bts1} \right) \right) +$$
$$= \beta_1^{-2} F_{0ts1} \sin\left(\frac{\pi t_{ts1}}{t_{dts1}} \right) + R_1 \left(\beta_1^{-2} F_{0ts1} \sin\left(\frac{\pi t_{ts1}}{t_{dts1}} \right) - \beta_2^{-2} F_{0ts2} \sin\left(\frac{\pi t_{ts2}}{t_{dts2}} \right) \right) \tag{31}$$

which provides a perfect match for the equation in the physical space on setting $m_{ts} = \beta^3 m_{ps}$, $c_{ts} = \beta^2 c_{ps}$, $c_{\alpha_{ts}} = \beta^2 c_{\alpha_{ps}}$, $P_{ts}\left(L_{0ts} - x_{ts} \right) = \beta^2 P_{ps}\left(L_{0ps} - x_{ps} \right)$, $\mu_{ts} = \mu_{ps}$, $\alpha_{ts} = \alpha_{ps}$, R_1 satisfying Eq. (25), $F_{0ts} = \beta^2 F_{0ps}$, $t_{ts} = \beta t_{ps}$ and $t_{dts} = \beta t_{dps}$.

This is confirmed by the numerical simulation results presented in Figs. 20 and 21, respectively representing the displacement against time and the corresponding phase diagram. The details of the conical coils used is presented in Table 10 with other data found in Table 8. It is evident from the results in the figures that the first-order finite similitude theory can provide acceptable results in a situation where nonlinear behaviour is present in springs and dampers but also when friction is present.

Table 5:10: Conical springs for full-scale and trial models used in scaled system

Parameters	Conical Spring		
	Full-scale model $(\beta_0 = 1)$	Trial model 1 $(\beta_1 = 1/2)$	Trial model 2 $(\beta_2 = 1/4)$
D_1 (mm)	98.67	49.335	24.6675
D_2 (mm)	143	71.5	35.75
d (mm)	13.2	6.6	3.3
L_0 (mm)	409.2	204.6	102.3
n_i	1.5	1.5	1.5
n_a	7.13	7.13	7.13
S (MPa)	80000	80000	80000

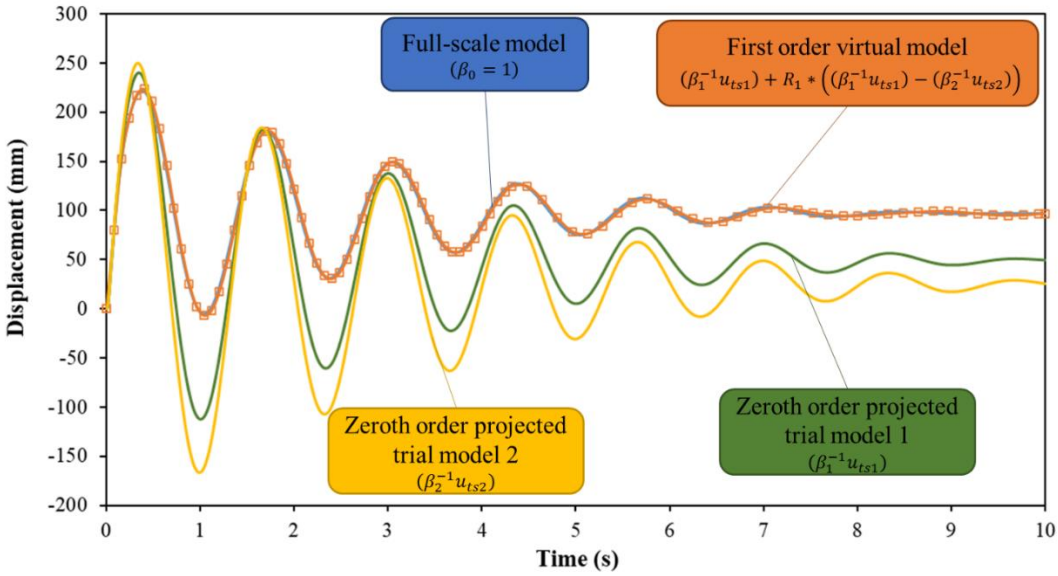

Figure 20: (colour online) The temporal behaviour of mass displacement of the full-scale model, projected trial model 1 and 2 designed based on the zeroth order theory which could not replicate the behaviour while the projected first order virtual model designed based on the first order finite similitude nearly captures the full-scale model response.

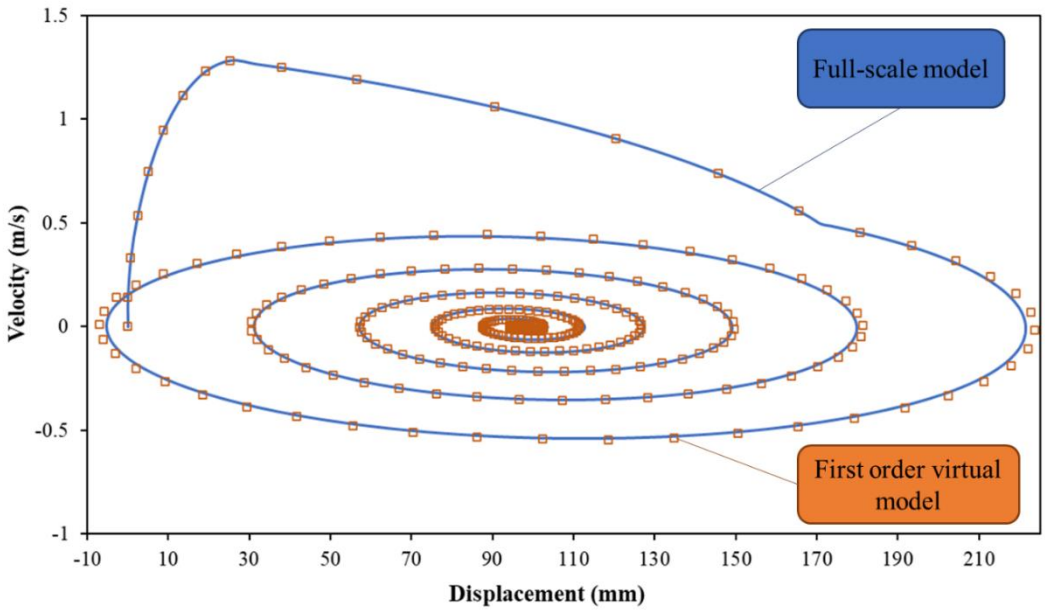

Figure 21: (colour online) The nonlinear spring phase response of the full-scale model, projected virtual model which is the combination of two distinct trial models (1 and 2) designed based on the zeroth order theory which could not replicate the behaviour while the first-order virtual model captures the global behaviour of the full-scale system response.

7. Conclusion

The paper aims to present the application of the finite-similitude theory to show how complex nonlinear mechanical dynamic systems, involving nonlinear viscous dampers, springs, and friction, can be scaled using the recently developed first-order finite similitude theory, where traditional scaling theories (e.g., dimensional analysis) are not able to satisfy complete similarity conditions. The high capability of this approach was illustrated for the proposed vibrational systems in which the response behaviour of the prototype was predicted with high accuracy by the combination of the response of two distinct scaled models without the requirement of any additional technique to be applied to the models. The resulting conclusions can be extracted from the proposed case studies including numerical and analytical analysis:

- The scale dependency of the nonlinear fluid viscous damper was investigated and a relationship $c_{\alpha_{ts}} = \beta^{\alpha} c_{\alpha_{ps}}$ was obtained for the identical material selection. In addition, it is concluded that the desired damping coefficient $c_{\alpha_{ts}} = \beta^{2} c_{\alpha_{ps}}$ between the full-scale and scaled model is always possible by changing the viscous damping fluid.
- A single-story case study confirmed that zeroth-order finite similitude is satisfactory in the case of realisable fluid material selection for the trial model damper, and complete replica scaling was shown possible.
- Scaling of stick-slip friction system was studied in the second case study, and it was demonstrated that the zeroth-order finite similitude (and consequently dimensional analysis) failed to capture the behaviour of the prototype, in contrast, the first-order finite similitude, which provided complete similarity. The study illustrated that the combination of two distinct scaled models can replicate the response behaviour of the physical model with complete agreement. This can be contrasted against replica zeroth-order models (i.e., no additional mass etc.) which gave rise to large errors, i.e., 75% and 93.75% errors for trial model 1 and 2, respectively.
- The scaling behaviour of a nonlinear spring-damper-friction system was examined according to the third case study. It was found that a large deviation was created between the response behaviour of full-scale and singly applied replica small-scale models. For displacement, the full-scale model was predicted with

errors up to 46.9% and 70.4% with dimensional scaling factors set respectively to 0.50 and 0.25. Exact replication (within numerical error) was provided with the first order finite similitude theory on combining the results of two distinct trial models and on correctly setting the extra independent degree of freedom R_1.

Acknowledgements

The authors would like to acknowledge The Ministry of National Education in Turkey and the Department of Civil Engineering at Firat University for providing support for Muhammed Atar to facilitate his doctoral research at the University of Manchester.

8. References

[1] Nayak S, Dutta SC. Failure of masonry structures in earthquake: A few simple cost effective techniques as possible solutions. Eng Struct 2016;106:53–67. https://doi.org/10.1016/j.engstruct.2015.10.014.

[2] Sedov LI, Friedman M, Holt M, Cole JD. Similarity and Dimensional Methods in Mechanics. J Appl Mech 1961. https://doi.org/10.1115/1.3640458.

[3] Buckingham E. On physically similar systems; Illustrations of the use of dimensional equations. Phys Rev 1914;4:345–76. https://doi.org/10.1103/PhysRev.4.345.

[4] Kline SJ, Radbill JR. Similitude and Approximation Theory. J Appl Mech 1966;33:238–238. https://doi.org/10.1115/1.3625015.

[5] Buckingham E. The principle of similitude . Nature 1915;96:396–7. https://doi.org/10.1038/096396d0.

[6] Casaburo A, Petrone G, Franco F, De Rosa S. A Review of Similitude Methods for Structural Engineering. Appl Mech Rev 2019;71. https://doi.org/10.1115/1.4043787.

[7] Dutson AJ, Wood KL. Using rapid prototypes for functional evaluation of evolutionary product designs. Rapid Prototyp J 2005;11:125–31. https://doi.org/10.1108/13552540510601246.

[8] Wissmunn JW. Dynamic Stability of Space Vehicles. Structural Dynamics Model Testing. KIRTLAND AFB: 1968.

[9] Luo Z, Wang Y, Zhu Y, Zhao X, Wang D. The similitude design method of thin-walled annular plates and determination of structural size intervals. Proc Inst Mech Eng Part C J Mech Eng Sci 2016;230:2158–68. https://doi.org/10.1177/0954406215592055.

[10] Simitses GJ, Rezaeepazhand J. Structural similitude and scaling laws for laminated beam-plates. Am. Soc. Mech. Eng. Aerosp. Div. AD, 1992.

[11] Budarapu PR, Zhuang X, Rabczuk T, Bordas SPA. Multiscale modeling of material failure: Theory and computational methods. Adv Appl Mech 2019;52:1–103. https://doi.org/10.1016/bs.aams.2019.04.002.

[12] Chen WQ. The renaissance of continuum mechanics. J Zhejiang Univ Sci A 2014;15:231–40. https://doi.org/10.1631/jzus.A1400079.

[13] Chen Y, Shabanov S, McDowell DL. Concurrent atomistic-continuum modeling of crystalline materials. J Appl Phys 2019;126:101101. https://doi.org/10.1063/1.5099653.

[14] Sharma A, Reddy GR, Vaze KK. Shake table tests on a non-seismically detailed RC frame structure. Struct Eng Mech 2012;41:1–24. https://doi.org/10.12989/sem.2012.41.1.001.

[15] Guerrero Bobadilla H, Ji T, Escobar JA. Experimental studies of a steel frame model with and without buckling-restrained braces. Rev Ing Sísmica 2016:33–52. https://doi.org/10.18867/ris.95.338.

[16] Guerrero H, Ji T, Escobar JA, Teran-Gilmore A. Effects of Buckling-Restrained Braces on reinforced concrete precast models subjected to shaking table excitation.

Eng Struct 2018;163:294–310. https://doi.org/10.1016/j.engstruct.2018.02.055.

[17] Nader MN, Astaneh-Asl A. Shaking Table Tests of Rigid, Semirigid, and Flexible Steel Frames. J Struct Eng 1996;122:589–96. https://doi.org/10.1061/(ASCE)0733-9445(1996)122:6(589).

[18] Kim SE, Lee DH, Ngo-Huu C. Shaking table tests of a two-story unbraced steel frame. J Constr Steel Res 2007;63:412–21. https://doi.org/10.1016/j.jcsr.2006.04.009.

[19] Petry S, Beyer K. Scaling unreinforced masonry for reduced-scale seismic testing. Bull Earthq Eng 2014;12:2557–81. https://doi.org/10.1007/s10518-014-9605-1.

[20] Zou Y, Lu XL. Shaking table model test on Shanghai World Financial Center. World Inf Earthq Eng 2007.

[21] Moghaddam M, Darvizeh R, Davey K, Darvizeh A. Scaling of the powder compaction process. Int J Solids Struct 2018;144–145:192–212. https://doi.org/10.1016/j.ijsolstr.2018.05.002.

[22] Sadeghi H, Davey K, Darvizeh R, Darvizeh A. A scaled framework for strain rate sensitive structures subjected to high rate impact loading. Int J Impact Eng 2019;125:229–45. https://doi.org/10.1016/j.ijimpeng.2018.11.008.

[23] Al-Tamimi A, Darvizeh R, Davey K. Experimental investigation into finite similitude for metal forming processes. J Mater Process Technol 2018;262:622–37. https://doi.org/10.1016/j.jmatprotec.2018.07.028.

[24] Ochoa-Cabrero R, Alonso-Rasgado T, Davey K. Scaling in biomechanical experimentation: A finite similitude approach. J R Soc Interface 2018. https://doi.org/10.1098/rsif.2018.0254.

[25] Sadeghi H, Davey K, Darvizeh R, Darvizeh A. Scaled models for failure under impact loading. Int J Impact Eng 2019;129:36–56. https://doi.org/10.1016/j.ijimpeng.2019.02.010.

[26] Davey K, Darvizeh R, Al-Tamimi A. Scaled metal forming experiments: A transport equation approach. Int J Solids Struct 2017;125:184–205. https://doi.org/10.1016/j.ijsolstr.2017.07.006.

[27] Davey K, Darvizeh R. Neglected transport equations: extended Rankine–Hugoniot conditions and J -integrals for fracture. Contin Mech Thermodyn 2016;28:1525–52. https://doi.org/10.1007/s00161-016-0493-2.

[28] Davey K, Sadeghi H, Darvizeh R, Golbaf A, Darvizeh A. A Finite Similitude Approach to Scaled Impact Mechanics. Int J Impact Eng 2021;148. https://doi.org/10.1016/j.ijimpeng.2020.103744.

[29] Wu JS. Analytical and Numerical Methods for Vibration Analyses. 2015. https://doi.org/10.1002/9781119137207.

[30] PEER Ground Motion Database - PEER Center n.d. https://ngawest2.berkeley.edu/spectras/273010/searches/251041/edit?fbclid=IwAR1xu9ySZ4HcvctPnKqU-rDzgeawvghlwaPRWOQIVCgwJPd7gp5ObcMveUA (accessed March 22, 2020).

[31] Kim NS, Lee JH, Chang SP. Equivalent multi-phase similitude law for pseudodynamic test on small scale reinforced concrete models. Eng Struct 2009;31:834–46. https://doi.org/10.1016/j.engstruct.2008.06.008.

[32] Abaqus U manual. Version 6.14. Dassault Systèmes Simulia Corp, Provid RI 2014.

[33] Anbuchezian A, Baskar G. Behaviour of Cold-Formed Steel Beams Under Cyclic Load Reversal. Int J Eng Sci 2013:22–30.

[34] Spiliopoulos K V., Panagiotou KD. A numerical procedure for the shakedown analysis of structures under cyclic thermomechanical loading. Arch Appl Mech 2015;85:1499–511. https://doi.org/10.1007/s00419-014-0947-6.

[35] Kauffman A, Memari A. Performance Evaluation of Different Masonry Infill Walls with Structural Fuse Elements Based on In-Plane Cyclic Load Testing. Buildings 2014;4:605–34. https://doi.org/10.3390/buildings4040605.

[36] Casaburo A, Petrone G, Meruane V, Franco F, De Rosa S. Support of Dynamic Measurements Through Similitude Formulations. Exp Tech 2021. https://doi.org/10.1007/s40799-021-00457-1.

[37] Lirola JM, Castañeda E, Lauret B, Khayet M. A review on experimental research using scale models for buildings: Application and methodologies. Energy Build 2017;142:72–110. https://doi.org/10.1016/j.enbuild.2017.02.060.

[38] Langhaar H. Dimensional analysis and theory of models. Robert E. Krieger publishing company; 1980.

[39] Jones N. Structural Impact. 2nd ed. Cambridge University Press; 2012.

[40] Altun O, Wolniak P, Mozgova I, Lachmayer R. AN ANALYSIS OF SCALING METHODS FOR STRUCTURAL COMPONENTS IN THE CONTEXT OF SIZE EFFECTS AND NONLINEAR PHENOMENA. Proc Des Soc Des Conf 2020;1:797–806. https://doi.org/10.1017/dsd.2020.320.

[41] Davey K, Darvizeh R, Atar M. A first order finite similitude approach to scaled aseismic structures. Eng Struct 2021;231:111739. https://doi.org/10.1016/j.engstruct.2020.111739.

[42] Nature LR-, 1915. The principle of similitude. CiNiiAcJp n.d.:66–8.

[43] Oshiro RE, Alves M. Predicting the behaviour of structures under impact loads using geometrically distorted scaled models. J Mech Phys Solids 2012;60:1330–49. https://doi.org/10.1016/j.jmps.2012.03.005.

[44] Mazzariol LM, Alves M. Experimental verification of similarity laws for impacted structures made of different materials. Int J Impact Eng 2019;133:103364. https://doi.org/10.1016/j.ijimpeng.2019.103364.

[45] Mascolo I. Recent Developments in the Dynamic Stability of Elastic Structures. Front Appl Math Stat 2019;5:51. https://doi.org/10.3389/fams.2019.00051.

[46] Evkin A, Krasovsky V, Lykhachova O, Marchenko V. Local buckling of axially compressed cylindrical shells with different boundary conditions. Thin-Walled Struct 2019;141:374–88. https://doi.org/10.1016/j.tws.2019.04.039.

[47] Stuart AM. Numerical analysis of dynamical systems. Acta Numer 1994;3:467–572. https://doi.org/10.1017/S0962492900002488.

[48] Jog CS, Agrawal M, Nandy A. The time finite element as a robust general scheme for solving nonlinear dynamic equations including chaotic systems. Appl Math Comput 2016;279:43–61. https://doi.org/10.1016/j.amc.2015.12.007.

[49] Mazzariol LM, Alves M. Similarity laws of structures under impact load: Geometric and material distortion. Int J Mech Sci 2019;157–158:633–47. https://doi.org/10.1016/j.ijmecsci.2019.05.011.

[50] Riddoch DJ, Cicirello A, Hills DA. Response of a mass-spring system subject to Coulomb damping and harmonic base excitation. Int J Solids Struct 2020;193–194:527–34. https://doi.org/10.1016/j.ijsolstr.2020.02.037.

[51] Li C, Yuan Y, He P, Yuan J, Yu H. Improved equivalent mass-spring model for seismic response analysis of two-dimensional soil strata. Soil Dyn Earthq Eng 2018;112:198–202. https://doi.org/10.1016/j.soildyn.2018.05.001.

[52] De La Cruz ST, Rodríguez MA, Hernández V. Using Spring-Mass Models to Determine the Dynamic Response of Two-Story Buildings Subjected to Lateral Loads, 2012, p. 1–8.

[53] Marino L, Cicirello A. Experimental investigation of a single-degree-of-freedom system with Coulomb friction. Nonlinear Dyn 2020;99:1781–99. https://doi.org/10.1007/s11071-019-05443-2.

[54] Hou CY. Behavior explanation and a new model for nonlinear viscous fluid dampers with a simple annular orifice. Arch Appl Mech 2012;82:1–12. https://doi.org/10.1007/s00419-011-0534-z.

[55] Seleemah AA, Constantinou MC. Investigation of Seismic Response of Buildings with Linear and Nonlinear Fluid Viscous Dampers. 1997.

[56] Farahi Shahri S, Roohollah Mousavi S. Seismic behavior of beam-to-column connections with elliptic slit dampers. Steel Compos Struct 2018;26:289–301. https://doi.org/10.12989/scs.2018.26.3.289.

[57] Mousavi SA, Esfandiyari R, Zahrai SM. Experimental Study on Two Full Scale Iranian Viscous Dampers, 2018, p. 11–2.

[58] Ata AA, Kamel AG. Numerical evaluation of the effect of Combined Pendulum Tuned Mass Damper on a basic vibrating system. Int J Mechatronics Appl Mech 2018;4:270.

[59] Kasai K, Pu WC, Wada A. Response of Passively-Controlled Tall Buildings in Tokyo during 2011 Great East Japan Earthquake. iitk.ac.in, 2012.

[60] Esfandiyari R, Nejad SM, Marnani JA, Mousavi SA, Zahrai SM. Seismic behavior of structural and non-structural elements in RC building with bypass viscous dampers. Steel Compos Struct 2020;34:487–97. https://doi.org/10.12989/scs.2020.34.4.487.

[61] Pekcan G, Mander JB, Chen SS. Fundamental considerations for the design of non-linear viscous dampers. Earthq Eng Struct Dyn 1999;28:1405–25. https://doi.org/10.1002/(SICI)1096-9845(199911)28:11<1405::AID-EQE875>3.0.CO;2-A.

[62] Symans MD, Constantinou MC. Passive Fluid Viscous Damping Systems for Seismic Energy Dissipation. J Earthq Technol 1998;35:185–206.

[63] Asher JW, Young RP, Ewing RD. Seismic isolation design of the San Bernardino County Medical Center replacement project. Struct Des Tall Build 1996;5:265–79. https://doi.org/10.1002/(SICI)1099-1794(199612)5:4<265::AID-TAL77>3.0.CO;2-X.

[64] Terenzi G. Dynamics of SDOF Systems with Nonlinear Viscous Damping. J Eng Mech 1999;125:956–63. https://doi.org/10.1061/(ASCE)0733-9399(1999)125:8(956).

[65] Awrejcewicz J, Olejnik P. Analysis of dynamic systems with various friction laws. Appl. Mech. Rev., vol. 58, American Society of Mechanical Engineers Digital Collection; 2005, p. 389–410. https://doi.org/10.1115/1.2048687.

[66] García Reyes LE. Stick-slip vibrations and chaos. J Chem Inf Model 2013;53:1689–99.

[67] Coutinho C. Structural reduced scale models based on similitude theory. 2017.

[68] Zohuri B. Dimensional analysis and self-similarity methods for engineers and scientists. 2015.

[69] Pawelski O. Ways and limits of the theory of similarity in application to problems of physics and metal forming. J Mater Process Tech 1992;34:19–30. https://doi.org/10.1016/0924-0136(92)90086-8.

[70] Barenblatt GI. Scaling, Self-similarity, and Intermediate Asymptotics - Google Books. 1996.

[71] Sadeghi H, Davey K, Darvizeh R, Rajabiehfard R, Darvizeh A. An investigation into finite similitude for high-rate loading processes: Advantages in comparison to dimensional analysis and its practical implementation. Int J Impact Eng 2020;140:103554. https://doi.org/10.1016/j.ijimpeng.2020.103554.

[72] Davey K, Darvizeh R, Atar M, Golbaf A. A Study of Scale Effects in Discrete Scaled Dynamic Systems. Int J Mech Sci 2021;199:106399. https://doi.org/10.1016/j.ijmecsci.2021.106399.

[73] Ochoa-Cabrero R, Alonso-Rasgado T, Davey K. Scaling in biomechanical experimentation: a finite similitude approach. J R Soc Interface 2018;15:20180254. https://doi.org/10.1098/rsif.2018.0254.

[74] Davey K, Mondragon R. A non-physical enthalpy method for the numerical solution of isothermal solidification. Int J Numer Methods Eng 2010;84:214–52. https://doi.org/10.1002/nme.2896.

[75] Davey K, Darvizeh R, Golbaf A, Sadeghi H. The breaking of geometric similarity. Int J Mech Sci 2020;187:105925. https://doi.org/10.1016/j.ijmecsci.2020.105925.

[76] Darvizeh R, Davey K. A transport approach for analysis of shock waves in cellular materials. Int J Impact Eng 2015;82:59–73. https://doi.org/10.1016/j.ijimpeng.2014.11.006.

[77] Lin WH, Chopra AK. Earthquake response of elastic SDF systems with non-linear fluid viscous dampers. Earthq Eng Struct Dyn 2002;31:1623–42. https://doi.org/10.1002/eqe.179.

[78] Rodríguez S, Seim C, US TI-P of the third, 1994 undefined. Earthquake protective systems for the seismic upgrade of the Golden Gate bridge. Proc. third US-Japan Work. Earthq. Prot. Syst. Bridg., 1994, p. 4–147.

[79] Hou C-Y. Fluid Dynamics and Behavior of Nonlinear Viscous Fluid Dampers. J Struct Eng 2008;134:56–63. https://doi.org/10.1061/(ASCE)0733-9445(2008)134:1(56).

[80] Hibbett, Karlsson, Sorensen. ABAQUS/standard: User's Manual. 1998.

[81] Syrakos A, Dimakopoulos Y, Tsamopoulos J. Theoretical study of the flow in a fluid damper containing high viscosity silicone oil: Effects of shear-thinning and

viscoelasticity. Phys Fluids 2018;30:030708. https://doi.org/10.1063/1.5011755.

[82] Narkhede DI, Sinha R. Behavior of nonlinear fluid viscous dampers for control of shock vibrations. J Sound Vib 2014;333:80–98. https://doi.org/10.1016/j.jsv.2013.08.041.

[83] Taylor Devices I. Fluid Viscous Dampers Manual. 2020.

[84] Galvanetto U, Bishop SR. Characterisation of the dynamics of a four-dimensional stick-slip system by a scalar variable. Chaos, Solitons and Fractals 1995;5:2171–9. https://doi.org/10.1016/0960-0779(94)00226-G.

[85] Van De Vrande BL, Van Campen DH, De Kraker A. An approximate analysis of dry-friction-induced stick-slip vibratons by a smoothing procedure An Approximate Analysis of Dry-Friction-Induced Stick-Slip Vibrations by a Smoothing Procedure *. Nonlinear Dyn 1999;19:157–69. https://doi.org/10.1023/A:1008306327781.

[86] GALVANETTO U, BISHOP SR, BRISEGHELLA L. MECHANICAL STICK-SLIP VIBRATIONS. Int J Bifurc Chaos 1995;05:637–51. https://doi.org/10.1142/s0218127495000508.

[87] Xu H, Jin X, Huang Z. Random Response of Spring–Damper–Mass–Belt System with Coulomb Friction. J Vib Eng Technol 2020;8:685–93. https://doi.org/10.1007/s42417-019-00168-3.

[88] Jin X, Xu H, Wang Y, Huang Z. Approximately analytical procedure to evaluate random stick-slip vibration of Duffing system including dry friction. J Sound Vib 2019;443:520–36. https://doi.org/10.1016/j.jsv.2018.12.001.

[89] Paredes M, Rodriguez E, Sartor M, Paredes M, Rodriguez E, Sartor M, et al. Analytical Behavior Law for a Constant Pitch Conical Compression. J Mech Des Am Soc Mech Eng 2006;6.

[90] Garevski M, Hristovski V, Talaganov, Kosta; Stojmanovska M. Experimental Investigations of 1/3-Scale R/C Frame with Infill Walls Building Structures. Proc. 13th World Conf. Earthq. Eng., 2004, p. 772.

[91] Mohammed A, Hughes TG, Mustapha A. The effect of scale on the structural behaviour of masonry under compression. Constr Build Mater 2011;25:303–7. https://doi.org/10.1016/j.conbuildmat.2010.06.025.

[92] Knappett JA, Reid C, Kinmond S, O'Reilly K. Small-scale modeling of reinforced concrete structural elements for use in a geotechnical centrifuge. J Struct Eng 2011;137:1263–71. https://doi.org/10.1061/(ASCE)ST.1943-541X.0000371.

[93] Li S, Zuo Z, Zhai C, Xu S, Xie L. Shaking table test on the collapse process of a three-story reinforced concrete frame structure. Eng Struct 2016;118:156–66. https://doi.org/10.1016/j.engstruct.2016.03.032.

[94] Bairrao R, Vaz C. Shaking table testing of civil engineering structures-The LNEC 3D simulator experience. 2th World Conf Earthq Eng 2000;2129.

[95] Carrillo J, Gonzalez G, Llano L. Evaluation of mass-rig systems for shaking table experiments. DYNA 2012;79:159–67.

[96] Saiidi MS, Douglas B. Shake Table Testing of Flexure Dominated Reinforced Concrete Bridge Columns Report No . CCEER 99-13 Patrick Laplace Center for Earthquake Engineering Research. 1999.

[97] Chen X, Guan Z, Li J, Spencer BF. Shake Table Tests of Tall-Pier Bridges to Evaluate Seismic Performance. J Bridg Eng 2018;23. https://doi.org/10.1061/(ASCE)BE.1943-5592.0001264.

[98] Davey K, Darvizeh R, Atar M, Golbaf A. A Study of Scale Effects in Discrete Scaled Dynamic Systems. Int J Mech Sci 2021.

[99] Darvizeh R, Davey K. Non-physical finite element method: Multiple material discontinuities. Comput Struct 2016;164:145–60. https://doi.org/10.1016/j.compstruc.2015.11.010.

[100] Darvizeh R, Davey K. Non-physical finite element modelling of high speed normal crushing of cellular materials. Int J Impact Eng 2015;82:130–43. https://doi.org/10.1016/j.ijimpeng.2015.04.002.

[101] Szymczak C, Kujawa M. Flexural buckling and post-buckling of columns made of aluminium alloy. Eur J Mech A/Solids 2019;73:420–9. https://doi.org/10.1016/j.euromechsol.2018.10.006.

[102] Ramberg W, Osgood WR. Description of stress-strain curves by three parameters. Natl Advis Comm Aeronaut 1943.

[103] Szymczak C, Kujawa M. Local buckling of thin-walled channel member flange made of aluminum alloy. AIP Conf. Proc., 2017. https://doi.org/10.1063/1.4977688.

[104] Theofanous M, Gardner L. Testing and numerical modelling of lean duplex stainless steel hollow section columns. Eng Struct 2009;31:3047–58. https://doi.org/10.1016/j.engstruct.2009.08.004.

[105] Ahmed S, Ashraf M. Numerical investigation on buckling resistance of stainless steel hollow members. J Constr Steel Res 2017;136:193–203. https://doi.org/10.1016/j.jcsr.2017.05.017.

[106] Kasivitamnuay J, Singhatanadgid P. Scaling laws for displacement of elastic beam by energy method. Int J Mech Sci 2017;128–129:361–7. https://doi.org/10.1016/j.ijmecsci.2017.05.001.

[107] Alves M, Oshiro RE. Scaling the impact of a mass on a structure. Int J Impact Eng 2006;32:1158–73. https://doi.org/10.1016/j.ijimpeng.2004.09.009.

[108] Luo Z, Zhu Y, Zhao X, Wang D. Determining Dynamic Scaling Laws of Geometrically Distorted Scaled Models of a Cantilever Plate. J Eng Mech 2016;142:04015108. https://doi.org/10.1061/(asce)em.1943-7889.0001028.

[109] Wu W, Ge S, Yuan Y, Ding W, Anastasopoulos I. Seismic response of subway station in soft soil: Shaking table testing versus numerical analysis. Tunn Undergr Sp Technol n.d.;100:103389. https://doi.org/10.1016/j.tust.2020.103389.

[110] Rahnavard R, Fard FFZ, Hosseini A, Suleiman M. Nonlinear analysis on progressive collapse of tall steel composite buildings. Case Stud Constr Mater 2018;8:359–79. https://doi.org/10.1016/j.cscm.2018.03.001.

[111] Song Z, Su C. Computation of Rayleigh Damping Coefficients for the Seismic Analysis of a Hydro-Powerhouse. Shock Vib 2017;2017:1–11. https://doi.org/10.1155/2017/2046345.

[112] Chen XM, Duan J, Qi H, Li YG. Rayleigh Damping in Abaqus/Explicit Dynamic Analysis. Appl Mech Mater n.d.;627:288–94.

https://doi.org/10.4028/www.scientific.net/amm.627.288.

[113] Cremer L, Heckl M. Structure-Borne Sound. 1988. https://doi.org/10.1007/978-3-662-10121-6.

[114] Vince Adams and Abraham Askenazi. Building Better Products with Finite Element Analysis. vol. 127. New York: American Society of Mechanical Engineers; n.d.

[115] Bachmann H, Ammann WJ, Deischl F, Eisenmann J, Floegl I, Hirsch GH, et al. Vibration Problems in Structures. 1995. https://doi.org/10.1007/978-3-0348-9231-5.

[116] Orban F. Damping of materials and members in structures. J Phys Conf Ser 2011;268. https://doi.org/10.1088/1742-6596/268/1/012022.

[117] Banazadeh M, Ghanbari A, Ghanbari R. Seismic performance assessment of steel moment-resisting frames equipped with linear and nonlinear fluid viscous dampers with the same damping ratio. J Constr Steel Res 2017;136:215–28. https://doi.org/10.1016/j.jcsr.2017.05.022.

[118] CSI. SAP2000. Analysis Reference Manual. CSI Berkeley (CA, USA) Comput Struct INC 2016.

[119] Ras A, Boumechra N. Seismic energy dissipation study of linear fluid viscous dampers in steel structure design. Alexandria Eng J 2016;55:1–12. https://doi.org/10.1016/j.aej.2016.07.012.

[120] Boksmati JI, Madabhushi GSP. Centrifuge modelling of structures with oil dampers under seismic loading. Earthq Eng Struct Dyn 2020;49:356–74. https://doi.org/10.1002/eqe.3243.

[121] Huneault J, Kamil J, Higgins A, Plant D. Dynamic tensile strength of silicone oils. AIP Conf. Proc., 2018. https://doi.org/10.1063/1.5044825.

Chapter

SIX

Paper four: Application of first-order finite similitude in structural mechanics and earthquake engineering

Overview

After investigation into the simplified equivalent models (mass-spring-damper) and their behaviour with scaling, an optimum scaling design has been obtained and implemented in this paper for buildings exposed to earthquake loads. The new theory of scaling proposes the possibility of designing and testing buildings and structures in new ways, which is also the focus of this article. The selected complex case-studies proved that the application of the proposed scaling theory is straightforward, and it is possible to reconstruct full-scale model behaviour with higher accuracy. The capability of the finite similitude theory has been shown through the examination of structural elements under various loadings and high-rise buildings under earthquake excitation. In addition, another important feature of the first-order finite similitude is presented in the case of breaking geometric similarity for a thin-walled beam, where the first-order theory captured the global behaviour of the full-scale model with an exact match.

Authors Contribution: Keith Davey and R. Darvizeh were involved in planning and supervised the work and writing-editing manuscript. **M. Atar** processed the numerical data, performed all the analysis, drafted the manuscript, and designed the figures. K. Davey and R. Darvizeh aided in interpreting the results. All authors discussed the results and commented on the manuscript.

Details: Earthquake Engineering and Structural Dynamics. Received: 12 February 2021. Revised: 24 August 2021. Accepted: 26 August 2021. Publication date: 08 September 2021.

Paper DOI: https://doi.org/10.1002/eqe.3545

APPLICATION OF FIRST-ORDER FINITE SIMILITUDE IN STRUCTURAL MECHANICS AND EARTHQUAKE ENGINEERING

Muhammed Atar, Keith Davey, Rooholamin Darvizeh

School of Mechanical, Aerospace and Civil Engineering,

The University of Manchester, ManchesterM13 9PL, UK

Abstract

An important experimental approach for the testing of earthquake-resistant structures is scaled experimentation with experimental designs impacted upon by the similitude theory of dimensional analysis. Unfortunately, the type of similitude provided by dimensional analysis seldom applies to complex structures, which is particularly problematic when scaling ratios are large. The issue is one of scale effects where the behaviour of the scaled version of any full-size structure can be markedly different.

Recently however a *new theory of scaling* called *finite similitude* has emerged in the open literature that confirms that the similitude offered by dimensional analysis is just one of a countable infinite number of alternative possibilities. The new theory of scaling raises the possibility that buildings and structures can be designed and tested in new ways and this aspect is the focus of this paper.

Similitude rules for single and two scaled experiments are examined to illustrate the benefits provided by alternative forms of similitude. The two types of similitude examined are termed *zeroth order* and *first order finite similitude*, which are shown to be two forms in an infinite number of alternative possibilities efficiently defined using a recursive relationship. The theory of scaling is founded on the metaphysical concept of space scaling yet provides the means to establish all scale dependencies for structural components and high-rise steel buildings along with buildings equipped with non-linear-fluid viscous dampers for resisting earthquake loading conditions. It is shown through case-studies of increasing complexity how the new theory can be applied to reconstruct full-scale behaviours but also revealed are some of the limitations of the new approach.

Keywords: finite similitude, scaled structures, dimensional analysis, time history analysis, scaled experimentation.

1. Introduction

Earthquake testing methods such as laboratory tests for massive structures such as tall bridges and skyscrapers commonly built today have become more challenging and less applicable. More feasible is the testing of scaled models to study the behaviour of such structures, as undoubtedly these forms of test are easier to perform and invariably are more cost effective to implement. Sized tests are especially recommended as one of the few experimental solutions for situations where it is impossible to test a real prototype. Although scaled experimentation has some significant limitations it still plays a critical role in process, product design and testing for systems. The obstacles to scaling are mainly related to the nonlinear relationships that exist between physical and scaled processes, which manifest as changes in physical behaviour with scale. Geometric scale dependencies are readily visible with geometric measures of length, area, and volume scaling linearly, quadratically and cubically, respectively. Important changes affected by changes in geometric measures in the structural analysis are surface forces and body forces with the latter decreasing at a faster rate than the former with scale. The presence of scale effects, which can be marked, has undoubtedly diminished the importance of scaled experimentation in recent times coupled with the ever-increasing sophistication of computational modelling, which has invariably accelerated this decline.

The issues surrounding scaling are generally well appreciated by the academic and industrial communities and it is appreciated that dimensional analysis provides the bedrock on which scaled experimentation is built, being fundamental to the concept of similarity. The prevailing view is that similar structures behave in the same way, and similarity can be investigated by applying dimensional analysis [2]. Similarity is rarely achievable for all but the simplest of structures and dimensional analysis provides no solution to dissimilar structures. In many respects, the concept of similarity, which is defined by dimensional analysis has not changed significantly for over a century and remains the dominant approach for academic and industrial scaled research. Linked to dimensional analysis is the Buckingham Pi theorem which reveals an inner dependence between dimensional variables [3] and more importantly brings into existence the dimensionless Pi groups. If it transpires that the Pi groups in the dimensionless equations

governing the behaviour of the scaled and full-scale structures match, then the two structures are defined to be similar. However, as mentioned above, this situation is rarely met in reality [4] and the approach has shown little success in complex structures. Structural engineering has a long history of investigations with scaled experimentation, but it is apparent on inspection of early historical references that most early forms of analysis were somewhat rudimentary in nature. The early work of Buckingham [3] provided the basis for more realistic scale models and the first significant application can be attributed to him [5], although the study was purely theoretical in scope. The ground-breaking work of Buckingham [3] was followed by an almost exponential rise in the numbers of publications investigating the application of scaled methods.

In a general sense, scaled experimentation is principally about the establishment of scaling rules, which provides a means to transfer obtained pieces of information from the scaled experiment to the full scale. The focus here is on earthquake seismic tests but it is recognized that there exist limitations with scaling. Practical limitations might be the unavailability of materials with the required material properties but also the availability of suitable experimental equipment can place constraints on what is possible. In the case of seismic testing a critically important and often utilized piece of apparatus is a shake table. Well-researched scaling rules are often imposed in the application of shake-table studies, as achieving complete similarity is unlikely. Many scaled experiments have been performed and publications produced addressing this issue to better understand the behaviour of structures under earthquake excitations. Sharma et al. [14], Nayak et al. [1], Guerrero et al. [16], and Garevski et al. [90], studied the behaviour of scaled-down structures in order to predict the behaviour of physical models by applying several similarity laws. The benefits and limitations of using different materials in small-scaled models were investigated in reference [10]. Other studies include investigations into aspects of inelastic behaviour of structures [18] and unreinforced structures such as masonry at half scale [19]. Research using relatively high scaling factors included the application of two-dimensional base ground motion, which induces complex behaviour for a high-rise tall building [20] at a 1/50 scale. Another example at 1/40 scale is the scaling of high-rise buildings studied to investigate the behaviour of huge structures [91] [92].

The difficulty with all the scaled experimental studies mentioned above is that they are all constrained by the limited capability of dimensional analysis with the prevalence of scale effects as presently defined. A particular example is related to weight and body forces and the associated requirement in scaling for mass to be added to the scaled model [93]. Typically, masses are added in the form of blocks attached to slabs but fixing one problem invariably produces another as it can be anticipated that the behaviour of the supporting frame will not be correct during collapse. The blocks of mass can move and even collide under deformation conditions and the result can be unrepresentative behaviour. Additional mass is often essential when scaling down dimensions whilst maintaining the material properties of the prototype. The added mass however comes with drawbacks as it makes movement and control invariably more complex [94][95]. Simulator control becomes more difficult since additional mass has the potential to produce overturning moments. This often means that specimens have to be designed using bigger scaling factors and involve control measures so that the above drawbacks can to a certain degree be accommodated depending on the payload capacities of the shake table utilized [94]. Investigated in reference [96] is a rotational system involving restraining cables to limit the extent of translation of rotational mass. The device was designed to allow mass movement up to a maximum displacement limit at which point the restraining cables stopped further movement; the cessation of mass movement was termed specimen failure. Unfortunately however, the scaled system cannot be said to be truly representative and in particular the loading and overall stiffness of the scaled model was influenced [96]. Another study [97] concerned with the seismic performance of a tall bridge using a shake table test also required additional mass. The precise distribution of the mass could be through the pier height determined by means of repeated numerical trials to finalize the location of the masses. It is evident that additional mass comes with problems and an alternative option is to increase the acceleration according to similarity laws. Unfortunately, this solution comes with its own shortcoming since for representative behaviours of high-rise buildings it is needed to apply large accelerations. This is practically difficult to arrange due to the limits of laboratory shake table capacities.

It is clear from the evidence of past experimental studies that the limitations imposed by the current definition of similarity has led to all manner of

contortions to address the unrepresentative behaviour of scaled models. The present situation is not satisfactory, and the solutions investigated involving additional mass, makeshift scaling rules, artificially high accelerations are not fit for purpose. To address this problem this paper examines two alternative forms of similitude that form part of a new *scaling theory* termed *finite similitude* [21–26]. The work here is designed to provide additional evidence on the merit of the newer forms of similarity and add to earlier works done in the fields of: metal forming [23], impact mechanics [25], powder compaction [21], and biomechanics [24]. These studies were limited to one scaled experiment under the similitude rule named zeroth-order finite similitude. Both zeroth-order finite similitude and dimensional analysis are underpinned by proportional field relationships, assumed a *priori* for dimensional analysis, and returned a *posteriori* from the invariance principle applied to define zeroth-order finite similitude. Consequently, it is possible for each of the approaches to replicate each of the others similitude conditions. Despite this association however, zeroth-order finite similitude has the advantage of being part of a holistic scaling theory with scaling identities and the number of freedoms identified, which provides a route for direct optimization (see references [21,23] for greater details). Dimensional analysis on the other hand is well known, links fully to approximate physics with the retention of dominant dimensionless terms, and benefits from its association with the Buckingham Pi theorem for reducing the number of arguments in a dimensioned expression. The work presented here is concerned with both zeroth-order and first-order similitude, so involves both one and two-scaled experiments although focusing on seismic studies. The proposed two-experiment approach to scaled experimentation first appeared in references [28,98] for the study of impact mechanics and discrete dynamic systems. The work here extends the application of the method to seismic systems involving steel buildings and non-linear damping, and for the first time the breaking of geometric similarity in structural members.

The starting point for the finite similitude theory is rather unusual in that it begins with a concept that cannot be physically enacted, which is space scaling. The concept is introduced in Sec. 2, where it is shown how metaphysical-space scaling provides the correct founding theory for the *theory of scaling* providing an intuitive vision for scaling. The mathematics of space scaling is relatively

straightforward and ultimately provides the means to examine scaled structural mechanics. This achieved in a roundabout way however, which first requires describing the impact of space scaling on control volumes as these underpin mechanics in its transport form. The key step in the finite similitude theory presented in Sec. 2 is the projection of transport equations defined on the trial space (where the scaled experiment resides) onto the physical space (where the full-scale structure resides). This projection reveals in one form or another all the scale dependencies possible in structural mechanics. The approach effectively transforms the problem of scaling into one whose objective is the revealing of those fields that are only defined implicitly by the projection between trial and physical space. This can be achieved with the application of similitude rules and unlike dimensional analysis the finite similitude approach is not limited to a single similitude condition. Alternative rules of similitude are presented in Sec. 3, where a countable infinite number of similitude identities are defined under what is termed high-order finite similitude. The rules provide a calculus for scaling in that they describe how scaled systems change with scale. Integration of the differential equations defined by high-order finite similitude links experiments at distinct scales. The two integrated forms of interest in this paper presented in Sec. 3 are termed zeroth order and first order finite similitude and involve one and two scaled experiments, respectively. To demonstrate the practical advantage of the new scaling theory in structural mechanics the behaviour of important structural elements is examined under the new rules of scaling. Considered in Sec. 4 are a beam-strut model exposed to a point load, a column buckling analysis and a thin-section problem, which breaks the rule of geometric similarity by allowing thickness to be constrained. A more complicated structure is considered in Sec. 5, where the first-order finite similitude rule is applied to a high-rise steel building exposed to a real earthquake load. Further complication is added in Sec. 6, where an eight-story steel construction equipped with nonlinear fluid viscous dampers is examined under scaling and subject to earthquake excitation. Through standard structural elements to building designs with and without nonlinear dampers the paper aims to demonstrate the benefits and validity of the new scaling theory. The paper ends with a brief set of conclusions confirming that the downside of additional scaled experiments is counterbalanced by the benefits of increased flexibility and accuracy.

2. The theory of scaling: a review of finite similitude

The difficulty with all past studies into scaled experimentation is the absence of a scaling theory that can account for all scale dependencies that arise. The finite-similitude theory accounts for scaled dependencies by means of a metaphysical concept of space scaling. Although it is evidently impossible to scale space the concept can nevertheless be defined mathematically by introducing a map between the space which houses the full-scale experiment (the physical space) and the space where the scaled experiment resides (the trial space). In mathematical terms the temporally invariant map between coordinate functions in the physical and trial space take the form $x_{ps} \mapsto x_{ts}$, where the subscripts "ps" and "ts" signify physical and trial space, respectively. In differential terms and limiting the space scaling to isotropic scaling the map takes the form $d\boldsymbol{x}_{ts} = \beta d\boldsymbol{x}_{ps}$, which in coefficient terms gives $dx^i_{ts} = \beta dx^i_{ps}$. It is assumed here that coordinate system in each space is orthonormal and under this restriction positive scalar β indicates the extent of linear isotropic scaling with $0 < \beta < 1$ for contraction, $\beta = 1$ for no scaling and $\beta > 1$ for expansion. Although space contraction is of particular interest with scaled-down experiments the theory does allow scaling up also. As Newtonian physics is the focus of the study absolute times t_{ps} and t_{ts} are assumed to exist with each space possessing a single measure of time. It is also necessary to establish a relationship between t_{ps} and t_{ts}, which in differential terms takes the form $dt_{ts} = g dt_{ps}$ for positive scalar g [28].

2.1. Control Volume Motion

To relate the effect space scaling has on the governing physics it is necessary to have the physics described by an appropriate formulation. The correct approach is one based on a control-volume formulation as control volumes are basically regions of space and hence are immediately impacted upon by space scaling. Although in some respects this approach might appear remote from structural engineering it is nevertheless necessary and is simply the path followed by the theory from space to control volumes (regions of space) to transport equations (laws of nature) and finally to structural field relationships.

The mathematics of control volume motion which can be found in reference [76,99,100] and involves transport of a control volume Ω_{ts}^{*} (in the trial space) by means of a velocity field $\boldsymbol{v}_{ts}^{*}$. To define the motion of anything it is generally with respect to something else, and by comparing Ω_{ts}^{*} with a reference control volume Ω_{ts}^{*ref} it is possible to define the following partial derivative,

$$\boldsymbol{v}_{ts}^{*}=\frac{D^{*}\boldsymbol{x}_{ts}^{*}}{D^{*}t_{ts}}=\left.\frac{\partial \boldsymbol{x}_{ts}^{*}}{\partial t_{ts}}\right|_{\boldsymbol{\chi}_{ts}} \tag{1}$$

where coordinate points $\boldsymbol{\chi}_{ts}\in\Omega_{ts}^{*ref}$ and $\boldsymbol{x}_{ts}\in\Omega_{ts}^{*}$, and $\frac{D^{*}}{D^{*}t_{ts}}$ represents a partial temporal derivative where the reference point $\boldsymbol{\chi}_{ts}$ is held constant.

The exact same apparatus can be utilized in the physical space but motion of the two control volumes must be related in some manner. Note that as shown in reference [28] there exists a map between two control volumes in physical and trial spaces such that $d\boldsymbol{x}_{ts}^{*}=\beta d\boldsymbol{x}_{ps}^{*}$, i.e., essentially that provided by the space scaling map. The maps $d\boldsymbol{x}_{ts}^{*}=\beta d\boldsymbol{x}_{ps}^{*}$ and $dt_{ts}=gdt_{ps}$ immediately provide a similitude velocity relationship $\boldsymbol{v}_{ts}^{*}=g^{-1}\beta\boldsymbol{v}_{ps}^{*}$ which is a relatively simple expression relating the velocities of the moving control volumes in the two spaces. With the synchronization of the moving control volumes established it is now possible to examine the governing equations for structural mechanics in transport form.

2.2. Transport form of projected structural mechanics

The key step in the finite-similitude theory is the projection of the governing transport equations for the trial space onto the physical space because it is through this operation that scale dependencies are exposed. For structural analysis, the four transport equations (essentially eight as two are vector equations) of interest are those for volume, continuity, momentum and movement. The related transport equations can be written in the form:

$$\frac{D^{*}}{D^{*}t_{ts}}\int\limits_{\Omega_{ts}^{*}}dV_{ts}^{*}-\int\limits_{\Gamma_{ts}^{*}}\boldsymbol{v}_{ts}^{*}\cdot\boldsymbol{n}_{ts}d\Gamma_{ts}^{*}=0 \tag{2a}$$

$$\frac{D^{*}}{D^{*}t_{ts}}\int\limits_{\Omega_{ts}^{*}}\rho_{ts}dV_{ts}^{*}+\int\limits_{\Gamma_{ts}^{*}}\rho_{ts}\left(\boldsymbol{v}_{ts}-\boldsymbol{v}_{ts}^{*}\right)\cdot\boldsymbol{n}_{ts}d\Gamma_{ts}^{*}=0 \tag{2b}$$

$$\frac{D^*}{D^* t_{ts}} \int_{\Omega^*_{ts}} \rho_{ts} \boldsymbol{v}_{ts} dV^*_{ts} + \int_{\Gamma^*_{ts}} \rho_{ts} \boldsymbol{v}_{ts} \left(\boldsymbol{v}_{ts} - \boldsymbol{v}^*_{ts} \right) \cdot \boldsymbol{n}_{ts} d\Gamma^*_{ts} - \int_{\Gamma^*_{ts}} \boldsymbol{\sigma}_{ts} \cdot \boldsymbol{n}_{ts} d\Gamma^*_{ts} - \int_{\Omega^*_{ts}} \rho_{ts} \boldsymbol{b}_{ts} dV^*_{ts} = 0 \tag{2c}$$

$$\frac{D^*}{D^* t_{ts}} \int_{\Omega^*_{ts}} \rho_{ts} \boldsymbol{u}_{ts} dV^*_{ts} + \int_{\Gamma^*_{ts}} \rho_{ts} \boldsymbol{u}_{ts} \left(\boldsymbol{v}_{ts} - \boldsymbol{v}^*_{ts} \right) \cdot \boldsymbol{n}_{ts} d\Gamma^*_{ts} - \int_{\Omega^*_{ts}} \rho_{ts} \boldsymbol{v}_{ts} dV^*_{ts} = 0 \tag{2d}$$

where ρ_{ts} is mass density, $\boldsymbol{v}_{ts}$ is material velocity, $\boldsymbol{u}_{ts}$ is material displacement, $\boldsymbol{\sigma}_{ts}$ is Cauchy stress and $\boldsymbol{b}_{ts}$ is specific-body force (i.e. force per unit mass) for the trial space.

These equations are sufficient for physical modelling in structural engineering, with Eq. (2a) enforcing control volume synchronization, Eq. (2b) allowing for density to change, Eq. (2c) being the all-important momentum equation, and Eq. (2d) first introduced in reference [27] providing a description for displacement $\boldsymbol{u}_{ts}$. With the governing constraining equations defined the next step in the finite similitude theory is the most critical as it quantifies either explicitly or implicitly all scale dependencies. This quantification is achieved by projecting the transport equations in the trial space (i.e., Eqs. (2)) onto the physical space. The projection is made possible by the existence of the map between the control volumes in the physical and trial space, Thus the relationship $d\boldsymbol{x}^*_{ts} = \beta d\boldsymbol{x}^*_{ps}$ provides the expressions $dV^*_{ts} = \beta^3 dV^*_{ps}$ and $\boldsymbol{n}_{ts} d\Gamma^*_{ts} = \beta^2 \boldsymbol{n}_{ps} d\Gamma^*_{ps}$, and recalling the time relationship $dt_{ts} = g dt_{ps}$, it is possible to substitute these into Eqs. (3). In addition to multiplication of Eqs. (2) by g each equation is individually multiplied by the scaling parameters α^1_0, α^ρ_0, α^v_0 and α^u_0 (the role of these is explained below) to provide

$$\alpha^1_0 T^1_0(\beta) = \frac{D^*}{D^* t_{ps}} \int_{\Omega^*_{ps}} \alpha^1_0 \beta^3 dV^*_{ps} - \int_{\Gamma^*_{ps}} \alpha^1_0 \beta^3 \boldsymbol{v}^*_{ps} \cdot \boldsymbol{n}_{ps} d\Gamma^*_{ps} = 0 \tag{3a}$$

$$\alpha^\rho_0 T^\rho_0(\beta) = \frac{D^*}{D^* t_{ps}} \int_{\Omega^*_{ps}} \alpha^\rho_0 \beta^3 \rho_{ts} dV^*_{ps} + \int_{\Gamma^*_{ps}} \alpha^\rho_0 \beta^3 \rho_{ts} \left(\boldsymbol{V}_{ps} - \boldsymbol{v}^*_{ps} \right) \cdot \boldsymbol{n}_{ps} d\Gamma^*_{ps} = 0 \tag{3b}$$

$$\alpha^v_0 T^v_0(\beta) = \frac{D^*}{D^* t_{ps}} \int_{\Omega^*_{ps}} \left(\alpha^v_0 g^{-1} \beta \right) \beta^3 \rho_{ts} \boldsymbol{V}_{ps} dV^*_{ts} + \int_{\Gamma^*_{ps}} \left(\alpha^v_0 g^{-1} \beta \right) \beta^3 \rho_{ts} \boldsymbol{V}_{ps} \left(\boldsymbol{V}_{ts} - \boldsymbol{v}^*_{ps} \right) \cdot \boldsymbol{n}_{ps} d\Gamma^*_{ps}$$
$$- \int_{\Gamma^*_{ps}} \boldsymbol{\Sigma}_{ps} \cdot \boldsymbol{n}_{ps} d\Gamma^*_{ps} - \int_{\Omega^*_{ps}} \boldsymbol{B}_{ps} dV^*_{ps} = 0$$

(3c)

$$\alpha_0^u T_0^u(\beta) = \frac{D^*}{D^* t_{ps}} \int_{\Omega_{ps}^*} \left(\alpha_0^u \beta\right) \beta^3 \rho_{ts} \boldsymbol{U}_{ts} dV_{ps}^* + \int_{\Gamma_{ts}^*} \left(\alpha_0^u \beta\right) \beta^3 \rho_{ts} \boldsymbol{U}_{ps} \left(\boldsymbol{V}_{ps} - \boldsymbol{v}_{ps}^*\right) \cdot \boldsymbol{n}_{ps} d\Gamma_{ps}^*$$

$$- \int_{\Omega_{ps}^*} \left(\alpha_0^u \beta\right) \beta^3 \rho_{ts} \boldsymbol{V}_{ps} dV_{ps}^* = 0 \qquad \text{(3d)}$$

where $\boldsymbol{V}_{ps} = \beta^{-1} g \boldsymbol{v}_{ts}$, $\boldsymbol{U}_{ps} = \beta^{-1} \boldsymbol{u}_{ts}$, $\boldsymbol{\Sigma}_{ps} = \alpha_0^v g \beta^2 \boldsymbol{\sigma}_{ts}$ and $\boldsymbol{B}_{ps} = \alpha_0^v g \beta^3 \rho_{ts} \boldsymbol{b}_{ts}$

Although somewhat complicated looking, Eqs. (3) are no more than Eqs. (2) but played out on the physical space; no approximation is involved in this projection. The importance of Eqs. (3) is that they reveal all scale dependencies in one form or another. Some of the scale dependencies are explicit and recognizable, such as β^3 and β^2 which arise from changes in the geometric measures of volume and area, yet others are implicit, i.e. tensor field $\boldsymbol{\Sigma}_{ps}(\beta)$, vector fields $\boldsymbol{V}_{ps}(\beta)$, $\boldsymbol{U}_{ps}(\beta)$, and $\boldsymbol{B}_{ps}(\beta)$, and scalar field $\rho_{ts}(\beta)$. The dependence of these fields on β is a consequence of the fact that the trial space is at a particular β and changing this influences the fields in that space and likewise those projected onto the physical space. The problem of scaling has been transformed into a problem where the objective is to make explicit those fields that are an implicit function of β. Once this is achieved then scaling is solved since it is then possible to know what happens at full scale from a scaled experiment. To reveal the field dependencies there are two main approaches, with the first approach requiring more information (e.g., size and surface effects) about the specific problem under consideration. A more generic approach is to assume that the physical behaviours follow a particular similitude rule. Similitude rules provide the means to design experiments and a particular advantage offered by Eqs. (3) is that unlike dimensional analysis, alternative similitude rules can be explored. The downside is that similitude rules are invariably restrictive and consequently there is no guaranteed that an experimental arrangement will fall within the solution space provided by a particular rule. However, with physical modelling and the use of alternative materials the solution space offered by a similitude rule can be enlarged but this invariably requires the existence of substitute materials with the necessary peculiar properties.

3. Similitude rules

The focus of this section is on the definition of similitude with the objective to reveal the behaviours of the hidden fields in Eqs. (3). The main transport equations can be succinctly represented in the form $\alpha_0^{\psi} T_0^{\psi} = 0$, where ψ can be set to 1, ρ, v and u. The first and possibly an obvious similitude assumption is that $\alpha_0^{\psi} T_0^{\psi}(\beta)$ does not change with β, which in mathematically terms is the identity,

$$\frac{d}{d\beta}\left(\alpha_0^{\psi} T_0^{\psi}\right) \equiv 0 \tag{4}$$

where the symbol "$\equiv$" signifies identically zero, which means the left-hand side of this equation vanishes completely under the derivative.

The identity is equivalent to what is provided by dimensional analysis since integration between the limits β and $\beta = 1$ provides $\alpha_0^{\psi} T_0^{\psi}(\beta) \equiv \alpha_0^{\psi} T_0^{\psi}(1) = T_{0ps}^{\psi}$, with the necessity that $\alpha_0^{\psi}(1) = 1$, required so that projected transport equations at $\beta = 1$ match $T_{0ps}^{\psi} = 0$. The identity $\alpha_0^{\psi} T_0^{\psi}(\beta) \equiv T_{0ps}^{\psi}$ provides an invariance between the projected trial-space equations (and by implication the original trial-space equations), with the physical space transport equations. Note the role played by $\alpha_0^{\psi}(\beta)$ in facilitating the application of a single identity (i.e., Eq. (4)) to all the transport equations, which can be likened to the role played by making equations dimensionless in dimensional analysis. Detailed studies on the application of Eq. (4) (termed zeroth order finite similitude) can be found in references [21–23,25,26], where specific zeroth-order relationships relating to density, velocity, displacement etc. can be found. The advantage offered by Eqs. (3) is that unlike dimensional analysis the approach is not limited to a single similitude identity and a countable infinite number of identities can be readily defined as follows:

3.1. Definition (High-order finite similitude)

The similitude rule for k^{th}-order finite similitude is identified by the lowest derivative that satisfies:

$$T_{k+1}^{\psi} = \frac{d}{d\beta}\left(\alpha_k^{\psi} T_k^{\psi}\right) \equiv 0 \tag{5}$$

for all $\beta > 0$ with $\alpha_0^{\psi} T_0^{\psi}$ defined by Eqs. (3) and the scalars α_k^{ψ} being a function of β with $\alpha_k^{\psi}(1) = 1$.

Note the contention here that similarity is no more than imposed rules that provide a convenient means to reveal hidden field relationships and that for the past century only one rule has been assumed to exist. However, despite Eq. (5) being a mere definition, it possesses certain attributes that make it highly suited to similarity. Firstly, lower-order forms of similitude are contained in higher-order forms; for example, zeroth order ($T_1^{\psi} \equiv 0$) automatically satisfies first order ($T_2^{\psi} = \frac{d}{d\beta}\left(\alpha_1^{\psi} T_1^{\psi}\right) \equiv 0$), and any higher order (easily shown by induction), which is a desirable if not necessary feature. All the scaling functions α_k^{ψ} play identical roles, i.e., the annihilation of β in the equations $\alpha_k^{\psi} T_k^{\psi} = 0$ to satisfy the similitude rule Eq. (6). The equations $\alpha_k^{\psi} T_k^{\psi} = 0$ are in the form of transport equations whose fields are derivatives (with respect to β) of those fields that appear in Eqs. (3) (i.e., in $\alpha_0^{\psi} T_0^{\psi} = 0$); this aspect is not explored further here. Shown below is how Eq. (5) can be integrated on forming a divided-difference table, which enables discrete identities to be formed with relative ease for application to scaled experimentation. It transpires that Eq. (5) leads to physically intuitive proportionality relationships for certain fields, field differences, field differences of differences and so on. Each increment in order requires an additional scaled experiment with zeroth order requiring only one scaled experiment, first order requiring two and so on. The reason for this is related to the order of the highest derivative in the similitude rule and for example substitution for $T_1^{\psi} = \frac{d}{d\beta}\left(\alpha_0^{\psi} T_0^{\psi}\right)$ into the identity $T_2^{\psi} = \frac{d}{d\beta}\left(\alpha_1^{\psi} T_1^{\psi}\right) \equiv 0$ provides,

$$T_2^{\psi} = \frac{d}{d\beta}\left(\alpha_1^{\psi} T_1^{\psi}\right) = \frac{d}{d\beta}\left(\alpha_1^{\psi} \frac{d}{d\beta}\left(\alpha_0^{\psi} T_0^{\psi}\right)\right) \equiv 0 \qquad (6a)$$

which is the similitude rule for first-order finite similitude and was first introduced in reference [28].

The two derivatives present in Eq. (6a) indicate that on integration, two scaled experiments are involved with a similitude rule that connects these to the full-scale system. The next level up is second order, which takes the form,

$$T_3^{\psi} = \frac{d}{d\beta}\left(\alpha_2^{\psi} T_2^{\psi}\right) = \frac{d}{d\beta}\left(\alpha_2^{\psi} \frac{d}{d\beta}\left(\alpha_1^{\psi} T_1^{\psi}\right)\right) = \frac{d}{d\beta}\left(\alpha_2^{\psi} \frac{d}{d\beta}\left(\alpha_1^{\psi} \frac{d}{d\beta}\left(\alpha_0^{\psi} T_0^{\psi}\right)\right)\right) \equiv 0 \qquad (6b)$$

and the presence of three nested derivatives indicates the need for three scaled experiments.

3.2. First-order Solutions

The prime interest in this paper is on the application of first-order finite similitude to non-trivial practical structural-engineering problems. Prior to examining the first order rules it is necessary to substitute into Eqs. (3) pertinent zeroth-order conditions obtained from identity Eq. (4), which are $\rho_{ps} = \alpha_0^{\rho}\beta^3\rho_{ts}$, $\alpha_0^1 = \beta^{-3}$, $\alpha_0^{v} = g\beta^{-1}\alpha_0^{\rho}$ and $\alpha_0^{u} = \beta^{-1}\alpha_0^{\rho}$ to provide

$$\alpha_0^{\rho}T_0^{\rho}(\beta) = \frac{D^*}{D^*t_{ps}}\int_{\Omega_{ps}^*}\rho_{ps}dV_{ps}^* + \int_{\Gamma_{ps}^*}\rho_{ps}\left(\boldsymbol{V}_{ps} - \boldsymbol{v}_{ps}^*\right)\cdot\boldsymbol{n}_{ps}d\Gamma_{ps}^* = 0 \tag{7a}$$

$$\alpha_0^{v}T_0^{v}(\beta) = \frac{D^*}{D^*t_{ps}}\int_{\Omega_{ps}^*}\rho_{ps}\boldsymbol{V}_{ps}dV_{ts}^* + \int_{\Gamma_{ps}^*}\rho_{ps}\boldsymbol{V}_{ps}\left(\boldsymbol{v}_{ts} - \boldsymbol{v}_{ps}^*\right)\cdot\boldsymbol{n}_{ps}d\Gamma_{ps}^*$$
$$-\int_{\Gamma_{ps}^*}\boldsymbol{\Sigma}_{ts}\cdot\boldsymbol{n}_{ps}d\Gamma_{ps}^* - \int_{\Omega_{ps}^*}\boldsymbol{B}_{ts}dV_{ps}^* = 0 \tag{7b}$$

$$\alpha_0^{u}T_0^{u}(\beta) = \frac{D^*}{D^*t_{ps}}\int_{\Omega_{ps}^*}\rho_{ps}\boldsymbol{U}_{ts}dV_{ps}^* + \int_{\Gamma_{ps}^*}\rho_{ps}\boldsymbol{U}_{ps}\left(\boldsymbol{v}_{ps} - \boldsymbol{v}_{ps}^*\right)\cdot\boldsymbol{n}_{ps}d\Gamma_{ps}^* - \int_{\Omega_{ps}^*}\rho_{ps}\boldsymbol{V}_{ps}dV_{ps}^* = 0 \tag{7c}$$

where $\boldsymbol{\Sigma}_{ps} = \alpha_0^{v}g\beta^2\boldsymbol{\sigma}_{ts}$, $\boldsymbol{B}_{ts} = \alpha_0^{v}g\beta^3\rho_{ts}\boldsymbol{b}_{ts} = g^2\beta^{-1}\boldsymbol{b}_{ts}$, and where it is recognized that the condition $\alpha_0^1 = \beta^{-3}$ ensures that Eq. (3a) satisfies Eq. (4) (and consequently Eq. (6a)), so is of no further concern.

To avoid the necessity for second-order finite similitude the term $\boldsymbol{V}_{ts} - \boldsymbol{v}_{ps}^*$ is replaced by the zeroth-order approximation $\boldsymbol{v}_{ts} - \boldsymbol{v}_{ps}^*$ in the movement and momentum equations to reflect the fact that convective-type terms are of little concern in structural engineering. The transformation of Eqs. (6) into the required discrete integrated form can be readily achieved by means of a divided-difference table (see Table 1) and observe that the focus on behaviour at $\beta_0 = 1$ and down scaling means backward differences are required. In addition, unlike a traditional divided-difference table a mean-value theorem is applied to ensure exact differences are returned. In particular, the first divided differences in column three in Table 1 are obtained from the identities,

Table 6:1: Divided difference table for first-order theory

β_i	$\alpha_0^{\psi}\mathbb{T}_0^{\psi}(\beta_i)$	First Divided	Second Divided

		Difference	Difference
β_2	$\alpha_0^{\psi}\mathbf{T}_0^{\psi}\left(\beta_2\right)$		
		$\alpha_1^{\psi}\mathbf{T}_1^{\psi}\left(\beta_2^1\right)$	
β_1	$\alpha_0^{\psi}\mathbf{T}_0^{\psi}\left(\beta_1\right)$		$\dfrac{\alpha_1^{\psi}\mathbf{T}_1^{\psi}\left(\beta_1^0\right)-\alpha_1^{\psi}\mathbf{T}_1^{\psi}\left(\beta_2^1\right)}{\beta_1^0-\beta_2^1}\equiv 0$
		$\alpha_1^{\psi}\mathbf{T}_1^{\psi}\left(\beta_1^0\right)$	
β_0	$\alpha_0^{\psi}\mathbf{T}_0^{\psi}\left(\beta_0\right)$		

$$\alpha_1^{\psi}\mathbf{T}_1^{\psi}\left(\beta_2^1\right)\equiv\alpha_1^{\psi}\left(\beta_2^1\right)\frac{\alpha_0^{\psi}\mathbf{T}_0^{\psi}\left(\beta_1\right)-\alpha_0^{\psi}\mathbf{T}_0^{\psi}\left(\beta_2\right)}{\beta_1-\beta_2} \tag{8a}$$

$$\alpha_1^{\psi}\mathbf{T}_1^{\psi}\left(\beta_1^0\right)\equiv\alpha_1^{\psi}\left(\beta_1^0\right)\frac{\alpha_0^{\psi}\mathbf{T}_0^{\psi}\left(\beta_0\right)-\alpha_0^{\psi}\mathbf{T}_0^{\psi}\left(\beta_1\right)}{\beta_0-\beta_1} \tag{8b}$$

where $\beta_2\le\beta_2^1\le\beta_1$ and $\beta_1\le\beta_1^0\le\beta_0$ on application of a mean-value theorem, and where β_2 and β_1 are distinct scales such that $\beta_2<\beta_1<\beta_0=1$.

The second divided difference in column four in Table 1 is identically zero as is evident on integration of Eq. (6a) between the limits β_2^1 and β_1^0. It follows then on substitution of Eqs. (8) into the identity $\alpha_1^{\psi}T_1^{\psi}\left(\beta_1^0\right)\equiv\alpha_1^{\psi}T_1^{\psi}\left(\beta_2^1\right)$, and following some reorganization, that the required discrete sought identity

$$\alpha_0^{\psi}\mathbf{T}_0^{\psi}\left(\beta_0\right)\equiv\alpha_0^{\psi}\mathbf{T}_0^{\psi}\left(\beta_1\right)+R_1^{\psi}\left(\alpha_0^{\psi}\mathbf{T}_0^{\psi}\left(\beta_1\right)-\alpha_0^{\psi}\mathbf{T}_0^{\psi}\left(\beta_2\right)\right) \tag{9}$$

is obtained where,

$$R_1^{\psi}=\left(\frac{\alpha_1^{\psi}\left(\beta_2^1\right)}{\alpha_1^{\psi}\left(\beta_1^0\right)}\right)\left(\frac{\beta_0-\beta_1}{\beta_1-\beta_2}\right) \tag{10}$$

and where R_1^{ψ} takes the form of a parameter arising for the indeterminacy of the function $\alpha_1^{\psi}(\beta)$.

Note that Eq. (9) provides transport equations for the physical space formed from information at the two scales β_2 and β_1. It is by this means that equations constraining the behaviour at the two scales β_2 and β_1 also constrain the behaviour at the full scale β_0. Application of Eq. (9) to the governing transport equations (i.e., Eqs. (7)), return the all-important first-order field identities

$$\boldsymbol{v}_{ps}=\boldsymbol{V}_{ps}\left(\beta_1\right)+R_1^{\rho}\left(\boldsymbol{V}_{ps}\left(\beta_1\right)-\boldsymbol{V}_{ps}\left(\beta_2\right)\right) \tag{11a}$$

$$\boldsymbol{v}_{ps} = \boldsymbol{V}_{ps}(\beta_1) + R_1^{v}\left(\boldsymbol{V}_{ps}(\beta_1) - \boldsymbol{V}_{ps}(\beta_2)\right) \tag{11b}$$

$$\boldsymbol{\sigma}_{ps} = \boldsymbol{\Sigma}_{ps}(\beta_1) + R_1^{v}\left(\boldsymbol{\Sigma}_{ps}(\beta_1) - \boldsymbol{\Sigma}_{ps}(\beta_2)\right) \tag{11c}$$

$$\boldsymbol{b}_{ps} = \boldsymbol{B}_{ps}(\beta_1) + R_1^{v}\left(\boldsymbol{B}_{ps}(\beta_1) - \boldsymbol{B}_{ps}(\beta_2)\right) \tag{11d}$$

$$\boldsymbol{u}_{ps} = \boldsymbol{U}_{ps}(\beta_1) + R_1^{u}\left(\boldsymbol{U}_{ps}(\beta_1) - \boldsymbol{U}_{ps}(\beta_2)\right) \tag{11e}$$

$$\boldsymbol{v}_{ps} = \boldsymbol{V}_{ps}(\beta_1) + R_1^{u}\left(\boldsymbol{V}_{ps}(\beta_1) - \boldsymbol{V}_{ps}(\beta_2)\right) \tag{11f}$$

where (as mentioned above) scaling is solved once the relationships for the fields are obtained.

Three velocity fields are provided in Eqs (11) but there can be only one and therefore for a consistent velocity expression it is necessary that $R_1 = R_1^{\rho} = R_1^{v} = R_1^{u}$; achieved by setting identical the functions $\alpha_1^{\rho}, \alpha_1^{v}$ and α_1^{u}. Any additional fields of interest can be easily derived from Eqs. (11) and for convenience the fields of interest in this paper are presented in Table 2.

Table 6:2: General zeroth-order and first-order finite similitude relationships

Properties	Zeroth-order identities	First-order identities
Density	$\rho_{ps} = \alpha_{01}^{\rho}\rho_{ts1}\beta_1^3$	$\rho_{ps} = \alpha_{01}^{\rho}\rho_{ts1}\beta_1^3 + R_1\left(\alpha_{01}^{\rho}\rho_{ts1}\beta_1^3 - \alpha_{02}^{\rho}\rho_{ts2}\beta_2^3\right)$
Displacement	$\boldsymbol{u}_{ps} = \beta_1^{-1}\boldsymbol{u}_{ts1}$	$\boldsymbol{u}_{ps} = \beta_1^{-1}\boldsymbol{u}_{ts1} + R_1\left(\beta_1^{-1}\boldsymbol{u}_{ts1} - \beta_2^{-1}\boldsymbol{u}_{ts2}\right)$
Velocity	$\boldsymbol{v}_{ps} = g_1\beta_1^{-1}\boldsymbol{v}_{ts1}$	$\boldsymbol{v}_{ps} = g_1\beta_1^{-1}\boldsymbol{v}_{ts1} + R_1(g_1\beta_1^{-1}\boldsymbol{v}_{ts1} - g_2\beta_2^{-1}\boldsymbol{v}_{ts2})$
Acceleration	$\boldsymbol{a}_{ps} = g_1^2\beta_1^{-1}\boldsymbol{a}_{ts1}$	$\boldsymbol{a}_{ps} = g_1^2\beta_1^{-1}\boldsymbol{a}_{ts1} + R_1(g_1^2\beta_1^{-1}\boldsymbol{a}_{ts1} - g_2^2\beta_2^{-1}\boldsymbol{a}_{ts2})$
Stress	$\boldsymbol{\sigma}_{ps} = \alpha_{01}^{\rho}g_1^2\beta_1\boldsymbol{\sigma}_{ts1}$	$\boldsymbol{\sigma}_{ps} = \alpha_{01}^{\rho}g_1^2\beta_1\boldsymbol{\sigma}_{ts1} + R_1\left(\alpha_{01}^{\rho}g_1^2\beta_1\boldsymbol{\sigma}_{ts1} - \alpha_{02}^{\rho}g_2^2\beta_2\boldsymbol{\sigma}_{ts2}\right)$
Strain	$\boldsymbol{\varepsilon}_{ps} = \boldsymbol{\varepsilon}_{ts1}$	$\boldsymbol{\varepsilon}_{ps} = \boldsymbol{\varepsilon}_{ts1} + R_1\left(\boldsymbol{\varepsilon}_{ts1} - \boldsymbol{\varepsilon}_{ts2}\right)$
Force	$\boldsymbol{F}_{ps} = \alpha_{01}^{\rho}g_1^2\beta_1^{-1}\boldsymbol{F}_{ts1}$	$\boldsymbol{F}_{ps} = \alpha_{01}^{\rho}g_1^2\beta_1^{-1}\boldsymbol{F}_{ts1} + R_1(\alpha_{01}^{\rho}g_1^2\beta_1^{-1}\boldsymbol{F}_{ts1} - \alpha_{02}^{\rho}g_2^2\beta_2^{-1}\boldsymbol{F}_{ts2})$
Moment	$\boldsymbol{M}_{ps} = \alpha_{01}^{\rho}g_1^2\beta_1^{-2}\boldsymbol{M}_{ts1}$	$\boldsymbol{M}_{ps} = \alpha_{01}^{\rho}g_1^2\beta_1^{-2}\boldsymbol{M}_{ts1} + R_1(\alpha_{01}^{\rho}g_1^2\beta_1^{-2}\boldsymbol{M}_{ts1} - \alpha_{02}^{\rho}g_2^2\beta_2^{-2}\boldsymbol{M}_{ts2})$

The field relationships in Table 2 are exact, but it is recognized that errors are very much a feature of experimental studies. Although this is the topic of future work, the similitude identities however do provide some insight into the effect of error and to illustrate this consider for example the displacement identity $\boldsymbol{u}_{ps} = \beta_1^{-1}\boldsymbol{u}_{ts1} + R_1\left(\beta_1^{-1}\boldsymbol{u}_{ts1} - \beta_2^{-1}\boldsymbol{u}_{ts2}\right)$. The reality of scaled experimentation is errors $\boldsymbol{\delta}_{ts1}^{u}$ and $\boldsymbol{\delta}_{ts2}^{u}$ in the trial-space field displacements $\boldsymbol{u}_{ts1}$ and $\boldsymbol{u}_{ts2}$, respectively, which on substitution returns the identity $\boldsymbol{\delta}_{ps}^{u} = \beta_1^{-1}\boldsymbol{\delta}_{ts1}^{u} + R_1\left(\beta_1^{-1}\boldsymbol{\delta}_{ts1}^{u} - \beta_2^{-1}\boldsymbol{\delta}_{ts2}^{u}\right)$, where $\boldsymbol{\delta}_{ps}^{u}$ is the error in $\boldsymbol{u}_{ps}$. Although the actual error in the physical space depends very much on the problem and how close the virtual model replicates the physical behaviour, this error equation nevertheless provides insight into the required accuracy needed in the trial spaces to achieve acceptable outcomes in the physical space.

4. Scaling of structural elements

This focus in this section is on the scaled behaviour of basic structural elements such as columns, beams, and struts under static loads. The purpose here is twofold, firstly to provide a gentle introduction into the application of the similitude theory and, secondly, to understand better the response of more complex structures through insights gleaned from an appreciation about the behaviour of basic structural elements under scaling. The relatively simple case studies examined in this section are analysed both analytically and numerically with the aid of the finite element package ABAQUS [32].

4.1. Scaling of Beam-Strut Model

Beams are important structural components that can withstand loads primarily by resisting bending and serve to transfer loads to walls, girders, and adjacent compression members. An appreciation of how beams scale is important for scaled experiments and to that end consider a simple setup of an I-section steel beam connected to a circular hollow steel strut. The arrangement examined is depicted in Fig. 1, where shown are both the full and scaled models, which have been recreated in the Abaqus finite element software and each are subjected to a

concentrated force at the free end. The models in Abaqus are meshed with identical numbers of elements of type B31, which is a 2-noded linear beam element and identical materials are used for both the trial-space and full-scale models. To verify the types of analysis, an initial comparison was performed between analytical and numerical models. This provided end deflections of 22.425mm and 22.419mm for the respective analytical and numerical models, so providing high confidence in the modelling approach.

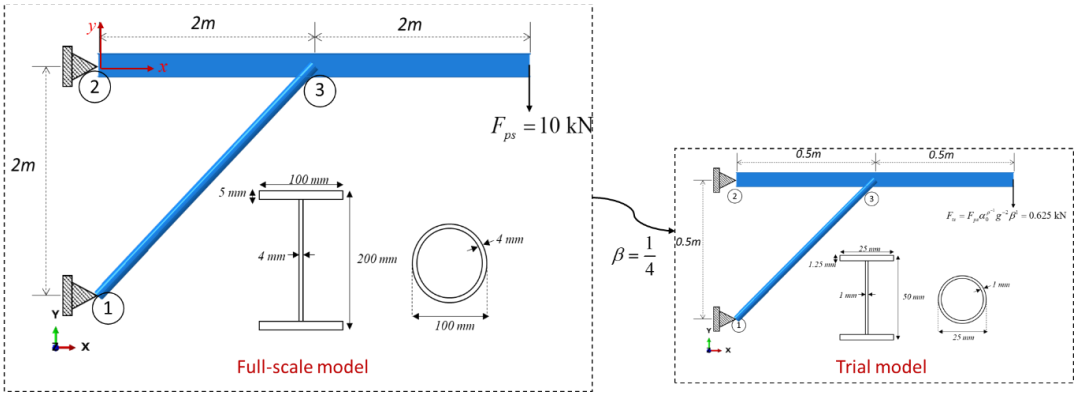

Figure 1: Full-scale and trial model of the beam-strut model

Shear force and bending moment are described by the respective expressions,

$$V_{ps}(x_{ps}) = \begin{cases} -F_{ps} & 0 < x_{ps} < 2 \\ F_{ps} & 2 < x_{ps} < 4 \end{cases} \tag{12a}$$

$$M_{ps}(x_{ps}) = \begin{cases} -F_{ps}x_{ps} & 0 < x_{ps} < 2 \\ F_{ps}x_{ps} & 2 < x_{ps} < 4 \end{cases} \tag{12b}$$

and examination of Table 2 provides the zeroth-order scaling identities $V_{ps} = \alpha_0^{\rho} g^2 \beta^{-1} V_{ts}$ and $M_{ps} = \alpha_0^{\rho} g^2 \beta^{-2} M_{ts}$.

In a similar fashion the standard expression for normal stress, scales according to the zeroth-order relationship $\sigma_{ps} = \alpha_{01}^{\rho} g_1^2 \beta_1 \sigma_{ts1}$ in Table 2 since

$$\sigma_{ps} = \frac{M_{ps} y_{ps}}{I_{ps}} = \frac{\alpha_0^{\rho} g^2 \beta^{-2} M_{ts} \beta^{-1} y_{ts}}{\beta^{-4} I_{ts}} = \alpha_0^{\rho} g^2 \beta \frac{M_{ts} y_{ts}}{I_{ts}} = \alpha_0^{\rho} g^2 \beta \sigma_{ts} \tag{13}$$

where I_{ps} and I_{ts} are second moments of area, y_{ps} and y_{ts} the distances measured from the neutral axes of the beams in their respective spaces.

Note that the similitude relationships provide the means to communicate the behaviour of the trial model to the physical space. They in effect provide the

projected-trial model identified in Table 3, where maximum bending moments, reaction forces at the supports, and end displacements both analytically and numerically obtained, are tabulated. Note that the projected-trial models provide an almost perfect match for both analytical and numerical models when compared with the full-space results. A slightly greater mismatch is observed on a direct comparison of analytically and numerically obtained results. Even at this early stage, the benefit offered by scaling is being revealed with high levels of conformity.

Table 6:3: Detailed comparison of full-scale and projected trial model for beam-strut model

		Analytical			Numerical (FEM)		
		Trial Model	Projected Trial Model	Full-scale Model	Trial Model	Projected Trial Model	Full-scale Model
End Displacement (mm)		5.6065	22.4260	22.425	5.6047	22.4191	22.4190
Reaction force (kN)	Rx @1 Ry @1	1.25 1.25	20 20	20 20	1.25 1.202	20 19.232	19.999 19.250
	Rx @2 Ry @2	1.25 0.625	20 20	20 10	1.25 0.576	20 9.226	19.999 9.228
Maximum Moment (MNmm)		0.3125	20	20	0.313	20.320	20.271
Maximum Stress (N/mm^2)		169.5682	169.5682	169.5682	171.865	171.865	171.865

4.2. Scaling of a Steel Column Exposed to Buckling

Examined in this section are the phenomena of linear buckling and post-buckling of an important structural element, i.e., the I-section column. The buckling phenomenon might be anticipated to provide a challenge for scaled experimentation since initial imperfections can influence the outcome. Understanding the scaled behaviour of buckling for columns and beams under axial compression load is of interest as flexural and torsional stability problems can result. A detailed analytical and numerical examination into the buckling of

an I-section aluminium-alloy column is provided in reference [101]. Flexural buckling is reasonably well captured by the simple relationship,

$$P_{cr} = \frac{\pi^2 EI}{L_{eff}^2} \tag{14}$$

where P_{cr} is the critical buckling load, E is Young's modulus of the material, I is the cross-sectional second moment of area, and L_{eff} is the effective length, which is dictated by column boundary conditions.

Prior to the investigation of the scaled effects on scaled columns, the proposed I-section column model is verified analytically and numerically in accordance with the study presented in reference [101]. The details of the full and scaled models are provided in Fig. 2. Initial verification results for critical-buckling loads are tabulated in Table 4 for both analytical and numerical predictions and contrasted with those of reference [30]. The closeness of the predictions provides good confidence in the proposed models. The simply supported column (6m in length) is made of aluminium alloy 5083 with material properties: Youngs modulus $E = 67600\,\text{MPa}$, Poisson ratio $\nu = 0.33$, and yield stress $\sigma_y = 159.1\,\text{MPa}$. The stress-strain behaviour of the aluminium alloy is described by the Ramberg-Osgood relationship [102],

$$\varepsilon = \frac{\sigma}{E} + K\left(\frac{\sigma}{\sigma_y}\right)^{n-1} \tag{15}$$

where the material constants $K = 0.002$ and $n = 8.8202$ [103].

The analytical solution is verified with the Abaqus finite element software package and to obtain the critical buckling load, a linear buckling analysis is performed initially. The model makes use of shell elements of type S4R with reduced integration, which are a 4-noded doubly curved, thin element and the mesh consists of a total of 46800 nodes. After linear-buckling analysis, post-buckling analysis is performed to observe the behaviour of the column on applying nonlinear material properties (i.e., Eq. (15)). The Ramberg-Osgood law is applied in Abaqus with deformational plasticity by the specification of two parameters, which are yield offset $\alpha = KE/\sigma_y$ and the hardening exponent $n-1$ [80].

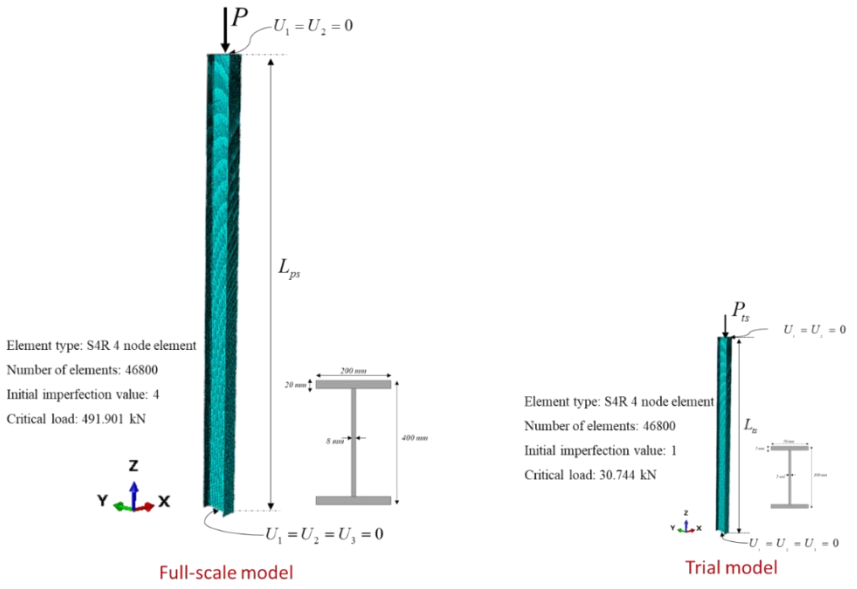

Figure 2: Finite element model with applied load and boundary conditions and cross-section of the full-scale and trial model

Table 6:4: Critical buckling load of a simply supported I-section column.

	Current Analysis		Szymczak and Kujawa [30]	
	Analytical	Numerical	Analytical	Numerical
Linear-buckling load (kN)	494.496	491.901	494.5	491.2

The main instability analysis is performed in Abaqus using the Static-RIKS command, which is a variation on the classical arc-length method for defining an initial geometric imperfection. The global imperfection amplitude is set to $L/1500$ (L is column length), which generally provides promising results when compared to experimental tests [104][105]. With this setup, the model is now primed for investigation of the load-deflection under scaling.

4.2.1. Scaling of flexural column buckling

The *finite similitude* theory is applied to the models depicted in Fig. 2 with a length scaling factor of $\beta = \frac{1}{4}$ and by means of the *zeroth-order theory* (i.e., identity Eq. (5)) the structure under scaling is investigated. The material of the column is the same for both scaled and full-scale models with scaling parameters obtained via the scaling rules (see Table 2). An initial comparison is made for linear buckling analysis for the full-scale and trial model as shown in Fig. 3.

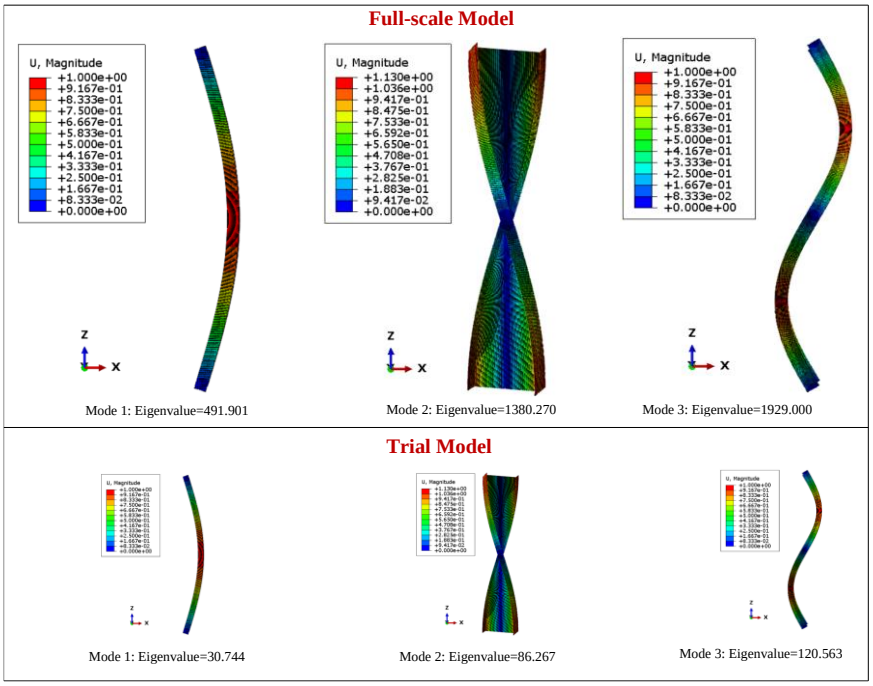

Figure 3: Comparison between linear buckling eigenmodes and eigenvalues (critical buckling load) of full-scale and trial model.

The critical load obtained from linear buckling analysis is in exact agreement for both the full-scale and trial-scale models, where the full-scale critical load equates to β^{-2} times that of trial-space model. This is anticipated from Eq. (14), since Table 2 provides the stress and strain relationships $\boldsymbol{\sigma}_{ps} = \alpha_{01}^{\rho} g^2 \beta \boldsymbol{\sigma}_{ts}$ and $\boldsymbol{\varepsilon}_{ps} = \boldsymbol{\varepsilon}_{ts1}$, and consequently $E_{ps} = \alpha_0^{\rho} g^2 \beta E_{ts}$, which on substitution into Eq. (15) gives,

$$\left(P_{cr}\right)_{ps} = \frac{\pi^2 E_{ps} I_{ps}}{\left(L_{eff}\right)_{ps}^2} = \frac{\pi^2 \left(\alpha_0^{\rho} g^2 \beta E_{ts}\right)\left(\beta^{-4} I_{ts}\right)}{\beta^{-2}\left(L_{eff}\right)_{ts}^2} = \left(\alpha_0^{\rho} g^2 \beta\right)\beta^{-2} \frac{\pi^2 E_{ts} I_{ts}}{\left(L_{eff}\right)_{ts}^2} = \alpha_0^{\rho} g^2 \beta^{-1} \left(P_{cr}\right)_{ts} \qquad (16)$$

which is in accordance with force relationship $\boldsymbol{F}_{ps} = \alpha_0^{\rho} g^2 \beta^{-1} \boldsymbol{F}_{ts}$ (see Table 2) but since $E_{ps} = E_{ts}$ it follows that $\alpha_0^{\rho} g^2 \beta = 1$ and consequently $\left(P_{cr}\right)_{ps} = \beta^{-2}\left(P_{cr}\right)_{ts}$.

The outcome of the post-buckling, nonlinear-stability analysis is provided in Fig. 4, where the projected trial-space results are contrasted against the full-scale predictions. Perfect agreement is achieved for the load-deflection response of the column, providing further evidence of the efficacy of the zeroth-order theory in this case.

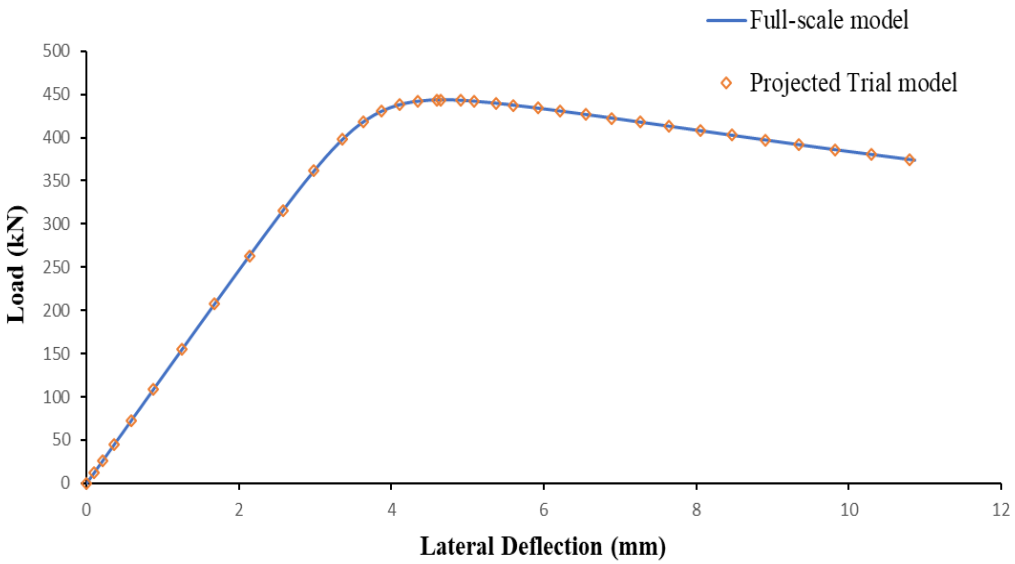

Figure 4: Load–lateral displacement curves for comparison.

4.3. The Thin-section Problem

The relatively simple examples considered thus far satisfy Eq. (4) and the rules of zeroth-order finite similitude. It is of interest at this stage to maintain the relative simplicity but introduce a problem that fails to satisfy Eq. (4) yet conforms to identity Eq. (6a), i.e., *first-order finite similitude*. An important area of active research for scaled experimentation is around the concept of geometric similarity as defined by dimensional analysis. It can be desirable on practical grounds to break the rules of geometric similarity especially if thin structural elements are involved, where one or more of the structural dimensions are significantly smaller than the others. For pronounced scaling ratios that are often needed when scaling large structures (e.g., bridges, skyscrapers) the limitation imposed by thinner sections can be particularly constraining. Unrepresentative behaviour such as localized buckling and tearing can be the product of very thin sections along with standard of-the-shelf items being unavailable. The open literature in this area is underpinned by dimensional analysis and is case dependent involving ad-hoc practical fixes and consequently does not provide a systematic unified solution [43,75,106–108]. It is of interest therefore to assess whether first-order finite similitude can provide any insight into this problem for structural elements. The scaling of a cantilever beam under a concentrated load is again examined but, in this case, geometric similarity is broken in some manner. Detailed in Fig. 5 is a

rectangular hollow box section cantilever beam possessing the critical feature of interest, i.e., a thin wall.

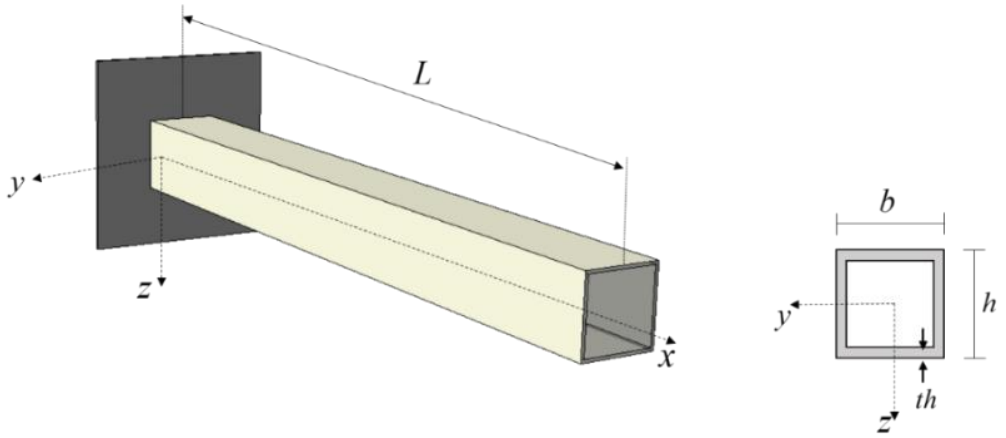

Figure 5: Rectangular hollow cross-section cantilever beam and cross-section

The detailed geometries are presented in Table 5 for full-scale, trial-1, and trial-2 models. The scaling factors for two trial-space models are set to $\beta_1 = \frac{1}{5}$ and $\beta_2 = \frac{1}{10}$ but imposed on the experimental designs is the constraint that the wall thickness *th* is greater or equal to 1mm (i.e., $th \geq 1\text{mm}$). Note from Table 5 that the geometric dimensions *h* (height), *b* (width) and *L* (length) are all scaled according to the geometric scaling rule, i.e., they scale with β. The thickness however is constrained and therefore does not obey this rule and, in both trial-space models it is set to the minimum required thickness of 1 mm.

Table 6:5: Material properties and geometric dimensions of box-section beams

	Variables	Full-scale	Trial-1 model	Trial-2 model
	b (mm)	50	10	5
	h (mm)	50	10	5
	th (mm)	4	1	1
	L (mm)	1000	200	100
	Density (ton/mm^3 x10^{-9})	7.85	7.85	7.85
	Young's modulus (GPa)	210	210	210
	Yield stress (MPa)	355	355	355
	Poisson ratio	0.3	0.3	0.3
Case Study 1	Applied Force (N)	2000	80	20
	Measured tip displacement (mm)	12.14	2.065	0.7
Case Study 2	Applied Force (N)	4500	215	82.5

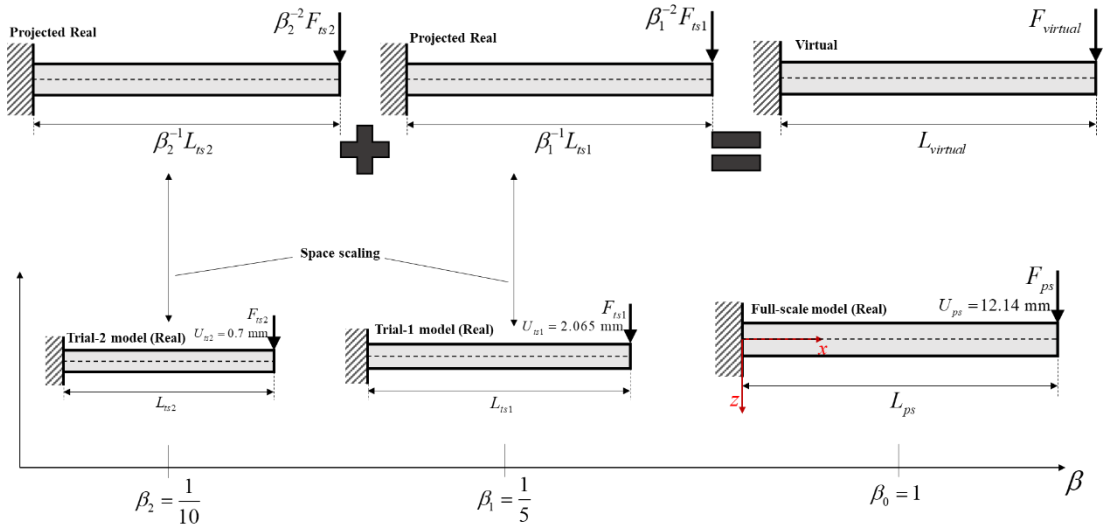

Figure 6: Physical space and Projected trial models for the cantilever beam

Shown in Fig. 6 is a schematic of the first order approach applied to the box-section beam involving two scaled experiments that are projected onto the physical space and combined to provide a virtual model that attempts to capture the behaviour of the full-scale system. The use identical of materials throughout

reduces the relationships $\alpha_{01}^{\rho} g_1^2 \beta_1 E_{ts1} = E_{ps}$ and $\alpha_{02}^{\rho} g_2^2 \beta_2 E_{ts1} = E_{ps}$ to $\alpha_{01}^{\rho} g_1^2 = \beta_1^{-1}$ and $\alpha_{02}^{\rho} g_2^2 = \beta_2^{-1}$ respectively, which simplifies the force and stress relationships in Table 2 to

$$F_{ps} = \beta_1^{-2} F_{ts1} + R_1 (\beta_1^{-2} F_{ts1} - \beta_2^{-2} F_{ts2}) \tag{17a}$$

$$\sigma_{ps} = \sigma_{ts1} + R_1 (\sigma_{ts1} - \sigma_{ts2}) \tag{17b}$$

where R_1 is the parameter defined by Eq. (10) that is required to be set, where the lateral beam deflection is,

$$U_{ps} = \beta_1^{-1} U_{ts1} + R_1 \left(\beta_1^{-1} U_{ts1} - \beta_2^{-1} U_{ts2} \right) \tag{17c}$$

Two case studies are considered with case study 1 limited to linear behaviour described by analytical relationships and case study 2 examining the nonlinear response but analysed numerically. The steel material used in the study is defined to behave as an elastic, perfectly plastic material. The loading conditions for both case studies are detailed in Tab. 5. Consider then the linear response of the cantilever, and since β_1, β_2 and F_{ps} are known, a convenient approach for the determination of R_1 is to firstly assume zeroth-order relationships for force and set $F_{ts1} = \beta_1^2 F_{ps}$ and $F_{ts2} = \beta_2^2 F_{ps}$, which ensures Eq. (17a) is satisfied. Secondly, the free-end tip displacements for each beam provided by the analytical relationships where $U_{ts1}^{max} = \frac{F_{ts1} L_{ts1}^3}{3 E_{ts1} I_{ts1}}$ and $U_{ts2}^{max} = \frac{F_{ts2} L_{ts2}^3}{3 E_{ts2} I_{ts2}}$ can be substituted into Eq. (17c) to give the value of R_1 to be,

$$R_1 = \frac{U_{ps}^{max} - \beta_1^{-1} U_{ts1}^{max}}{\beta_1^{-1} U_{ts1}^{max} - \beta_2^{-1} U_{ts2}^{max}} \tag{18}$$

which provides a simple procedure for the determination of R_1 in this case, which in this case provides $R_1 = 0.5465$.

The tip displacement for the full-scale and virtual model is calculated (with $R_1 = 0.5465$) and not too unexpectedly an exact match in this case, since R_1 is set

to ensure this outcome. With R_1 determined, Eq. (17c) can now be employed to provide a prediction for the beam displacement shown in Fig. 7(a), which perfectly replicates the behaviour of the full-scale beam. Similarly, Eq. (17b) provides the means to examine normal stress, the results of which are presented in Fig. 7. Note that normal stress at the outer fibres of the beam is in perfect agreement between the virtual and full-scale models as indicated in Fig. 7(b). However, this is not the full story since there is a deviation in the vicinity of the upper and lower walls of the virtual and full-scale beams. The normal stress is plotted along the mid-span of the two beams in Fig. 7(c). The reason for the difference is connected to the breakage of geometric similarity, which resulted in the two projected models in Fig. 6 having different outer-wall thicknesses and satisfying the inequalities $th < \beta_1^{-1} th_{ts1} < \beta_2^{-1} th_{ts2}$. This means that stress values exist in the virtual model that is not present in the full-scale model as illustrated in Fig. 7(c). The issue is of little real concern, however since the important field information recovered from the virtual is that which overlaps with the full-scale model and for this example at least full replication is achieved.

To examine the nonlinear response of the beam (case study 2) the commercial software package Abaqus is applied, with the beam represented with 2-noded linear beam elements (B31). The first order scaling parameter R_1 is obtained using Eq. (17a) using the forces detailed in Tab. 5, which returns a value $R_1 = 0.304$. Eq. (17c) is then applied to calculate the beam displacement of the first order virtual model, which is contrasted against the full-scale model as presented in Fig. 8(a), where an exact match is revealed. The reason for the exact prediction is shown in Fig. 8(b), where Eq. (7b) provides for perfect replication of the nonlinear stress-strain behaviour.

The study in this section demonstrates that first-order finite similitude can return an exact representation for a situation where the traditional definition of similarity does not hold. Although a relatively simple example and the focus of future work (with and without buckling), it nevertheless demonstrates two important features, i.e., an exact new form of similitude exists and breaking geometric similarity to a certain degree is possible and potentially very useful.

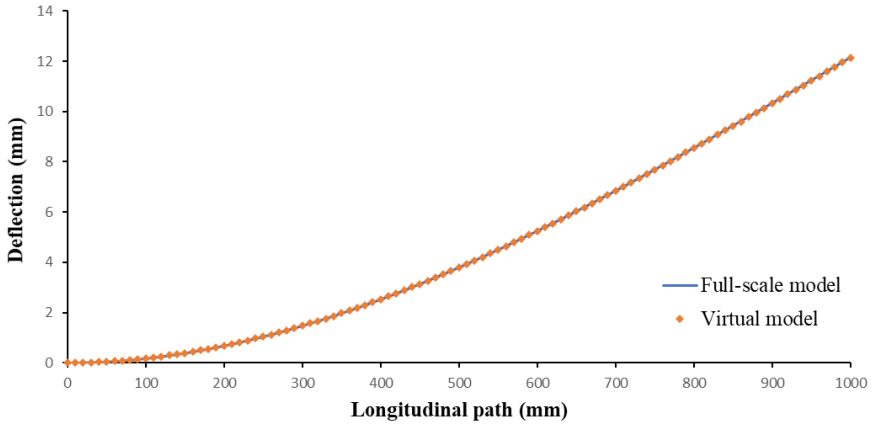

(a)

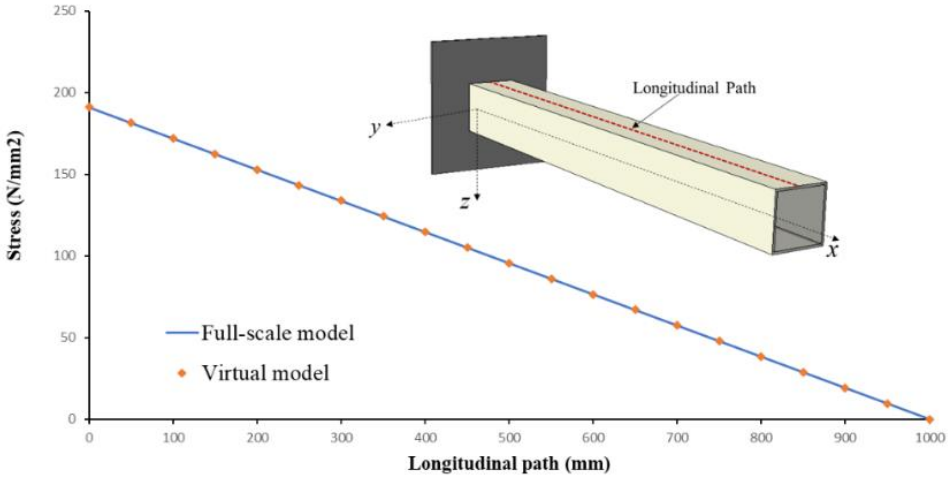

(b)

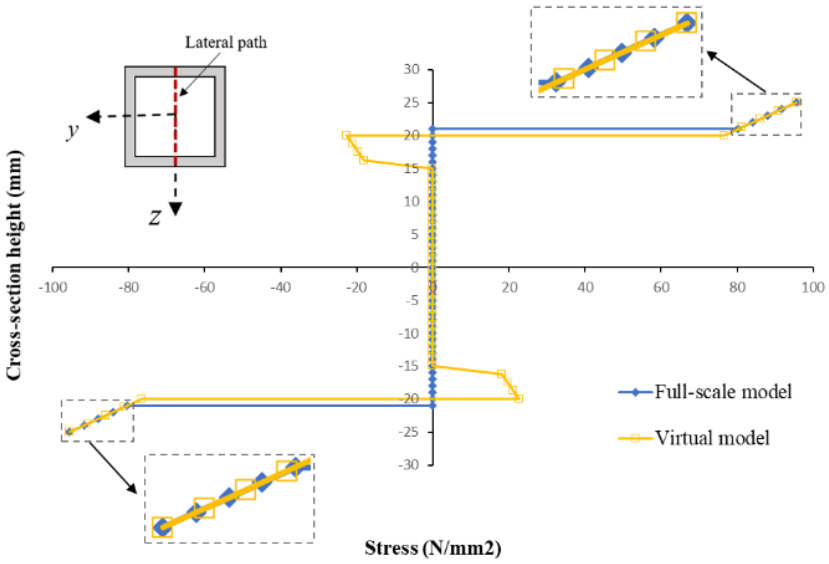

(c)

Figure 7: Global and local behaviour of the stress field (a) Beam deflection for the proposed design (b) Longitudinal distribution of the maximum normal stress (@$z=h/2$), (c) Lateral distribution of the normal stress at mid-span.

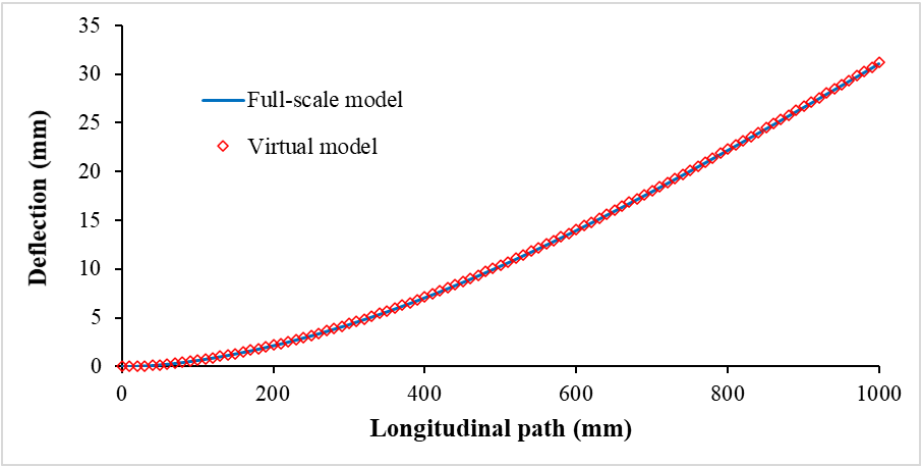

(a)

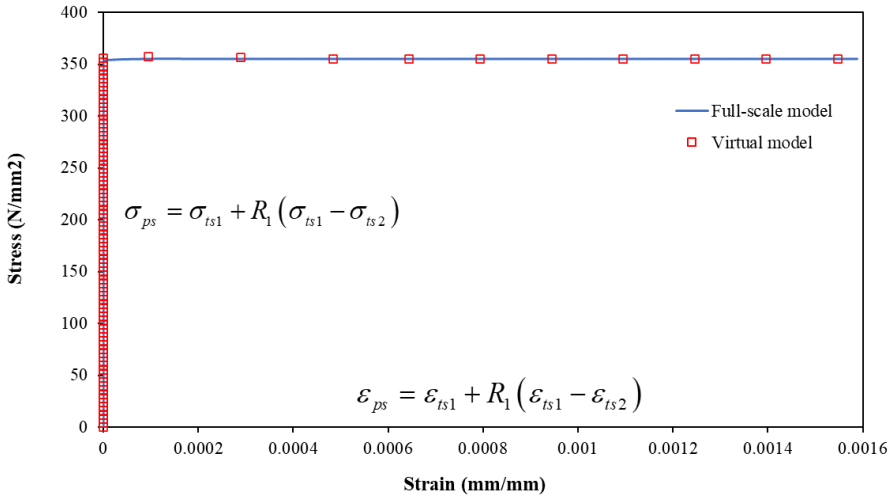

(b)

Figure 8: Nonlinear response of a cantilever beam subjected to an end load (a) Beam deflection along the length of the beam (b) Stress-strain curve at the clamped end.

5. Scaling of an eight-story long-span steel building

This section focuses on the application of zeroth and first-order finite similitude to the earthquake loading of a high-rise, long-span building structure. This type of building is selected as the case study to focus the analysis on how the finite-similitude theory can be applied in seismic scenarios. It is recognized as mentioned above that pronounced scaling factors can give rise to significant scale effects arising from mass and gravity. The traditional "solution" to this problem

is additional mass [93] or incrementation of the base acceleration. The case study here is designed to examine this problem to ascertain whether the new theory can provide a possible solution. Added-mass approaches are invariably breaking geometric similarity and increases in acceleration limit the materials that can be employed and can rule out the use of identical materials. Acceleration can be shown to be inversely proportional to the dimension scaling factor β, so it can take on impractically high values for buildings such as high rises.

In order to provide realism in the study, the Chi-Chi Earthquake, which yields very high dynamic earth pressures, is applied as the time-acceleration ground motion (depicted in Fig. 9 [109]). All beams and columns in all eight stories are identical (with the same cross-sectional area, length) and slabs in all eight stories. The building has a span of 7.2 m on each side with a floor height of 3.2 m and the slab thickness is assumed to be of 100 mm and the beams and columns are modelled with I sections (IPE450) and box profiles (Box 500×500×30), respectively [110].

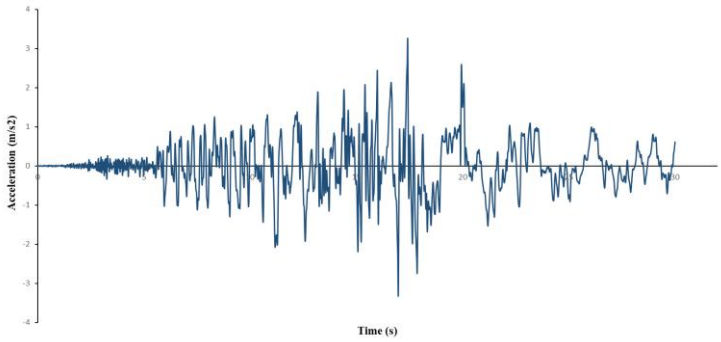

Figure 9: Acceleration – Time graph for Chi-Chi earthquake

The whole structure and all components are modelled in the Abaqus finite element software as depicted in Fig. 10, where the B31 linear beam element (i.e., a first-order, three-dimensional beam element) is utilized to simulate the columns and beams. The use of this element significantly reduces the number of degrees of freedom involved providing a convenient platform for repeat calculations. The slab is meshed with S4R elements (i.e., four-node shell elements) with each node having six degrees of freedom.

Figure 10: The eight-story building (a) CAD model (b) Finite element meshed parts

Another important consideration when modelling steel or reinforced concrete structures is critical damping. Abaqus has several methods for the dissipation of energy in dynamic systems with the specification of damping sources. Four different damping sources exist in Abaqus; these are: material and damping system; damping with time integration; modal damping; and global damping. In the case of earthquake phenomena best practice for implicit and explicit methods is Rayleigh damping [111,112] with the critical viscous damping factor for this analysis is set to 5% [113–116].

The scaled models are designed according to the similarity laws with identical materials used for both full-scale and trial models to test out their ability to capture the effects of earthquake loading on a full-scale building structure. The dimension scales selected for the study are $\beta_1 = \frac{1}{10}$ and $\beta_2 = \frac{1}{20}$, and both zeroth and first-order theories are applied with details presented in Table 6.

Table 6:6: Material properties for physical, trial 1 and trial 2 models

Properties	Physical Model	Trial 1 Model	Trial 2 Model
Material (Steel)	S355	S355	S355
Density (kg/m^3)	7850	7850	7850
Young's modulus (GN/m^2)	210	210	210
Yield stress (MN/m^2)	3.55	3.55	3.55
Damping ratio (ξ)	5%	5%	5%
Gravity (m/s^2)	9.807	9.807	9.807
Acceleration (m/s^2)	1	1	1

Scaling factors	$\beta_0 = 1$	$\beta_1 = 1/10$	$\beta_2 = 1/20$
Time (s)	$g_0 = 1$	$g_1 = 1/10$	$g_2 = 1/20$
Additional mass (kg)		No add. mass	No add. mass

The aim here is to adopt identical materials for both full-scale and trial models and consequently the zeroth order relationships for density ($\rho_{ps} = \alpha_{01}^{\rho}\rho_{ts1}\beta_1^3$) and Young's modulus ($E_{ps} = \alpha_{01}^{\rho}g_1^2\beta_1 E_{ts1}$) reduce to $\rho_{ps} = \rho_{ts1}$ and $E_{ps} = E_{ts1}$ with $\alpha_{01}^{\rho} = \beta_1^{-3}$ and $g_1 = \beta_1$. This latter condition provides the zeroth-order acceleration relationship $\boldsymbol{a}_{ts1} = \beta_1^{-1}\boldsymbol{a}_{ps}$ (see Table 2), which confirms that as $\beta_1 \to 0$ the acceleration applied to the scaled model increases as $\beta_1^{-1} \to \infty$. It is appreciated that increasing the acceleration can return promising results but there is patently a limit to what is practicable. Staying within a reasonable range for acceleration for pronounced scaling factors excludes both dimensional analysis and zeroth-order finite similitude.

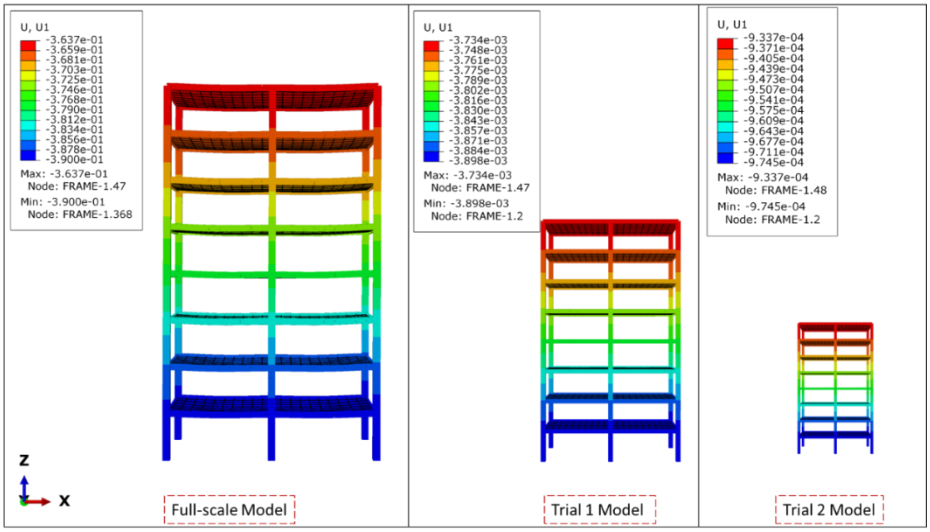

Figure 11: Numerical deformed shapes of the physical and scaled models

It is of interest to examine the scope of *first-order finite similitude*, which combines the information from two scaled experiments, to deal with this issue. The first-order acceleration relationship $\boldsymbol{a}_{ps} = g_1^2\beta_1^{-1}\boldsymbol{a}_{ts1} + R_1(g_1^2\beta_1^{-1}\boldsymbol{a}_{ts1} - g_2^2\beta_2^{-1}\boldsymbol{a}_{ts2})$ (see Table 2) is the focus here in view of the limitations mentioned above. Recall that each trial model is restricted to designs utilising the same material and zeroth-order considerations provide the relationships $\alpha_{01}^{\rho} = \beta_1^{-3}$ & $\alpha_{02}^{\rho} = \beta_2^{-3}$ and $g_1 = \beta_1$ & $g_2 = \beta_2$. Observe that these latter two conditions mean that the first-order

relationship for acceleration reduces to $\boldsymbol{a}_{ps} = \beta_1 \boldsymbol{a}_{ts1} + R_1(\beta_1 \boldsymbol{a}_{ts1} - \beta_2 \boldsymbol{a}_{ts2})$. The ground acceleration (as shown in Fig. 9) is assumed to act in one direction with identical accelerations applied in all models, i.e., $a_{ps} = a_{ts1} = a_{ts2}$, and additionally it is an evident requirement is that gravitational accelerations are equal, i.e., $G_{ps} = G_{ts1} = G_{ts2}$. These constraints imposed on the equation $\boldsymbol{a}_{ps} = \beta_1 \boldsymbol{a}_{ts1} + R_1(\beta_1 \boldsymbol{a}_{ts1} - \beta_2 \boldsymbol{a}_{ts2})$ provide $R_1 = \frac{1-\beta_1}{\beta_1 - \beta_2} = 18$.

The full-scale and both trial models are simulated by the Abaqus finite element software (details above) and the results obtained are presented in Figs. 11, 12 and 13. The roof displacement and the story drift of the physical model and the first-order virtual model are presented using the first-order displacement relationship in Tab. 2.

The results obtained illustrate the vast promise and the benefits of two scaled experiments over a single experiment. This example demonstrates the ability of the finite similitude theory to evaluate the behaviour of structures with information gleaned from two experiments. The result in Fig. 12 shows that the extracted results are orders of magnitude more accurate than those obtainable from a single experiment. It also worth emphasising that no recourse to additional mass or other acceleration increments is needed and the way this is achieved is not by changing the problem but by changing the similitude condition.

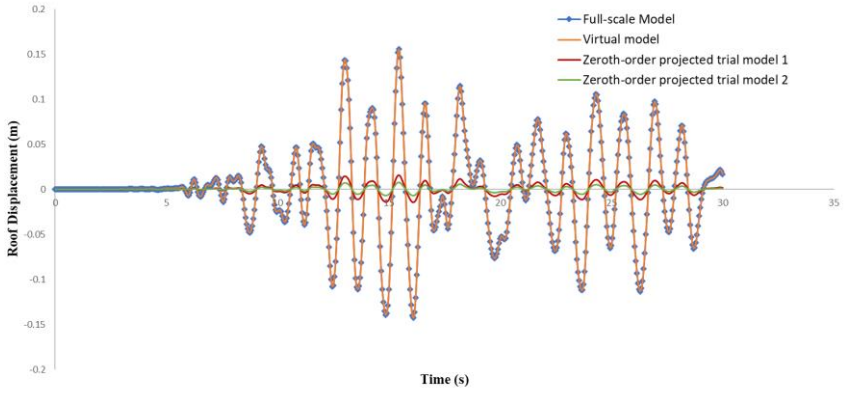

Figure 12: Comparison of the top displacement of the full-scale model, first-order and zeroth-order virtual models

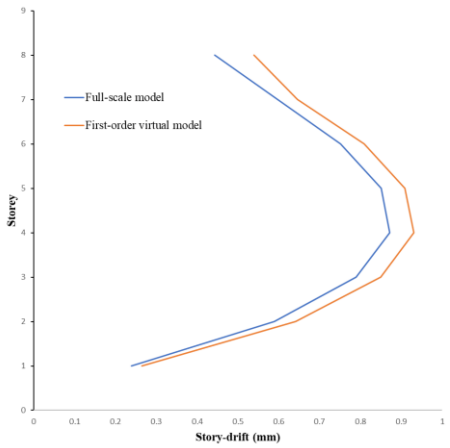

Figure 13: Story drift analysis of the full-scale and virtual models

Additionally, to examine the nonlinear dynamic response of the eight story long-span building depicted in Fig. 10, it is subjected a gradually increasing cyclic dynamic loading as detailed in Fig. 14(a). Nonlinear analysis is performed on each of the trial models, and the results of these are combined in accordance with the first-order theory and presented in Fig. 14(b). Examination of this figure reveals a high level of agreement with the full-scale model confirming once again the efficacy of the first order similitude condition. All the models in this study are made of identical material with properties tabulated in Table 7 and $R_1 = 18$ as in the earthquake loading case.

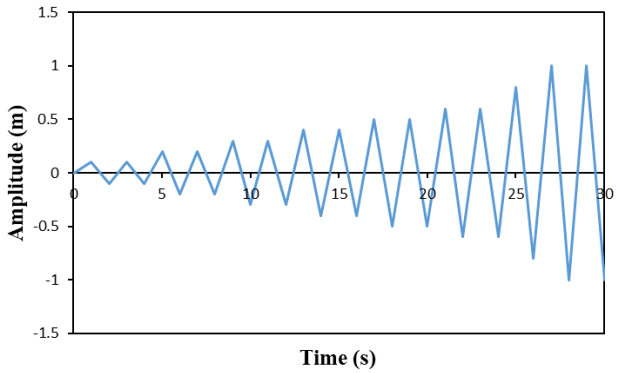

(a)

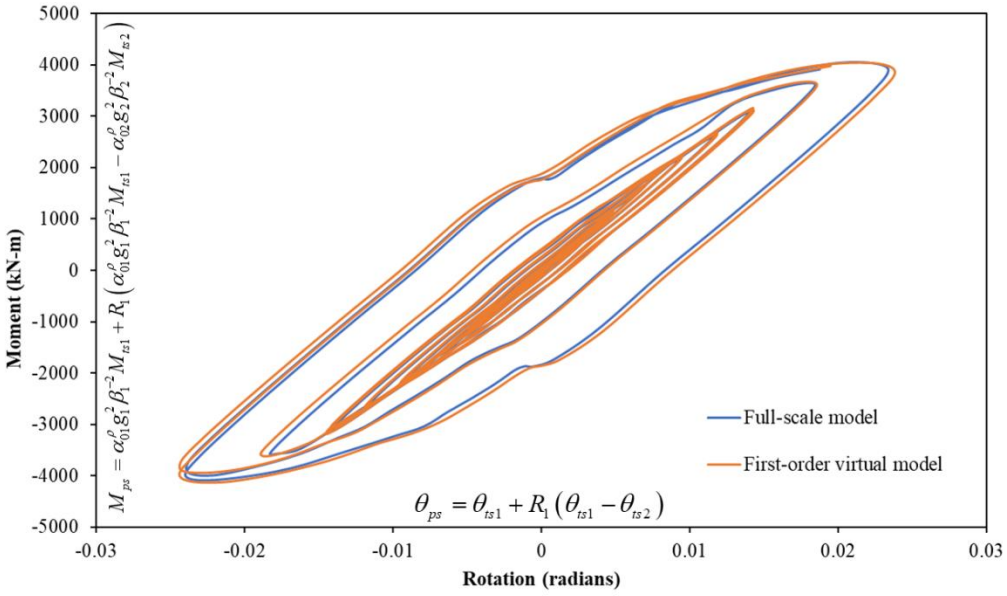

(b)

Figure 14: (a) Applied cyclic loading scheme (b) moment-rotation response of the full-scale and virtual models

6. Seismic performance of a steel building equipped with nonlinear fluid viscous dampers

Additional sophistication is incorporated into the building design investigated in this section with the inclusion of dampers in the structure. The steel construction frame examined involves eight stories and six bays in each direction, where the area plan is 36m x 36m, and the elevation view of the structure is detailed in Fig. 15 with column and beam sections [117] identified. The detailed section properties of the beams and columns are listed in Table 7. The steel used for all structural elements in full-scale and scaled-down models is ST37 steel grade. In addition, to perform a nonlinear time history analysis, the commercial finite element Sap2000 software package [118] is used and the Northridge (1994) acceleration-time (see Fig. 16) data is applied in the x-direction of the building as a ground motion. The structural damping is estimated to be at 5% and the placement of the fluid viscous dampers (FVDs) and the building details are in accordance with reference [117].

Table 6:7: Cross-sections of the beams and columns [117].

Structure	Story	C1	C2	B1	B2
8-story steel frame	1	RHS 360 × 20	RHS 550 × 30	W 18 × 46	W 21 × 111
	2	RHS 240 × 20	RHS 500 × 30	W 18 × 46	W 21 × 111
	3	RHS 200 × 20	RHS 450 × 25	W 18 × 46	W 21 × 111
	4	RHS 180 × 18	RHS 450 × 25	W 18 × 46	W 21 × 111
	5	RHS 180 × 18	RHS 400 × 20	W 18 × 46	W 21 × 93
	6	RHS 180 × 18	RHS 400 × 20	W 18 × 46	W 21 × 73
	7	RHS 180 × 18	RHS 360 × 20	W 18 × 46	W 21 × 50
	8	RHS 180 × 18	RHS 300 × 20	W 18 × 40	W 21 × 44
Slab (Shell)	All	100 mm thickness			

It is widely recognised that one of the most effective devices to dissipate energy during the action of an earthquake is a fluid viscous damper [119]. The details of the fluid viscous damper used in this study are provided by Mehdi et al. [117]. The main parameters of the viscous dampers are the damping coefficient, velocity exponent α and the lateral stiffness provided by the supporting bar, which in that case are 2942.5 kNs/m, 0.5 and 39004 kN/m respectively.

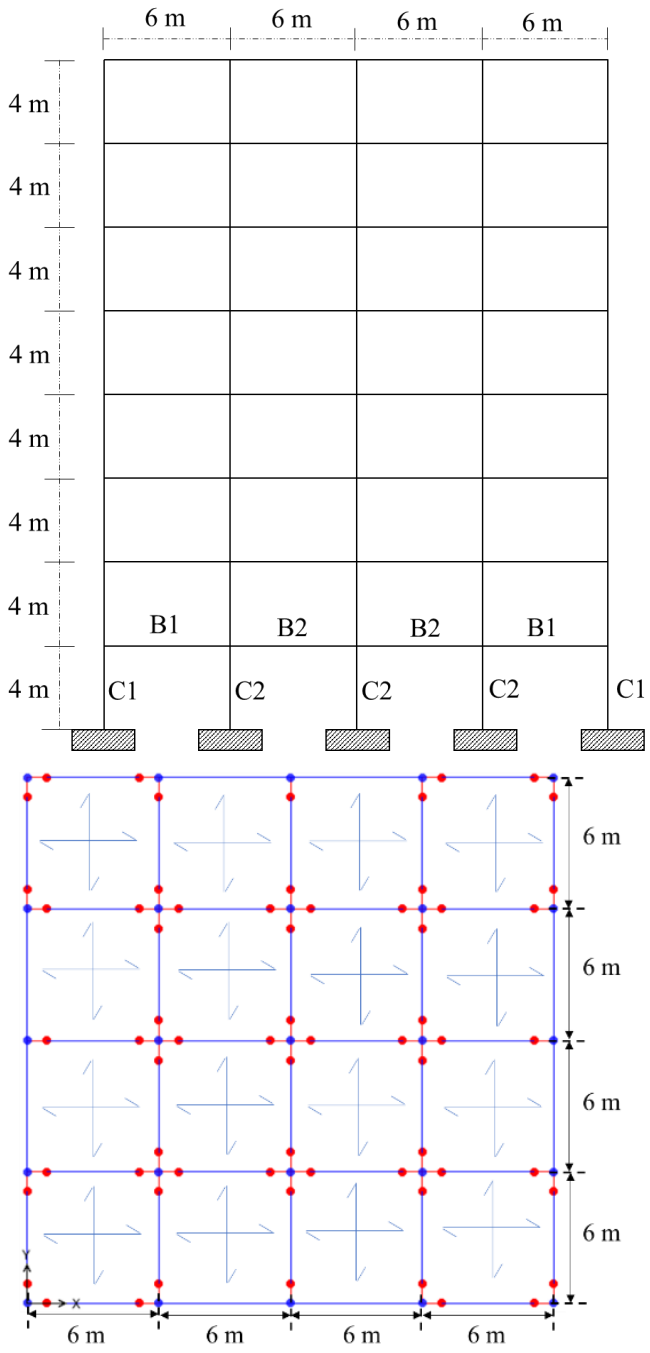

Figure 15: Elevation view and the plan grid layout of the model

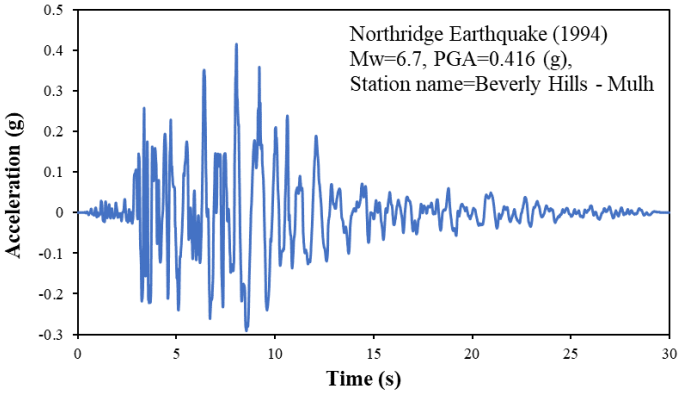

Figure 16: Applied Northridge earthquake record

The fluid viscous damper is defined as a link property in Sap2000 and the fluid damper is constrained to act only along the axial direction of the damper and thus constrained in directions that are perpendicular to its axis. Fig. 17 shows the 2D elevation view of the structure along with the placements of the FVDs.

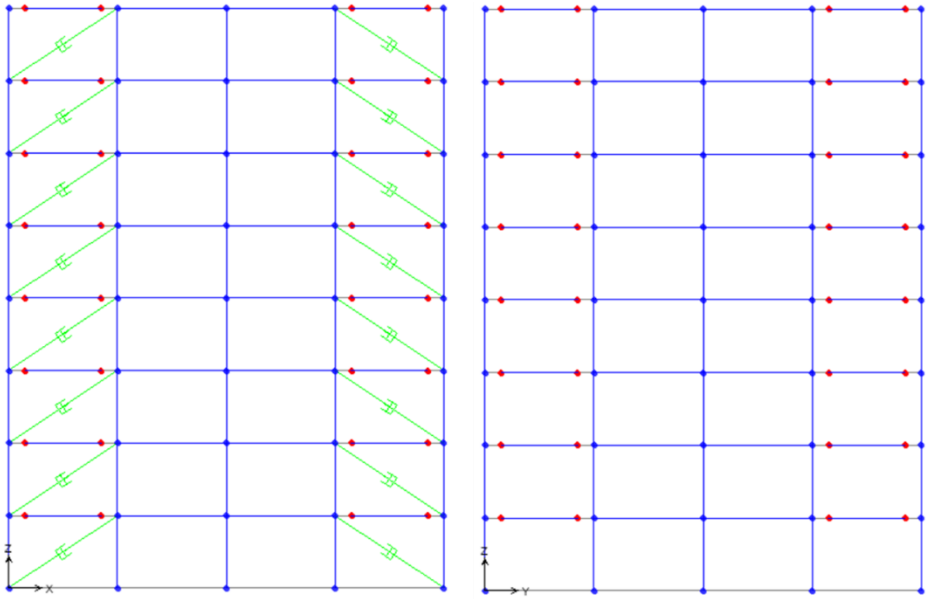

Figure 17: Sap2000 elevation view of the model with FVDs

Based on a mesh-sensitivity study (see Tab. 8), the minimum numbers of elements for the beams and columns to guarantee convergence of the numerical solution, capturing the behaviour of the structure are 320 and 200, respectively; this mesh is applied in the presented case study.

Table 6:8: Mesh sensitivity analysis results

Column elements	Beam elements	Total number of elements	Max. top displacement (m)
200	320	520	0.3705
1000	1600	2600	0.3706
4000	6400	10400	0.3706
8000	12800	20800	0.3699

With the full-scale model now defined, the geometric scaling parameters are set for trial models 1 and 2, which are $\beta_1 = \frac{1}{6}$ and $\beta_2 = \frac{1}{10}$, respectively. These scaling factors should be selected carefully according to laboratory capacities and equipment limitations. As a preliminary investigation a controlled displacement pushover analysis is performed prior to full dynamic analysis of the proposed building. Such an analysis provides an opportunity to observe nonlinear behaviour under quasistatic loading. This is facilitated by the application of hinge properties applied automatically to the ends of the beams to observe how localised plastic behaviour translates to an overall nonlinear response. The nonlinear static pushover analysis is conducted on both trial models and a moment-rotation graphs are produced and presented in Fig. 19 (b), where perfect agreement, between full scale and individual scaled models is revealed.

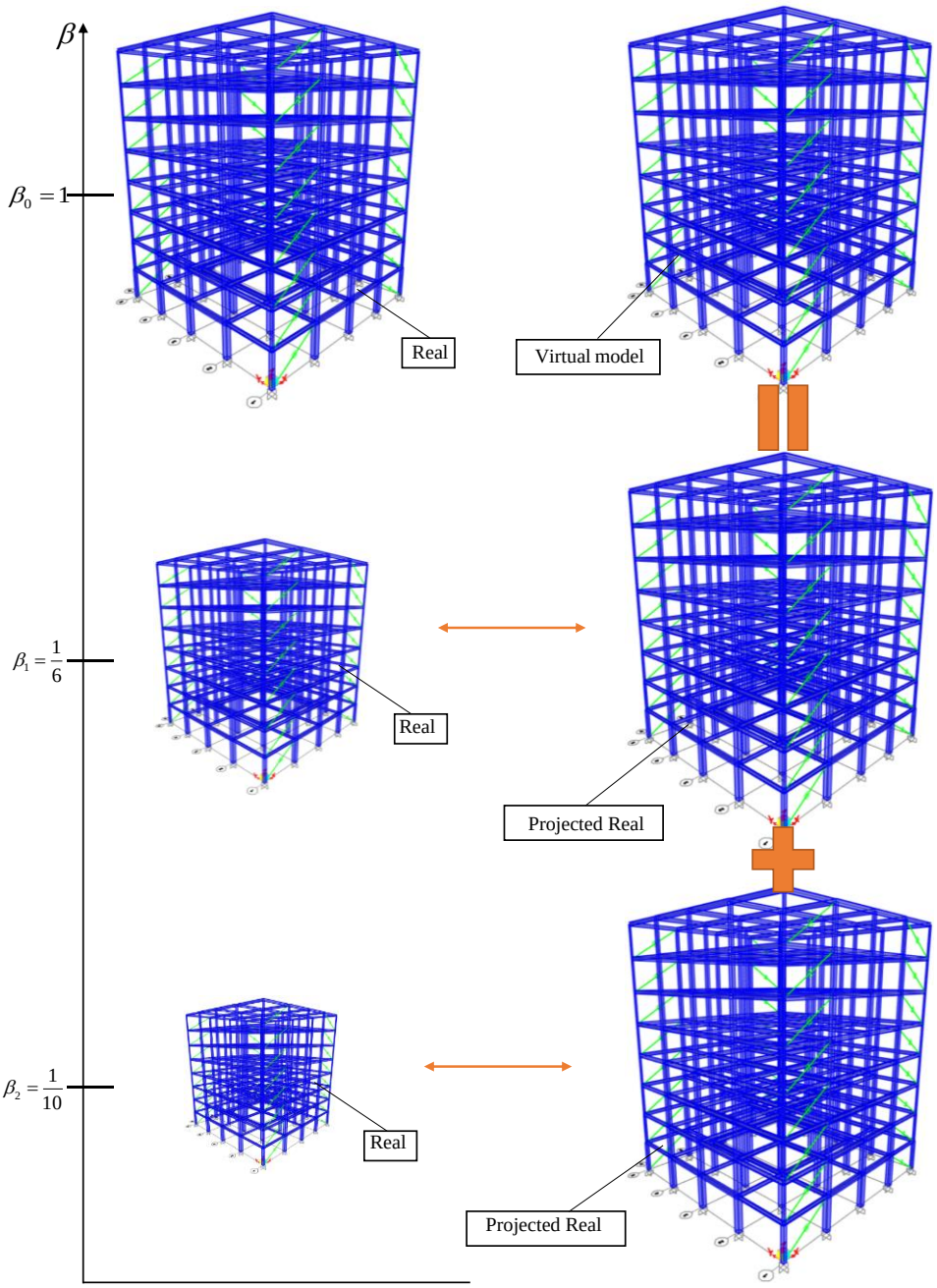

Figure 18: Full-scale and scaled models of the 8-story steel building

For dynamic analysis, it is not possible to capture the buildings behaviour using a single scaled model due to the added complexity involved, necessitating the need for additional scaling degrees of freedom. In this case, the scaled models are analysed using the same software (i.e., Sap2000) to observe their behaviour to predict the full-scale model behaviour under earthquake loading. The configuration of the three models is presented in Fig. 18 along with corresponding projected models. Given that identical materials are used throughout the scaling parameters related to density and time are set to $\alpha_{01}^{\rho} = \beta_1^{-3}$

& $\alpha_{02}^{\rho} = \beta_2^{-3}$ and $g_1 = \beta_1$ & $g_2 = \beta_2$. The boundary and loading conditions are defined as in the previous case study, where gravitational acceleration and applied acceleration is equal for the three models, which as above, returns $R_1 = 12.5$ from the relationship $R_1 = \frac{1-\beta_1}{\beta_1-\beta_2}$

The damping coefficients for structural damping and the FVDs follow different scaling rules as described in reference [72]. The Rayleigh damping coefficients for structural damping obeys the relationship $c_{ps} = \beta^{-2} c_{ts}$, which can be contrasted with the damping coefficients for the FVDs, which satisfy the relationship $c_{ps} = \beta^{-\alpha} c_{ts}$, where this latter condition assumes no change in the damping fluid used. Note, however, it is possible to achieve the identity $c_{ps} = \beta^{-2} c_{ts}$ for the FVDs with a change in damping fluid. This is a practical change but it does require that the damping fluid has an appropriate viscosity [120,121]. Both these options are explored here.

Fig. 19 (a) and 20 present the behaviour of the full-scale model and the virtual model with the damping coefficients for the FVDs behaving as $c_{ps} = \beta^{-\alpha} c_{ts}$ and $c_{ps} = \beta^{-2} c_{ts}$, respectively. It is clear on examination of Fig. 19 (a) that there is a significant difference between the virtual and full-scale results with a mismatch in oscillation frequency. In comparison to the prediction in Fig. 19 (a), Fig. 20 highlights the benefits of changing the silicone oil in the scaled FDVs. In this case the behaviour of the FVDs follows the same scaling behaviour as structural damping and the outcome is a small overall error. The results demonstrate promising agreement with the full-scale model outputs and indicate the benefit of careful material selection. Further evidence of the high level of agreement between the models is found in Figs. 21 and 22 with results for story displacement & inter-story drift ratios, and the base shear force, respectively. Overall, the results obtained from the first-order finite similitude theory provide confidence in the efficacy of the approach for predicting the behaviour of tall buildings.

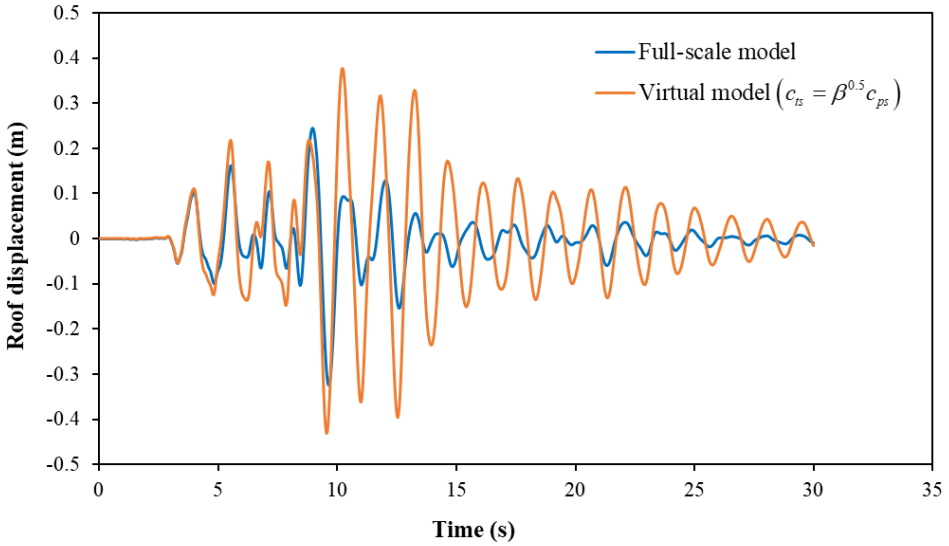

(a)

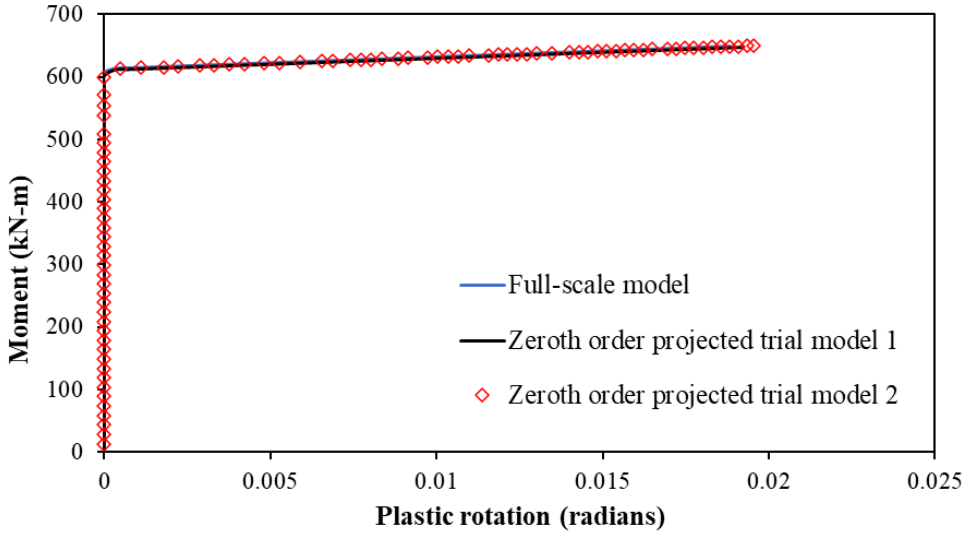

(b)

Figure 19: (a) Roof displacement comparison between full-scale and virtual models with the same silicone oil in the trial nonlinear FVDs, (b) Moment-rotation comparison of full-scale and zeroth-order projected trial models.

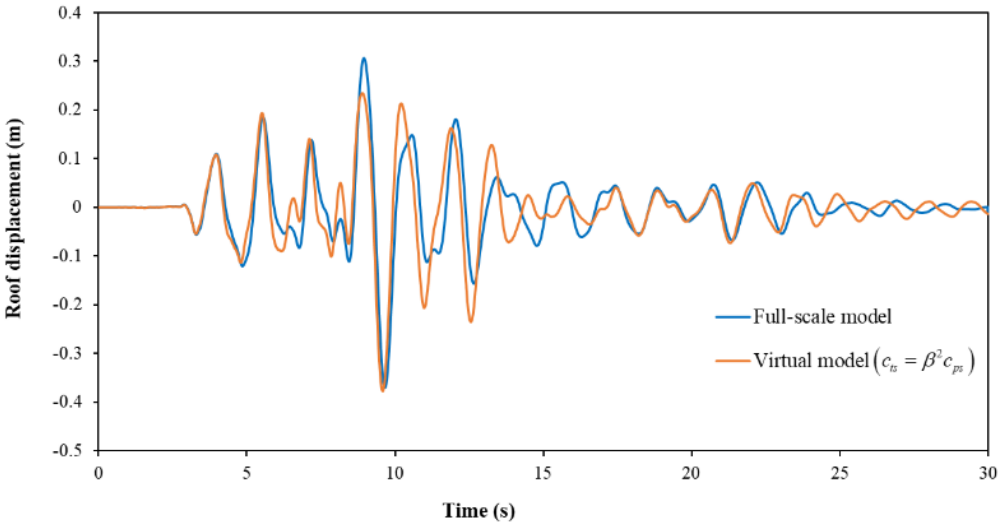

Figure 20: Roof displacement comparison of the full-scale and virtual model with alternative silicone oil in the trial nonlinear FVDs

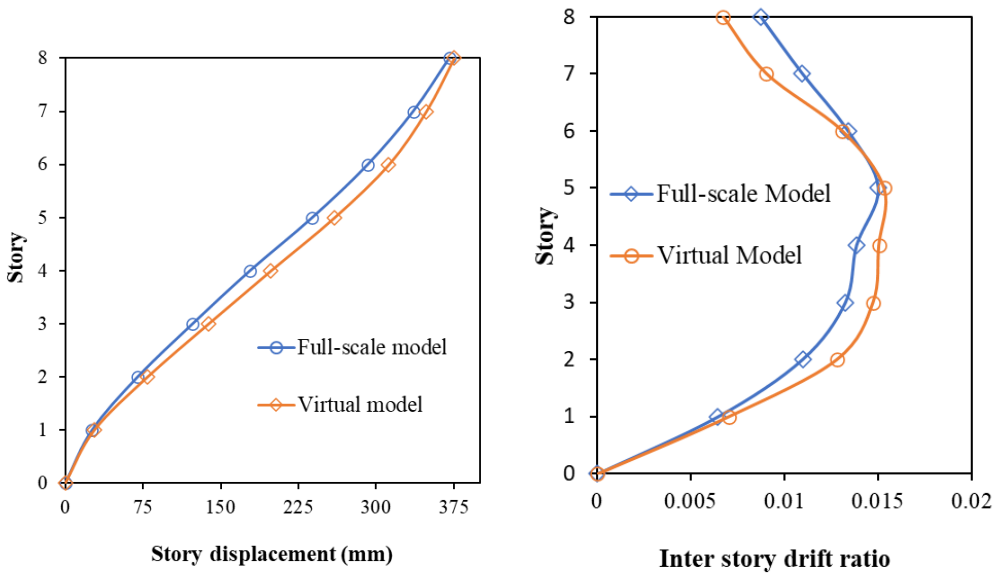

(a) (b)

Figure 21: (a) Story displacement and (b) inter-story drift ratio comparison for full-scale and virtual models

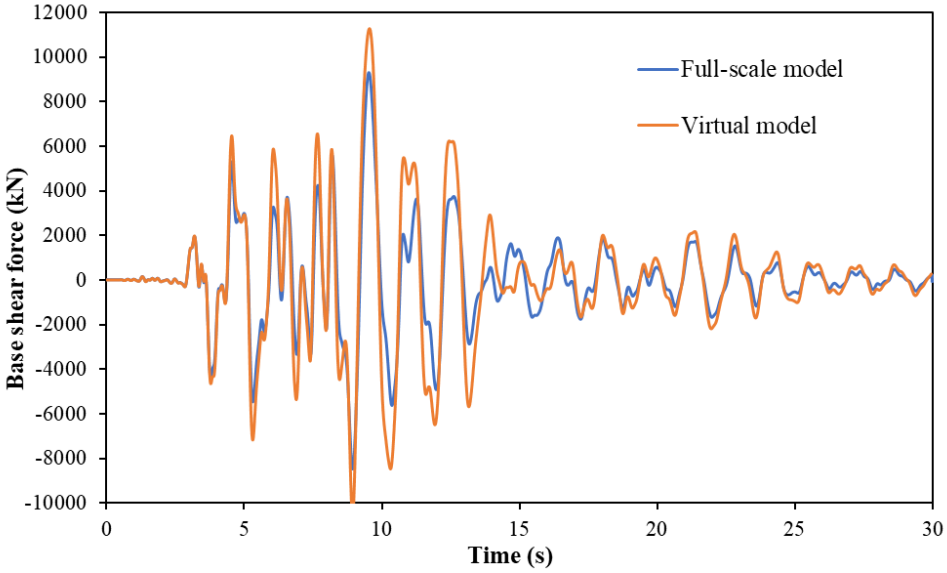

Figure 22: Base shear force comparison of the full-scale and virtual models

7. Conclusion

The paper focused on the application of the finite-similitude theory by means of an initial examination of structural elements through to the analysis of whole-building structures under earthquake excitation. Two trial models at distinct scales were combined to predict full-scale behaviour in situations where classical dimensional analysis failed. The efficacy of this approach was demonstrated with a high level of accuracy returned in the results and no requirement for additional mass or base accelerations to be artificially raised. The following conclusions can be drawn from the specific trials involving both analytical and numerical analysis:

1. The robustness and efficacy of a new form of similitude involving two scaled experiments have been reaffirmed through analytical and numerical studies applied to basic and practical structural engineering case studies.
2. It has been demonstrated how the first-order finite similitude rule provides an approach that enables identical ground accelerations (and gravitational) to be applied to full and scaled models. This was achieved without recourse to material substitutions and extraordinary experimental setups (e.g., use of centrifuge systems or additional mass techniques). This was demonstrated for an eight-story steel building case study where the two-experiment approach returned predictions of full-scale behaviour with no error (i.e., 0%

error) contrasted against a like-for-like single-experimental result (i.e., no additional mass, same material) of 90% error.

3. The first-order finite similitude rule has been confirmed to provide accurate predictions for a high-rise building containing non-linear viscous dampers, although a degree of physical modelling was required, i.e., the substitution of damping oil in the scaled dampers. The case study demonstrated that the combination of two trial models could replicate the physical behaviour of the full-scale model with accuracy for roof displacement and maximum story displacement.
4. The first-order finite similitude rule has been shown to be able to break the rule of geometric similarity as traditionally defined. This was demonstrated for a thin-walled beam, where the theory successfully captured the exact global behaviour of the full-scale model for displacement and stress, despite the wall thickness not following geometric scaling.
5. Nonlinear material responses were captured exactly in the thin-sectioned cantilever beam and in the pushover analysis for an 8-story steel building. No consideration was given to ductile responses arising from concrete cracking at this stage but there exists no barrier to their inclusion given the generic nature of the proposed scaling approach.

Acknowledgements

The authors would like to acknowledge The Ministry of National Education in Turkey and the Department of Civil Engineering at Firat University for providing support for Muhammed Atar to facilitate his doctoral research at the University of Manchester.

8. References

[1] Nayak S, Dutta SC. Failure of masonry structures in earthquake: A few simple cost effective techniques as possible solutions. Eng Struct 2016;106:53–67. https://doi.org/10.1016/j.engstruct.2015.10.014.

[2] Sedov LI, Friedman M, Holt M, Cole JD. Similarity and Dimensional Methods in Mechanics. J Appl Mech 1961. https://doi.org/10.1115/1.3640458.

[3] Buckingham E. On physically similar systems; Illustrations of the use of dimensional equations. Phys Rev 1914;4:345–76. https://doi.org/10.1103/PhysRev.4.345.

[4] Kline SJ, Radbill JR. Similitude and Approximation Theory. J Appl Mech 1966;33:238–238. https://doi.org/10.1115/1.3625015.

[5] Buckingham E. The principle of similitude . Nature 1915;96:396–7. https://doi.org/10.1038/096396d0.

[6] Casaburo A, Petrone G, Franco F, De Rosa S. A Review of Similitude Methods for Structural Engineering. Appl Mech Rev 2019;71. https://doi.org/10.1115/1.4043787.

[7] Dutson AJ, Wood KL. Using rapid prototypes for functional evaluation of evolutionary product designs. Rapid Prototyp J 2005;11:125–31. https://doi.org/10.1108/13552540510601246.

[8] Wissmunn JW. Dynamic Stability of Space Vehicles. Structural Dynamics Model Testing. KIRTLAND AFB: 1968.

[9] Luo Z, Wang Y, Zhu Y, Zhao X, Wang D. The similitude design method of thin-walled annular plates and determination of structural size intervals. Proc Inst Mech Eng Part C J Mech Eng Sci 2016;230:2158–68. https://doi.org/10.1177/0954406215592055.

[10] Simitses GJ, Rezaeepazhand J. Structural similitude and scaling laws for laminated beam-plates. Am. Soc. Mech. Eng. Aerosp. Div. AD, 1992.

[11] Budarapu PR, Zhuang X, Rabczuk T, Bordas SPA. Multiscale modeling of material failure: Theory and computational methods. Adv Appl Mech 2019;52:1–103. https://doi.org/10.1016/bs.aams.2019.04.002.

[12] Chen WQ. The renaissance of continuum mechanics. J Zhejiang Univ Sci A 2014;15:231–40. https://doi.org/10.1631/jzus.A1400079.

[13] Chen Y, Shabanov S, McDowell DL. Concurrent atomistic-continuum modeling of crystalline materials. J Appl Phys 2019;126:101101.

https://doi.org/10.1063/1.5099653.

[14] Sharma A, Reddy GR, Vaze KK. Shake table tests on a non-seismically detailed RC frame structure. Struct Eng Mech 2012;41:1–24. https://doi.org/10.12989/sem.2012.41.1.001.

[15] Guerrero Bobadilla H, Ji T, Escobar JA. Experimental studies of a steel frame model with and without buckling-restrained braces. Rev Ing Sísmica 2016:33–52. https://doi.org/10.18867/ris.95.338.

[16] Guerrero H, Ji T, Escobar JA, Teran-Gilmore A. Effects of Buckling-Restrained Braces on reinforced concrete precast models subjected to shaking table excitation. Eng Struct 2018;163:294–310. https://doi.org/10.1016/j.engstruct.2018.02.055.

[17] Nader MN, Astaneh-Asl A. Shaking Table Tests of Rigid, Semirigid, and Flexible Steel Frames. J Struct Eng 1996;122:589–96. https://doi.org/10.1061/(ASCE)0733-9445(1996)122:6(589).

[18] Kim SE, Lee DH, Ngo-Huu C. Shaking table tests of a two-story unbraced steel frame. J Constr Steel Res 2007;63:412–21. https://doi.org/10.1016/j.jcsr.2006.04.009.

[19] Petry S, Beyer K. Scaling unreinforced masonry for reduced-scale seismic testing. Bull Earthq Eng 2014;12:2557–81. https://doi.org/10.1007/s10518-014-9605-1.

[20] Zou Y, Lu XL. Shaking table model test on Shanghai World Financial Center. World Inf Earthq Eng 2007.

[21] Moghaddam M, Darvizeh R, Davey K, Darvizeh A. Scaling of the powder compaction process. Int J Solids Struct 2018;144–145:192–212. https://doi.org/10.1016/j.ijsolstr.2018.05.002.

[22] Sadeghi H, Davey K, Darvizeh R, Darvizeh A. A scaled framework for strain rate sensitive structures subjected to high rate impact loading. Int J Impact Eng 2019;125:229–45. https://doi.org/10.1016/j.ijimpeng.2018.11.008.

[23] Al-Tamimi A, Darvizeh R, Davey K. Experimental investigation into finite similitude for metal forming processes. J Mater Process Technol 2018;262:622–37. https://doi.org/10.1016/j.jmatprotec.2018.07.028.

[24] Ochoa-Cabrero R, Alonso-Rasgado T, Davey K. Scaling in biomechanical experimentation: A finite similitude approach. J R Soc Interface 2018. https://doi.org/10.1098/rsif.2018.0254.

[25] Sadeghi H, Davey K, Darvizeh R, Darvizeh A. Scaled models for failure under impact loading. Int J Impact Eng 2019;129:36–56. https://doi.org/10.1016/j.ijimpeng.2019.02.010.

[26] Davey K, Darvizeh R, Al-Tamimi A. Scaled metal forming experiments: A transport equation approach. Int J Solids Struct 2017;125:184–205. https://doi.org/10.1016/j.ijsolstr.2017.07.006.

[27] Davey K, Darvizeh R. Neglected transport equations: extended Rankine–Hugoniot conditions and J -integrals for fracture. Contin Mech Thermodyn 2016;28:1525–52. https://doi.org/10.1007/s00161-016-0493-2.

[28] Davey K, Sadeghi H, Darvizeh R, Golbaf A, Darvizeh A. A Finite Similitude Approach to Scaled Impact Mechanics. Int J Impact Eng 2021;148. https://doi.org/10.1016/j.ijimpeng.2020.103744.

[29] Wu JS. Analytical and Numerical Methods for Vibration Analyses. 2015. https://doi.org/10.1002/9781119137207.

[30] PEER Ground Motion Database - PEER Center n.d. https://ngawest2.berkeley.edu/spectras/273010/searches/251041/edit?fbclid=IwAR1xu9ySZ4HcvctPnKqU-rDzgeawvghlwaPRWOQIVCgwJPd7gp5ObcMveUA (accessed March 22, 2020).

[31] Kim NS, Lee JH, Chang SP. Equivalent multi-phase similitude law for pseudodynamic test on small scale reinforced concrete models. Eng Struct 2009;31:834–46. https://doi.org/10.1016/j.engstruct.2008.06.008.

[32] Abaqus U manual. Version 6.14. Dassault Systèmes Simulia Corp, Provid RI 2014.

[33] Anbuchezian A, Baskar G. Behaviour of Cold-Formed Steel Beams Under Cyclic Load Reversal. Int J Eng Sci 2013:22–30.

[34] Spiliopoulos K V., Panagiotou KD. A numerical procedure for the shakedown analysis of structures under cyclic thermomechanical loading. Arch Appl Mech 2015;85:1499–511. https://doi.org/10.1007/s00419-014-0947-6.

[35] Kauffman A, Memari A. Performance Evaluation of Different Masonry Infill Walls with Structural Fuse Elements Based on In-Plane Cyclic Load Testing. Buildings 2014;4:605–34. https://doi.org/10.3390/buildings4040605.

[36] Casaburo A, Petrone G, Meruane V, Franco F, De Rosa S. Support of Dynamic Measurements Through Similitude Formulations. Exp Tech 2021. https://doi.org/10.1007/s40799-021-00457-1.

[37] Lirola JM, Castañeda E, Lauret B, Khayet M. A review on experimental research using scale models for buildings: Application and methodologies. Energy Build 2017;142:72–110. https://doi.org/10.1016/j.enbuild.2017.02.060.

[38] Langhaar H. Dimensional analysis and theory of models. Robert E. Krieger publishing

company; 1980.

[39] Jones N. Structural Impact. 2nd ed. Cambridge University Press; 2012.

[40] Altun O, Wolniak P, Mozgova I, Lachmayer R. AN ANALYSIS OF SCALING METHODS FOR STRUCTURAL COMPONENTS IN THE CONTEXT OF SIZE EFFECTS AND NONLINEAR PHENOMENA. Proc Des Soc Des Conf 2020;1:797–806. https://doi.org/10.1017/dsd.2020.320.

[41] Davey K, Darvizeh R, Atar M. A first order finite similitude approach to scaled aseismic structures. Eng Struct 2021;231:111739. https://doi.org/10.1016/j.engstruct.2020.111739.

[42] Nature LR-, 1915. The principle of similitude. CiNiiAcJp n.d.:66–8.

[43] Oshiro RE, Alves M. Predicting the behaviour of structures under impact loads using geometrically distorted scaled models. J Mech Phys Solids 2012;60:1330–49. https://doi.org/10.1016/j.jmps.2012.03.005.

[44] Mazzariol LM, Alves M. Experimental verification of similarity laws for impacted structures made of different materials. Int J Impact Eng 2019;133:103364. https://doi.org/10.1016/j.ijimpeng.2019.103364.

[45] Mascolo I. Recent Developments in the Dynamic Stability of Elastic Structures. Front Appl Math Stat 2019;5:51. https://doi.org/10.3389/fams.2019.00051.

[46] Evkin A, Krasovsky V, Lykhachova O, Marchenko V. Local buckling of axially compressed cylindrical shells with different boundary conditions. Thin-Walled Struct 2019;141:374–88. https://doi.org/10.1016/j.tws.2019.04.039.

[47] Stuart AM. Numerical analysis of dynamical systems. Acta Numer 1994;3:467–572. https://doi.org/10.1017/S0962492900002488.

[48] Jog CS, Agrawal M, Nandy A. The time finite element as a robust general scheme for solving nonlinear dynamic equations including chaotic systems. Appl Math Comput 2016;279:43–61. https://doi.org/10.1016/j.amc.2015.12.007.

[49] Mazzariol LM, Alves M. Similarity laws of structures under impact load: Geometric and material distortion. Int J Mech Sci 2019;157–158:633–47. https://doi.org/10.1016/j.ijmecsci.2019.05.011.

[50] Riddoch DJ, Cicirello A, Hills DA. Response of a mass-spring system subject to Coulomb damping and harmonic base excitation. Int J Solids Struct 2020;193–194:527–34. https://doi.org/10.1016/j.ijsolstr.2020.02.037.

[51] Li C, Yuan Y, He P, Yuan J, Yu H. Improved equivalent mass-spring model for seismic response analysis of two-dimensional soil strata. Soil Dyn Earthq Eng

2018;112:198–202. https://doi.org/10.1016/j.soildyn.2018.05.001.

[52] De La Cruz ST, Rodríguez MA, Hernández V. Using Spring-Mass Models to Determine the Dynamic Response of Two-Story Buildings Subjected to Lateral Loads, 2012, p. 1–8.

[53] Marino L, Cicirello A. Experimental investigation of a single-degree-of-freedom system with Coulomb friction. Nonlinear Dyn 2020;99:1781–99. https://doi.org/10.1007/s11071-019-05443-2.

[54] Hou CY. Behavior explanation and a new model for nonlinear viscous fluid dampers with a simple annular orifice. Arch Appl Mech 2012;82:1–12. https://doi.org/10.1007/s00419-011-0534-z.

[55] Seleemah AA, Constantinou MC. Investigation of Seismic Response of Buildings with Linear and Nonlinear Fluid Viscous Dampers. 1997.

[56] Farahi Shahri S, Roohollah Mousavi S. Seismic behavior of beam-to-column connections with elliptic slit dampers. Steel Compos Struct 2018;26:289–301. https://doi.org/10.12989/scs.2018.26.3.289.

[57] Mousavi SA, Esfandiyari R, Zahrai SM. Experimental Study on Two Full Scale Iranian Viscous Dampers, 2018, p. 11–2.

[58] Ata AA, Kamel AG. Numerical evaluation of the effect of Combined Pendulum Tuned Mass Damper on a basic vibrating system. Int J Mechatronics Appl Mech 2018;4:270.

[59] Kasai K, Pu WC, Wada A. Response of Passively-Controlled Tall Buildings in Tokyo during 2011 Great East Japan Earthquake. iitk.ac.in, 2012.

[60] Esfandiyari R, Nejad SM, Marnani JA, Mousavi SA, Zahrai SM. Seismic behavior of structural and non-structural elements in RC building with bypass viscous dampers. Steel Compos Struct 2020;34:487–97. https://doi.org/10.12989/scs.2020.34.4.487.

[61] Pekcan G, Mander JB, Chen SS. Fundamental considerations for the design of non-linear viscous dampers. Earthq Eng Struct Dyn 1999;28:1405–25. https://doi.org/10.1002/(SICI)1096-9845(199911)28:11<1405::AID-EQE875>3.0.CO;2-A.

[62] Symans MD, Constantinou MC. Passive Fluid Viscous Damping Systems for Seismic Energy Dissipation. J Earthq Technol 1998;35:185–206.

[63] Asher JW, Young RP, Ewing RD. Seismic isolation design of the San Bernardino County Medical Center replacement project. Struct Des Tall Build 1996;5:265–79. https://doi.org/10.1002/(SICI)1099-1794(199612)5:4<265::AID-TAL77>3.0.CO;2-X.

[64] Terenzi G. Dynamics of SDOF Systems with Nonlinear Viscous Damping. J Eng

Mech 1999;125:956–63. https://doi.org/10.1061/(ASCE)0733-9399(1999)125:8(956).

[65] Awrejcewicz J, Olejnik P. Analysis of dynamic systems with various friction laws. Appl. Mech. Rev., vol. 58, American Society of Mechanical Engineers Digital Collection; 2005, p. 389–410. https://doi.org/10.1115/1.2048687.

[66] García Reyes LE. Stick-slip vibrations and chaos. J Chem Inf Model 2013;53:1689–99.

[67] Coutinho C. Structural reduced scale models based on similitude theory. 2017.

[68] Zohuri B. Dimensional analysis and self-similarity methods for engineers and scientists. 2015.

[69] Pawelski O. Ways and limits of the theory of similarity in application to problems of physics and metal forming. J Mater Process Tech 1992;34:19–30. https://doi.org/10.1016/0924-0136(92)90086-8.

[70] Barenblatt GI. Scaling, Self-similarity, and Intermediate Asymptotics - Google Books. 1996.

[71] Sadeghi H, Davey K, Darvizeh R, Rajabiehfard R, Darvizeh A. An investigation into finite similitude for high-rate loading processes: Advantages in comparison to dimensional analysis and its practical implementation. Int J Impact Eng 2020;140:103554. https://doi.org/10.1016/j.ijimpeng.2020.103554.

[72] Davey K, Darvizeh R, Atar M, Golbaf A. A Study of Scale Effects in Discrete Scaled Dynamic Systems. Int J Mech Sci 2021;199:106399. https://doi.org/10.1016/j.ijmecsci.2021.106399.

[73] Ochoa-Cabrero R, Alonso-Rasgado T, Davey K. Scaling in biomechanical experimentation: a finite similitude approach. J R Soc Interface 2018;15:20180254. https://doi.org/10.1098/rsif.2018.0254.

[74] Davey K, Mondragon R. A non-physical enthalpy method for the numerical solution of isothermal solidification. Int J Numer Methods Eng 2010;84:214–52. https://doi.org/10.1002/nme.2896.

[75] Davey K, Darvizeh R, Golbaf A, Sadeghi H. The breaking of geometric similarity. Int J Mech Sci 2020;187:105925. https://doi.org/10.1016/j.ijmecsci.2020.105925.

[76] Darvizeh R, Davey K. A transport approach for analysis of shock waves in cellular materials. Int J Impact Eng 2015;82:59–73. https://doi.org/10.1016/j.ijimpeng.2014.11.006.

[77] Lin WH, Chopra AK. Earthquake response of elastic SDF systems with non-linear fluid viscous dampers. Earthq Eng Struct Dyn 2002;31:1623–42.

https://doi.org/10.1002/eqe.179.

[78] Rodríguez S, Seim C, US TI-P of the third, 1994 undefined. Earthquake protective systems for the seismic upgrade of the Golden Gate bridge. Proc. third US-Japan Work. Earthq. Prot. Syst. Bridg., 1994, p. 4–147.

[79] Hou C-Y. Fluid Dynamics and Behavior of Nonlinear Viscous Fluid Dampers. J Struct Eng 2008;134:56–63. https://doi.org/10.1061/(ASCE)0733-9445(2008)134:1(56).

[80] Hibbett, Karlsson, Sorensen. ABAQUS/standard: User's Manual. 1998.

[81] Syrakos A, Dimakopoulos Y, Tsamopoulos J. Theoretical study of the flow in a fluid damper containing high viscosity silicone oil: Effects of shear-thinning and viscoelasticity. Phys Fluids 2018;30:030708. https://doi.org/10.1063/1.5011755.

[82] Narkhede DI, Sinha R. Behavior of nonlinear fluid viscous dampers for control of shock vibrations. J Sound Vib 2014;333:80–98. https://doi.org/10.1016/j.jsv.2013.08.041.

[83] Taylor Devices I. Fluid Viscous Dampers Manual. 2020.

[84] Galvanetto U, Bishop SR. Characterisation of the dynamics of a four-dimensional stick-slip system by a scalar variable. Chaos, Solitons and Fractals 1995;5:2171–9. https://doi.org/10.1016/0960-0779(94)00226-G.

[85] Van De Vrande BL, Van Campen DH, De Kraker A. An approximate analysis of dry-friction-induced stick-slip vibratons by a smoothing procedure An Approximate Analysis of Dry-Friction-Induced Stick-Slip Vibrations by a Smoothing Procedure *. Nonlinear Dyn 1999;19:157–69. https://doi.org/10.1023/A:1008306327781.

[86] GALVANETTO U, BISHOP SR, BRISEGHELLA L. MECHANICAL STICK-SLIP VIBRATIONS. Int J Bifurc Chaos 1995;05:637–51. https://doi.org/10.1142/s0218127495000508.

[87] Xu H, Jin X, Huang Z. Random Response of Spring–Damper–Mass–Belt System with Coulomb Friction. J Vib Eng Technol 2020;8:685–93. https://doi.org/10.1007/s42417-019-00168-3.

[88] Jin X, Xu H, Wang Y, Huang Z. Approximately analytical procedure to evaluate random stick-slip vibration of Duffing system including dry friction. J Sound Vib 2019;443:520–36. https://doi.org/10.1016/j.jsv.2018.12.001.

[89] Paredes M, Rodriguez E, Sartor M, Paredes M, Rodriguez E, Sartor M, et al. Analytical Behavior Law for a Constant Pitch Conical Compression. J Mech Des Am Soc Mech Eng 2006;6.

[90] Garevski M, Hristovski V, Talaganov, Kosta; Stojmanovska M. Experimental

Investigations of 1/3-Scale R/C Frame with Infill Walls Building Structures. Proc. 13th World Conf. Earthq. Eng., 2004, p. 772.

[91] Mohammed A, Hughes TG, Mustapha A. The effect of scale on the structural behaviour of masonry under compression. Constr Build Mater 2011;25:303–7. https://doi.org/10.1016/j.conbuildmat.2010.06.025.

[92] Knappett JA, Reid C, Kinmond S, O'Reilly K. Small-scale modeling of reinforced concrete structural elements for use in a geotechnical centrifuge. J Struct Eng 2011;137:1263–71. https://doi.org/10.1061/(ASCE)ST.1943-541X.0000371.

[93] Li S, Zuo Z, Zhai C, Xu S, Xie L. Shaking table test on the collapse process of a three-story reinforced concrete frame structure. Eng Struct 2016;118:156–66. https://doi.org/10.1016/j.engstruct.2016.03.032.

[94] Bairrao R, Vaz C. Shaking table testing of civil engineering structures-The LNEC 3D simulator experience. 2th World Conf Earthq Eng 2000;2129.

[95] Carrillo J, Gonzalez G, Llano L. Evaluation of mass-rig systems for shaking table experiments. DYNA 2012;79:159–67.

[96] Saiidi MS, Douglas B. Shake Table Testing of Flexure Dominated Reinforced Concrete Bridge Columns Report No . CCEER 99-13 Patrick Laplace Center for Earthquake Engineering Research. 1999.

[97] Chen X, Guan Z, Li J, Spencer BF. Shake Table Tests of Tall-Pier Bridges to Evaluate Seismic Performance. J Bridg Eng 2018;23. https://doi.org/10.1061/(ASCE)BE.1943-5592.0001264.

[98] Davey K, Darvizeh R, Atar M, Golbaf A. A Study of Scale Effects in Discrete Scaled Dynamic Systems. Int J Mech Sci 2021.

[99] Darvizeh R, Davey K. Non-physical finite element method: Multiple material discontinuities. Comput Struct 2016;164:145–60. https://doi.org/10.1016/j.compstruc.2015.11.010.

[100] Darvizeh R, Davey K. Non-physical finite element modelling of high speed normal crushing of cellular materials. Int J Impact Eng 2015;82:130–43. https://doi.org/10.1016/j.ijimpeng.2015.04.002.

[101] Szymczak C, Kujawa M. Flexural buckling and post-buckling of columns made of aluminium alloy. Eur J Mech A/Solids 2019;73:420–9. https://doi.org/10.1016/j.euromechsol.2018.10.006.

[102] Ramberg W, Osgood WR. Description of stress-strain curves by three parameters. Natl Advis Comm Aeronaut 1943.

[103] Szymczak C, Kujawa M. Local buckling of thin-walled channel member flange made of aluminum alloy. AIP Conf. Proc., 2017. https://doi.org/10.1063/1.4977688.

[104] Theofanous M, Gardner L. Testing and numerical modelling of lean duplex stainless steel hollow section columns. Eng Struct 2009;31:3047–58. https://doi.org/10.1016/j.engstruct.2009.08.004.

[105] Ahmed S, Ashraf M. Numerical investigation on buckling resistance of stainless steel hollow members. J Constr Steel Res 2017;136:193–203. https://doi.org/10.1016/j.jcsr.2017.05.017.

[106] Kasivitamnuay J, Singhatanadgid P. Scaling laws for displacement of elastic beam by energy method. Int J Mech Sci 2017;128–129:361–7. https://doi.org/10.1016/j.ijmecsci.2017.05.001.

[107] Alves M, Oshiro RE. Scaling the impact of a mass on a structure. Int J Impact Eng 2006;32:1158–73. https://doi.org/10.1016/j.ijimpeng.2004.09.009.

[108] Luo Z, Zhu Y, Zhao X, Wang D. Determining Dynamic Scaling Laws of Geometrically Distorted Scaled Models of a Cantilever Plate. J Eng Mech 2016;142:04015108. https://doi.org/10.1061/(asce)em.1943-7889.0001028.

[109] Wu W, Ge S, Yuan Y, Ding W, Anastasopoulos I. Seismic response of subway station in soft soil: Shaking table testing versus numerical analysis. Tunn Undergr Sp Technol n.d.;100:103389. https://doi.org/10.1016/j.tust.2020.103389.

[110] Rahnavard R, Fard FFZ, Hosseini A, Suleiman M. Nonlinear analysis on progressive collapse of tall steel composite buildings. Case Stud Constr Mater 2018;8:359–79. https://doi.org/10.1016/j.cscm.2018.03.001.

[111] Song Z, Su C. Computation of Rayleigh Damping Coefficients for the Seismic Analysis of a Hydro-Powerhouse. Shock Vib 2017;2017:1–11. https://doi.org/10.1155/2017/2046345.

[112] Chen XM, Duan J, Qi H, Li YG. Rayleigh Damping in Abaqus/Explicit Dynamic Analysis. Appl Mech Mater n.d.;627:288–94. https://doi.org/10.4028/www.scientific.net/amm.627.288.

[113] Cremer L, Heckl M. Structure-Borne Sound. 1988. https://doi.org/10.1007/978-3-662-10121-6.

[114] Vince Adams and Abraham Askenazi. Building Better Products with Finite Element Analysis. vol. 127. New York: American Society of Mechanical Engineers; n.d.

[115] Bachmann H, Ammann WJ, Deischl F, Eisenmann J, Floegl I, Hirsch GH, et al. Vibration Problems in Structures. 1995. https://doi.org/10.1007/978-3-0348-9231-5.

[116] Orban F. Damping of materials and members in structures. J Phys Conf Ser 2011;268. https://doi.org/10.1088/1742-6596/268/1/012022.

[117] Banazadeh M, Ghanbari A, Ghanbari R. Seismic performance assessment of steel moment-resisting frames equipped with linear and nonlinear fluid viscous dampers with the same damping ratio. J Constr Steel Res 2017;136:215–28. https://doi.org/10.1016/j.jcsr.2017.05.022.

[118] CSI. SAP2000. Analysis Reference Manual. CSI Berkeley (CA, USA) Comput Struct INC 2016.

[119] Ras A, Boumechra N. Seismic energy dissipation study of linear fluid viscous dampers in steel structure design. Alexandria Eng J 2016;55:1–12. https://doi.org/10.1016/j.aej.2016.07.012.

[120] Boksmati JI, Madabhushi GSP. Centrifuge modelling of structures with oil dampers under seismic loading. Earthq Eng Struct Dyn 2020;49:356–74. https://doi.org/10.1002/eqe.3243.

[121] Huneault J, Kamil J, Higgins A, Plant D. Dynamic tensile strength of silicone oils. AIP Conf. Proc., 2018. https://doi.org/10.1063/1.5044825.

Chapter SEVEN

Conclusions and Future works

7.1 Conclusions

The primary goal of this thesis was to validate and evaluate a novel scaling theory and to demonstrate the applicability of a similitude rule called finite similitude in situations where classical scaling theories fail. The new concept of scaling opens up new possibilities for designing, testing, and evaluating structures, which is the focus of this thesis. Similitude rules are investigated for both single (zeroth-order) and two scaled (first-order) experiments in order to demonstrate the benefits of alternative similitude forms. The finite similitude theory combines several concepts to create a universal scaling theory applicable to all branches of physics. One of the primary distinctions between the concept of finite similitude is space scaling and space distortion via which objects can be scaled up or down. The thesis examines the new scaling theory for investigating the aseismic behaviour of structures, how discrete mechanical dynamic systems can be used to initiate scaling parameters, how complex nonlinear mechanical dynamic systems involving nonlinear viscous dampers, springs, and friction can be scaled, and the examination of structural elements through the analysis of the whole-building subjected to earthquake loads. This novel concept introduces new scaling factors and also introduces an entirely new framework for scaling using transport equations. This research examines the analytical and numerical evaluation of various approaches, as well as the design issues and limitations of experiments involving scaled-down models that preciously represent full-scale processes. The following major conclusions can be drawn from the tasks examined:

Introducing First-order similitude theory based on two scaled experiments:

- In the field of structural mechanics, a new form of finite similitude has been established that detects all scale dependencies either explicitly or implicitly. This novel similitude theory has been developed in differential form (possibly

integrated using finite differences), which enables the reconstruction of full-scale model behaviour by combining the results from two distinct scaled models. As a result, it is possible to target additional material properties for matching between the virtual and physical full-scale models (for example, yield stress, Young's modulus, and density in earthquake-resistant structures).

- Scaling theory is straightforward and applicable to analytical, numerical, and experimental data. Additionally, the theory guides the researcher in determining whether the single experiment is sufficient to provide the best solutions, as zeroth-order finite similitude is nested within first-order finite similitude.

Evaluation of the first-order theory through practical structural and earthquake engineering applications:

- As previously stated, one of the primary challenges is the inability to scale gravitational acceleration, particularly when considering high-rise buildings and gravity dams. With regard to the new theory, it is possible to disregard the rules required in traditional scaling theories; to employ additional techniques such as additional mass or the use of different materials. It has been demonstrated that the first-order finite similitude rule provides a technique for applying similar ground accelerations (and gravity) to physical and scaled models. This was accomplished without the use of unusual experimental settings or material substitutions (e.g., use of centrifuge systems or additional mass techniques). This was demonstrated in a case study of an eight-story steel structure, where the two-experiment technique predicted full-scale behaviour more accurately than zeroth-order theory (i.e., no additional mass, same material).
- Dimensional analysis and other conventional scaling theories have difficulty accounting for scale effects such as strain, which is dimensionless. The solution to the scale effects is provided by the first-order finite similitude with the property of proportional field differences. With regard to the new theory, it is reasonable to assume that one of the primary problems has been resolved. Additionally, the newly established proportional theory enables the avoidance of computational iterative processes while providing an easy and efficient method for obtaining scaling parameters.

- It has been demonstrated that the first-order finite similitude rule is capable of violating the standard definition of geometric similarity. This was demonstrated for a thin-walled beam, where the theory effectively reproduced the precise global behaviour of the full-scale model for displacement and stress despite the wall thickness not following geometric scaling.

- While some physical modelling was required, such as substituting damping oil for the scaled dampers, the first-order finite similitude rule was verified to produce accurate predictions for a high-rise structure with non-linear viscous dampers. In the case study, the combination of two trial models successfully reproduced the full-scale model's physical behaviour in terms of roof displacement and maximum storey displacement.

Application of the zeroth and first-order similitude in discrete dynamic systems:

- The scaling behaviour of a nonlinear spring-damper-friction system was investigated. It was discovered that there is a significant difference in reaction behaviour between full-scale and single applied replica small-scale models. When the results of two distinct trial models were combined and the additional independent degree of freedom was configured appropriately, the first order finite similitude theory produced exact replication (within numerical error).
- The concept of finite similitude has been extended to encompass all scale dependencies that occur in the domain of discrete mechanical system mechanics. Scaled dependences on mass, springs, structural damping, and viscous dashpots have been defined. The scale dependency of a nonlinear fluid viscous damper was investigated, and a relationship for equivalent material selection was discovered. Additionally, it is determined that by varying the viscous damping fluid, the appropriate damping coefficient can always be obtained between the full-scale and scaled models. In the case of selecting an achievable fluid material for the trial model damper, zeroth-order finite similitude has been demonstrated to be adequate, as has complete replica scaling (i.e., A single-story case study).
- It was demonstrated that first-order theory is required for accurately describing the reaction of a discrete mechanical system to friction, whereas zeroth-order theory is insufficient for replica scaling. The scaling of a stick-slip friction system was investigated, and it was discovered that the zeroth-order finite

similitude (and thus dimensional analysis) failed to accurately represent the prototype's behaviour, whereas the first-order finite similitude did. The study demonstrated that by combining two different scaled models, the response behaviour of the actual model can be accurately reproduced.

- Analyses and numerical simulations indicated that if physically feasible, zeroth-order scaling was optimal for linear mass-spring-dashpot models, and that the dashpot trials considered here required a substitute fluid.

Application of the zeroth and first-order similitude in Continuous structural elements:

- Analytical and numerical models have been used to investigate first-order theory, which proves to be significantly better than zeroth-order (single-scale) theory. As compared to a single scaled experiment, a two scaled experiments yields higher accuracy for aseismic structures. The proposed method reduced the inaccuracy associated with a single scaled experiment to a near-perfect match when two scaled experiments were combined for the cyclically loaded three-story building.
- The advantage of matching yield stress and Young's modulus was significant for cyclic loading of a two bay, three storey frames, confirming the gains possible with the novel technique.
- It has been demonstrated that for identical material scaled experiments in cases where gravity has a negligible effect, such as the beam-strut model exposed to a quasi-static point load and elasto-plastic buckling of I-section columns, a single scaled experiment is sufficient to accurately replicate the behaviour of the full-scale model.

7.2 Recommendations for future research

Due to the constraints imposed by the dimension analysis, the present scaling approach was validated and demonstrated to be an effective methodology capable of overcoming some of the issues identified in the literatures. Due to the fact that this work is a compilation of preliminary analytical and numerical studies utilising the theory of finite similitude in structural dynamics and earthquake systems, not all facets of the subjects can be covered. The following recommendations are made for future efforts:

- **Ductile material size dependency:** In the presented research, the material properties (specifically yield stress) of metallic materials were assumed to be identical, which is inaccurate for high-rise or large structures, or for large geometric scaling factors. This can be accomplished experimentally [57-61] through the use of standard material characterization tests at various scales. As is well known, material properties play a significant role in structural design and are critical input parameters for numerical modelling and simulation results [71]. The accuracy of the mechanical material properties has a significant effect on the obtained results. Thus, future research can begin by experimentally determining the material properties of the scaled-model, and then scaling parameters and optimal design can be determined accordingly.
- **Size dependence of brittle materials:** Based on research on brittle concrete materials and the strong size dependence of their behaviour outside of the elastic limit, it is critical to conduct standard material tests for each scaled experiment at distinct sizes. References [62-67] discuss the limitations of concrete when it is scaled down. Similar work described in this report can be repeated for structures made entirely of concrete, such as gravity dams. However, because the behaviour of concrete materials in compression and tension is distinct, and the inclusion of damage parameters, a higher order finite similitude is required to provide sufficient degree of freedom for scaled experimentation design.
- **Scaling composite structures (Reinforced concrete):** The majority of real-world structural applications involve at least two distinct materials, most notably concrete and steel. The classical dimensional analysis-based approaches may address this type of problem through the use of averaging techniques on the material properties of composite structures, which are limited to the structures' elastic behaviour. However, in real-world applications such as structures subjected to seismic excitations, the structure exhibits nonlinear behaviour and damage, the design of scaled experiments clearly requires a higher degree of freedom, which necessitates the use of multiple scaled experiments, which can be provided by first-order finite similitude and an optimization algorithm. In this case, it is worthwhile to investigate whether the first-order approach works only if the violation of the zeroth-order similitude does not introduce new physics that is captured by the scaled

experiments (i.e. the material state does not change with the violation of the zeroth-order similitude).

- **Structures subjected to impulsive loading exhibit finite similitude:** While earthquakes and cyclic loads were primarily used as sources of excitation in this study, there are some other real-world situations such as structures subjected to extreme conditions (explosion, blast) [68-70]. There are many physical parameters in that affects the design of scale experiments, including the mass of explosive material, its distance from the object, the properties of the medium between the explosive material and the building (e.g. air), and the reinforced structure's physical properties. Thus, it is clear that classical dimension analysis cannot provide sufficient degrees of freedom to scale both structure and source of excitation, necessitating the use of first-order finite similitude.

References

[1] Aoyama, H., 2001. Design of modern high-rise reinforced concrete structures (Vol. 3). World Scientific.

[2] Zhou, X. and Li, G., 2010. Shaking table model test of a steel-concrete composite high-rise building. Journal of Earthquake Engineering, 14(4), pp.601-625.

[3] Young, D.F., 1971. Basic principles and concepts of model analysis. Experimental Mechanics, 11(4), pp.325-336.

[4] Casaburo, A., Petrone, G., Franco, F. and De Rosa, S., 2019. A review of similitude methods for structural engineering. Applied Mechanics Reviews, 71(3).

[5] Chambers, J.R., 2009. Modeling ight: The role of dynamically scaled free ight models in support of NASA's aerospace programs. Report NASA SP-2009-575. National Aeronautics and Space Administration.

[6] Stuart, A.M., 1994. Numerical analysis of dynamical systems. Acta numerica, 3, pp.467-572.

[7] Jog, C.S., Agrawal, M. and Nandy, A., 2016. The time finite element as a robust general scheme for solving nonlinear dynamic equations including chaotic systems. Applied Mathematics and Computation, 279, pp.43-61.

[8] Kline, S.J., 2012. Similitude and approximation theory. Springer Science & Business Media.

[9] Li, S., Zuo, Z., Zhai, C., Xu, S. and Xie, L., 2016. Shaking table test on the collapse process of a three-story reinforced concrete frame structure. Engineering Structures, 118, pp.156-166.

[10] Bairrao, R. and Vaz, C., 2000, January. Shaking table testing of civil engineering structures-The LNEC 3D simulator experience. In Proceedings 12th World Conference on Earthquake Engineering. Auckland, New Zealand, Paper (Vol. 2129).

[11] Carrillo, J., Gonzalez, G. and Llano, L., 2012. Evaluation of mass-rig systems for shaking table experiments. Dyna, 79(176), pp.159-167.

[12] Chambers, J., 2015. Modeling Flight NASA Latest Version: The role of dynamically scale Free Flight Models in support of NASA aerospace programs (Vol. 3). Joseph Chambers.

[13] Coutinho, C.J.P., 2017. Structural reduced scale models based on similitude theory (Doctoral dissertation, Universidade do Porto (Portugal)).

[14] Wood, D.M., Crewe, A. and Taylor, C., 2002. Shaking table testing of geotechnical models. International Journal of Physical Modelling in Geotechnics, 2(1), pp.01-13.

[15] Zohuri, B., 2015. Dimensional analysis and self-similarity methods for engineers and scientists. Springer.

[16] Barenblatt, G.I., 2003. Scaling (Vol. 34). Cambridge University Press.

[17] Kline, S.J., 2012. Similitude and approximation theory. Springer Science & Business Media.

[18] Dutson, A.J. and Wood, K.L., 2005. Using rapid prototypes for functional evaluation of evolutionary product designs. Rapid Prototyping Journal.

[19] Altun, O., Wolniak, P., Mozgova, I. and Lachmayer, R., 2020, May. An analysis of scaling methods for structural components in the context of size effects and nonlinear phenomena. In Proceedings of the Design Society: Design Conference (Vol. 1, pp. 797-806). Cambridge University Press.

[20] Sedov, L. I., 1959. Similarity and Dimensional Methods in Mechanics. Academic Press, New York.

[21] Meymand, P.J., 1998. Shaking table scale model tests of nonlinear soil-pile-superstructure interaction in soft clay. University of California, Berkeley.

[22] Butterfield, R., 1999. Dimensional analysis for geotechnical engineers. Geotechnique, 49(3), pp.357-366.

[23] Macagno, E.O., 1971. Historico-critical review of dimensional analysis. Journal of the Franklin Institute, 292(6), pp.391-402.

[24] Jha, A., Sedaghati, R. and Bhat, R., 2005, April. Dynamic testing of structures using scale models. In 46th AIAA/ASME/ASCE/AHS/ASC Structures, Structural Dynamics and Materials Conference (p. 2259).

[25] Baker, W.E., Westine, P.S. and Dodge, F.T., 1991. Similarity methods in engineering. Dynamics. Elsevier.

[26] Simitses, G.J. and Rezaeepazhand, J., 1992. Structural similitude and scaling laws for laminated beam-plates. In: Topics in composite materials and structures; Proceedings of the Sessions, pp.37-45.

[27] Sonin, A.A., 2001. The Physical Basis of Dimensional Analysis. Department of Mechanical Engineering, MIT, Cambridge, MA.

[28] Kim, N.S., Lee, J.H. and Chang, S.P., 2009. Equivalent multi-phase similitude law for pseudodynamic test on small scale reinforced concrete models. Engineering Structures, 31(4), pp.834-846.

[29] Langhaar, H.L., 1951. Dimensionless analysis and theory of models. John Wiley & Sons, New York.

[30] Hubbert, M.K., 1937. Theory of scale models as applied to the study of geologic structures. Bulletin of the Geological Society of America, 48(10), pp.1459-1520.

[31] Sedran, G., Stolle, D.F. and Horvath, R.G., 2001. An investigation of scaling and dimensional analysis of axially loaded piles. Canadian geotechnical journal, 38(3), pp.530-541.

[32] G.K. Wilby, 1975. Response of Concrete Structures to Seismic Motions (Ph.D. Thesis), University of Canterbury, Christchurch, New Zealand.

[33] Hansen, T.C. and Mattock, A.H., 1966, February. Influence of Size and Shape of Member on the Shrinkage and Creep of Concrete. In Journal Proceedings (Vol. 63, No. 2, pp. 267-290).

[34] Chowdhury, A.H. and White, R.N., 1977, November. Materials and modeling techniques for reinforced concrete frames. In Journal Proceedings (Vol. 74, No. 11, pp. 546-551).

[35] Moncarz, P.D., 1981. Theory and application of experimental model analysis in earthquake engineering. Stanford University.

[36] Lirola, J.M., Castaneda, E., Lauret, B. and Khayet, M., 2017. A review on experimental research using scale models for buildings: Application and methodologies. Energy and Buildings, 142, pp.72-110.

[37] Li, S., Zuo, Z., Zhai, C., Xu, S. and Xie, L., 2016. Shaking table test on the collapse process of a three-story reinforced concrete frame structure. Engineering Structures, 118, pp.156-166.

[38] Bairrao, R. and Vaz, C., 2000, January. Shaking table testing of civil engineering structures-The LNEC 3D simulator experience. In Proceedings 12th World Conference on Earthquake Engineering. Auckland, New Zealand, Paper (Vol. 2129).

[39] Carrillo, J., Gonzalez, G. and Llano, L., 2012. Evaluation of mass-rig systems for shaking table experiments. Dyna, 79(176), pp.159-167.

[40] Saiidi MS, Douglas B., 1999. Shake Table Testing of Flexure Dominated Reinforced Concrete Bridge Columns Report No: CCEER 99-13 Patrick Laplace Center for Earthquake Engineering Research.

[41] Chen, X., Guan, Z., Li, J. and Spencer Jr, B.F., 2018. Shake table tests of tall-pier bridges to evaluate seismic performance. Journal of Bridge Engineering, 23(9), p.04018058.

[42] Sharma, A., Reddy, G.R. and Vaze, K.K., 2012. Shake table tests on a non-seismically detailed RC frame structure. Structural Engineering and Mechanics, 41(1), pp.1-24.

[43] Guerrero, H., Ji, T. and Escobar, J.A., 2016. Experimental studies of a steel frame model with and without Buckling-Restrained Braces. Ingeniería sísmica, (95), pp.33-52.

[44] Nader, M.N. and Astaneh-Asl, A., 1996. Shaking table tests of rigid, semirigid, and flexible steel frames. Journal of Structural Engineering, 122(6), pp.589-596.

[45] Pawelski, O., 1964. Beitrag zur Ahnlichkeitstheorie der Umformtechnik (Contribution to Theory of Similitude in Forming Technology). Archiv f. Eisenhiuttenwesen. p. 1-10.

[46] Nguyen, V.B., Seo, J., Huh, J., Ahn, J.H. and Haldar, A., 2021. Seismic response investigation of 1/20 scale container crane through shake table test and finite element analysis. Ocean Engineering, 234, p.109266.

[47] Pawelski, O., 1992. Ways and limits of the theory of similarity in application to problems of physics and metal forming. Journal of Materials Processing Technology, 34(1-4), pp.19-30.

[48] Ozkahriman, F., 2009. Physical and numerical dynamic response modeling of slopes and embankments (Doctoral dissertation, Drexel University).

[49] Xu, Z., Xu, P. and Xiao, C., 2013. A study on the seismic performance of steel-reinforced concrete frame-concrete core wall high-rise mixed structure by large-scale shaking table tests and numerical simulations. Earthquake engineering & structural dynamics, 42(13), pp.1951-1969.

[50] Sadeghi, H., Davey, K., Darvizeh, R., Rajabiehfard, R. and Darvizeh, A., 2020. An investigation into finite similitude for high-rate loading processes: Advantages in comparison to dimensional analysis and its practical implementation. International Journal of Impact Engineering, 140, p.103554.

[51] Ochoa-Cabrero, R., Alonso-Rasgado, T. and Davey, K., 2018. Scaling in biomechanical experimentation: a finite similitude approach. Journal of The Royal Society Interface, 15(143), p.20180254.

[52] Moghaddam, M., Darvizeh, R., Davey, K. and Darvizeh, A., 2018. Scaling of the powder compaction process. International Journal of Solids and Structures, 144, pp.192-212.

[53] Davey, K., Darvizeh, R. and Al-Tamimi, A., 2017. Scaled metal forming experiments: a transport equation approach. International Journal of Solids and Structures, 125, pp.184-205.

[54] Sadeghi, H., Davey, K., Darvizeh, R. and Darvizeh, A., 2019. Scaled models for failure under impact loading. International Journal of Impact Engineering, 129, pp.36-56.

[55] Sadeghi, H., Davey, K., Darvizeh, R. and Darvizeh, A., 2019. A scaled framework for strain rate sensitive structures subjected to high rate impact loading. International Journal of Impact Engineering, 125, pp.229-245.

[56] Davey, K., Sadeghi, H., Darvizeh, R., Golbaf, A. and Darvizeh, A., 2021. A finite similitude approach to scaled impact mechanics. International Journal of Impact Engineering, 148, p.103744.

[57] Strnadel, B. and Brumek, J., 2013, July. The Size Effect in Tensile Test of Steels. In Pressure Vessels and Piping Conference (Vol. 55713, p. V06BT06A058). American Society of Mechanical Engineers.

[58] Morquio, A. and Riera, J.D., 2004. Size and strain rate effects in steel structures. Engineering structures, 26(5), pp.669-679.

[59] Zhao, Y.H., Guo, Y.Z., Wei, Q., Topping, T.D., Dangelewicz, A.M., Zhu, Y.T., Langdon, T.G. and Lavernia, E.J., 2009. Influence of specimen dimensions and strain measurement methods on tensile stress–strain curves. Materials Science and Engineering: A, 525(1-2), pp.68-77.

[60] Yuan, W.J., Zhang, Z.L., Su, Y.J., Qiao, L.J. and Chu, W.Y., 2012. Influence of specimen thickness with rectangular cross-section on the tensile properties of structural steels. Materials Science and Engineering: A, 532, pp.601-605.

[61] Hyde, T.H., Sun, W. and Williams, J.A., 2007. Requirements for and use of miniature test specimens to provide mechanical and creep properties of materials: a review. International Materials Reviews, 52(4), pp.213-255.

[62] Fládr, J. and Bílý, P., 2018. Specimen size effect on compressive and flexural strength of high-strength fibre-reinforced concrete containing coarse aggregate. Composites Part B: Engineering, 138, pp.77-86.

[63] Casaburo, A., Petrone, G., Franco, F. and De Rosa, S., 2019. A review of similitude methods for structural engineering. Applied Mechanics Reviews, 71(3).

[64] An, M.Z., Zhang, L.J. and Yi, Q.X., 2008. Size effect on compressive strength of reactive powder concrete. Journal of China University of Mining and Technology, 18(2), pp.279-282.

[65] Bažant, Z.P. and Xiang, Y., 1997. Size effect in compression fracture: splitting crack band propagation. Journal of engineering mechanics, 123(2), pp.162-172.

[66] Bažant, Z.P., 1999. Size effect on structural strength: a review. Archive of applied Mechanics, 69(9), pp.703-725.

[67] Bažant, Z.P., 2000. Size effect. International Journal of Solids and Structures, 37(1-2), pp.69-80.

[68] Masi, F., Stefanou, I. and Maffi-Berthier, V., 2020. Scaling laws for the rigid-body response of masonry structures under blast loads. arXiv preprint arXiv:2012.09494.

[69] Draganić, H., Varevac, D. and Lukić, S., 2018. An overview of methods for blast load testing and devices for pressure measurement. Advances in Civil Engineering, 2018.

[70] Reifarth, C., Castedo, R., Santos, A.P., Chiquito, M., López, L.M., Pérez-Caldentey, A., Martínez-Almajano, S. and Alañon, A., 2021. Numerical and experimental study of externally reinforced RC slabs using FRPs subjected to close-in blast loads. International Journal of Impact Engineering, p.103939.

[71] Pantano, M.F., Espinosa, H.D. and Pagnotta, L., 2012. Mechanical characterization of materials at small length scales. Journal of Mechanical Science and technology, 26(2), pp.545-561.

[72] Wu, H., Lei, H. and Lai, T., 2021. Shaking table tests for seismic response of orthogonal overlapped tunnel under horizontal seismic loading. Advances in Civil Engineering.

[73] Westine, P.S., Dodge, F.T. and Baker, W.E., 2012. Similarity methods in engineering dynamics: theory and practice of scale modelling. Elsevier.

[74] Zohuri, B., 2017. Dimensional analysis beyond the Pi theorem (Vol. 1). Cham, Switzerland: Springer International Publishing.